University of Science and Technology of China

A dissertation for doctor's degree

Measurement of the Forward-Backward Charge Asymmetry(A_{FB}) using $p\bar{p} \to Z/\gamma* \to e^+e^-$ events in $\sqrt{S} = 1.96$ TeV

Author's Name : Hang Yin

Speciality : High Energy Physics

Supervisors : Prof. Liang Han

Finished Time : June 2010

ABSTRACT

Title of dissertation: Measurement of the Forward-Backward Charge Asymmetry(A_{FB}) using $p\bar{p} \to Z/\gamma* \to e^+e^-$ events in $\sqrt{S} = 1.96$ TeV

Hang Yin, Doctor of Philosophy, 2010

Dissertation directed by: Professor Liang Han
Department of Modern Physics

This dissertation describes a measurement of the forward-backward asymmetry(A_{FB}) in $p\bar{p} \to Z/\gamma^* \to ee$ events using 5.0 fb^{-1} data collected by the DØ detector at the Fermilab Tevatron. The A_{FB} is measured as a function of the invariant mass of the electron-positron pair. Along with obtaining normalized differential cross section $\frac{1}{\sigma} \times \frac{d\sigma}{dM}$ and Z to light quark couplings, we measured the Standard Model(SM) fundamental parameter, the effective weak mixing angle $\sin^2\theta_{eff}^{lept}$, with an unprecedented precise in light quark sector, namely the single DØ measurement has surpassed the LEP combination of four experiment results of inclusive hadronic charge asymmetry.

Publications as Primary Author

- "Measurement of the forward-backward charge asymmetry and extraction of $\sin^2\theta_W^{eff}$ in $p\bar{p} \to Z/\gamma^* \to e^+e^- + X$ events produced at $\sqrt{s} = 1.96$ TeV", V. M. Abazov *et al.*

  Phys. Rev. Lett. **101**, 191801 (2008).

- "Search for scalar neutrino particles in e+μ final states in $p\bar{p}$ collisions at $\sqrt{s}$ = 1.96 TeV", V. M. Abazov *et al.*

  Phys. Rev. Lett. **100**, 241803 (2008).

- "Search for τ sneutrino particles in the electron plus muon final state at DØ", conference note 5894.

- "Search for high-mass narrow resonances in the di-electron channel at DØ", conference note 5923.

DØ Notes as Primary Author

- **Note 5603:** Measurement of the forward-backward charge asymmetry in $p\bar{p} \rightarrow Z/\gamma* + X \rightarrow ee + X$ events produced at $\sqrt{s} = 1.96$ TeV (RunIIa)

- **Note 5867:** Measurement of the forward-backward charge asymmetry in $p\bar{p} \rightarrow Z/\gamma* + X \rightarrow ee + X$ events produced at $\sqrt{s} = 1.96$ TeV (RunIIb)

- **Note 5299:** Search for sneutrino resonance in the $e + \mu$ final states in RPV SUSY at DØ (RunIIa)

- **Note 5648:** Search for sneutrino resonance in the $e + \mu$ final states in RPV SUSY at DØ (RunIIb)

- **Note 5894:** Search for sneutrino resonance in the $e + \mu$ final states in RPV SUSY at DØ (RunIIb conference note)

- **Note 5564:** A Study of electron charge misidentification in Run IIa data

- **Note 5635:** Study of electron track matching parameters with RunIIb data

- **Note 5761:** Electron and photon identification with p20 data

Presentations

- " Measurement of A_{FB} and Extraction of $\sin^2\theta_W^{eff}$ in $p\bar{p} \rightarrow Z/\gamma^* \rightarrow e^+e^- + X$ ", APS April Meeting, St. Louis, MO, April 14th, 2008.

- " Measurement of the Forward-Backward Charge Asymmetry(A_{FB}) in $p\bar{p} \rightarrow Z/\gamma^* \rightarrow e^+e^-$ events at $\sqrt{S}$=1.96 TeV ", Lake Louise Winter Institute 2010 Conference, Alberta, Canada, Feb. 16th, 2010.

- Major DØ internal talks:

  - "Stability check of Calorimeter calibration", Calorimeter Algorithm meeting, Fermilab, Nov. 27, 2007

  - "p20 electron track match study", Calorimeter Algorithm meeting, Fermilab, Feb. 20, 2008

  - "Update on Diem trigger OR - V15 study", Trigger study Group meeting, Fermilab, Feb. 21, 2008

  - "Measurement of A_{FB} and Extraction of $\sin^2\theta_W^{eff}$ in $p\bar{p} \rightarrow Z/\gamma^* \rightarrow e^+e^- + X$ ", All DØ meeting, Fermilab, April 4, 2008:

  - "Stability check of Calorimeter calibration", Calorimeter Algorithm meeting, Fermilab, Oct. 8, 2008

  - "Stability check of Calorimeter calibration", Calorimeter Algorithm meeting, Fermilab, Jan. 7, 2009

– "Energy scale lumi dependence", Electron identification meeting, Fermilab, Oct. 1, 2009

– "ϕ inter-calibration of Calorimeter", Calorimeter calibration meeting, Fermilab, Dec. 10, 2009

– "Measurement of Forward-Backward Asymmetry(A_{FB}) in $p\bar{p} \rightarrow Z/\gamma^* \rightarrow e^+e^- + X$", Electroweak meeting meeting, Fermilab, Dec. 10, 2009

The main innovations in this thesis are listed blow:

- DI-ELECTRON TRIGGER EFFICIENCY:

  Determined the di-electron trigger efficiency for the first time at DØ. With increasing instantaneous luminosity, the OR of single electron triggers is not fully efficient for electrons with transverse momentum (p_T) less than 30 GeV. This threshold (30 GeV) is too tight for many analyses. Di-electron trigger can be used to improve the trigger efficiency in low p_T region, almost all analyses with di-electron or diphoton final state (precision measurements of Z boson properties using $Z \rightarrow ee$ events, search for new di-electron resonance and search for SM Higgs boson in $H \rightarrow \gamma\gamma$ channel) benefit from this study.

- ELECTRON TRACK MATCH:

  Studied the electron track-matching requirement for Run IIb data, the new requirement has greatly reduced the probability for a jet to fake an electron.

- ELECTRON ENERGY CORRECTION:

  Studied the electron energy scale versus instantaneous luminosity and derived

correction factors. This correction helped to improve the electron energy resolution for the whole Run IIb data.

- INTER-CALIBRATION OF CALORIMETERS:

  Performed ϕ inter-calibration for both the electromagnetic and hadronic calorimeters after the 2009 shutdown. The ϕ inter-calibration is mainly to uniformize the response of each η ring and reduce the constant term for the calorimeter energy resolution. This is very important for almost all analyses done at DØ. Performed the stability check of calibration constants every six months since July 2007 and monitored the calorimeter performance over time.

- ELECTRON ENERGY SCALE/RESULUTION:

  Studied the energy scale/resulution of electron, which make the Monte Carlo has a reasonable agreement with real data in the Z-pole region. The agreement in Z-pole mass region make the precise measurements of W and Z bosons' properties is possible.

- UNFOLDING:

  Distributions measured in high-energy physics(HEP) experiments are often distorted or transformed by limited acceptance and finite resolution of the detectors. The unfolding of measured distributions is an important, in this analysis, we used the response matrices method to do the unfolding.

- HIGH ORDER CORRECTIONS:

  The Geant Monte Carlo(MC) used in DØ is PYTHIA, which is a leading or-

der(LO) generator. In this analysis, in order to compare the measurements directly with LEP and SLD results, we do the next-next-to-leading order(NNLO) k-factor correction at first, and then with the next-to-leading order(NLO) generator ZGRAD2, we measured the NLO EW final state radiation(FSR) corrections, and apply 2D($M_Z - \cos\theta*$) reweighting on the signal, which make precise measurements on Tevatron can compared with LEP, SLD directly.

To my family

parents, wife, son and sister.

Acknowledgements

During this thesis writing, I know it is the time to thank all of people who kindly provided me help in different ways. This work would not have been possible without them help.

First I would like to thank my advisor Professor Liang Han, for his tireless guidance and useful discussion. When I started working at DØ, he patiently taught me almost all of things need for HEP, from Linux system operations to how to write a $C++$ program, from the Feynman-Diagram to the detectors of hadronic collider. I feel very lucky to have worked with him for the past five years and appreciate all the skills and knowledge that I have learned from him, and I believe those will continue to benefit me in my future. I also extend my appreciation specially to Professor Yanwen Liu, who gave me a lot of help on my service works when he stayed in FermiLab 2007.

Secondly, I would like to thank Professor Junjie Zhu(University of Michigan), for taking such good care of me. He taught me so much and been like my advisor at FermiLab. Each time I had anything do not understand, I could always turn to him for help, and he always could make a complicate problem became problem can be easily solved. I really feel very lucky to

have worked with him for past three years.

Thirdly, I would like to thank all the people in DØ Electroweak group, specially thank Professor Heidi Schellman, she gave me so many fresh ideals during the analysis. Also thank Professor Tim Bolton, Martin Grunewald, and Andrew Askew and all members in EB-021(chaired by Cecilia Gerber) for many useful discussion and comments.

I would like to thank all the students in our USTC HEP group: Xuebing Bu, Hongtang Wei, Pengfei Ding, Chenwei Gong and Siqi Yang. I also had a wonderful experience working in the calorimeter calibration group and electron-identification group, it was pleasant to work with those wonderful people. Sorry that I cannot mention all their names here, because it will be really long list. Many thanks to the friends I got to know in Fermilab: Junjie Zhu, Yunhe Xie, Weigang Geng, Zhenyu Ye, Tingjun Yang, Zhiyi Liu, Chun Xun, Feng Guo, Guo Chen, Xiao Cai and Yu Zeng. With all of them, my stay in Fermilab and USTC turns to a lot more enjoyable and delightful.

Finally I would like to thank my family and my wife Guoxia Pang, who sharing the last five years of her life with me. I would have never made it without her love and support.

Contents

List of Figures

LIST OF FIGURES

Chapter 1

Introduction

1.1 Standard Model

One of the main goals of particle physics is to understand what matter is made of, and what are the forces in nature through which matter interacts. Our current understanding of the fundamental forces is contained in the description of the gravitational, the strong, the weak and the electromagnetic interactions among elementary particles. These forces are transmitted by specific fields or particles which are equivalent concepts in relativistic quantum field theory.

In the 1960s, S.L. Glashow, A. Salam and S. Weinberg unified the electromagnetic and weak interactions into the electroweak theory [1], which, together with Quantum Chromodynamics (the theory of the strong interaction) [2], forms the Standard Model (SM) of particle physics. The SM is a quantum field theory that includes $SU(3)_C$ color symmetry of strong interaction, and $SU(2)_W \times U(1)_Y$ weak isospin doublet and supercharge symmetry of electroweak interaction. The SM provides a very elegant

theoretical framework and it has successfully passed very precise tests [3].

Both electroweak and QCD theories are gauge field theories, meaning that they model the forces between fermions by coupling them to bosons which mediate the forces. The Lagrangian of each set of mediating bosons is invariant under gauge transformation, so these mediating bosons are referred to as gauge bosons. The eight massless gluons, g_α, mediate strong interactions among quarks. The massless photon, γ, is the exchange particle in electromagnetic interactions, and the three massive weak bosons, $W^\pm$ and Z, are the corresponding intermediate bosons that mediate the weak interaction. Table 1.1 summarizes the fundamental forces and the properties of their gauge bosons [4].

Force	Boson Name	Symbol	Charge ($\|e\|$)	Spin	Mass (GeV/c^2)
Strong	Gluon	g	0	1	0
Electromagnetic	Photon	γ	0	1	0
Weak	W-boson	$W^\pm$	±1	1	80.423 ± 0.039
	Z-boson	Z^0	0	1	91.1876 ± 0.0021
Gravitational	Graviton	G	0	2	0

Table 1.1: Fundamental forces and gauge bosons.

Apart from the gauge bosons, there are six leptons and six quarks. The six leptons are electron, μ, τ and the corresponding neutrinos; the six quarks are up, down, charm, strange, bottom, and top quarks. These six leptons and six quarks are fermions of spin $s = \frac{1}{2}$ and can be grouped into three generations (also called families) as shown

in Table 1.2. As we know, the weak charged current interaction is parity-violating, and connects, for example, the left-handed (LH) states of neutrino and electron. On the other hand the electromagnetic interaction is parity-conserving and involves both LH and RH states of the electron. Hence we have to assign the lepton states to a LH doublet and a RH singlet, as follows (here we just consider the case of the first generation leptons: electron and electron neutrino)

$$R_e = (e)_R \tag{1.1}$$

$$L_e = \begin{pmatrix} \nu_e \\ \\ e^- \end{pmatrix}_L$$

where the LH and RH components of a field ψ are defined by

$$\psi_R = \frac{1-\gamma_5}{2}\psi \tag{1.2}$$

$$\psi_L = \frac{1+\gamma_5}{2}\psi \tag{1.3}$$

here γ_5 is the chirality operator. The charged currents are thus defined as

$$J_\mu^+ = \bar{\nu}\gamma_\mu \frac{1+\gamma_5}{2} e = \bar{\nu}_L \gamma_\mu e_L = \bar{\psi}_L \gamma_\mu \tau^+ \psi_L \tag{1.4}$$

and

$$J_\mu^- = \bar{e}\gamma_\mu \frac{1+\gamma_5}{2} \nu = \bar{e}_L \gamma_\mu \nu_L = \bar{\psi}_L \gamma_\mu \tau^- \psi_L \tag{1.5}$$

where $\tau^\pm = \tau_1 \pm \tau_2$ are the Pauli operators suitable for describing $I = 1/2$ systems, γ_μ are Dirac matrices. The neutral current will be

$$J_\mu^{(3)} = \bar{\psi}_L \gamma_\mu \tau_3 \psi_L = \bar{\psi}\gamma_\mu \frac{1+\gamma_5}{2} I_3 \psi = \frac{1}{2}(\bar{\nu}_L \gamma_\mu \nu_L - \bar{e}_L \gamma_\mu e_L) \tag{1.6}$$

Generation	Leptons (spin=$\frac{1}{2}$)		
	Flavors	Charge ($\|e\|$)	Mass (MeV/c^2)
1	e	-1	0.511
	ν_e	0	$< 3 \times 10^{-6}$
2	μ	-1	105.66
	ν_μ	0	< 0.19
3	τ	-1	1776.99 ± 0.29
	ν_τ	0	< 18.2
	Quarks (spin=$\frac{1}{2}$)		
	Flavors	Charge ($\|e\|$)	Mass (MeV/c^2)
1	u	$+2/3$	$1.5 - 5$
	d	$-1/3$	$3 - 9$
2	c	$+2/3$	$(1.0 - 1.4) \times 10^3$
	s	$-1/3$	$60 - 170$
3	t	$+2/3$	$(178.0 \pm 4.3) \times 10^3$
	b	$-1/3$	$(4.0 - 4.5) \times 10^3$

Table 1.2: Three generations of elementary particles.

The electroweak theory is the unified description of two fundamental interactions: electromagnet interaction and the weak interaction. These two forces appear very different at low energies, but above the unification energy, on the order of 100 GeV, they would merge into a single electroweak interaction. During 1960s, S.L. Glashow, A. Salam, and S. Weinberg [1] unified the weak and electromagnetic. And more important thing, the renormalizable of electroweak theory [5][6] make this theory has the predictive power. The theory predicted the existence of neutral currents and W and Z gauge bosons. In 1973 Weak Neutral Currents(WNC) were discovered simultaneously by two neutrino experiments at CERN [7] and Fermilab [8], and within a few years the first measurements of $\sin^2\theta_W$ was made [9]. In 1983 the discovery of the W and Z gauge bosons[10] proved possible to measure their masses with great precision, which has allowed a stringent comparison of the electroweak theory with experiment.

The electroweak interaction is based on an $SU(2)$ group of "weak isospin", I, and a $U(1)$ group of "weak hypercharge", Y. The Lagrangian energy density of fermions with the fields $\mathbf{W}_\mu$ and B_μ is the product of the fermion currents with the fields, that is, of the form [12] [13]

$$L = g\mathbf{J}_\mu \bullet \mathbf{W}_\mu + g' J^Y_\mu B_\mu \tag{1.7}$$

where $\mathbf{J}_\mu$ and J^Y_μ represent respectively the isospin and hypercharge currents of the fermions, and g, g' are the couplings of fermions to $\mathbf{W}_\mu$ and B_μ. If we define the weak hypercharge as $Y = Q - I_3$, where Q is the electric charge and I_3 the third component of weak isospin, then the corresponding relation among the currents is

$$J^Y_\mu = J^{em}_\mu - J^{(3)}_\mu \tag{1.8}$$

where J^{em}_μ is the electromagnetic current, coupling to the charge Q, and $J^{(3)}_\mu$ is the

third component of the isospin current $\mathbf{J}_\mu$.

The Lagrangian is thus

$$L = g\mathbf{J}_\mu \bullet \mathbf{W}_\mu + g' J^Y_\mu B_\mu \tag{1.9}$$

$$= g(J^{(1)}_\mu W^{(1)}_\mu + J^{(2)}_\mu W^{(2)}_\mu) + g(J^{(3)}_\mu W^{(3)}_\mu) + g'(J^{em}_\mu - J^{(3)}_\mu)B_\mu \tag{1.10}$$

where $W^{(i)}_\mu$, $i = 1, 2, 3$, are the weak bosons of the $SU(2)_L$ group, and B_μ is the hypercharge boson of the $U(1)_Y$ group. The physical bosons consist of the charged particles $W^\pm_\mu$ and the neutrals Z_μ and A_μ. Thus, if we set

$$W^\pm_\mu = \frac{1}{\sqrt{2}}(W^{(1)}_\mu + iW^{(2)}_\mu) \tag{1.11}$$

then

$$L = (g/\sqrt{2})(J^-_\mu W^+_\mu + J^+_\mu W^-_\mu) + J^{(3)}_\mu(gW^{(3)}_\mu - g'B_\mu) + J^{em}_\mu g' B_\mu \tag{1.12}$$

$$= \frac{g}{\sqrt{2}}(J^-_\mu W^+_\mu + J^+_\mu W^-_\mu) + \frac{g}{\cos\theta_W}(J^{(3)}_\mu - \sin^2\theta_W J^{em}_\mu)Z_\mu + g\sin\theta_W J^{em}_\mu A_\mu \tag{1.13}$$

$$= L_{CC} + L_{NC} + L_{em} \tag{1.14}$$

where $J^\pm_\mu = J^{(1)}_\mu \pm iJ^{(2)}_\mu$ and the angle θ_W is called the weak mixing angle (or Weinberg angle), this equation shows that the interaction contains the weak charge-changing current

$$L_{CC} = \frac{g}{\sqrt{2}}(J^-_\mu W^+_\mu + J^+_\mu W^-_\mu) \tag{1.15}$$

a weak neutral current

$$L_{NC} = \frac{g}{\cos\theta_W}(J^{(3)}_\mu - \sin^2\theta_W J^{em}_\mu)Z_\mu \tag{1.16}$$

and the electromagnetic current

$$L_{em} = g\sin\theta_W J^{em}_\mu A_\mu \tag{1.17}$$

for which we know the coupling to be e. Hence

$$e = g \sin\theta_W = g' \cos\theta_W \tag{1.18}$$

and

$$\sin\theta_W = \frac{g'}{\sqrt{g^2 + g'^2}}, \tag{1.19}$$

$$\cos\theta_W = \frac{g}{\sqrt{g^2 + g'^2}} \tag{1.20}$$

In Vector and Axial-Vector($V - A$) theory, the charged current matrix element is [14]

$$|M| = \frac{G}{\sqrt{2}}[\bar{e}\gamma_\mu(1+\gamma_5)\nu][\bar{\nu}\gamma_\mu(1+\gamma_5)e] \tag{1.21}$$

where G is the Fermi coupling constant. Compared with the expressions 1.14, 1.4 and 1.5, in the limit of $q^2 \ll M_W^2$, we have

$$|M| = \left(\frac{g}{\sqrt{2}}\right)^2 \frac{1}{M_W^2}\left[\bar{e}\gamma_\mu \frac{1+\gamma_5}{2}\nu\right]\left[\bar{\nu}\gamma_\mu \frac{1+\gamma_5}{2}e\right] \tag{1.22}$$

so that

$$\frac{G}{\sqrt{2}} = \frac{g^2}{8M_W^2} \tag{1.23}$$

it follows that

$$M_W = \left(\frac{\sqrt{2}\ g^2}{8\ G}\right)^{1/2} = \left(\frac{\sqrt{2}\ e^2}{8\ G \sin^2\theta_W}\right)^{1/2} \tag{1.24}$$

With given equations of $W_\mu^{(3)}$ and B_μ,

$$W_\mu^{(3)} = \frac{gZ_\mu + g'A_\mu}{\sqrt{g^2 + g'^{\,2}}} \tag{1.25}$$

$$B_\mu = \frac{-g'Z_\mu + gA_\mu}{\sqrt{g^2 + g'^{\,2}}} \tag{1.26}$$

we find

$$Z_\mu = W_\mu^{(3)} \cos\theta_W - B_\mu \sin\theta_W \tag{1.27}$$

$$A_\mu = W_\mu^{(3)} \sin\theta_W + B_\mu \cos\theta_W \tag{1.28}$$

so that, using the empirical fact that the photon is massless and orthogonal to the Z, we get

$$M_Z = \left(\frac{\sqrt{2}\ e^2}{8\ G}\right)^{1/2} \frac{1}{\sin\theta_W \cos\theta_W} = \frac{M_W}{\cos\theta_W} \tag{1.29}$$

There are fundamental parameters in SM, which should be determined by experiment, conventionally can be chosen as α, G_F, M_Z, M_W and $\sin^2\theta_W$. In the current structure of the SM, only three of them are independent, and the first most precise-measured three are chose as input. With given fine structure constant α_{EM} ($g^2\sin^2\theta_W/4\pi$), the Fermi coupling constant G_F, and Z boson mass M_Z, the mass of W boson can be determined. Three measurable SM input parameters(not counting the Higgs boson mass, m_H, and the fermion masses and mixing.) is shown in the following

$$\alpha_{EM} = 1/(137.0359895 \pm 0.0000061) \tag{1.30}$$

$$G_F = 1.16639(\pm 0.00002) \times 10^{-5}\ \text{GeV}^{-2} \tag{1.31}$$

$$M_Z = 91.1884 \pm 0.0022\ \text{GeV}/c^2 \tag{1.32}$$

The fine structure constant is measured from the quantum Hall effect [15]; the Fermi coupling constant is measured from the muon lifetime ($\Gamma(\mu^- \to e^-\bar{\nu}_e\nu_\mu) = G^2 m_\mu^5/(192\pi^3)$) [15], and M_Z is measured directly by the combined experiments at the CERN e^+e^- collider LEP [16]. In the SM at tree level, the relationship between the weak and electromagnetic couplings is given by where G_F is the Fermi constant, α

is the electromagnetic fine-structure constant, M_W is the W boson mass. With these inputs, $\sin^2\theta_W$ and the W boson mass M_W can be calculated with given m_t and m_H. m_H can be constrained by $\sin^2\theta_W$ and M_W, which is shown in Fig. 1.3.

1.2 Weak mixing angle

The weak mixing angle is an important parameter of the Standard Model. The value of $\sin^2\theta_W$ is depends on the renormalization prescription, according to the different dependence on the m_t and m_H, there are five schemes leading to values, which are shown in Table 1.3 and described below.

Scheme	Notation and Value
On-Shell	$s_W^2 = \sin^2\theta_W \approx 0.2231$
NOV	$s_{M_Z}^2 = \sin^2\theta_W \approx 0.2311$
$\overline{MS}$	$\hat{s}_Z^2 = \sin^2\theta_W \approx 0.2312$
$\overline{MS}$ ND	$\hat{s}_{ND}^2 = \sin^2\theta_W \approx 0.2314$
Effective	$\bar{s}_f^2 = \sin^2\theta_W \approx 0.2315$

Table 1.3: The weak mixing angle value with difference schemes.

- At tree level it relates the masses of the W and Z bosons [23],

$$\sin^2\theta_W \to s_W^2 = 1 - \frac{m_W^2}{m_Z^2} \tag{1.33}$$

- $s_{M_Z}^2$

The $s^2_{M_Z}$ [24] is obtained from M_Z by removing the (m_t, M_H) dependent term from Δr.

$$s^2_{M_Z} c^2_{M_Z} \equiv \frac{\pi\alpha(M_Z)}{\sqrt{2}G_F M_Z^2} \tag{1.34}$$

Given $\alpha(M_Z)^{-1} = 128l.91 \pm 0.02$ yields $s^2_{M_Z} = 0.23108 \mp 0.00005$. Since the m_t dependence has been removed by definition, $s^2_{M_Z}$ has a smaller uncertainty than other schemas. However, the m_t uncertainty reemerges when other quantities are predicted in the terms of M_Z. Both s^2_W and $s^2_{M_Z}$ depend not only on the gauge couplings but also on the spontaneous-symmetry breaking, and both definitions are awkward in the presence of any extension of SM which perturbs the value of M_Z(or M_W).

- Modified minimal subtraction($\overline{MS}$)

  The modified minimal subtraction($\overline{MS}$) scheme introduces the quantity

$$\sin^2\hat{\theta}_W(\mu) \equiv \frac{\hat{g}'^2}{\hat{g}^2(\mu) + \hat{g}'^2(\mu)} \tag{1.35}$$

  where the couplings $\hat{g}$ and $\hat{g}'$ are defined by modified minimal subtraction and the scale μ is chosen to be M_Z for many electroweak processes. $\hat{s}^2_Z = \sin^2\hat{\theta}_W(M_Z)$ is extracted from M_Z, which is less sensitive to m_t and most types of new physics than other scheme, but it is also useful to comparing with the predictions of grand unification. According to whether or how finite $\alpha ln(m_t/M_Z)$ terms are decoupled, there are several variant definitions of $\sin^2\hat{\theta}_W(M_Z)$.

- Non-decouple($\hat{s}^2_{ND}$)

A variant $\overline{MS}$ quantity $\hat{s}^2_{ND}$ does not decouple the $\alpha ln(m_t/M_Z)$ terms [25]. It is related to $\hat{s}^2_Z$ by

$$\hat{s}^2_Z = \hat{s}^2_{ND}/(1+\frac{\alpha}{\pi}d) \tag{1.36}$$

$$d = \frac{1}{3}\left(\frac{1}{\hat{s}^2}-\frac{8}{3}\right)\left[(1+\frac{\alpha_s}{\pi})ln\frac{m_t}{m_Z}-\frac{15\alpha_s}{8\pi}\right] \tag{1.37}$$

Thus, $\hat{s}^2_Z - \hat{s}^2_{ND} \sim -0.0002$ for $m_t = 172.7$ GeV.

- Effective $\sin^2\theta_{eff}$

As describe in Sec.1.1, the neutrals bosons Z_μ and A_μ can be written as:

$$\begin{pmatrix} A_\mu \\ Z_\mu \end{pmatrix} = \begin{pmatrix} \cos\theta_W & \sin\theta_W \\ -\cos\theta_W & \cos\theta_W \end{pmatrix} \begin{pmatrix} B_\mu \\ W^(3)_\mu \end{pmatrix} \tag{1.38}$$

And the weak neutral current interaction term can be written as

$$-\frac{g}{2\cos\theta_W}\sum_i \bar{\Psi}_i\gamma_\mu(g^i_V - g^i_A\gamma_5)\Psi_i Z_\mu \tag{1.39}$$

The vector(g^i_V) and axial-vector(g^i_A) couplings of the Z boson with fermions depends on charge Q, and the third component of weak-isospin I^f_3:

$$g^i_V \equiv (I^f_3 - 2Q_f\sin^2\theta_W) \tag{1.40}$$

$$g^i_A \equiv I^f_3 \tag{1.41}$$

The electroweak radiative corrections to the couplings at the Z-pole up to all orders can be absorbed into complex form factors, R_f for the overall scale and K_f for the on-shell electroweak mixing angle, resulting in complex effective couplings:

$$\mathcal{G}^f_V = \sqrt{R_f}(I^f_3 - 2Q_f K_f \sin^2\theta_W) \tag{1.42}$$

$$\mathcal{G}^f_A = \sqrt{R_f} I^f_3 \tag{1.43}$$

In terms of the real parts of the complex form factors,

$$\rho_f \equiv \Re(R_f) = 1 + \Delta\rho_{se} + \Delta\rho_f \tag{1.44}$$

$$k_f \equiv \Re(k_f) = 1 + \Delta k_{se} + \Delta k_f \tag{1.45}$$

The effective electroweak mixing angle and the real effective couplings are defined as:

$$\sin^2\theta^f_{eff} \equiv k_f \sin^2\theta_W \tag{1.46}$$

$$g^f_V \equiv \sqrt{\rho_f}(I^f_3 - 2Q_f \sin^2\theta^f_{eff}) \tag{1.47}$$

$$g^f_A \equiv \sqrt{\rho_f} I^f_3 \tag{1.48}$$

so that

$$\frac{g^f_V}{g^f_A} = \Re\left(\frac{\mathcal{G}^f_V}{\mathcal{G}^f_A}\right) = 1 - 4 \mid Q_f \mid \sin^2\theta^f_{eff} \tag{1.49}$$

The quantities $\Delta\rho_{se}$ and Δk_{se} are universal corrections arising from the propagator self-energies, which have sensitivity to the Higgs field, while $\Delta\rho_f$ and Δk_f are flavor-specific vertex corrections. The radiative corrections to the propagators and vertices are shown in Fig.1.1 and 1.2 (For vertices correction, just take LEP b channel as example).

1.2.1 Experimental results of $\sin^2\theta^{eff}_W$

Precise determinations of $\sin^2\theta^{lept}_{eff}$ have been measured at various energy scale Q: atomic parity violation experiments [17] with Q below 0.01 GeV, the Moller scattering experiment using polarized electron beam scattering off unpolarized electrons in a liquid hydrogen target with an average Q of 0.16 GeV [18], the NuTeV experiment using deep inelastic scattering of neutrinos/anti-neutrinos from isoscalar target with

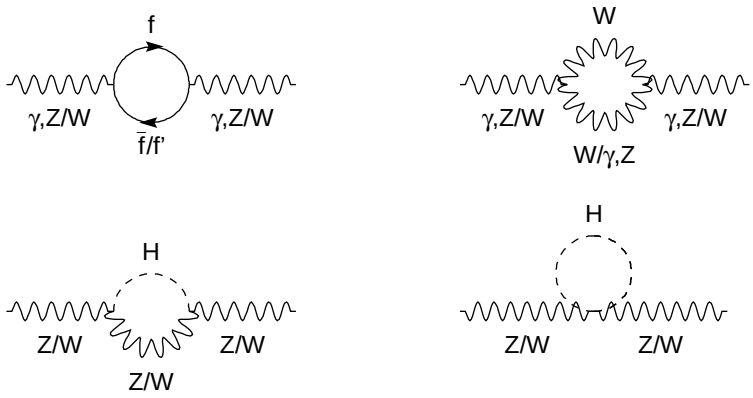

Figure 1.1: Higher-order corrections to the gauge boson propagators due to boson and fermion loops.

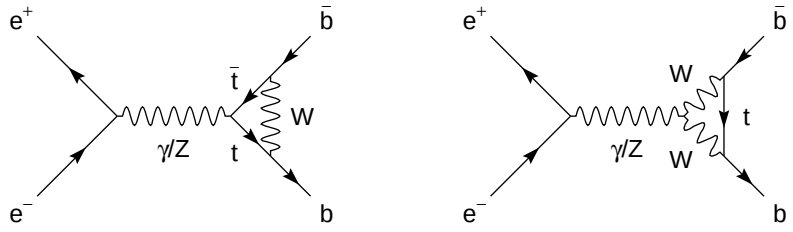

Figure 1.2: Vertex corrections to the process $e^+e^- \to b\bar{b}$ at LEP.

an average of Q of 2 GeV [22], the LEP experiments using unpolarized e^+/e^- beams and the SLD experiment using polarized beams to measure various asymmetries [21] with Q around Z resonance. The current world average value of $\sin^2\theta_{eff}^{lept}$ is dominated by the results from the LEP b-quark forward-backward asymmetry ($A_{fb}^{0,b}$) and the SLD left-right asymmetry ($A_l(SLD)$). The measured $\sin^2\theta_{eff}^{lept}$ values from these two most precise measurements diff by about three standard deviation.(the measurement from LEP of $A_{FB}^{0,b}$ is 2.4 σ from the fit [21],which is shown in Fig. 1.4.) The LEP experiments also measured the effective weak mixing angle in inclusive hadronic charge asymmetry Q_{fb}^{had}, dominated by significant systematic uncertainty due to the ambiguity of charge separation in light quark events. The Drell-Yan production of charged lepton pair at the Tevatron is the inverse process of the $e^+e^- \rightarrow q\bar{q}$;contrasting to the large uncertainty of final state quark at LEP, the initial quark components at Tevatron are governed by well-understood parton distribution function (PDF), and therefore with sufficient statistics in Tevatron Run II, the data collected by the CDF and D0 collaborations could lead to a measurement of $\sin^2\theta_{eff}^{lept}$ with a precision comparable to that of the current world average. And the NuTeV measurement of $\sin^2\theta_W$ is 2.9 σ from the fit [22].

Unfortunately in Run I, DØ does not have the magnet surround the tracking detector, so it is impossible to determine the charge of lepton, therefore cannot measure the forward-backward asymmetry. So in 2001, DØpublished a paper only with the differential cross section measurement, which is shown in Fig.1.5. And in RunII, with 2 T magnetic field and tracking detector, DØ experiment can measure this forward-backward charge asymmetry, we published the results using 1.1 fb^{-1} Run II data [28].

The A_{FB} results from all Tevatron experiments agree with the SM prediction pretty well, which is shown in Fig.1.6.

In addition, the invariant mass dependent A_{FB} measurement also provides direct probe of relative strengths of the vector and axial-vector couplings of u and d light quarks. At the LEP and SLD experiments, it is hard to distinguish between light flavor partons, and thus SM relations are assumed to extract Z-light parton coupling constants. While at the Tevatron, the dominant production processes are $u\bar{u} \rightarrow ee$ and $d\bar{d} \rightarrow ee$, so we can have a direct probe of the Z-light quark couplings using $Z \rightarrow ee$ events we collected. Similar preliminary results have been shown by H1 and ZEUS experiments, but with larger uncertainties, which is shown in Fig. 1.7. With 5 fb^{-1} of data, we expect to have the more precise measurement of Z-light quark couplings.

1.3 The Forward-Backward charge asymmetry

In Tevatron, the Drell-Yan process is $q\bar{q} \rightarrow Z/\gamma* \rightarrow e^+e^-$, which is the reverse process of LEP hadronic productions, with more events in Tevatron than LEP, the $\sin^2\theta_W^{eff}$ can be measured more precisely. the lowest order via photon and Z boson exchange is shown in Fig. 1.8. Here the fermion q is a quark. The neutral current couplings of a fermion f to the Z boson has vector and axial-vector components:$J^{Zf}\ \bar{f}(g_V^f + g_A^f\gamma_5)f$, where g_V^f and g_A^f are vector and axial-vector couplings of the fermion to the Z respectively.

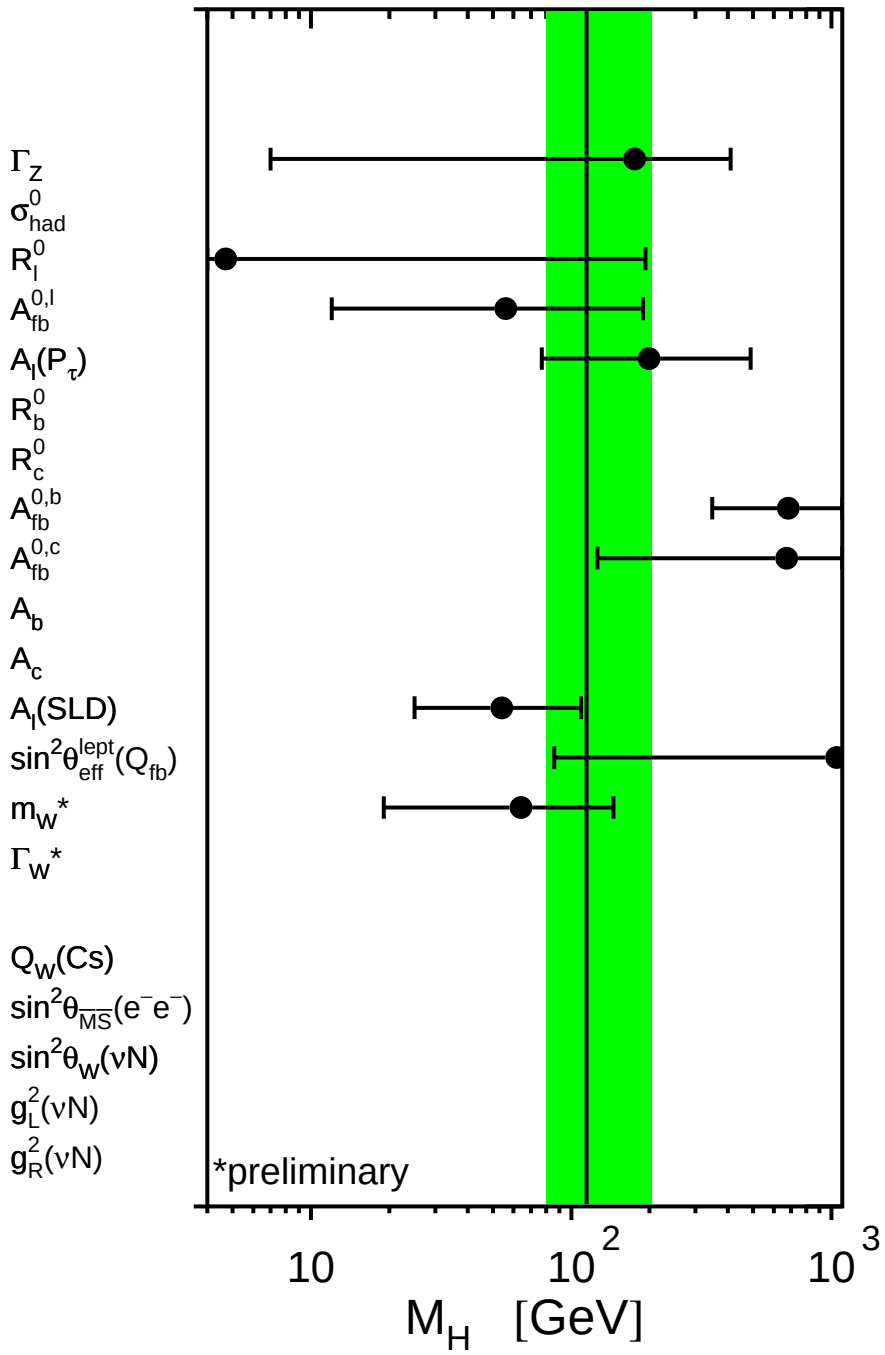

Figure 1.3: Constraints on the mass of the Higgs boson from each pseudo-observable. The Higgs-boson mass and its 68% CL uncertainty is obtained from a five-parameter SM fit to the observable..

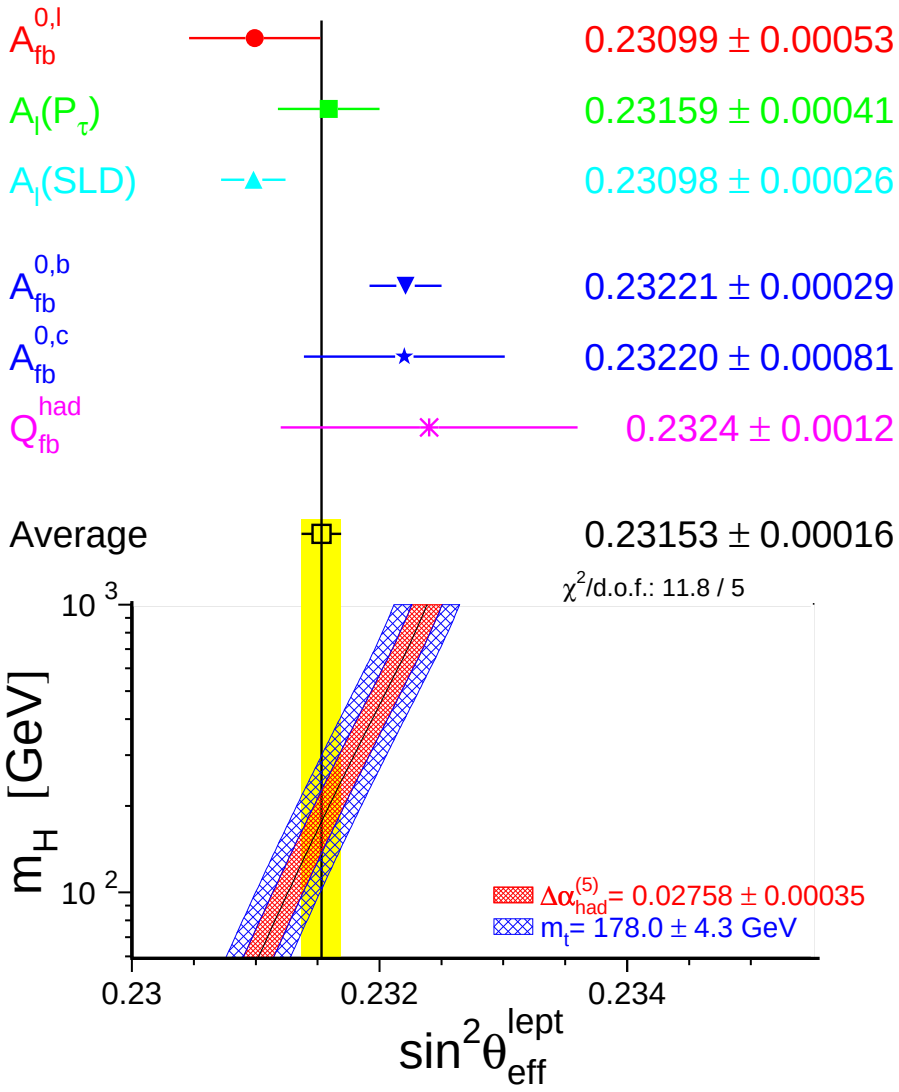

Figure 1.4: Comparison of the effective electroweak mixing angle $\sin^2\theta_W$ from LEP and SLC. Also shown is the SM prediction for $\sin^2\theta_W$ as a function of m_H. The additional uncertainty of the SM prediction is shown as the bands.

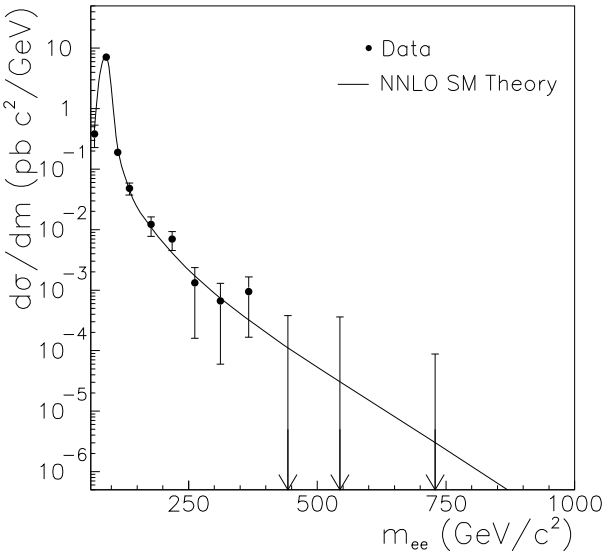

Figure 1.5: DØRunI published 120 pb^{-1} $d\sigma/dM$results.

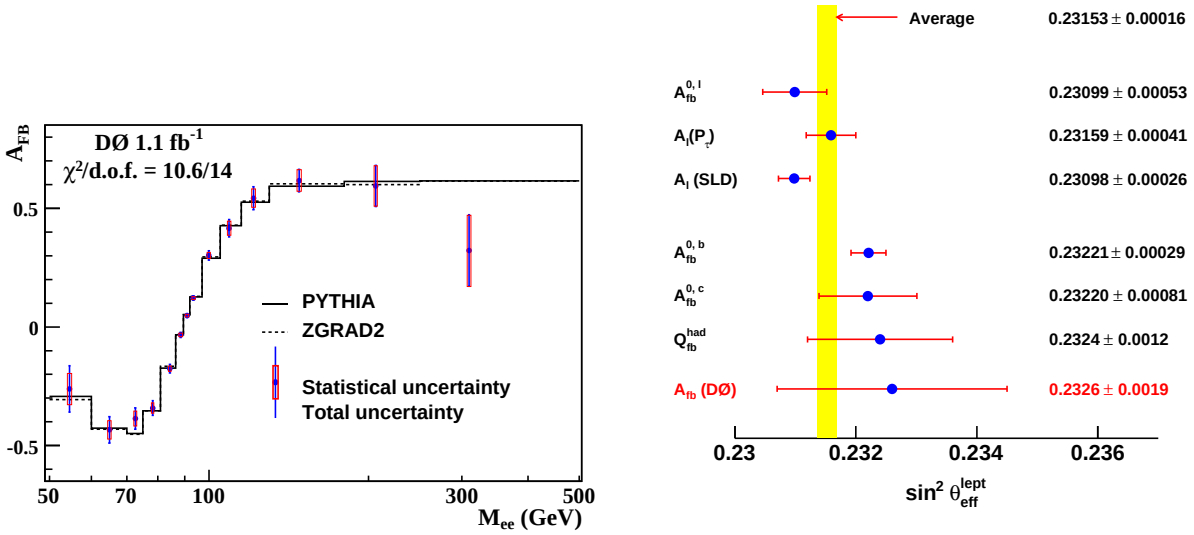

Figure 1.6: DØ RunII published 1.1 fb^{-1} results. The left plot is the A_{FB} results, and right one is measured $\sin^2\theta_W$ results.

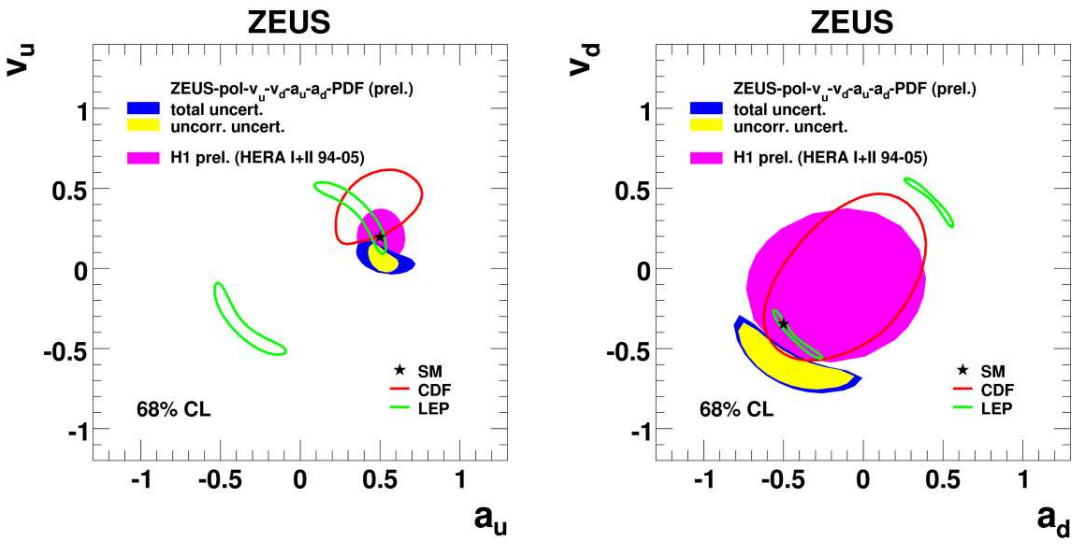

Figure 1.7: Z to u/d quark couplings from other experiments. The Red contour is CDF RunII[27] results, green contour is LEP[21] results, the pink region is results from H1 experiment, Blue and yellow region is results from ZEUS experiment.

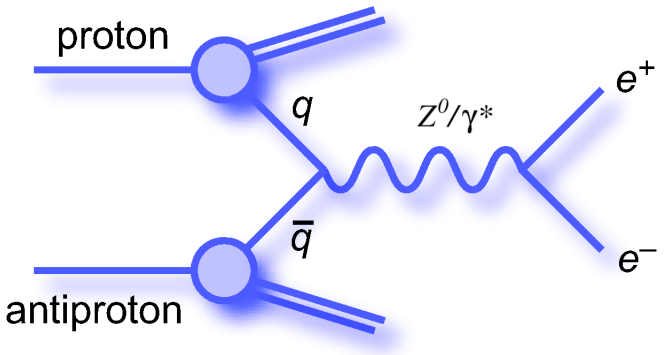

Figure 1.8: The lowest-order s-channel Feynman diagrams for $f\bar{f} \rightarrow Z/\gamma* \rightarrow e^+e^-$

The differential cross section for fermion pair production around can be written as:

$$\frac{d\sigma(q\bar{q}\to e^+e^-)}{d\cos\theta} = C\frac{\pi\alpha^2}{2s}\left[Q_e^2Q_q^2(1+\cos^2\theta) + Q_eQ_qRe(\chi(x))\left(2g_V^qg_A^e(1+\cos^2\theta)+4g_A^qg_A^e\cos\theta\right)\right.$$
$$\left. + \mid\chi(s)\mid^2\left((g_V^{q\,2}+g_A^{q\,2})(g_V^{e\,2}+g_A^{e\,2})(1+\cos^2\theta)+8g_V^qg_A^qg_V^eg_A^e\cos\theta\right)\right] \quad (1.50)$$

where C is the color factor, θ is the emission angle of the lepton (anti-lepton) relative to the quark(anti-quark) in the rest frame of the lepton pair, and

$$\chi(s) = \frac{1}{\cos^2\theta_W\sin^2\theta_W}\frac{s}{s-M_Z^2+i\Gamma_ZM_Z} \quad (1.51)$$

The first and the third terms in Eq. 1.50 correspond to the pure $\gamma*$ and Z exchange respectively while the second term corresponds to the $Z/\gamma*$ interference. The angular dependence of the various term is either $\cos\theta$ or $(1+\cos^2\theta)$. The $\cos\theta$ terms integrate to zero in the total cross section but induce the forward-backward asymmetry.

The differential cross section in Eq. 1.50 simplified into:

$$\frac{d\sigma}{d\cos\theta} = A(1+\cos^2\theta)+B\cos\theta \quad (1.52)$$

where A and B are functions dependent on the weak isospin and charge of the incoming fermions and Q^2 of the interaction. Events with $\cos\theta > 0$ are called forward events, and events with $\cos\theta < 0$ are called backward events. The integrated cross section for forward events is thus $\sigma_F = \int_0^1 \frac{d\sigma}{d\cos\theta}d\cos\theta$ and the integrated cross section for backward events is $\sigma_B = \int_{-1}^0 \frac{d\sigma}{d\cos\theta}d\cos\theta$. The forward-backward charge asymmetry A_{FB} is defined as

$$\begin{aligned} A_{FB} &= \frac{\sigma_F-\sigma_B}{\sigma_F+\sigma_B} \\ &= \frac{\int_0^1\frac{d\sigma}{d\cos\theta}d\cos\theta - \int_{-1}^0\frac{d\sigma}{d\cos\theta}d\cos\theta}{\int_0^1\frac{d\sigma}{d\cos\theta}d\cos\theta + \int_{-1}^0\frac{d\sigma}{d\cos\theta}d\cos\theta} \end{aligned}$$

$$\begin{aligned} &= \frac{N_F - N_B}{N_F + N_B} \\ &= \frac{3B}{8A} \end{aligned} \tag{1.53}$$

where N_F and N_B are numbers of forward and backward events. This asymmetry depends on the vector and axial-vector couplings of the quarks and leptons to the Z boson and is therefore sensitive to the effective weak mixing angle $\sin^2\bar{\theta}_W$. At the Tevatron, A_{FB} is measured as a function of the invariant mass of the di-lepton pair. The largest asymmetries occur at parton center-of-mass energies of around 70 GeV and above 120 GeV. At the Z-pole, the asymmetry is dominated by the couplings of the Z boson and arises from the interference of the vector and axial components of its coupling. At large invariant mass, the asymmetry is dominated by Z/γ^* interference and is almost constant.

When the incoming quarks participating in the Drell-Yan process have no transverse momentum relative to their parent baryons, θ is determined unambiguously from the four-momenta of the leptons by calculating the angle that the lepton makes with the proton beam in the center-of-mass frame of the electron pair. When either of the incoming quarks has significant transverse momentum, however, there exists an ambiguity in the four-momenta of the incoming quarks in the frame of the di-lepton pair, since one can not determine the four-momenta of the quark and anti-quark individually. The Collins-Soper formalism[19] is adopted to minimize the effects of the transverse momentum of the incoming quarks. In this formalism, the polar axis is defined as the bisector of the proton beam momentum and the negative of the anti-proton beam momentum when they are boosted into the center-of-mass frame of the di-lepton pair, which is shown in Fig. 1.9. The variable θ^* is defined as the angle between the lepton

and the polar axis. Let Q (Q_T) be the four momentum (transverse momentum) of the di-lepton pair, P_1 and P_2 be the four-momentum of the lepton and anti-lepton respectively, all measured in the lab frame. Then $\cos\theta^*$ is given by

$$\cos\theta^* = \frac{2}{Q\sqrt{Q^2+Q_T^2}}(P_1^+P_2^- - P_1^-P_2^+) \tag{1.54}$$

where $P_i^{\pm} = \frac{1}{\sqrt{2}}(P_i^0 \pm P_i^3)$, and P^0 and P^3 represent energy and the longitudinal component of the momentum.

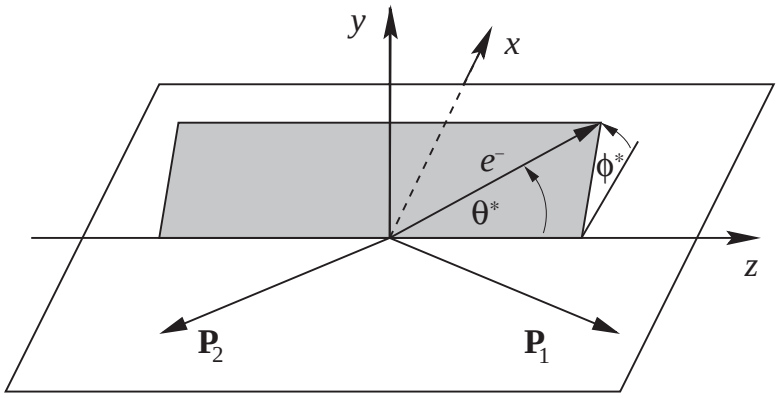

Figure 1.9: The Collins-Soper reference frame.

Fig. 1.10 shows the $\cos\theta^*$ distribution and the di-lepton invariant mass distribution for forward and backward events using $Z/\gamma^* \to ee$ events generated with PYTHIA [55] generator with Z/γ^* mass between 50 and 600 GeV. Fig. 1.11 shows the A_{FB} as a function of the di-lepton invariant mass distribution using PYTHIA.

The standard model (SM) tree level prediction for A_{FB} as a function of $\hat{s}$ for $q\bar{q} \to Z/\gamma^* \to e^+e^-$ is shown in Fig. 1.12 for u and d quarks.

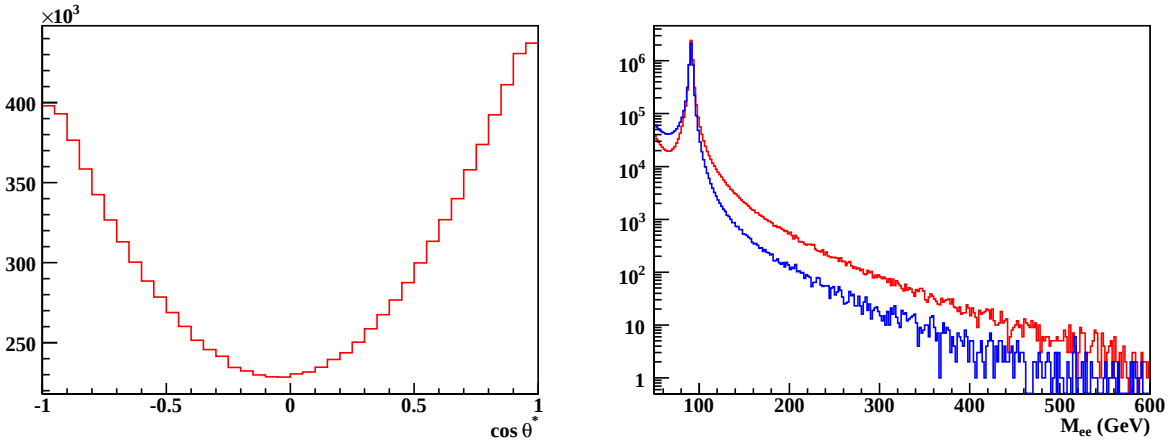

Figure 1.10: $\cos\theta^*$ and di-electron invariant mass distribution (Red for forward events and Blue for backward events) for $Z/\gamma^* \to ee$ events generated with PYTHIA.

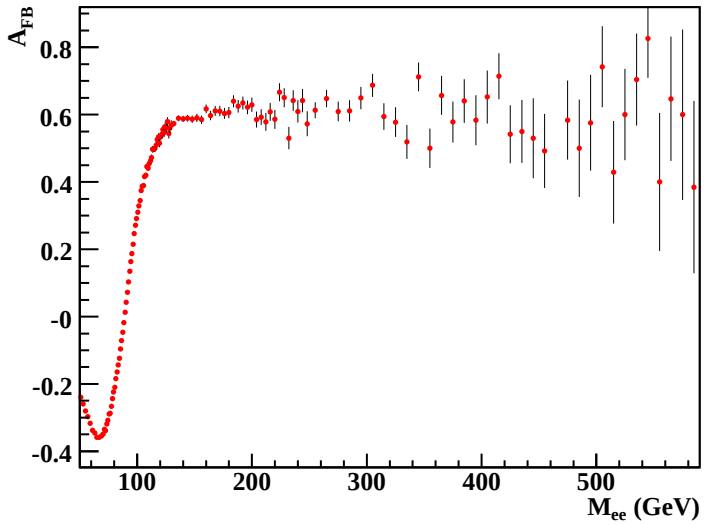

Figure 1.11: A_{FB} as a function of the di-lepton invariant mass for $Z/\gamma^* \to ee$ events generated with PYTHIA.

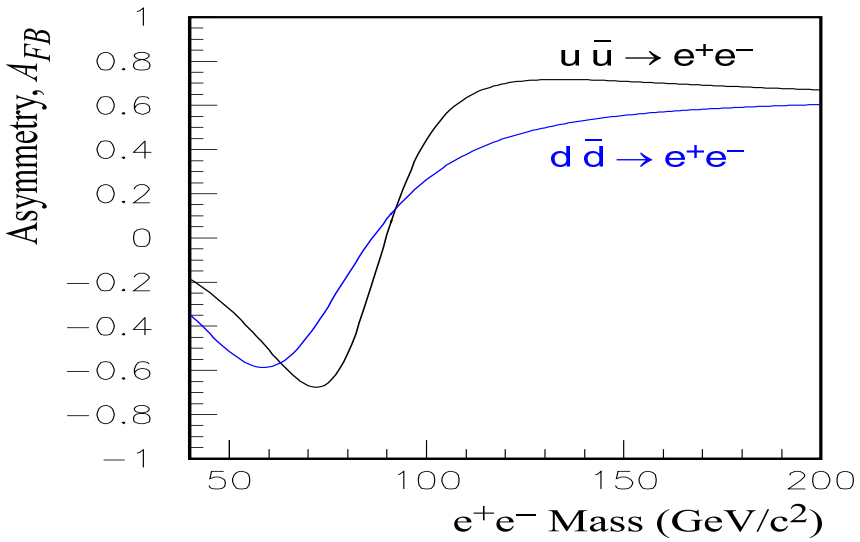

Figure 1.12: The standard model tree level prediction of the forward-backward asymmetry as a function of e^+e^- invariant mass for $u\bar{u} \rightarrow e^+e^-$ and $d\bar{d} \rightarrow e^+e^-$.[20]

Chapter 2

Experimental Apparatus

2.1 The Accelerator

The Fermi National Accelerator Laboratory is currently the site of the world's highest center-of-mass energy proton-antiproton colliding beam accelerator, the Tevatron. It consists of several stages that increases the energy of the protons and antiprotons. Figure 2.1 shows the layout of the accelerator system. A detailed description of the Tevatron can be found at [29].

The acceleration process begins with the Pre-accelerator, or "PreAcc"; it is the source of the negatively charged hydrogen ions accelerated by the linear accelerator. It first converts hydrogen gas to ionized hydrogen gas (H^-). Next, an extractor plate accelerates the ions to a kinetic energy of 18 keV, and a Cockcroft-Walton accelerator propels the ions to an energy of 750 keV. The ions are then injected into a linear accelerator (the Linac), where they are accelerated to an energy of 400 MeV. When the ions enter the Booster, a circular synchrotron nearly half a kilometer in circumference,

they are passed through a thin carbon foil which strips off the electrons, leaving a beam of H^+ ions, which are bare protons. The steady beam of protons travels around the Booster, collecting more protons with each turn. After six revolutions, the Booster contains about 3×10^{12} protons, and the Linac ceases suppling them. The Booster then restores the bunch structure to the beam and accelerates the protons to 8 GeV.

After the Booster, the protons are injected into a larger synchrotron, the Main Injector. The Main Injector is about two miles in circumference, and replaces the Main Ring that was used in Run I of the Tevatron. With the Main Injector there is a factor of three increase in the number of protons that can be delivered to the Tevatron over what was possible in Run I. The Main Injector provides a 120 GeV proton beam for the production of antiprotons, and it also accelerates protons and antiprotons from an energy of 8 GeV to an energy of 150 GeV and then injects them into the Tevatron. The extracted 120 GeV protons are directed onto a nickel target to produce antiprotons. For every about 10^5 incident protons, one antiproton is produced. The antiprotons are produced with a wide range of momenta. They are focused and stored in the Debuncher and Accumulator rings, where the beams are cooled, creating a beam of 8 GeV antiprotons to be injected into the Main Injector, and accelerated to 150 GeV. The 150 GeV antiprotons are then injected into the Tevatron in the direction opposite to the proton beam.

The Tevatron is a 4-mile circumference synchrotron ring where the beams are accelerated to 980 GeV. It contains near 1,000 superconducting magnets which operate at a temperature of 4.6 Kelvin and provide a field of 4.2 Tesla. Once protons and antiprotons are accelerated to 980 GeV, low-beta quadrupole magnets squeeze the beams

to small transverse dimensions. The beams are then brought into collision at two interaction points: BØ, where the CDF detector was built and DØ, the location of the other multipurpose detector, also called DØ since it was named after its interaction point.

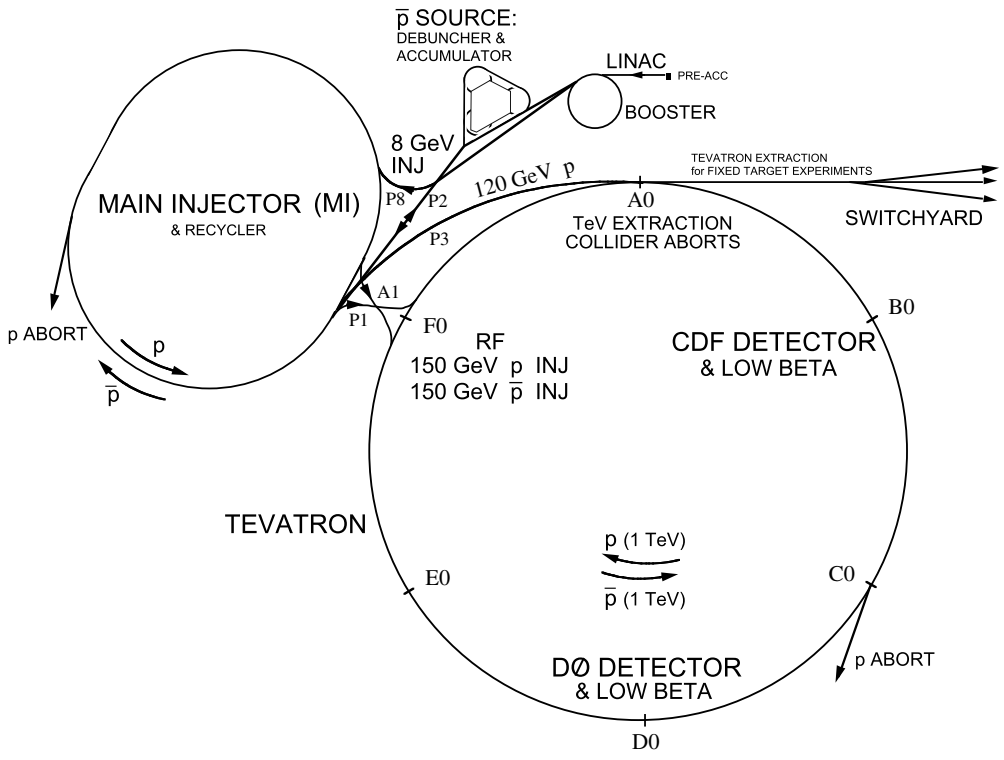

Figure 2.1: The general layout of the collider facility at Fermilab.

The bunch structure for Run I and Run II is shown in Fig. 2.2. In Run I, the accelerator delivered 6 bunches of protons and antiprotons ("6×6" bunches), separated by a 3.5 μs gap. This gap was used to form the trigger and sample the detector baselines prior to the next crossing. In Run II, the proton antiproton bunches circulate in superbunches of 4.36 μs duration, with a 2.64 μs gap spacing between them. The spacing between each bunch is 396 ns ("36 × 36" bunches).

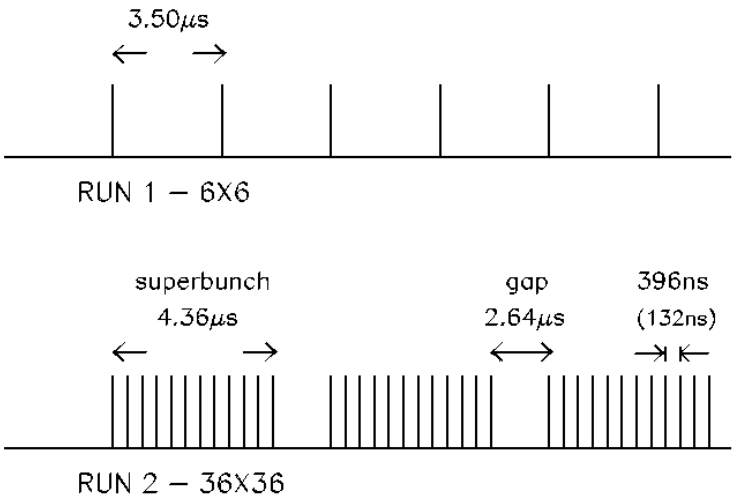

Figure 2.2: Tevatron bunch scheme for Run I (top) and Run II (bottom).

2.2 DØ Detector

The DØ detector is a multipurpose particle detector designed for the study of high mass and large transverse energy phenomena. Initial operation started in 1992 with Run I of the Tevatron accelerator; it has played a key role in experimental high energy physics [30]. One example of this was the discovery of the top quark in 1995 with the CDF detector [31].

Since the Tevatron accelerator complex has been upgraded, the instantaneous luminosity was increased from 10^{31} cm^{-2}s^{-1} in Run I to 10^{32} cm^{-2}s^{-1} in Run II. Also the Tevatron beam energy was increased from 900 GeV to 980 GeV, increasing the $p\bar{p}$ center-of-mass collisions from 1.8 TeV to 1.96 TeV.

To take advantage of these improvements, the DØ detector went through a major upgrade. The upgraded DØ detector consists of three major subsystems: a tracking system with superconducting solenoid magnet, a nearly 4π solid angle uranium liq-

uid argon calorimeter with two additional preshower detectors, and a muon toroidal spectrometer. Figure 2.3 shows an overview of the entire DØ detector [32].

2.2.1 The DØ Coordinate System

The following convention for coordinates is used: the direction of the protons is the positive z direction, the positive x direction points away from the center of the Tevatron ring and thus the positive y direction points up.

In $p\bar{p}$ collisions, one can use the image that two "bags" of elementary particles (quarks, antiquarks and gluons) collide. One is usually interested in events where two of these elementary particles undergo a so-called "hard-scattering" interaction; their annihilation produces new particles at high transverse momentum. The center-of-mass system (CMS) of this hard interaction usually has a boost along the z-axis. Many of the particles produced in the collision, for example the remnants of the proton not participating in the hard-scattering interaction, escape down the beam pipe. Hence the longitudinal boost of the CMS of the hard scattering partons cannot be measured. The transverse momentum of the particles that escape down the beam pipe is negligible compared to the detector resolution, making it possible to apply conservation of energy and momentum in the transverse plane. This makes the transverse energy/momentum and the missing transverse energy ($\not\!\!E_T$), defined as the transverse energy imbalance, extensively used in hadron collider physics. The rapidity y of a particle (defined as $y = \frac{1}{2}\ln\left(\frac{E+p_z}{E-p_z}\right)$) is also generally used. The advantage of using rapidity is that it is invariant under the Lorentz transformation. If the energy of a particle is much larger than its mass ($m/E \to 0$), the pseudorapidity $\eta = -\log\tan(\theta/2)$ becomes a very good

approximation to y (where θ is the polar angle with respect to the proton beam).

2.2.2 Tracking System

One of the biggest changes to the DØ detector between Run I and Run II was the addition of a new tracking system inside the calorimeter's bore. Figure 2.4 shows the various components of the inner tracking detectors in DØ. The inner detectors are surrounded by a 2 Tesla superconducting solenoid magnet, which bends the paths of charged particles with a curvature inversely proportional to their transverse momenta. Observing the curvature of a particle's path allows for a precise measurement of its momentum, as well as the sign of the particle's charge.

The Silicon Microstrip Tracker

The detector nearest to the interaction region is the Silicon Microstrip Tracker (SMT), which provides the high resolution position measurements of the charged particle paths that are used to reconstruct tracks and determine the vertex information [33]. Figure 2.5 shows an overview of the SMT detector. It consists of six 12 cm long barrels, with interspersed disks (12 F-disks and 4 H-disks), and has approximately 793,000 readout channels with a $r\phi$ hit resolution of approximately 10 μm. The tracks for high η particles are reconstructed in three dimensions primarily by the disks, while particles at small η are detected primarily by the barrels.

The Central Fiber Tracker

Surrounding the silicon detector and extending out to the solenoid magnet, is the Central Fiber Tracker (CFT), a detector which aids the SMT in reconstruction of charged particle tracks [34]. It makes use of 76,800 scintillating fibers and can detect

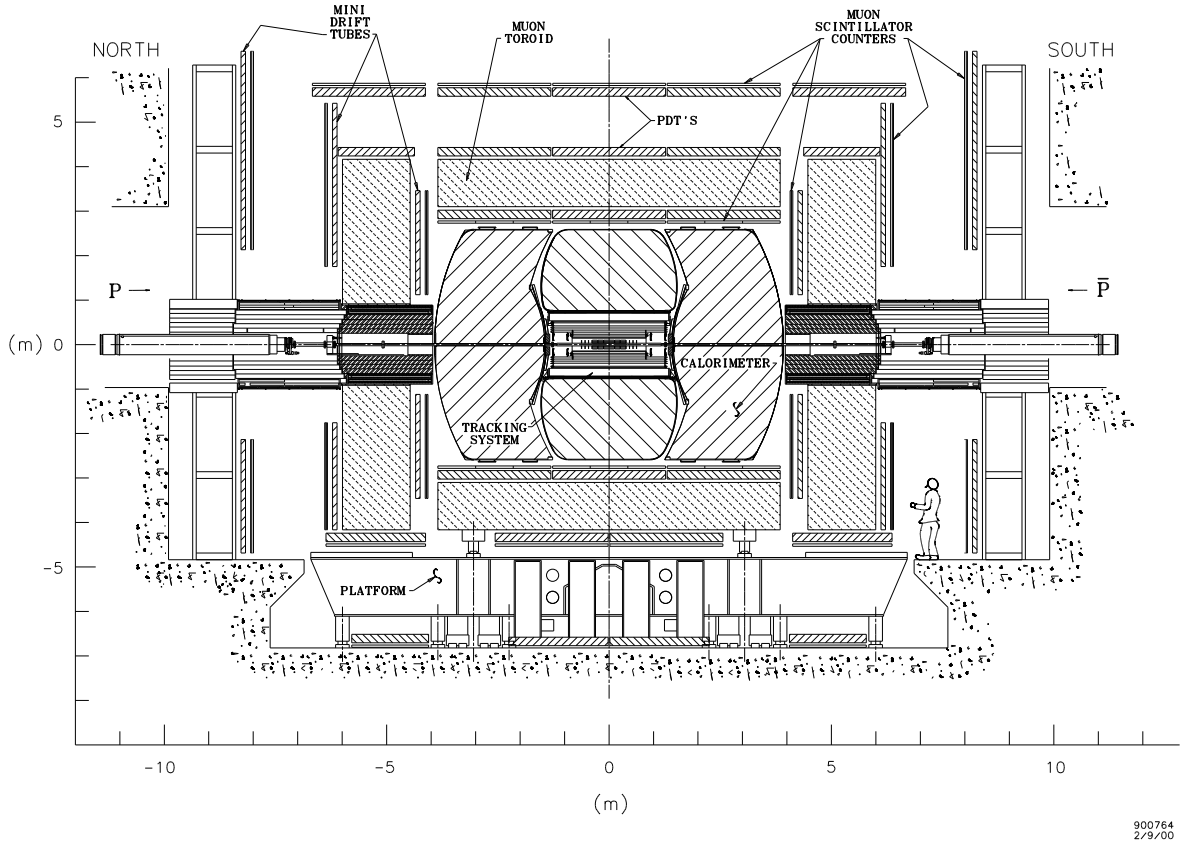

Figure 2.3: A view of the DØ Run II upgraded detector.

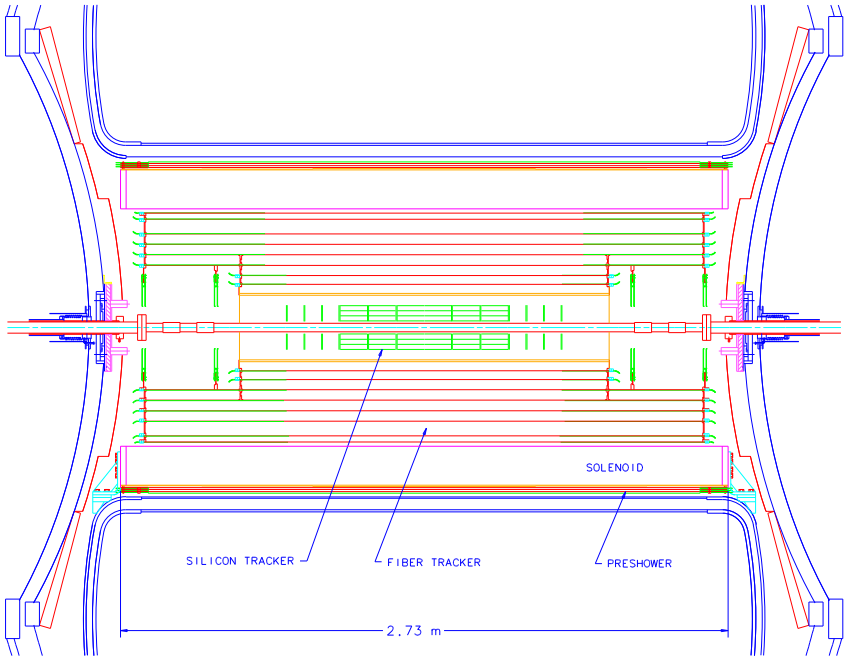

Figure 2.4: Cross-sectional view of the DØ tracking volume.

charged particles up to $|\eta|$ of about 2. Each ionizing particle produces an average of about 10 photons in each fiber, which are then detected using a Visible Light Photon Counter (VLPC) that converts the photons into an electrical pulse.

There are 8 super-layers; each super-layer is completely covered by two doublet layers of scintillating fibers. The innermost doublet layer is mounted along the axial direction to provide the ϕ information (called the x layer), and a stereo doublet-layer is on the top to provide the η (called the u/v layer, the u layer tilts 3 degree from the z axis clockwise and the v layer tilts 3 degree counter-clockwise). Since each fiber is 835 microns in diameter, the position resolution is on the order of 100 μm, corresponding to a ϕ resolution of 2×10^{-4} radians. Figure 2.6 shows a view of the CFT as well as an illustration of the doublet layer configuration.

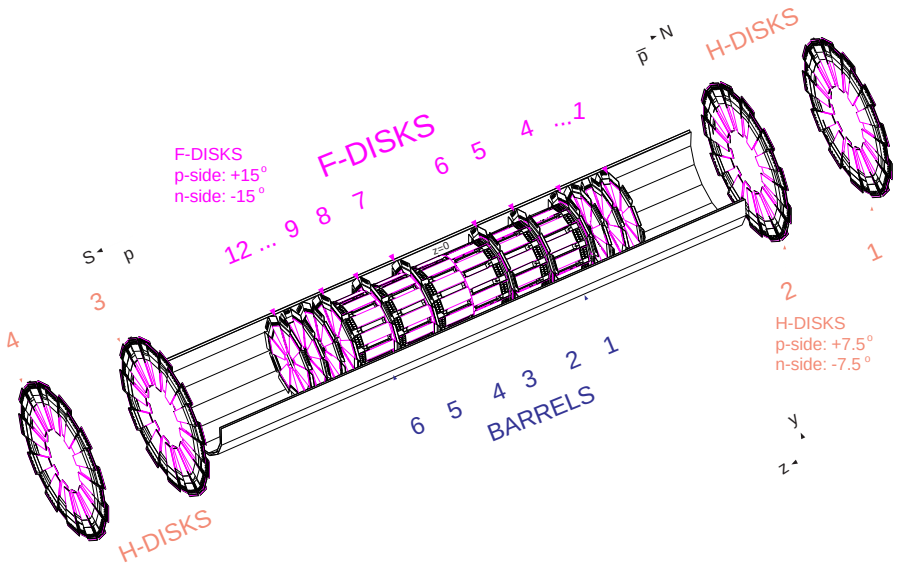

Figure 2.5: DØ Run II Silicon Microstrip Tracker detector.

2.2.3 Preshower Detectors

There are two preshower detectors located just before the calorimeters: a central preshower covering $|\eta| < 1.3$ (CPS), and a forward preshower covering $1.5 < |\eta| < 2.5$ (FPS) (shown in Fig. 2.7 and Fig. 2.8). The primary purpose of the preshower detectors is to provide discrimination between electrons/photons and hadronic jets by exploiting the differences between their energy loss mechanisms in showers.

The detectors function as a calorimeter by providing an early energy sampling and as a tracker by providing precise position measurements. The central system [35] consists of a lead radiator of two radiation lengths thickness at $\eta = 0$, followed by three layers of scitillating material arranged in an axial, $u - v$ geometry with a 22.5^0 stereo angle. The forward system [36] also consists of a lead radiator with a thickness of two radiation lengths, sandwiched between two layers of scitillating material. Each layer is made from two thinner layers of scintillating fibers, arranged in a $u - v$ geometry

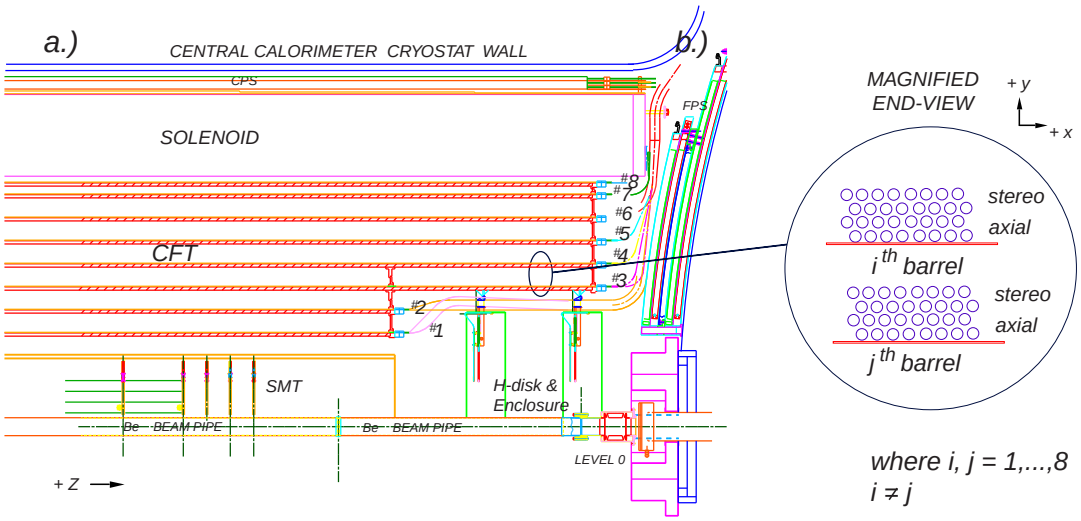

Figure 2.6: (a) A quarter r - z view of the CFT detector showing the nested eight barrel design. (b) A magnified r - ϕ end view of the two doublet layer configuration for two different barrels.

with a 22.5^0 stereo angle. Electrons are recognized based on the fact that muons and charged pions traversing the radiator will only deposit energy due to ionization, while electromagnetic particles will shower in the radiator.

2.2.4 Calorimeters

The DØ calorimeters have been designed to provide excellent measurement of the energy of photons, electrons and hadronic jets, by inducing them to create showers of energy using a large amounts of dense material. The energy in the showers is then sampled at many points, to determine its shape and energy. In this section, I first describe the energy measurement in the calorimeter, then describe the calorimeter and its performance.

Energy Measurement

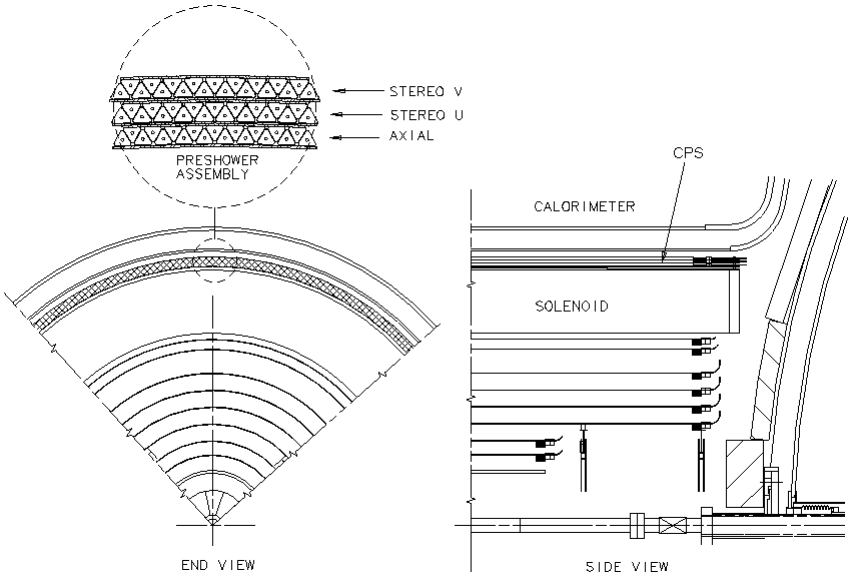

Figure 2.7: Cross-sectional end view (left) and side view (right) of the Central Preshower Detector.

EM objects interact primarily with materials via the following two processes: pair production ($\gamma \rightarrow e^+e^-$) and bremsstrahlung ($e \rightarrow e\gamma$). For each successive interaction the number of secondary particles increases while the average energy per particle decreases. It is the collection and measurement of these secondary particles that gives us information on the original EM object's energy. Because of these interactions, the energy of the original particle is expected to drop exponentially:

$$E(x) = E_0 e^{-x/X_0} \tag{2.1}$$

where E_0 is the particle's original energy, x is the distance traveled, and X_0 is the radiation length of the material being passed through. For uranium, X_0 is approximately 3.2 mm.

For hadrons the interaction with material occurs with the nuclei via the strong

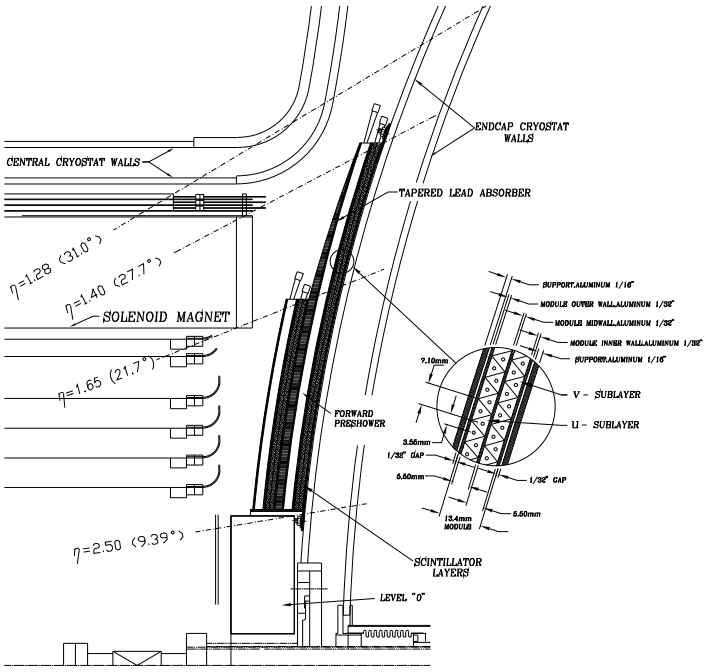

Figure 2.8: One quarter view of the Forward Preshower Detector.

nuclear force. These interactions also produce secondary particles, most of them are neutral pions (π^0) and charged pions ($\pi^{\pm}$). While the π^0s produce electrons and photons which interact electromagnetically, the charged pions interact strongly. This type of particle shower tends to develop over longer distances and is also larger. The analog of the radiation length for hadronic interactions is the nuclear interaction length (λ_0), which is about 10.5 cm for uranium.

DØ Calorimeters

Figure 2.9 shows an overview of the DØ calorimeter system [37]. The DØ calorimeters are compensating sampling calorimeters, using liquid argon as an active medium and depleted uranium as well as copper and steel as absorber material. The choice of this configuration was driven by its ease of segmentation, compensation properties, stability of calibration, and homogeneity of response. The high density of uranium

allows a compact detector that contains almost all shower energy while reducing cost. There are three liquid argon calorimeters housed in three separate cryostats - one central (CC) (with $|\eta| < 1.1$) and two endcaps (EC) (with $1.5 < |\eta| < 4.2$). In the inter-cryostat region ($1.1 < |\eta| < 1.4$), both "massless gaps" and an inter-cryostat detector (ICD) have been added to sample the shower energy that is lost by particles that transverse the module endplates and cryostat walls.

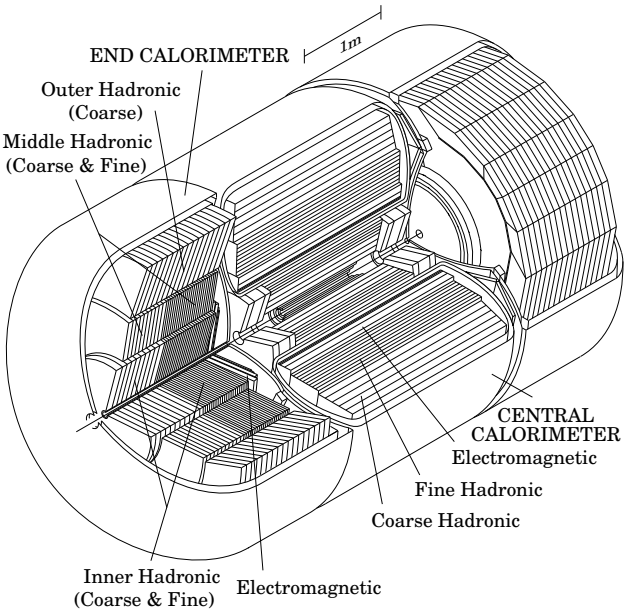

Figure 2.9: Overall view of the calorimeter system.

A typical calorimeter unit cell is shown in Fig. 2.12; it is made up of an alternating sandwich of signal boards and absorber material separated by a 2.3 mm liquid argon gap. The electric field is established by grounding the metal absorber plate and connecting the resistive surfaces of the signal boards to a positive high voltage (2.0 kV). Particles interact with the uranium and the liquid argon, thus producing charged particles in the liquid argon. These charged particles will then move in the electric field and be collected. The electron drift time across the argon gap is ~ 450 ns, which sets

the time scale for the signal charge collection. The gap thickness was chosen to be large enough to observe minimum ionizing particle (MIP) signals and to avoid fabrication difficulties.

The pattern and sizes of the readout cells were determined from several considerations. The transverse sizes of the cells were chosen to be comparable to the transverse sizes of showers: $\Delta R \sim 0.2$ for EM showers and $\Delta R \sim 0.5$ for hadronic showers (where $\Delta R = \sqrt{\Delta\eta^2 + \Delta\phi^2}$). Segmentation finer than this is useful in measuring the shape of electrons and jets. Longitudinal subdivision within the EM, fine hadronic and coarse hadronic sections is also useful since the longitudinal shower profiles help distinguish EM objects and hadron jets.

The final arrangement of the readout cells was chosen to give semi-projective readout towers of equal size in pseudorapidity that are subdivided in depth. The cells are first ganged into layers, and then arranged into semi-projective towers of size 0.1×0.1 in $\Delta\eta \times \Delta\phi$ and are segmented logitudinally into electromagnetic (EM), fine hadronic (FH), and coarse hadronic (CH) sections. A cross sectional view of one quarter of the detector, showing the η and depth segmentation is shown in Fig. 2.10. Each projective tower consists of 8 to 12 layers. To capture the profile of electromagnetic showers, the third layer of the EM section, which corresponds to the shower maximum, is segmented more finely transversely into 0.05×0.05 in $\Delta\eta \times \Delta\phi$ (See Fig. 2.11).

Different absorber plate materials were used in difference locations. The EM modules for both CC and EC used nearly pure depleted uranium; the thicknesses were 3 mm and 4 mm respectively. The fine hadronic module sections have 6 mm thick uranium-niobium (2%) alloy. The coarse hadronic module sections contain relatively

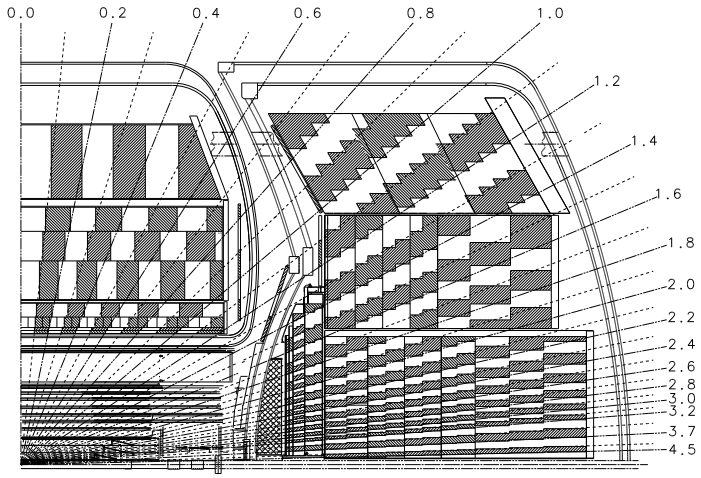

Figure 2.10: Side-view of one quarter of the DØ calorimeter system, showing segmentation and tower definitions. The line extending from the center of the detector denote the pseudorapidity coverage of cells and projected towers.

thick (46.5 mm) plates of either copper (CC) or stainless steel (EC). For the CC, the EM section consists of 32 modules, each subtending $2\pi/32 \approx 0.2$ radians in azimuth.

Table 2.1 and 2.2 list the major parameters for the central and endcap calorimeters. At $\eta = 0$, the CC has a total of 7.2 nuclear absorption lengths; at the smallest angle of the EC, the total is 10.3 nuclear absorption lengths.

Calorimeter Electronics

In Run II, the higher instantaneous luminosity of the Tevatron collider with the shorter bunch crossing interval of 132 ns (compared to the Run I bunch crossing interval of 3.5 μs) forces a faster readout time. At the same time, a low-noise performance and minimal channel-to-channel variations must be maintained, to prevent any degradation to the calorimeter's performance [38] [39]. A schematic of the electronics system is shown in Fig. 2.13.

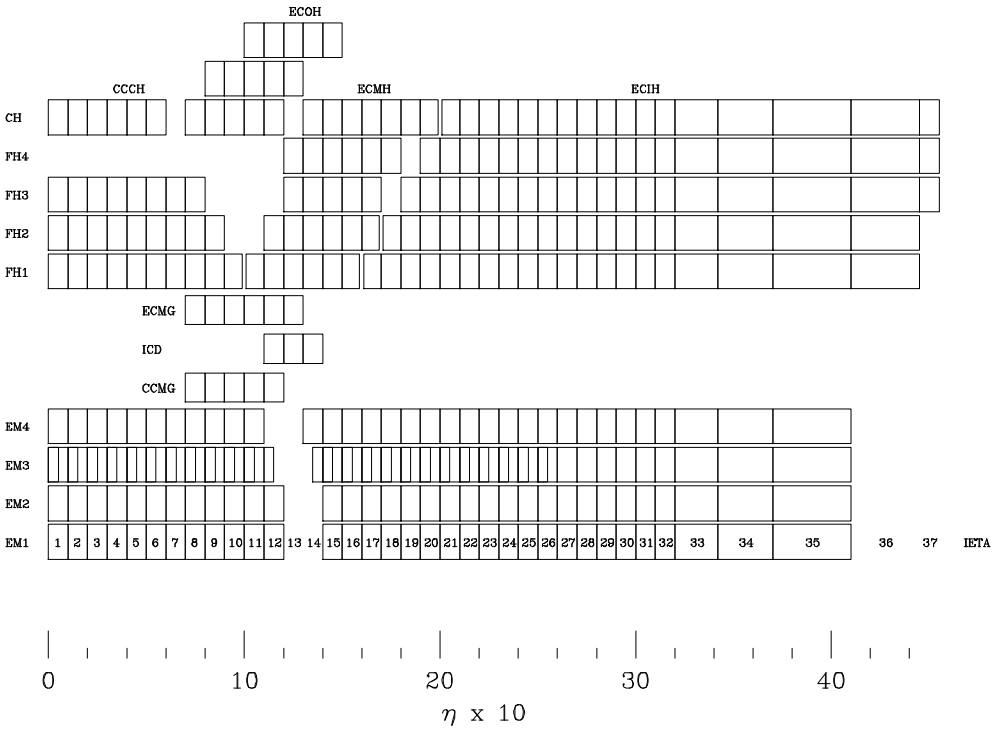

Figure 2.11: Calorimeter channel configuration in terms of depth and η.

The signal from each calorimeter readout cell is triangular with a very fast rise time and a decay time of 400 ns. Each signal is taken to a feedthrough port via 30 Ω resistive coaxial cables. The impedance-matched cabling maintains a low-noise transfer of the signal to the preamplifiers. The integrated circuits in the preamplifiers convert the charge to a voltage that is proportional to the input charge. In order to minimize electronic noise stemming from the shorter shaping times, the preamps incorporate a dual field effect transistor (FET) input design. The output signal from the preamplifier is approximately a step function with an about 400 ns rise time and a long fall time ($\sim 15\ \mu$s). As the values of the calorimeter cell capacitances range over a broad interval, 14 species of preamplifiers were built to match them. The preamplifier output signal is then shaped into a shorter one with a 320 ns rise time and a 500 ns decay time.

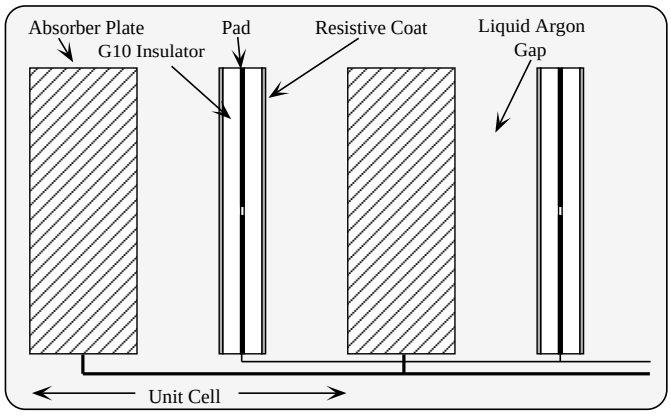

Figure 2.12: Schematic view of a representative calorimeter unit cell. The gap structure, grounded absorber plates, and signal boards are shown.

The shaped signals are sampled every 132 ns; the timing is tuned such that the shaped output can be sampled at its peak at about 320 ns. Because of this earlier sampling time compared to the liquid argon drift time of 430 ns, only $2/3^{rds}$ of the charge in the cell is used to form the preamplifier signal. Figure 2.14 shows the shape of signals from the calorimeter cell, the preamplifier and the shaper.

The signal is then split and sent to two paths. In one path it is amplified by a factor of $8g$ ($g \approx 1$) with respect to the other. The gain factor is defined by precision resistors. We will call the 2 paths $G = 8$ and $G = 1$ respectively. On each path the signal is sampled every 132 ns, and the measured voltage is stored in an analog memory called the Switched Capacitor Array (L1 SCA). On a trigger, a gain selector decides which of the 2 signals ($G = 1$ or $G = 8$) is most appropriate: the $G = 8$ one if the signal is below a certain saturation voltage, the $G = 1$ otherwise. The reason two paths are used is that the Analog-to-Digital Converters (ADCs) only have a 12-bit dynamic range, while a 15-bit range is needed. The SCA is a 48-element-deep storage

	EM	FH	CH
Number of Modules	32	16	16
Absorber	Uranium	Uranium	Copper
Absorber Thickness (mm)	3	6	46.5
Argon Gap (mm)	2.3	2.3	2.3
Number of Readout Layers	4	3	1
Cells per Readout Layer	$2, 2, 7, 10$	$20, 16, 14$	9
Total Radiation Length (X_0)	20.5	96.0	32.9
Total Interaction Length (λ)	0.76	3.2	3.2

Table 2.1: Central Calorimeter Module Parameters.

device that provides a buffer zone for saving analog information from a calorimeter channel until it can be processed through the ADC's after an event has occurred and a trigger has been received. The sample at the nominal peak time and the one earlier by 3×132 ns are then retrieved from the SCA memory and the earlier sample is subtracted from the nominal one in the baseline subtractor (BLS). The difference voltage is stored into another analog memory (L2 SCA). On a positive trigger decision, the voltage is retrieved from the memory and digitized in an ADC. The integer number is finally multiplied by 8 if the signal previously proceeded through the $G = 1$ path. The ADC counts are ultimately transferred to a host computer for storage and analysis.

The readout electronics of the DØ calorimeter is composed of 12 crates containing 12 ADC cards. Each card contains 384 channels which are distributed on 8 BLS cards, each treating the signals of 4 towers with 12 longitudinal depths each. All three calorimeter

	EM	IFH	ICH	MFH	MCH	OH
Number of Modules	1	1	1	16	16	16
Absorber	Uranium	UNb	SS	UNb	SS	SS
Absorber Thichness (mm)	4	6	46.5	6	46.5	46.5
Argon Gap (mm)	0.23	0.21	0.21	0.22	0.22	0.22
Number of Readout Layers	4	4	1	4	1	3
Cells per Readout Layer	$2, 2, 6, 8$	16	14	15	12	8
Total Radiation Length (X_0)	20.5	121.8	32.8	115.5	37.9	65.1
Total Interaction Length (λ)	0.95	4.9	3.6	4.0	4.1	7.0

Table 2.2: End Calorimeter Module Parameters. IFH, ICH, MFH, MCH, OH stand for inner fine hadronic, inner coarse hadronic, middle fine hadronic, middle coarse hadronic and outer hadronic section respectively. UNb and SS stand for Uranium-Niobium alloy and Stainless Steel.

cryostats together contain a total of $12 \times 12 \times (8 \times 4 \times 12) = 12 \times 12 \times 384 = 55296$ channels.

Calorimeter Performance

The performance of the calorimeter is very crucial for the W width measurement. The energy resolution can be described as arising from three major sources. The first is the noise term that has a fixed value, independent of the observed signal. The second is the sampling term which reflects statistical fluctuations in the energy deposited in the argon and therefore scales like the square root of the signal size. The third is the constant term, which reflects how well the response of different parts of the detector are

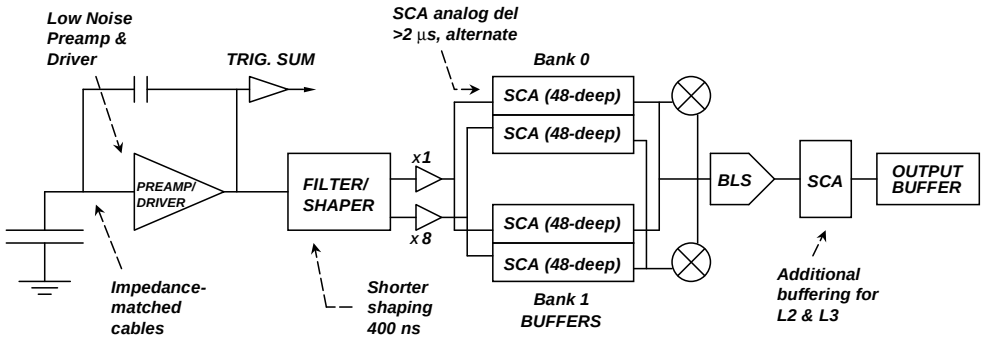

Figure 2.13: Schematic of the primary elements for the DØ calorimeter electronics.

equalized, in other words, how well we understand and calibrate the entire calorimeter. It therefore scales linearly with signal size, assuming the energy is distributed over approximately the same number of readout cells, independent of energy. The energy resolution is thus described using the following functional form:

$$\frac{\sigma_E}{E} = \sqrt{\left(\frac{N}{E}\right)^2 + \left(\frac{S}{\sqrt{E}}\right)^2 + C^2} \tag{2.2}$$

where N, S and C are the noise, sampling, and constant terms, respectively. In Run I, the three terms were determined to be: $N = 0.003$ GeV, $S_{EM} = 0.15$ GeV$^{1/2}$ [40] [41] and $C = 1.15^{+0.27}_{-0.36}\%$ [42].

2.2.5 Muon System

Surrounding the calorimeter is the muon system [43]. Muons are about 200 times heavier than electrons, and therefore they lose very little energy via bremsstrahlung, unlike electrons. Muon energy loss occurs due to ionization in the detector media, which is a low energy loss absorption process. Therefore, muons above a certain energy threshold (about 3 GeV) pass through the whole DØ detector. Also, since muons are measured after the electromagnetic and hadronic particle showers are absorbed in the

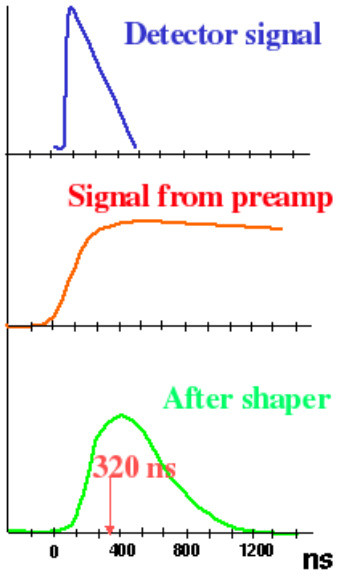

Figure 2.14: Electronics signal shape from the calorimeter cell, after the preamplifier and after the shaper.

calorimeters, muons can be identified in the middle of hadron jets with much greater purity than electrons.

To detect muons, a second tracking system is located outside the calorimeter. This has three layers of detectors giving position measurements, and a toroid magnet with a 1.8 T field located between the first and second layer, allowing a measurement of momentum. Position measurements are provided by drift chambers. These chambers collect charge ionized in a gas by the passage of a charged particle. The gas is held in a sealed volume. The chambers are arranged in planes, four planes make up the central muon system, surrounding the calorimeter and providing coverage up to $|\eta| < 1$. Two further planes of detectors are located at either end of the calorimeter, making up the forward muon system. These extend the detector coverage out to $|\eta| < 2.2$. The drift chambers provide an accurate (to within 0.5 mm) measurement of the coordinate

perpendicular to the sense wires (corresponding to η). The muon detectors also have layers of scintillating material arranged in pixels; these provide the best measurement of the other coordinate (corresponding to ϕ). Signals from the drift chambers and scintillators in each region are combined into segments. Segments are then joined in a fit, with a measurement of the bending in the toroidal magnetic field giving a measurement of muon momentum.

Chapter 3

Measurement Strategy

This analysis focuses on electron channel due to the low background, good energy resolution and good angular coverage of electrons in the DØ detector. The charge asymmetry A_{FB} is measured as a function of the invariant mass of the electron-positron pair.

As seen in Eq. 1.52, the most important thing is to measure number of forward and backward events N_F and N_B in each invariant mass bin. Also A_{FB} is really measured using the ratio of the forward and backward events, thus many systematic uncertainties cancelled. The measurement is done in the following steps:

- Apply event selection cuts and obtain number of selected forward and backward events for each invariant mass bin;
- Subtract QCD and other SM backgrounds;
- Apply the energy resolution corrections (called detector resolution unfolding);
- Apply the acceptance (kinematic and geometric) and efficiency corrections (called

acc×eff corrections);

- Apply charge mis-identification corrections;
- Measure the corrected A_{FB} and compare with the theoretical predictions.
- Extract $\sin^2\theta_W$ using the background-subtracted raw A_{FB} distribution from real data;
- Measure Z to light quark couplings(vector and axial-vector couplings).
- Measure the differential cross section of Drell-Yan process(d_σ/d_M).

Chapter 4

Event Selection

4.1 Data sample

The data sample used in this analysis was collected using the DØ detector between June 2002 and April 2009 (Run IIb sample), with run number from 160582 to 251254, duplicated events are removed. Only events passing the standard data quality requirements (dq_util: v2009-06-13) are kept for the final analysis. Events with negative instantaneous luminosity are also removed.

4.2 Trigger

For this measurement, we are interested in the channel with two high p_T electrons in the final state. We decided to look at events passed diem triggers instead of single EM triggers. In RunIIa, diem triggers are found to be 100% $\pm$ 0.001 efficient for selecting Z/γ^* events with electrons $p_T > 25$ GeV [44], but in RunIIb, since diem trigger terms are changed in L1, L2 and L3, trigger OR efficiency is not 100%. The CCCC and

CCEC trigger OR efficiency versus mass and two electrons pt are shown in Fig 4.1 [45]. Those efficiencies will be applied into all of the GEANT MC.

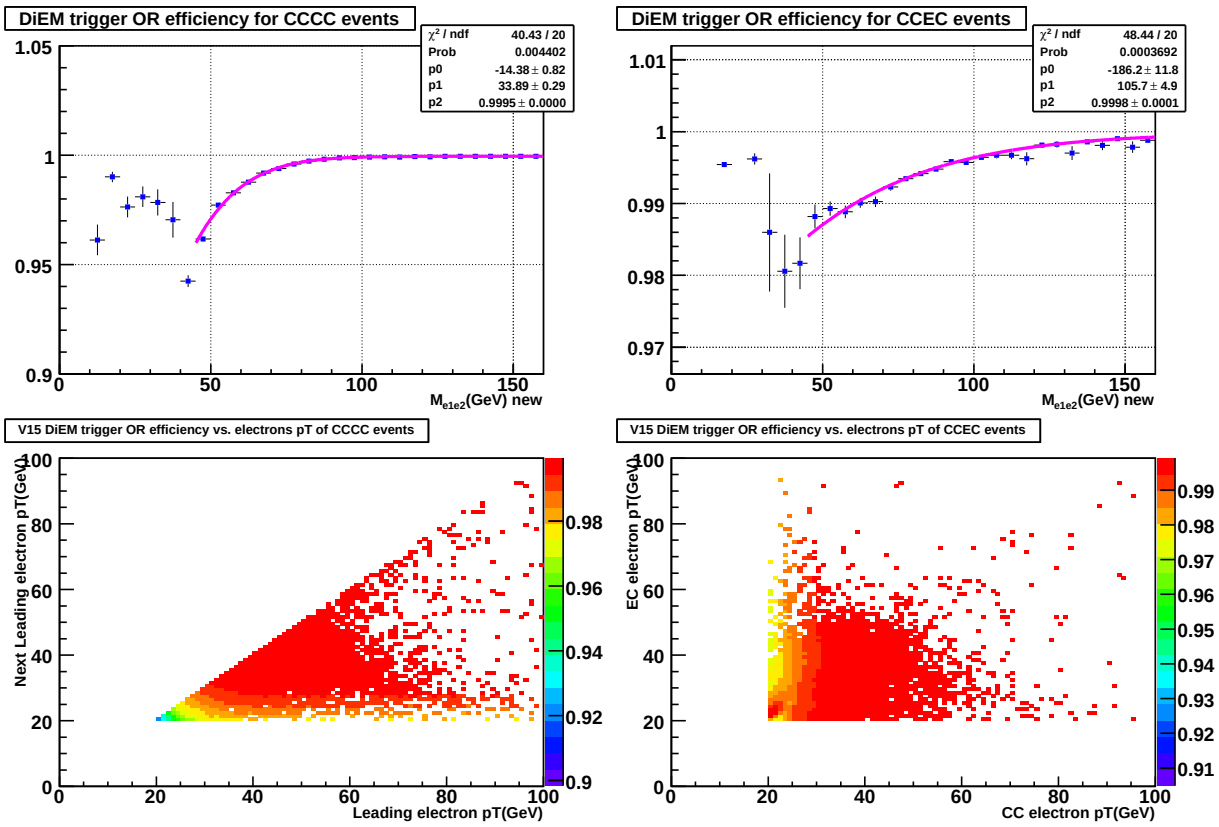

Figure 4.1: Diem trigger OR efficiency versus invariant mass, electron/positron p_T.

4.3 Integrated Luminosity

The total integrated luminosity is 4.947 fb^{-1}, and the integrated luminosity in each trigger epoch is listed in Table 4.1, and the luminosity uncertainty is 6.1% [46].

Trigger version	Integrated luminosity (pb^{-1})
v8-11	125.80
v12	230.96
v13	375.55
v14	333.38
v15	1621.63
v16	2259.81
all	4947.13

Table 4.1: Integrated luminosity for different trigger versions.

4.4 Event selection

The event selection is used to select signal events and suppress the backgrounds. The following cuts are used to select Z/γ^* candidates:

- $|z_{vtx}| < 40$ cm
- EM cluster requirements:
  - $p_T > 25$ GeV
  - CC: $|\eta^{det}| < 1$ or EC: $1.5 < |\eta^{det}| < 2.5$
  - ID=10, ±11, emf>0.9, iso<0.15 in CC and iso<0.1 in EC
  - HMx7< 12 in CC, HMx8< 10 in EC
  - Electron in CC region is required to have a spatial track matching (described below)

- In CC region, the electron is required to be far away from the module boundary with the extrapolated track phimod between 0.1 and 0.9
- Electron in EC region is required to have less activities in the tracker system around this electron (but no track matching requirement for this electron): the scalar sum of transverse momentum of all tracks in annulus cone $0.05 < dR < 0.4$ should be small than 1.5 GeV.

  The EC isolation variable is calculated differently for CC and EC electrons due to different clustering algorithms used in emreco for CC ($\Delta R < 0.2$) and EC ($R < 10$ cm), tighten the isolation requirement for EC electron to remove more QCD backgrounds.

  HMx8 cut is chosen based on the studies in [47] to reduce the QCD backgrounds in EC region. The EMID efficiency is found to be close to each other for cutting on 10 and 20, while QCD fake rate drops by a factor of 2.

- Track requirements (The track requirements used here are the agreed "standard" cuts used for several electroweak analyses related with electron charge, more details can be found in [48]):
  - Spatial track match with probability > 0.001
  - Track $p_T > 10$ GeV
  - At least two SMT hits and nine CFT hits
  - Track fit χ^2/ndf< 9.95
  - Beamspot corrected DCA < 0.02 cm

- Event requirements:
  - Pass at least one of the diem triggers
  - At least two EM clusters satisfying the above electron requirements
  - Invariant mass $50 < M_{ee} < 1000$ GeV
  - Only CC-CC and CC-EC events are used for this measurement
  - Both EM clusters are required to have matched track for CC-CC events, and the two clusters are further required to have opposite charges in order to determine forward/backward event unambiguously
  - For CC-EC events, only CC EM cluster is required to have track matching, and the sign of the CC EM cluster is used to determine forward/backward events. If the CC EM cluster is an electron (positron), the EC EM cluster is assumed to be a positron (electron)

4.5 Selected $Z/\gamma*$ candidates

After the above requirements, we have 157394 events selected with 73707 CC-CC events and 83687 CC-EC events. As mentioned before, we only look at events with dielectron invariant mass between 50 and 500 GeV, and the mass bins we chose are 50-60 GeV, 60-70 GeV, 70-75 GeV, 75-81 GeV, 81-86.5 GeV, 86.5-89.5 GeV, 89.5-92 GeV, 92-97 GeV, 97-105 GeV, 105-115 GeV, 115-130GeV, 130-180 GeV, 180-250 GeV, 250-500 GeV and 500-1000 GeV. The GEANT MC samples we used were generated with the generator-level Z/γ^* mass > 15 GeV. The reasons we chose to use these bins are the following:

- The bin widths chosen around Z pole were determined by the detector energy resolution;
- We used slightly asymmetric bin widths around the Z-pole due to the fact that more events shift to the low-mass side than high-mass side;
- We considered the fact that the generator-level A_{FB} reaches the miminum around 67 GeV, changes the sign around 89.2 GeV and becomes flat after 130 GeV;
- For the future analysis, we also plan to measure the u and d ratio in the proton based on Fig. 1.12, and the A_{FB} differences between $u\bar{u} \to Z/\gamma^*$ and $d\bar{d} \to Z/\gamma^*$ are significant around 50-70 GeV and 100-130 GeV;
- The bin widths for low mass and high mass regions were determined by the limited statistics. The numbers 60 GeV, 130 GeV, 250 GeV, 500 GeV were chosen due to the GEANT MC samples we have were generated with five different mass regions: 40-60 GeV, 60-130 GeV, 130-250 GeV, 250-500 GeV and $>$ 500 GeV.

The invariant mass, $\cos\theta^*$, electron/positron p_T and detector η distributions of all selected candidates are shown in Fig 4.2 for CC-CC events and in Fig 4.3 for CC-EC events. Number of events in each mass bin (also divided into forward/backward events) is listed in Table 4.2.

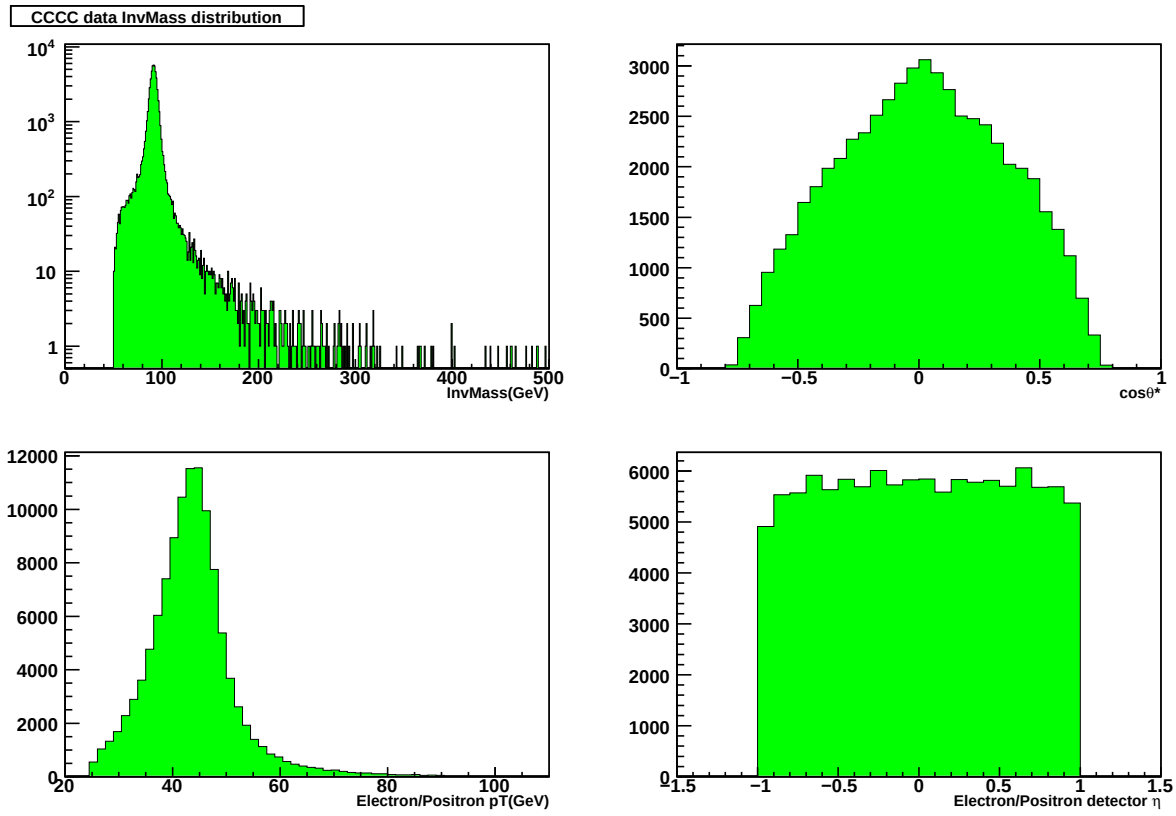

Figure 4.2: Invariant mass, $\cos\theta^*$, electron/positron p_T and detector η distributions for CC-CC candidates.

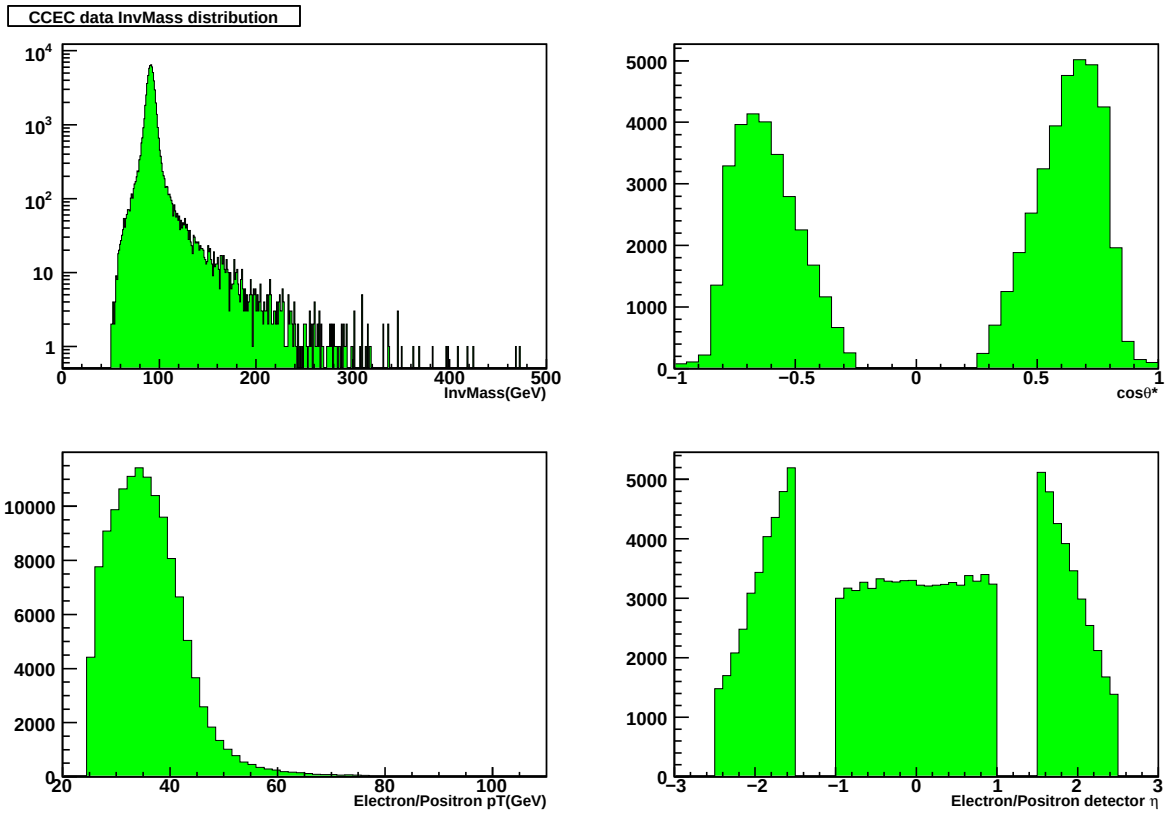

Figure 4.3: Invariant mass, $\cos\theta^*$, electron/positron p_T and detector η distributions for CC-EC candidates.

Mass Range (GeV)	CC-CC		CC-EC	
	Forward	Backward	Forward	Backward
$50 - 60$	272	309	53	64
$60 - 70$	466	707	239	418
$70 - 75$	409	537	281	489
$75 - 81$	851	1054	768	1223
$81 - 86.5$	3309	3519	3760	4178
$86.5 - 89.5$	6672	6644	8323	7636
$89.5 - 92$	9323	8807	11123	9558
$92 - 97$	12138	11041	14278	11365
$97 - 105$	2861	2182	3698	2155
$105 - 115$	678	432	1137	400
$115 - 130$	407	188	766	228
$130 - 180$	436	151	844	269
$180 - 250$	137	61	252	73
$250 - 500$	63	45	84	24
$500 - 1000$	7	1	1	0

Table 4.2: Number of forward and backward events after selection for CC-CC and CC-EC respectively.

Chapter 5

Efficiencies

5.1 Introduction

The GEANT MC simulation of $Z/\gamma^* \rightarrow ee$ uses the standard DØ chain, based on Pythia [55] with the CTEQ6L1 [56] parton distribution functions (PDFs), and is mainly used to understand the detector's geometric acceptance for electrons, the energy scale and resolution for electrons in the calorimeter.

The Pythia GEANT MC samples we used are listed in Table 5.1. Events with five different mass regions were generated with different integrated luminosities in order to get more events in both low- and high-mass regions. The number of GEANT MC events around Z peak (15.7 M) is about 15 times the number of observed Z's for the 3.9 fb^{-1} dataset (1 M). Fig. 5.1 shows the invariant mass of the generator level Z/γ^* boson mass distribution before and after taking into account different integrated luminosities for the five mass regions.

Since the default DØ GEANT MC simulation can not sufficiently describe the data,

Mass range	Request IDs	Events	SAM dataset definition
40-60 GeV	see below	4.6M	AFB-Zee-40-60GeV-p21-V1
60-130 GeV	see below	15.7M	AFB-Zee-60-130GeV-p21-V1
130-250 GeV	see below	2.7M	AFB-Zee-130-250GeV-p21-V1
250-500 GeV	see below	3.3M	AFB-Zee-250-500GeV-p21-V1
>500 GeV	see below	470k	AFB-Zee-500GeV-p21-V1

Table 5.1: PYTHIA GEANT MC $Z/\gamma^* \rightarrow ee$ samples used for A_{FB} studies. The request IDs for 40-60GeV sample are 104812-104836. And request IDs for 60-130GeV sample are 65752-65753, 65772-65774, 67772, 86882-86886, 86893-86897, 94342-94351, 99432, 99452-99465 and 110012-110051. The request IDs for 130-250GeV sample are 66372, 86892, 94192-94193 and 104837-104846. The request IDs for 250-500GeV sample are 66374, 94195-94198, 104847-104856 and 107932-107934. The request IDs for >500 GeV sample are 66376 and 94199-94200.

the relative scale factors between data and GEANT MC efficiencies were measured and applied to GEANT MC. We divide selection efficiencies into the following three categories: the preselection (ID, emf, iso cuts), EM identification (HMx7, HMx8) and track matching efficiency. In Sect. 5.2, we describe the method used to measure all efficiencies for data and GEANT MC, and the relative scale factor between data and GEANT MC for each efficiency is derived and applied on GEANT MC.

More corrections applied on the simulation are described in Sec. 5.3. The calorimeter energy scale and resolution in the simulation are tuned so that the mean and width of the Z peak in the simulation are consistent with those from the data (in Sect. 5.3.1),

and then the distributions of instantaneous luminosity and vertex in the simulation are reweighted to data. Since PYTHIA is a LO generator, in order to take advantage of theoretical advances we would like to compare our data to more accurate theoretical predictions. We start with PYTHIA events, and reweight the boson mass M, transverse momentum p_T and rapidity (y) distributions to agree with higher-order predictions.

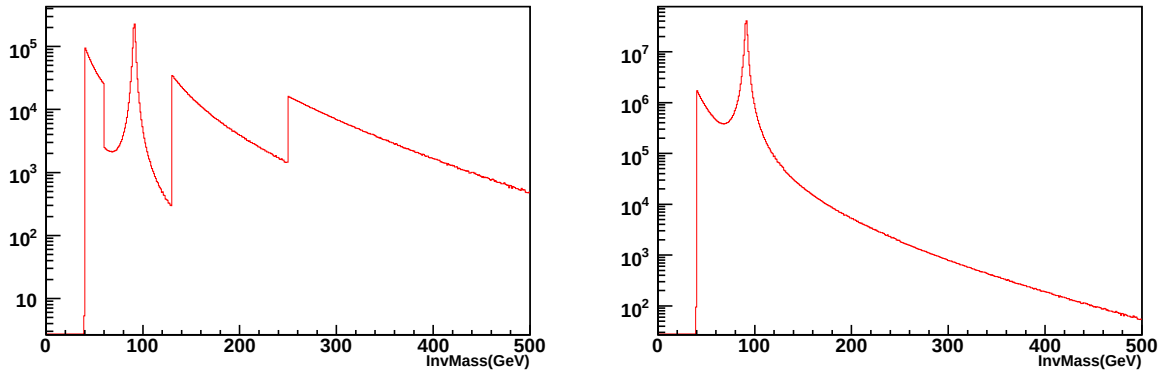

Figure 5.1: Invariant mass distribution of Z/γ^* boson for the GEANT MC samples we used. The left and right plots show number of events before and after taking into account different integrated luminosities for five different mass regions.

5.2 Electron efficiencies

5.2.1 Tag-Probe method

The standard Tag-and-Probe method is applied to data and GEANT MC samples: an electron candidate passing a requirement tighter than the offline selection cuts is set as a tag leg, the probe leg is selected by employing the Z mass constraint. Probe electrons

form a minimally biased electron sample with high purity and are optimal for studying the selection efficiencies. The requirements for the tag leg are required to be in CC fiducial region and the other requirements are listed below:

- transverse momentum $p_T > 30$ GeV;
- id= ± 11, iso < 0.10, emf > 0.95, HMx7 < 12;
- spatial track matching with probability $P(\chi^2) > 0.001$;
- Lhood8 > 0.90;
- $dz_{vtx} < 3$ cm to ensure that the track coming from primary vertex;
- Track $p_T > 25$ GeV, $0.8 < E/P < 1.2$;
- Track $r_{dca} < 0.2$ cm, $\chi^2/ndof < 5$, nCFT >= 9, nSMT >= 2.

5.2.2 Electron PreSelection efficiency

To obtain the probe leg, a test track opposite to the tag leg is selected with

- track $p_T > 15$ GeV, $dz_{vtx} < 3$ cm, $r_{dca} < 0.2$ cm, $\chi^2/ndof < 5$, nCFT >= 9, nSMT >= 2;
- opposite charge with the tag leg;
- $\Delta\phi(tag\ track,\ test\ track) > 2$;
- $70 < M(tag\ electron,\ test\ track) < 110$ GeV.

Test tracks are then matched with an EM cluster with ΔR <0.14 to obtain the probe EM cluster. The probe EM clusters that satisfying the following requirement are used for preselection efficiency study:

- ID=10, ±11, emf>0.9, iso<0.15(CC) iso<0.10(EC);
- $E_T > 25$ GeV;
- $70 < M(tagEM, probeEM) < 110$ GeV.

The preselection efficiency as a function of EM cluster E_T, detector η, detector ϕ and Vtx_Z respectively are shown in Fig. 5.2 for CC region and Fig. 5.3 for EC region.

The data/GEANT MC scale factor for the PreSelection efficiency is checked vs all four variables described above, and is found to have some dependence on the electron detector η. This dependence is plotted as a function of EM cluster detector η in Fig. 5.4, and this dependence is corrected in the GEANT MC simulation.

5.2.3 Electron ID efficiency

Based on PreSelection, we study electron ID efficiency in both CC and EC region. The probe EM cluster is selected with the PreSelection cuts, and then the number of probe EM clusters that have HMx7 < 12 (CC) and HMx8 < 10 and $\sum trk - pT > 1.5$GeV (EC) as the numerator. The electron ID efficiencies of an electron in both CC and EC region versus p_T, detector η, detector ϕ and Vtx_Z measured from $Z \rightarrow ee$ in MC and EM inclusive data samples are shown in Fig. 5.5 and Fig. 5.6.

The data/GEANT MC scale factor for the EMID efficiency is checked vs all four variables described above, and is found to have some dependence on the electron de-

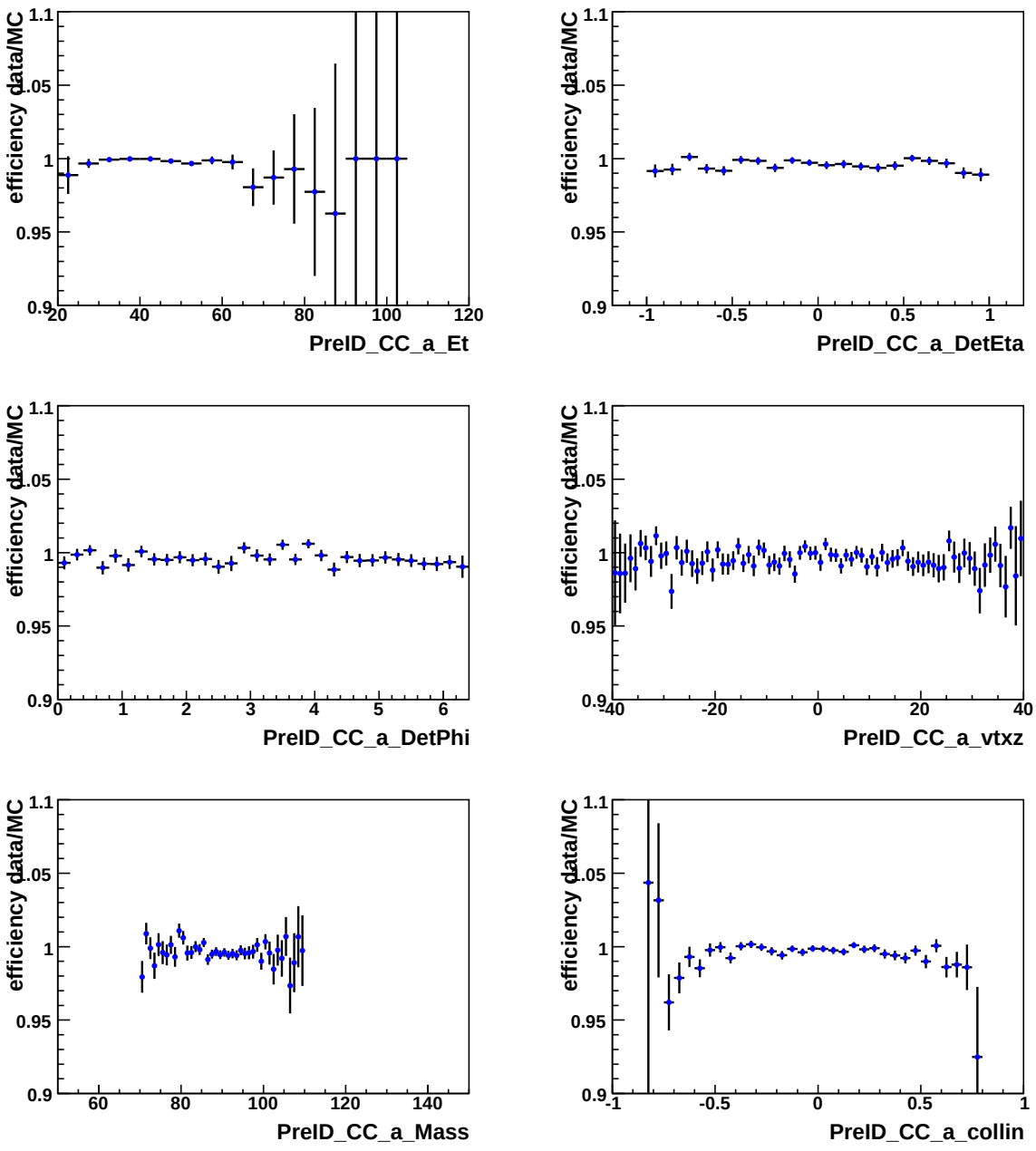

Figure 5.2: Pre-selection efficiencies (CC region) versus EM cluster p_T, detector η, detector ϕ , Vtx_Z ,invariant mass and collin angle of GEANT MC $Z \rightarrow ee$ and EM inclusive data respectively.

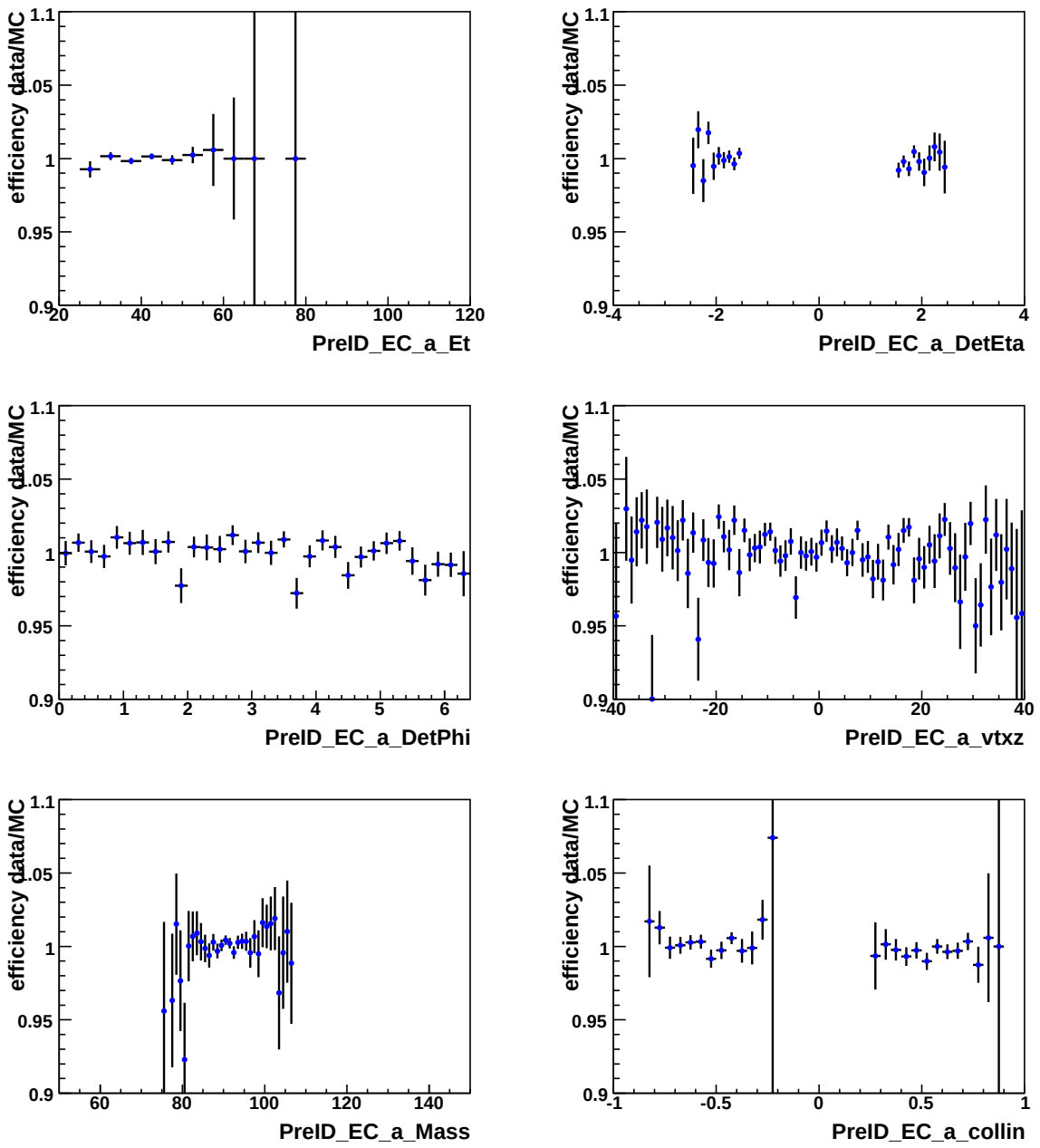

Figure 5.3: Pre-selection efficiencies (EC region) versus EM cluster p_T, detector η, detector ϕ, Vtx_Z invariant mass and collin angle of GEANT MC $Z \rightarrow ee$ events and EM inclusive data respectively.

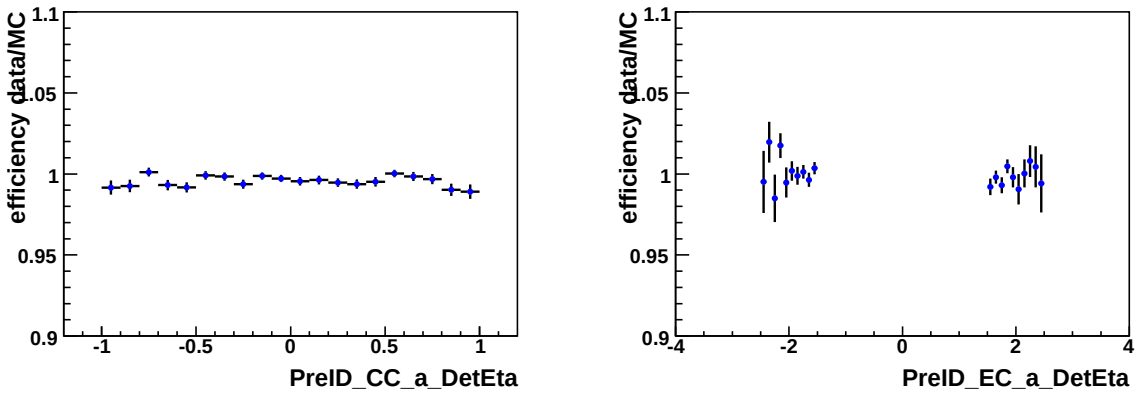

Figure 5.4: The ratio of electron PreSelection ID efficiency between data and MC as a function of EM cluster detector η.

tector η. This dependence is plotted as a function of EM cluster detector η in Fig. 5.7, and this dependence is corrected in the GEANT MC simulation.

5.2.4 Electron track match efficiency

Having analyzed calorimeter-based electron ID efficiency, we investigate spacial track match efficiency of an electron. The probe EM cluster is selected with the following requirements:

- In CC fiducial region;
- p_T >25 GeV;
- ID = 10 or ±11, iso< 0.15, emf> 0.9, HMx7< 12;
- $\Delta\phi$ (tag EM, probe EM) > 2.

For the cluster-track matching efficiency measurement, the number of EM clusters passing above probe criteria is taken as the denominator. Then, the number of probe

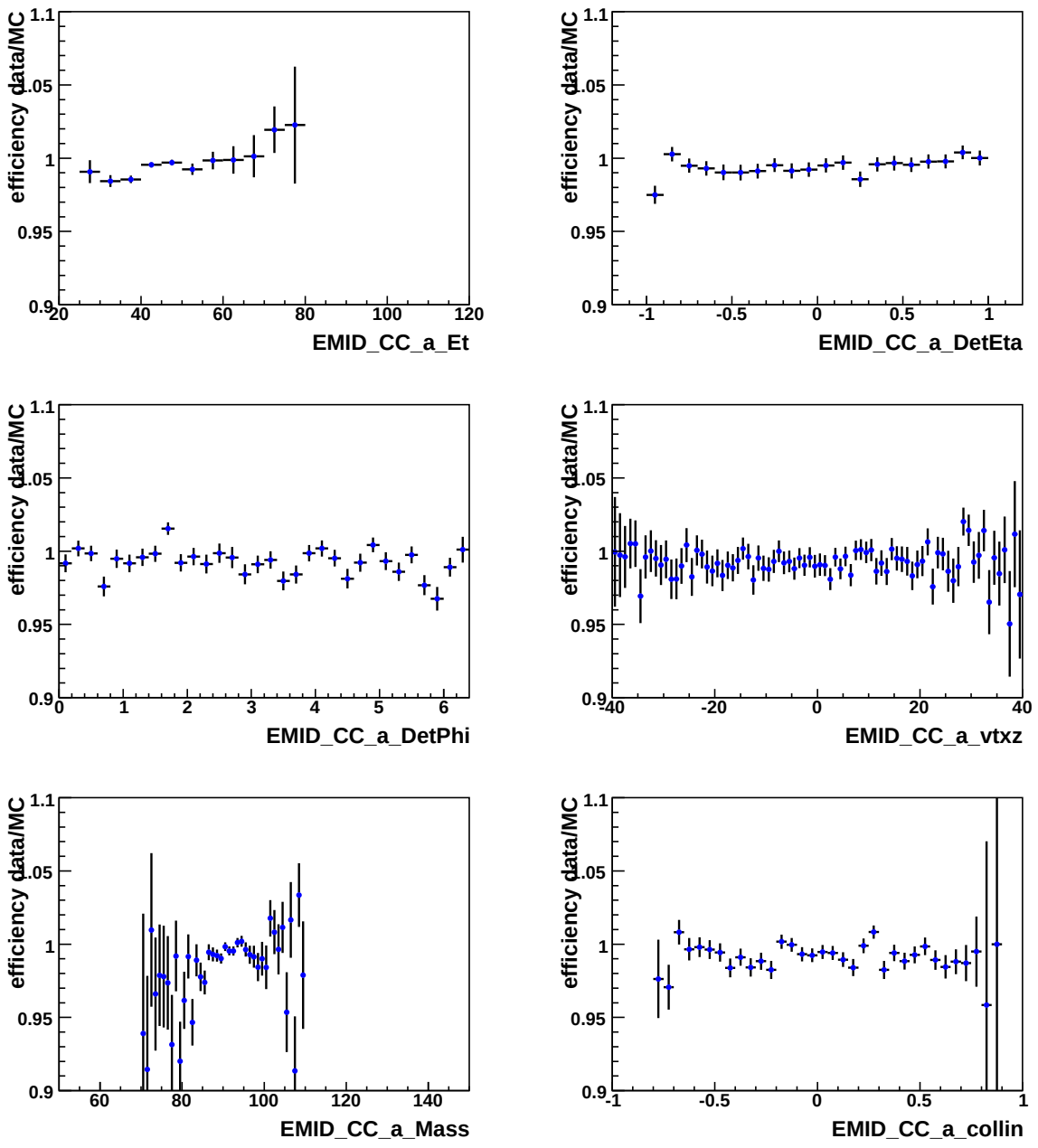

Figure 5.5: electron ID efficiencies (CC region) versus EM cluster p_T, detector η, detector ϕ, Vtx_Z, invariant mass and collin angle of GEANT MC $Z \rightarrow ee$ and EM inclusive data respectively.

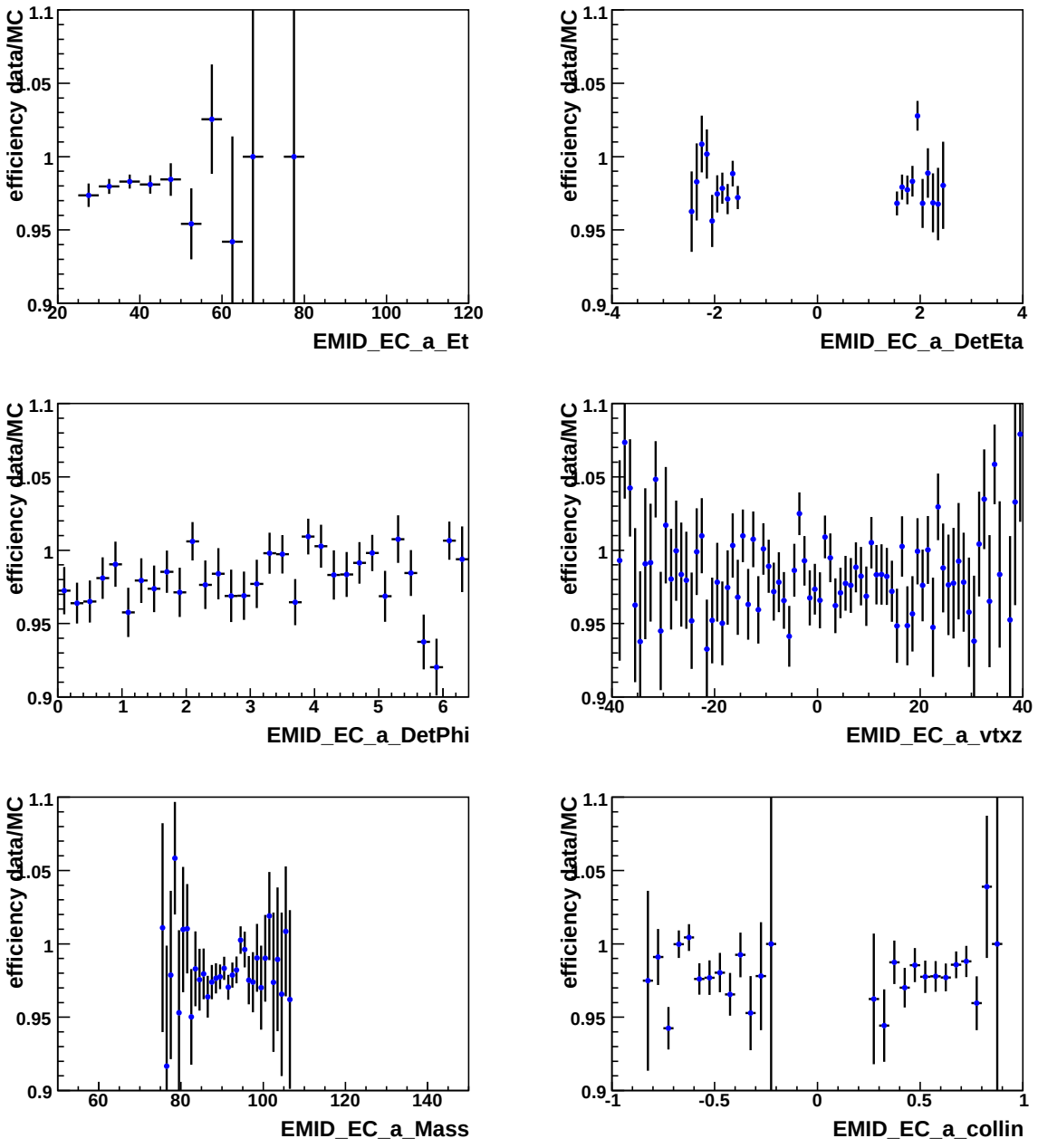

Figure 5.6: electron ID efficiencies (EC region) versus EM cluster p_T, detector η, detector ϕ, Vtx_Z, invariant mass and collin angle of GEANT MC $Z \rightarrow ee$ and EM inclusive data respectively.

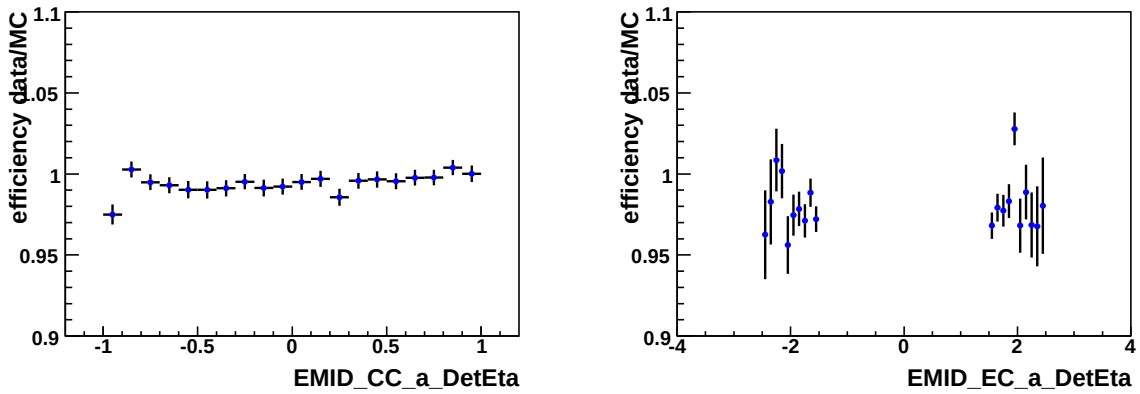

Figure 5.7: The ratio of electron EMID efficiency between data and MC as a function of EM cluster detector η.

EM clusters that have a spacial track matched with :

- $P(\chi^2) > 0.001$;
- track pT > 10 GeV;
- nCFT $>= 9$, nSMT $>= 2$;
- track fitting χ^2/ndof < 9.95;
- rdca < 0.02 cm(Corrected with beamspot).

is taken as the numerator. The track matching efficiencies of an electron versus E_T, η and ϕ measured from $Z \rightarrow ee$ in GEANT MC and EM inclusive data samples are shown in Fig. 5.8.

The data/GEANT MC scale factor for the EMID efficiency is checked vs all four variables described above, and is found to have some dependence on the electron physics η and Z of primary vertex. This dependence is plotted as a function of EM cluster

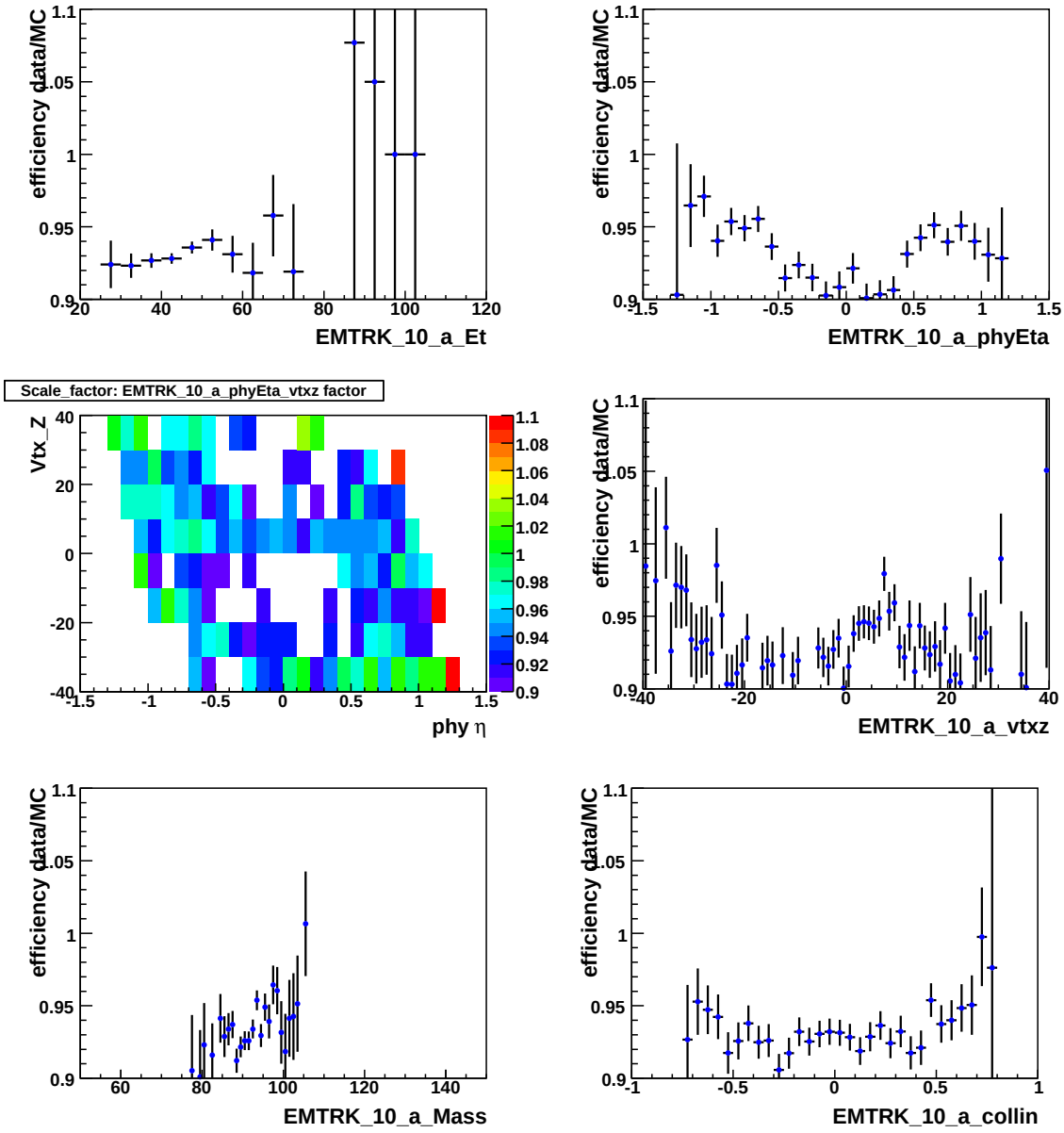

Figure 5.8: Track match efficiencies versus EM cluster p_T, physics η, Vtx_Z, invariant mass and collin angle of GEANT MC $Z \rightarrow ee$ and EM inclusive data respectively. For real data, the efficiency is lower for physics η close to 0, this is due to the CFT light yield. The structure shown with vtx$_Z$ is due to number of SMT hits requirement, the six regions correspond to six SMT barrels.

detector η in Fig. 5.9, and this dependence is corrected in the GEANT MC simulation.

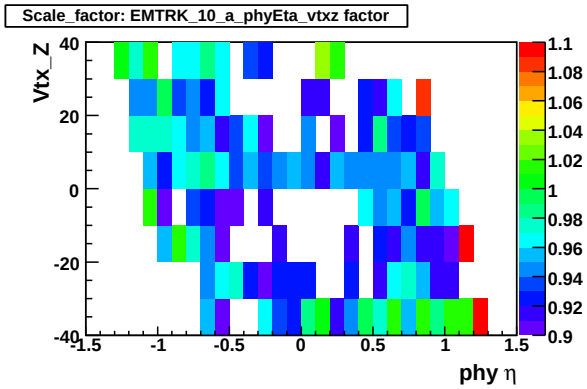

Figure 5.9: The ratio of electron track match efficiency between data and MC as a function of physics η and vtxz.

5.2.5 Electron identification corrections

To remove the electron identification difference between data and GEANT MC, we applied corrections for the PreSelection, Eletron ID and Track match on MC, which are shown below:

- PreSelection efficiency: applied in 1 dimension (detector η). Fig. 5.4
- Electron ID efficiencies: applied in 1 dimension (detector η). Fig. 5.7
- Track match efficiency: applied in 2 dimensions (physics η, vtx-Z). Fig. 5.9

5.3 MC Reweighting

5.3.1 Electron energy scale and resolution

The default DØ GEANT MC simulation predicts different Z peak and width compared with the real data, additional energy scaling and smearing need to be applied on GEANT MC in order to predict the right Z peak and width as those observed in data. The additional scaling is done using the following formula:

$$E^{'} = \alpha \times E^{\mathrm{GEANT}} \tag{5.1}$$

and the additional smearing is done using the following formula:

$$E^{\mathrm{smear}} = E^{'}(1 + c \times x) \tag{5.2}$$

where E^{GEANT}, $E^{'}$ and E^{smear} are the raw energy from GEANT MC simulation, the energy after scaling, and the energy after scaling and smearing respectively. α and c are the energy scaling and smearing parameters (CC and EC electrons have different α and c), and x is a random number generated with a Gaussian distribution with zero mean and unit sigma.

To measure the parameters for the additional energy scaling and smearing, we vary the energy scale and smearing parameters and then compare the Z invariant mass distributions from the tuned GEANT MC simulation and the data. We first use CC-CC Z events to determine CC parameters, and then use CC-EC events to determine EC parameters.

We vary the additional energy scaling parameter (energy smearing parameter), and calculate the χ^2 for the Z invariant mass between the data and the smeared

GEANT MC prediction. A second-order polynomial function is used to determine the best scaling parameters and a change of 1 for the overall χ^2 is used to determine the systematic uncertainty of these parameters. The scaling parameter is found to be 1.0021 $\pm$ 0.00027 for CC and 0.9941 $\pm$ 0.00027 for EC. The smearing parameter is found to be 0.025$\pm$0.002 for CC and 0.028$\pm$0.002 for EC. Since we did not introduce the energy offset for CC and EC electron in the Geant MC simulation (even though all data/MC comparison plots agree pretty well without the additional energy offset term), we decided to increase the uncertainty of both scaling and smearing parameters by varying the parameters by $\pm$1 simga for both CC and EC electrons.

5.3.2 Instantaneous luminosity and vertex reweighting

Data and GEANT MC simulation have different instantaneous luminosity and primary vertex distributions, and we reweight the two distributions in GEANT MC to reflect the real data distributions. More detailed information can be found in Appendix A.

5.3.3 Z boson M reweighting

A mass-dependent k-factor is introduced to include higher-order QCD corrections on the Z/γ^* boson invariant mass distribution. The K-factor is defined as [57]:

$$K = \frac{\sigma_{NNLO}\text{with NLO PDF}}{\sigma_{LO}\text{with LO PDF}} \tag{5.3}$$

The NNLO cross sections are obtained from the calculation of Hamberg *et. al.* [58]. The K-factor as a function of M_{ee} is shown in Table 6 of DØ note 4476, the K-factor changes from 1.30 at $M = 50$ GeV to 1.38 at $M = 600$ GeV, increasing by $\sim 6\%$.

5.3.4 Z boson p_T and y reweighting

The RESBOS generator [59] has been proven to give a more accurate theoretical description of the Z/γ^* boson transverse momentum and rapidity distributions. A boson p_T and y re-weighting scheme developed by S. Yacoob *et. al.* [60] is used here. To do this reweighting, Z pt and Z rapidity 2D distributions are get from RESBOS and PYTHIA generator, then we take the ratio distribution between RESBOS and PYTHIA to reweight the full MC, which are generated with PYTHIA.

5.4 ϕ-mod and luminosity correction on both data and MC

5.4.1 luminosity correction

For Run IIb data, we observed that the peak position of the Z boson shifts to lower value as instantaneous luminosity increases [49], while in full MC simulation, the dependence is the opposite way. To reduce this effect on the A_{FB} measurement, we apply luminosity corrections to the measured electron energy for both data and full MC. The correction funcitons can be found in Fig. 5.10. They were derived using the electron E/p peak position [50]. For RunIIb data, there are some differences between pre-2007 ShutDown and post-2007 ShutDown, so we applied two different corrections on those two data sets.

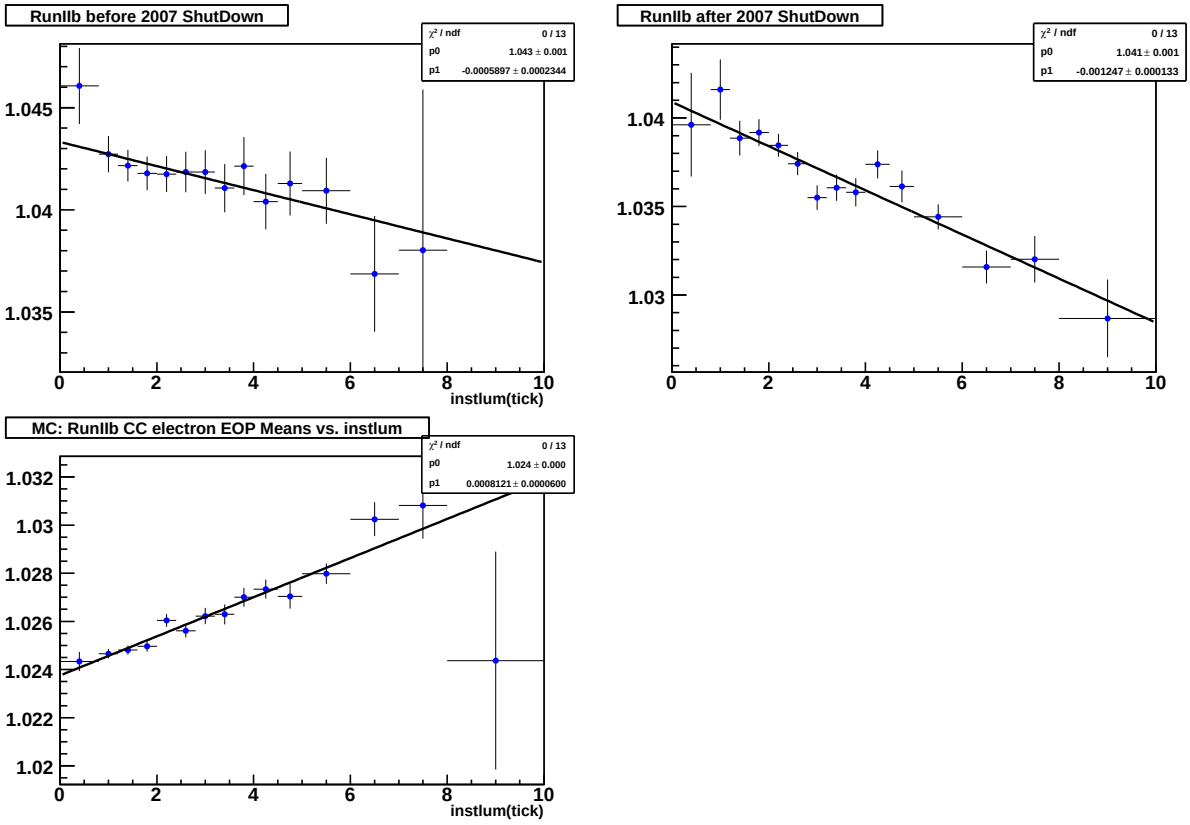

Figure 5.10: Electron EOP(electron E_t over electron p_T) mean values for difference instlum bins.

5.4.2 ϕ-mod correction

We also applied another electron energy correction for both data and MC [51]. This correction not only focuses on correct electrons not passing the ϕ-mod region, but also will correct electrons in ϕ-mod region in order to move the Z peak value into the LEP measured one[52](91.18 GeV).

5.4.3 Forward/Backward efficiencies

Since A_{FB} is calculated using the numbers of forward and backward events, we have to make sure the electron selection criteria we used have little difference for forward and backward events. In this chapter, we investigate the possible difference between forward and backward events due to the selection cuts.

5.4.4 Ratio of forward and backward efficiencies

We measure the ratio for PreSelection, EMID and track matching efficiencies for forward and backward events in both real data and GEANT MC simulation. Since there is very little in the detector and analysis cuts we used treat forward and backward events differently, the efficiencies for forward and backward events are very close to each other. Fig. 5.11 and Fig. 5.12 show the ratio of PreSelection efficiencies for forward and backward events in CC and EC regions for both data and GEANT MC simulation. Fig. 5.13 and Fig. 5.14 show the ratio of EMID efficiencies for forward and backward events in CC and EC regions for both data and GEANT MC simulation. Fig. 5.15 shows the ratio of EM track matching efficiencies for forward and backward events in CC region for both data and GEANT MC simulation.

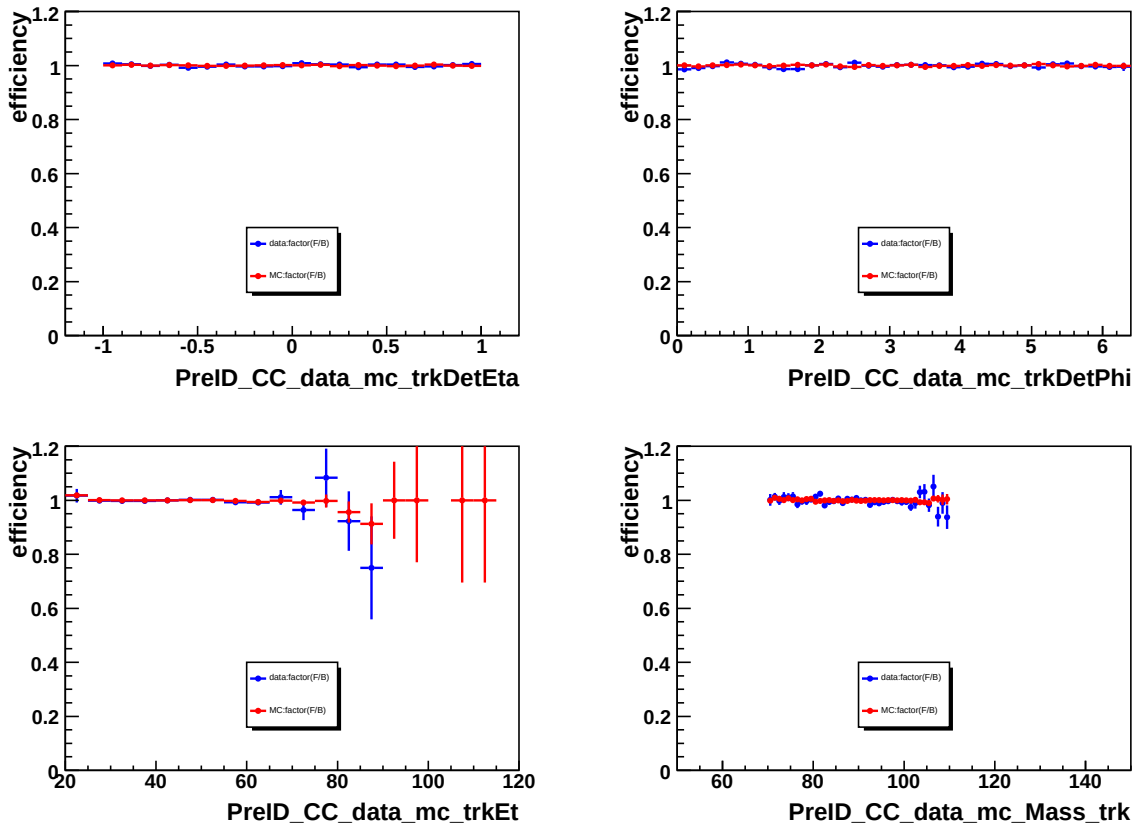

Figure 5.11: Ratio of PreSelection efficiencies for forward and backward events in CC region versus EM cluster p_T, detector η, detector ϕ and Mass of GEANT MC $Z \rightarrow ee$ and data respectively. The χ^2/ndof for those four plots are 15.8/20, 22.7/32, 5.6/14 and 52/40.

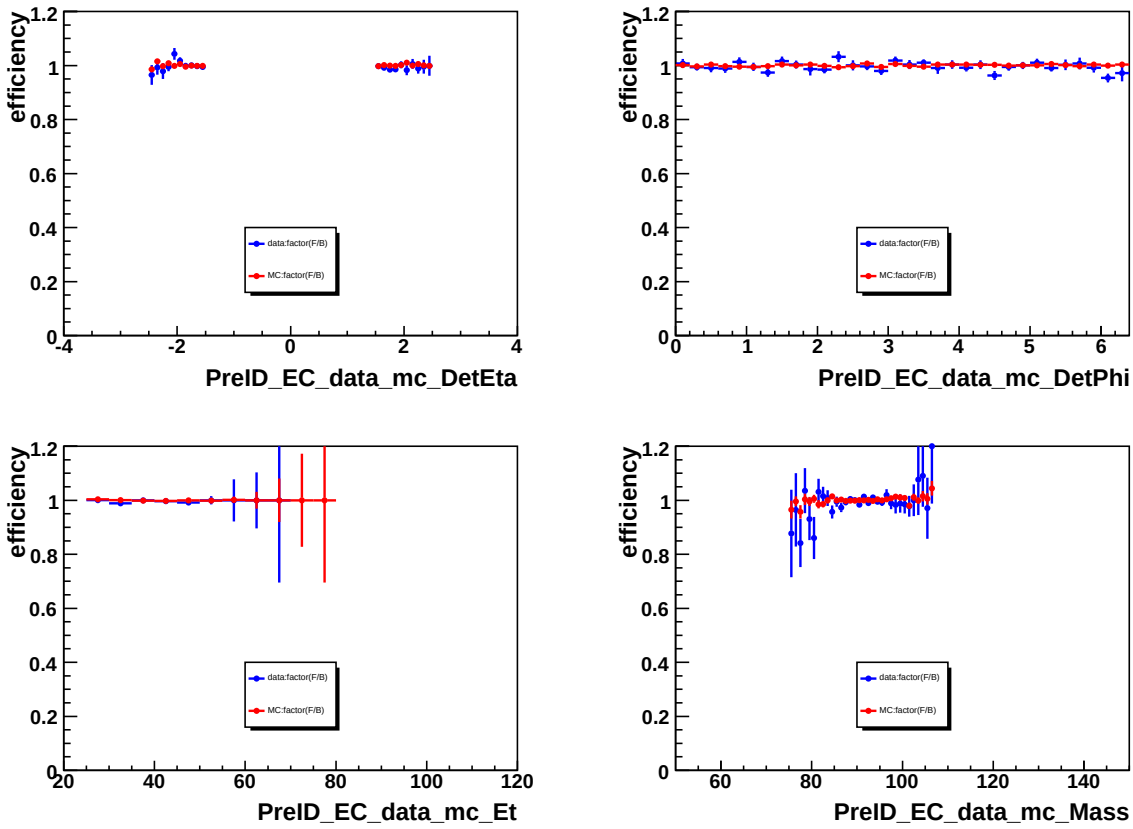

Figure 5.12: Ratio of PreSelection efficiencies for forward and backward events in EC region versus EM cluster p_T, detector η, detector ϕ and Mass of GEANT MC $Z \rightarrow ee$ and data respectively. The χ^2/ndof for those four plots are 16.4/20, 29.7/32, 6.3/9 and 36.4/32

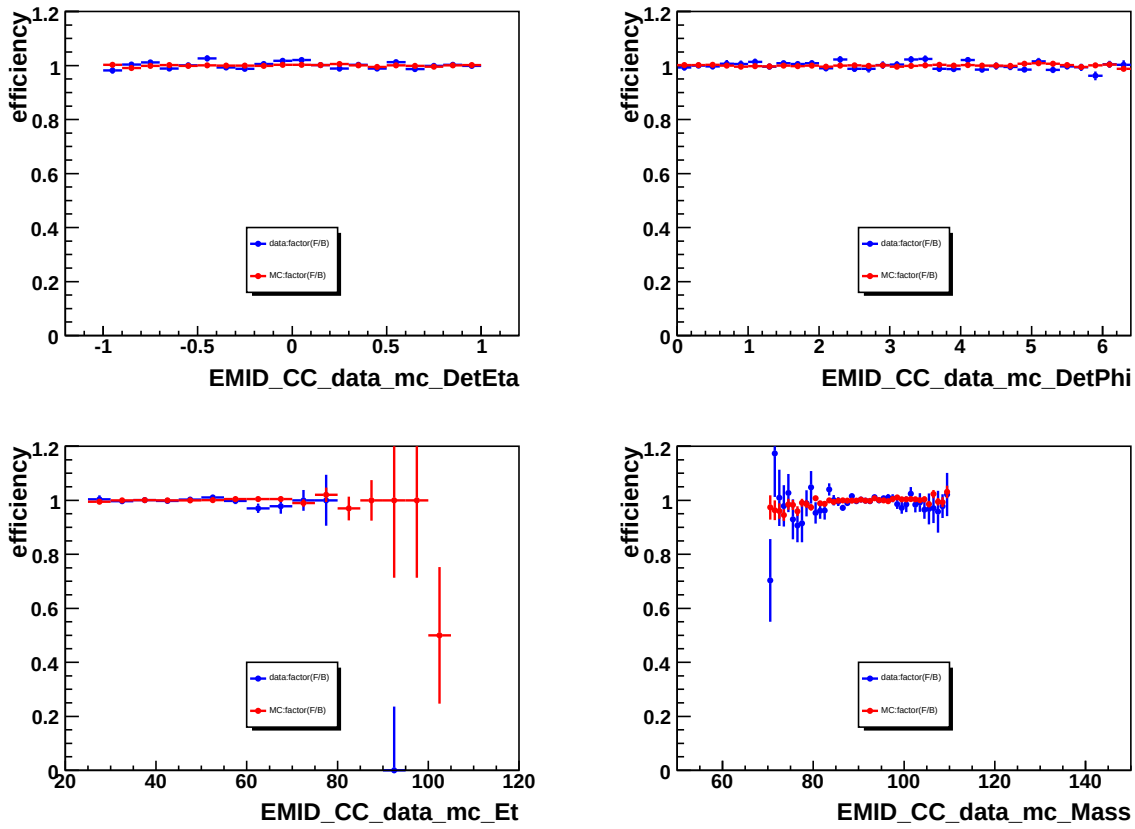

Figure 5.13: Ratio of EMID efficiencies for forward and backward events in CC region versus EM cluster p_T, detector η, detector ϕ and Mass of GEANT MC $Z \rightarrow ee$ and data respectively. The χ^2/ndof for those four plots are 26.6/20, 39.1/32, 7.76/11 and 36.4/40

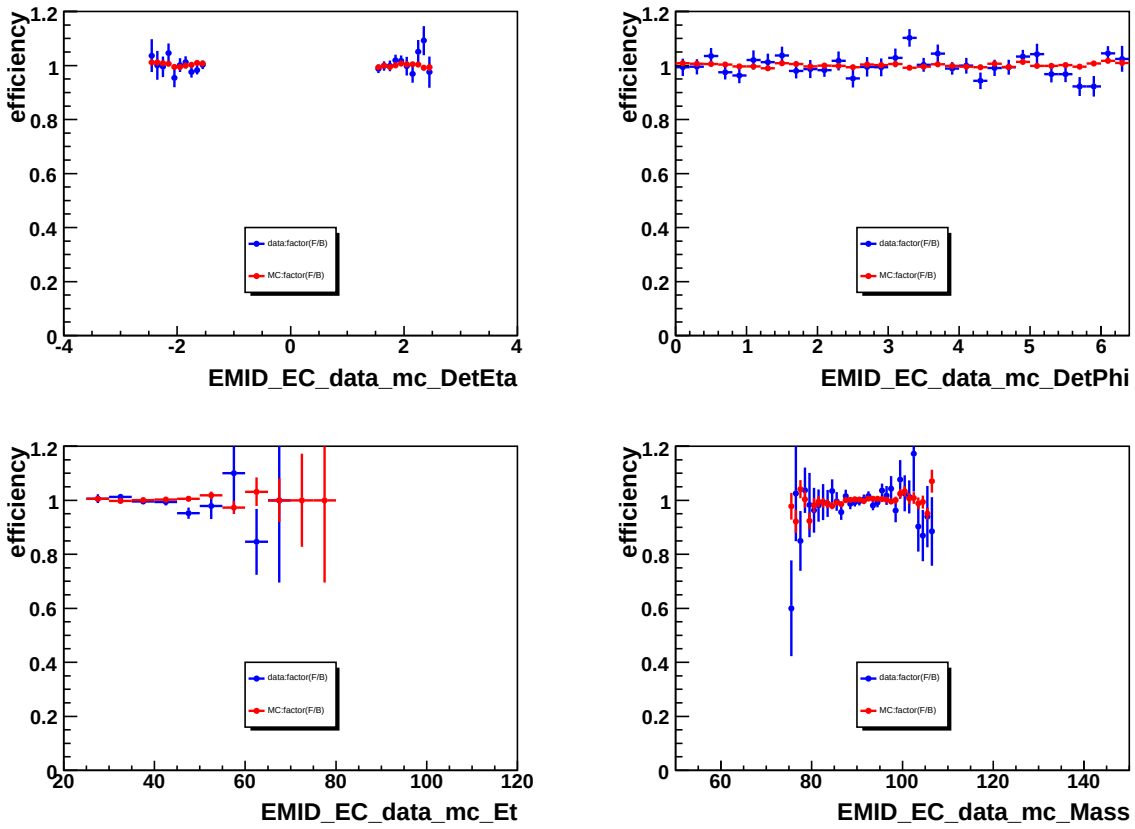

Figure 5.14: Ratio of EMID efficiencies for forward and backward events in EC region versus EM cluster p_T, detector η, detector ϕ and Mass of GEANT MC $Z \rightarrow ee$ and data respectively. The χ^2/ndof for those four plots are 14.0/20, 38.5/32, 12.6/9 and 23.9/32

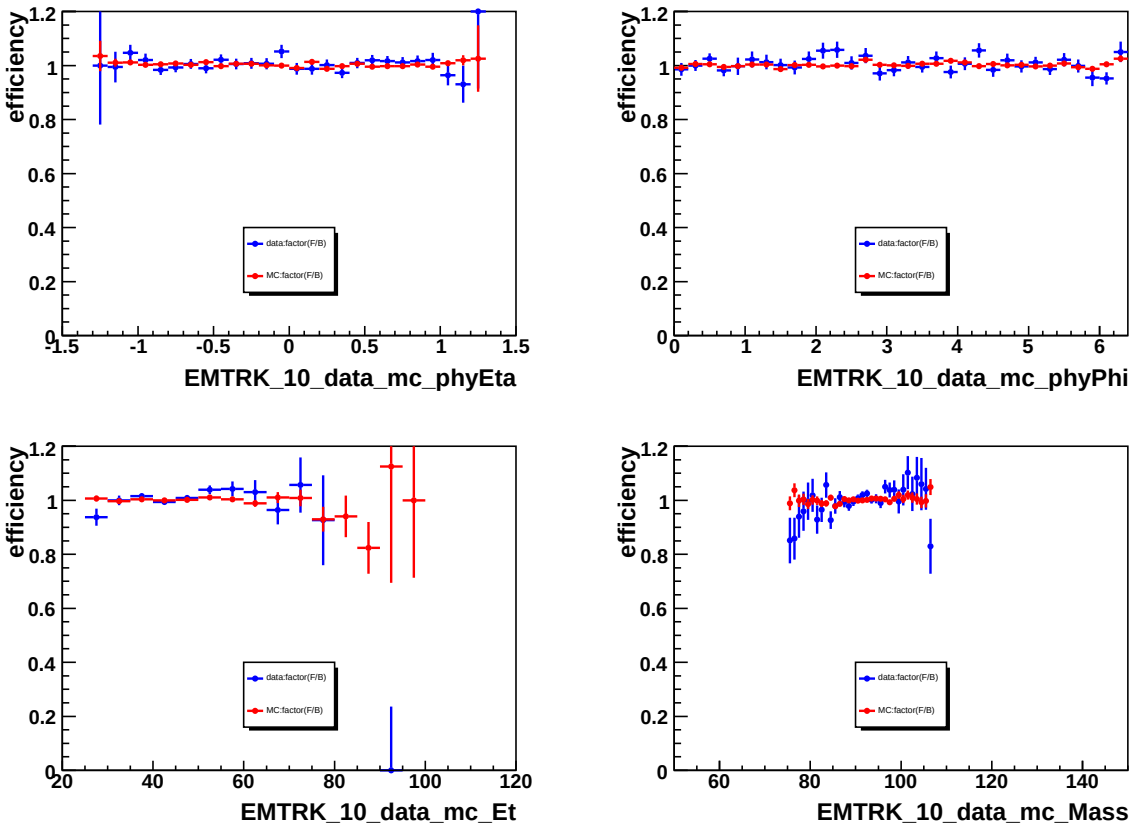

Figure 5.15: Ratio of electrons track match efficiencies for forward and backward events (CC only) versus EM cluster p_T, physics η, physics ϕ and Mass of GEANT MC $Z \rightarrow ee$ and data respectively. The χ^2/ndof for those four plots are 21.2/26, 30.1/32, 13.0/11 and 41.0/32

5.4.5 Fitted Ratio values for forward and backward efficiencies

We really care out is the difference between forward and backward events efficiencies, so we fit the ratio of each forward and backward efficiency to a straight line, and the fitted parameters with errors are listed in Table 5.2 for GEANT MC and in Table 5.4 for real data. The fit probabilities are shown in Table 5.3 and Table 5.5. The ratio between forward and backward efficiencies are observed to be consistent with 1 for both data and GEANT MC, and thus no obvious efficiency differences between forward and backward events observed.

	Det η	Det ϕ	p_T	Mass
PreSelect(CC)	1.000 ± 0.001	1.000 ± 0.001	1.000 ± 0.001	1.000 ± 0.001
PreSelect(EC)	1.000 ± 0.001	1.000 ± 0.001	0.999 ± 0.001	1.000 ± 0.001
EMID(CC)	1.000 ± 0.001	1.000 ± 0.001	1.000 ± 0.001	1.000 ± 0.001
EMID(EC)	1.000 ± 0.001	1.001 ± 0.001	1.001 ± 0.001	1.001 ± 0.001
	Phy η	Phy ϕ	p_T	Mass
TrkMatch	1.002 ± 0.001	1.002 ± 0.001	1.002 ± 0.001	1.001 ± 0.001

Table 5.2: Fitted value of foward and backward efficiencies in GEANT MC.

	Det η	Det ϕ	p_T	Mass
PreSelect(CC)	0.14	0.12	0.59	0.79
PreSelect(EC)	0.11	0.85	0.92	0.64
EMID(CC)	0.15	0.30	0.85	0.01
EMID(EC)	0.96	0.86	0.92	0.01
	Phy η	Phy ϕ	p_T	Mass
TrkMatch	0.14	0.11	0.44	0.42

Table 5.3: Fitting probabilities of GEANT MC.

	Det η	Det ϕ	p_T	Mass
PreSelect(CC)	1.000 ± 0.001	0.998 ± 0.001	0.999 ± 0.001	0.998 ± 0.001
PreSelect(EC)	0.996 ± 0.003	0.996 ± 0.003	0.996 ± 0.002	0.996 ± 0.002
EMID(CC)	1.001 ± 0.002	1.000 ± 0.002	1.000 ± 0.002	1.000 ± 0.002
EMID(EC)	0.999 ± 0.005	0.998 ± 0.005	0.998 ± 0.005	0.998 ± 0.006
	Phy η	Phy ϕ	p_T	Mass
TrkMatch	1.005 ± 0.004	1.004 ± 0.004	1.006 ± 0.004	1.005 ± 0.004

Table 5.4: Fitted value of foward and backward efficiencies in data.

	Det η	Det ϕ	p_T	Mass
PreSelect(CC)	0.87	0.94	0.91	0.21
PreSelect(EC)	0.18	0.50	0.66	0.52
EMID(CC)	0.20	0.17	0.01	0.47
EMID(EC)	0.83	0.18	0.41	0.25
	Phy η	Phy ϕ	p_T	Mass
TrkMatch	0.90	0.41	0.00	0.06

Table 5.5: Fitting probabilities of data.

Chapter 6

Backgrounds

The sources of background to the process $p\bar{p} \rightarrow Z/\gamma^* + X \rightarrow ee + X$ are:

- QCD events where jets are misidentified as electrons;
- $Z/\gamma^* \rightarrow \tau^+\tau^- \rightarrow e^+e^-\nu_\tau\nu_e\bar{\nu}_\tau\bar{\nu}_e$;
- $W + X \rightarrow e\nu + X$, where X is a jet/$\gamma$ misidentified as an electron;
- $\gamma + \gamma$ where γ is misidentified as an electron;
- $W^+W^- \rightarrow e^+e^-\nu_e\bar{\nu}_e$;
- $W^\pm Z$ where $Z \rightarrow e^+e^-$.
- $t\bar{t} \rightarrow Wb + W\bar{b} \rightarrow e\nu b + e\nu\bar{b}$.

The determination of A_{FB} requires knowledge of the number of background events and the forward-backward charge asymmetry of the background events in each mass bin.

The QCD background is the dominant background and is measured using real data, other backgrounds are all measured using tuned PYTHIA GEANT MC simulation and are mostly negligible.

6.1 PYTHIA GEANT MC samples

The PYTHIA GEANT MC samples we used to measure SM backgrounds are shown in Table. 6.1 with the cross sections from PYTHIA. And for $W + X$ backgrounds, we use ALPGEN + PYTHIA GEANT MC samples to estimate the contribution, those cross sections are shown in Table. 6.2

6.2 SM backgrounds

The standard model backgrounds are estimated using the PYTHIA GEANT Monte Carlo simulation. Since PYTHIA is a LO-based generator, we scale the LO cross section to the NLO calculations. The NLO cross sections are $\sigma(Z/\gamma^* \to \tau\tau) = 252 \pm 9$ pb from [53], $\sigma(WW \to e\nu e\nu) = 0.15 \pm 0.01$ pb and $\sigma(WZ \to 3l + \nu) = 0.1145 \pm 0.00016$ pb from [54]. The simulated events for each process which pass the selection requirements are used to determine both the invariant mass distributions and the expected forward-backward asymmetries. Number of expected events for each process are shown in Tab. 6.3, Tab. 6.4 and Tab. 6.5 for CC-CC events, Tab. 6.6, Tab. 6.7 and Tab. 6.8 for CC-EC events.

Channel	Events	xsection (pb)
$Z \rightarrow \tau\tau$ (15-60)	1.9M	363.1
$Z \rightarrow \tau\tau$ (60-130)	2.2M	179.6
$Z \rightarrow \tau\tau$ (130-250)	443k	1.348
$Z \rightarrow \tau\tau$ (250-500)	194k	0.1139
$Z \rightarrow \tau\tau$ (>500)	102k	0.004533
$\gamma + \gamma$(50-130)	1.1M	42.3
$\gamma + \gamma$(130-250)	1.1M	3.12
$\gamma + \gamma$(>250)	1.7M	0.49
$WW \rightarrow$ incl	711k	8.003
$WZ \rightarrow 3l + \nu$	364k	0.07844
$t\bar{t}$	1.1M	6.1

Table 6.1: GEANT MC samples ued for SM background studies.

6.3 QCD background

QCD dijet events may contribute as so-called instrumental background, where both jets are mis-reconstructed as electrons. Even though the rate for a jet to fake as an electron is fairly small due to the very tight track matching requirements we used, dijet events are still the dominant source of background in our sample due to the huge production rate. We do not expect any correlation between the charges of the two fake electrons in the dijet events.

The shape of QCD background is measured by inverting shower shape requirement

SM process	ReqId	σ (pb)
$W(l\nu)$+0lp excl.	CSG_alpgenpythia_w+0lp_lnu+0lp_excl_p211100_v2	5885.63
$W(l\nu)$+1lp excl.	CSG_alpgenpythia_w+1lp_lnu+1lp_excl_p211100_v2	1673.98
$W(l\nu)$+2lp excl.	CSG_alpgenpythia_w+2lp_lnu+2lp_excl_p211100_v2	401.08
$W(l\nu)$+3lp excl.	CSG_alpgenpythia_w+3lp_lnu+3lp_excl_p211100_v2	96.74
$W(l\nu)$+4lp excl.	CSG_alpgenpythia_w+4lp_lnu+4lp_excl_p211100_v2	22.07
$W(l\nu)$+2b+0lp incl.	CSG_alpgenpythia_w+2b+0lp_lnu+2b+0lp_excl_p211100_v2	13.75
$W(l\nu)$+2b+1lp incl.	CSG_alpgenpythia_w+2b+1lp_lnu+2b+1lp_excl_p211100_v2	6.33
$W(l\nu)$+2b+2lp incl.	CSG_alpgenpythia_w+2b+2lp_lnu+2b+2lp_excl_p211100_v2	2.25
$W(l\nu)$+2b+3lp incl.	CSG_alpgenpythia_w+2b+3lp_lnu+2b+3lp_incl_p211100_v2	1.07
$W(l\nu)$+2c+0lp incl.	CSG_alpgenpythia_w+2c+0lp_lnu+2c+0lp_excl_p211100_v2	35.87
$W(l\nu)$+2c+1lp incl.	CSG_alpgenpythia_w+2c+1lp_lnu+2c+1lp_excl_p211100_v2	19.83
$W(l\nu)$+2c+2lp incl.	CSG_alpgenpythia_w+2c+2lp_lnu+2c+2lp_excl_p211100_v2	8.03
$W(l\nu)$+2c+3lp incl.	CSG_alpgenpythia_w+2c+3lp_lnu+2c+3lp_incl_p211100_v2	3.75

Table 6.2: $W + X$ contribution is estimated with ALPGEN + PYTHIA Geant MC. The cross sections of W+jet are given at tree level, and NLO k-factor of 1.30 and 1.47 are applied to light quark (nlp) and heavy quark (2c and 2b) associations respectively.

for electrons in CC (HMx7 $>$ 30) and in EC (HMx8 $>$ 40) and dropping the electron track macth cuts and normalized as described below. The QCD shape around Z peak region is shown in Fig. 6.2. The systematic uncertainty due to the shape is estimated by using different shower shape cuts. Fig. 6.1 shows the QCD background shapes using different HMx cuts. The uncertainty due to the background shapes is included in the final uncertainty.

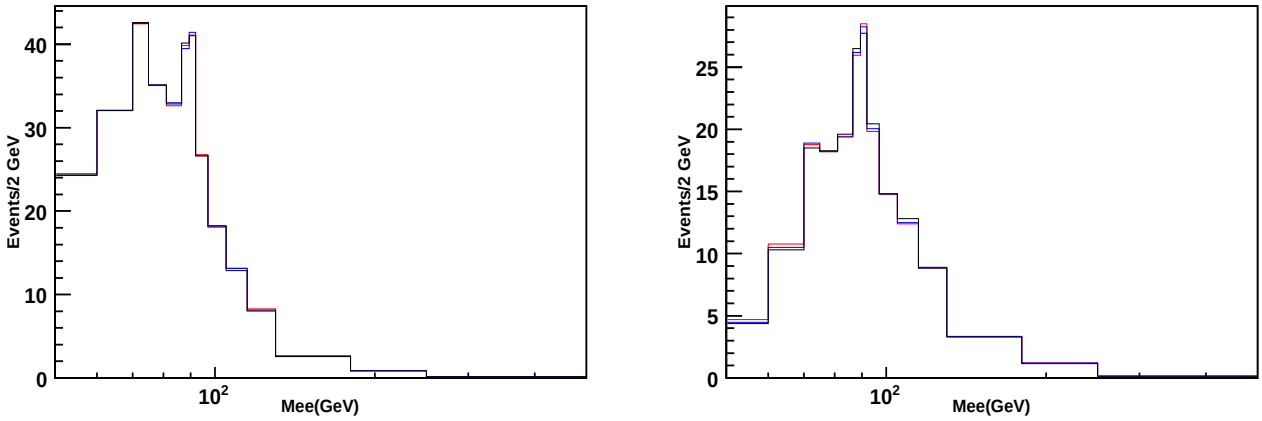

Figure 6.1: QCD background shapes for different HMx cuts in CCCC (Left) and CCEC (Right). For CCCC plot, Red line for HMx7 > 12, Blue line for HMx7 > 20 and Black line for HMx7 > 50. For CCEC plot, Red line for HMx7 > 30 in CC and HMx8 > 40 in EC, Blue line for HMx7 > 12 in CC and HMx8 > 20 in EC, Black line for HMx7 > 50 in CC and HMx8 > 75 in EC. The shape difference is propagated to the final A_{FB} systematic uncertainty.

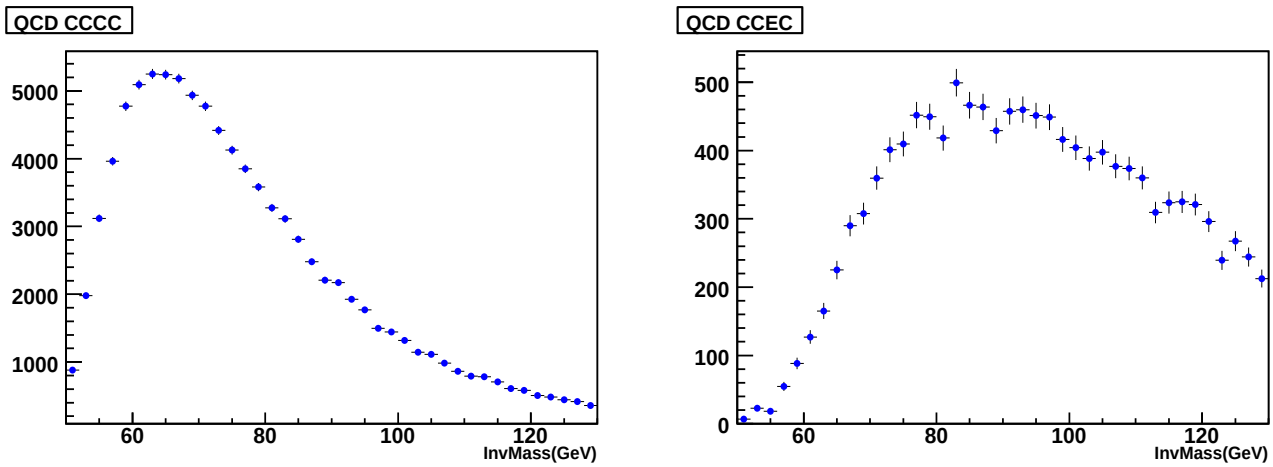

Figure 6.2: QCD background shapes for CCCC(Left) and CCEC(Right). There is no peak around Z peak region, which means we get a pure QCD sample, no contamination from $Z \rightarrow ee$.

Mass	$Z\tau\tau$		$W+X$	
	Forward	Backward	Forward	Backward
$50.0-60.0$	7.44± 0.71	5.13± 0.60	0.24± 0.17	0.53± 0.85
$60.0-70.0$	15.67± 1.20	15.16± 1.17	1.55± 0.88	0.30± 0.83
$70.0-75.0$	5.98± 0.64	5.14± 0.60	0.00± 0.00	0.80± 0.96
$75.0-81.0$	5.93± 0.64	2.25± 0.51	0.28± 0.31	0.14± 0.13
$81.0-86.5$	1.12± 0.49	0.17± 0.02	0.00± 0.00	0.05± 0.10
$86.5-89.5$	0.16± 0.02	0.38± 0.48	0.36± 0.61	0.00± 0.00
$89.5-92.0$	0.39± 0.48	0.05± 0.02	0.12± 0.10	0.00± 0.00
$92.0-97.0$	0.39± 0.03	0.10± 0.02	0.91± 1.25	0.00± 0.00
$97.0-105.0$	0.29± 0.03	0.14± 0.02	0.00± 0.00	0.26± 0.27
$105.0-115.0$	0.50± 0.04	0.15± 0.02	0.47± 0.33	0.26± 0.28
$115.0-130.0$	0.34± 0.03	0.11± 0.02	0.00± 0.00	0.12± 1.22
$130.0-180.0$	0.49± 0.04	0.32± 0.03	0.63± 0.69	0.66± 0.38
$180.0-250.0$	0.22± 0.02	0.09± 0.01	0.33± 0.29	0.10± 0.26
$250.0-500.0$	0.08± 0.01	0.03± 0.00	0.28± 0.36	0.00± 0.00
$500.0-1000.0$	0.00 ± 0.00	0.00 ± 0.00	0.00 ± 0.00	0.00 ± 0.00

Table 6.3: SM backgrounds $Z\tau\tau$ and $W+X$ forward and backward contibutions for the different mass bins of CC-CC events

The normalization is measured by fitting the data Z/γ^* invariant mass as a linear sum of signal, QCD and SM backgrounds in $[50, 130]$ GeV region. The QCD background is especially important for the high mass events which are off the Z resonance.

Mass	WW		WZ	
	Forward	Backward	Forward	Backward
50.0 – 60.0	0.83 ± 0.10	1.68 ± 0.17	0.08 ± 0.01	0.10 ± 0.01
60.0 – 70.0	2.17 ± 0.21	2.14 ± 0.21	0.10 ± 0.01	0.12 ± 0.01
70.0 – 75.0	0.92 ± 0.11	1.42 ± 0.15	0.08 ± 0.01	0.08 ± 0.01
75.0 – 81.0	0.69 ± 0.09	1.35 ± 0.14	0.15 ± 0.01	0.12 ± 0.01
81.0 – 86.5	0.79 ± 0.10	0.47 ± 0.08	0.36 ± 0.02	0.29 ± 0.02
86.5 – 89.5	0.70 ± 0.10	0.51 ± 0.08	0.75 ± 0.05	0.71 ± 0.04
89.5 – 92.0	0.28 ± 0.08	0.74 ± 0.10	1.41 ± 0.09	1.19 ± 0.07
92.0 – 97.0	0.57 ± 0.09	0.70 ± 0.10	1.63 ± 0.10	1.45 ± 0.09
97.0 – 105.0	0.93 ± 0.11	1.91 ± 0.19	0.28 ± 0.02	0.25 ± 0.02
105.0 – 115.0	1.21 ± 0.13	1.45 ± 0.15	0.08 ± 0.01	0.10 ± 0.01
115.0 – 130.0	1.38 ± 0.14	1.19 ± 0.13	0.08 ± 0.00	0.07 ± 0.00
130.0 – 180.0	2.39 ± 0.23	2.04 ± 0.20	0.10 ± 0.01	0.09 ± 0.01
180.0 – 250.0	1.27 ± 0.13	0.93 ± 0.11	0.05 ± 0.00	0.03 ± 0.00
250.0 – 500.0	0.85 ± 0.10	0.27 ± 0.08	0.02 ± 0.00	0.01 ± 0.00
500.0 – 1000.0	0.07 ± 0.07	0.00 ± 0.00	0.00 ± 0.00	0.00 ± 0.00

Table 6.4: SM backgrounds WW and WZ forward and backward contibutions for the different mass bins of CC-CC events

QCD background contributions are shown in Table 6.9 for CC-CC and Table 6.10 for CCEC events.

Mass	$\gamma\gamma$		$t\bar{t}$	
	Forward	Backward	Forward	Backward
$50.0 - 60.0$	0.22 ± 0.24	0.00 ± 0.00	0.59 ± 0.10	0.92 ± 0.15
$60.0 - 70.0$	0.07 ± 0.24	0.00 ± 0.00	1.20 ± 0.19	1.40 ± 0.22
$70.0 - 75.0$	0.00 ± 0.00	0.00 ± 0.00	0.77 ± 0.13	0.65 ± 0.11
$75.0 - 81.0$	0.00 ± 0.00	0.00 ± 0.00	0.86 ± 0.14	0.75 ± 0.12
$81.0 - 86.5$	0.00 ± 0.00	0.00 ± 0.00	0.76 ± 0.12	0.77 ± 0.12
$86.5 - 89.5$	0.00 ± 0.00	0.00 ± 0.00	0.29 ± 0.05	0.34 ± 0.06
$89.5 - 92.0$	0.00 ± 0.00	0.00 ± 0.00	0.44 ± 0.07	0.29 ± 0.05
$92.0 - 97.0$	0.00 ± 0.00	0.00 ± 0.00	0.64 ± 0.11	0.68 ± 0.11
$97.0 - 105.0$	0.00 ± 0.00	0.00 ± 0.00	0.83 ± 0.13	1.16 ± 0.19
$105.0 - 115.0$	0.00 ± 0.00	0.00 ± 0.00	0.60 ± 0.10	0.81 ± 0.13
$115.0 - 130.0$	0.00 ± 0.00	0.00 ± 0.00	0.81 ± 0.13	1.34 ± 0.22
$130.0 - 180.0$	0.01 ± 0.02	0.02 ± 0.02	2.19 ± 0.35	2.14 ± 0.34
$180.0 - 250.0$	0.03 ± 0.02	0.02 ± 0.02	0.86 ± 0.14	0.79 ± 0.13
$250.0 - 500.0$	0.01 ± 0.00	0.03 ± 0.00	0.28 ± 0.05	0.28 ± 0.05
$500.0 - 1000.0$	0.00 ± 0.00	0.00 ± 0.00	0.00 ± 0.00	0.00 ± 0.00

Table 6.5: SM backgrounds $\gamma\gamma$ and $t\bar{t}$ forward and backward contibutions for the different mass bins of CC-CC events

Mass	$Z\tau\tau$		$W + X$	
	Forward	Backward	Forward	Backward
$50.0 - 60.0$	1.48± 0.49	0.22± 0.48	10.69± 4.38	2.96± 1.56
$60.0 - 70.0$	6.36± 0.66	4.41± 0.57	13.58± 7.09	3.90± 2.24
$70.0 - 75.0$	7.17± 0.70	4.16± 0.56	13.60± 4.35	2.12± 0.90
$75.0 - 81.0$	5.54± 0.62	1.30± 0.49	14.43± 4.84	2.08± 1.21
$81.0 - 86.5$	2.30± 0.51	0.55± 0.48	17.86± 8.32	4.82± 2.46
$86.5 - 89.5$	0.51± 0.48	0.01± 0.02	6.20± 2.55	3.65± 1.49
$89.5 - 92.0$	1.14± 0.49	0.00± 0.00	7.74± 3.03	3.62± 1.61
$92.0 - 97.0$	0.42± 0.48	0.04± 0.02	16.31± 5.19	1.56± 0.82
$97.0 - 105.0$	0.34± 0.03	0.09± 0.02	19.93± 10.8	4.38± 2.58
$105.0 - 115.0$	0.40± 0.03	0.07± 0.02	17.00± 11.3	3.79± 2.57
$115.0 - 130.0$	0.48± 0.04	0.10± 0.02	24.16± 15.5	5.50± 3.67
$130.0 - 180.0$	1.44± 0.49	0.22± 0.48	31.31± 17.6	11.49± 10.1
$180.0 - 250.0$	0.23± 0.02	0.18± 0.48	13.96± 14.4	2.68± 2.87
$250.0 - 500.0$	0.08± 0.02	0.01± 0.00	3.63± 3.37	0.50± 0.74
$500.0 - 1000.0$	0.00 ± 0.00	0.00 ± 0.00	0.00 ± 0.00	0.00 ± 0.00

Table 6.6: SM backgrounds $Z\tau\tau$ and $W + X$ forward and backward contibutions for the different mass bins of CC-EC events

Mass	WW		WZ	
	Forward	Backward	Forward	Backward
$50.0 - 60.0$	0.30 ± 0.08	0.53 ± 0.09	0.03 ± 0.00	0.05 ± 0.00
$60.0 - 70.0$	0.33 ± 0.08	0.64 ± 0.09	0.06 ± 0.00	0.08 ± 0.00
$70.0 - 75.0$	0.19 ± 0.07	0.60 ± 0.09	0.06 ± 0.00	0.06 ± 0.00
$75.0 - 81.0$	0.42 ± 0.08	0.60 ± 0.09	0.09 ± 0.01	0.12 ± 0.01
$81.0 - 86.5$	0.39 ± 0.08	0.71 ± 0.10	0.21 ± 0.01	0.24 ± 0.01
$86.5 - 89.5$	0.21 ± 0.07	0.89 ± 0.11	0.54 ± 0.03	0.51 ± 0.03
$89.5 - 92.0$	0.36 ± 0.08	0.41 ± 0.08	0.87 ± 0.05	0.72 ± 0.04
$92.0 - 97.0$	0.74 ± 0.10	0.71 ± 0.10	1.18 ± 0.07	0.96 ± 0.06
$97.0 - 105.0$	0.84 ± 0.10	1.29 ± 0.14	0.27 ± 0.02	0.26 ± 0.02
$105.0 - 115.0$	1.13 ± 0.12	0.91 ± 0.11	0.17 ± 0.01	0.17 ± 0.01
$115.0 - 130.0$	1.91 ± 0.19	1.42 ± 0.15	0.21 ± 0.01	0.20 ± 0.01
$130.0 - 180.0$	5.27 ± 0.48	1.83 ± 0.18	0.49 ± 0.03	0.38 ± 0.02
$180.0 - 250.0$	2.05 ± 0.20	0.95 ± 0.11	0.32 ± 0.02	0.16 ± 0.01
$250.0 - 500.0$	0.65 ± 0.09	0.10 ± 0.07	0.19 ± 0.01	0.05 ± 0.00
$500.0 - 1000.0$	0.00 ± 0.00	0.00 ± 0.00	0.00 ± 0.00	0.00 ± 0.00

Table 6.7: SM backgrounds WW and WZ forward and backward contibutions for the different mass bins of CC-EC events

Mass	$\gamma\gamma$		$t\bar{t}$	
	Forward	Backward	Forward	Backward
50.0 – 60.0	0.80 ± 0.25	0.54 ± 0.25	0.09 ± 0.03	0.16 ± 0.03
60.0 – 70.0	3.02 ± 0.36	2.85 ± 0.35	0.20 ± 0.04	0.18 ± 0.04
70.0 – 75.0	1.08 ± 0.26	2.32 ± 0.32	0.10 ± 0.03	0.24 ± 0.04
75.0 – 81.0	1.59 ± 0.28	1.66 ± 0.28	0.13 ± 0.03	0.19 ± 0.04
81.0 – 86.5	2.26 ± 0.32	2.33 ± 0.32	0.08 ± 0.03	0.10 ± 0.03
86.5 – 89.5	1.16 ± 0.26	1.44 ± 0.27	0.08 ± 0.03	0.04 ± 0.02
89.5 – 92.0	0.29 ± 0.24	1.09 ± 0.26	0.14 ± 0.03	0.12 ± 0.03
92.0 – 97.0	2.00 ± 0.30	2.68 ± 0.34	0.10 ± 0.03	0.12 ± 0.03
97.0 – 105.0	2.00 ± 0.30	2.20 ± 0.31	0.28 ± 0.05	0.25 ± 0.05
105.0 – 115.0	1.91 ± 0.30	2.72 ± 0.34	0.22 ± 0.04	0.29 ± 0.05
115.0 – 130.0	2.00 ± 0.30	2.60 ± 0.33	0.71 ± 0.12	0.39 ± 0.07
130.0 – 180.0	4.50 ± 0.28	4.95 ± 0.39	0.86 ± 0.14	0.98 ± 0.16
180.0 – 250.0	2.81 ± 0.17	2.99 ± 0.18	0.47 ± 0.08	0.54 ± 0.09
250.0 – 500.0	1.23 ± 0.20	1.25 ± 0.20	0.09 ± 0.03	0.06 ± 0.02
500.0 – 1000.0	0.04 ± 0.01	0.03 ± 0.00	0.00 ± 0.00	0.00 ± 0.00

Table 6.8: SM backgrounds $\gamma\gamma$ and $t\bar{t}$ forward and backward contibutions for the different mass bins of CC-EC events

Mass	QCD	
	Forward	Backward
$50.0 - 60.0$	25.70 ± 0.00	25.62 ± 0.00
$60.0 - 70.0$	44.91 ± 0.00	44.70 ± 0.00
$70.0 - 75.0$	19.56 ± 0.00	19.80 ± 0.00
$75.0 - 81.0$	19.56 ± 0.00	19.14 ± 0.00
$81.0 - 86.5$	14.28 ± 0.00	14.43 ± 0.00
$86.5 - 89.5$	6.12 ± 0.00	6.11 ± 0.00
$89.5 - 92.0$	4.58 ± 0.00	4.77 ± 0.00
$92.0 - 97.0$	7.63 ± 0.00	7.85 ± 0.00
$97.0 - 105.0$	9.36 ± 0.00	8.93 ± 0.00
$105.0 - 115.0$	7.51 ± 0.00	7.49 ± 0.00
$115.0 - 130.0$	6.53 ± 0.00	6.50 ± 0.00
$130.0 - 180.0$	7.61 ± 0.00	7.40 ± 0.00
$180.0 - 250.0$	1.58 ± 0.00	1.77 ± 0.00
$250.0 - 500.0$	0.38 ± 0.00	0.43 ± 0.00
$500.0 - 1000.0$	0.01 ± 0.00	0.00 ± 0.00

Table 6.9: QCD backgrounds forward and backward contibutions for the different mass bins of CC-CC events

Mass	QCD	
	Forward	Backward
$50.0 - 60.0$	6.35 ± 0.04	6.39 ± 0.04
$60.0 - 70.0$	36.31 ± 0.09	38.45 ± 0.10
$70.0 - 75.0$	31.86 ± 0.09	32.08 ± 0.09
$75.0 - 81.0$	43.75 ± 0.10	44.54 ± 0.10
$81.0 - 86.5$	44.85 ± 0.10	42.56 ± 0.10
$86.5 - 89.5$	23.37 ± 0.08	22.27 ± 0.07
$89.5 - 92.0$	19.40 ± 0.07	17.59 ± 0.07
$92.0 - 97.0$	37.56 ± 0.10	38.47 ± 0.10
$97.0 - 105.0$	52.75 ± 0.11	56.26 ± 0.12
$105.0 - 115.0$	58.45 ± 0.12	61.46 ± 0.12
$115.0 - 130.0$	68.41 ± 0.13	70.15 ± 0.13
$130.0 - 180.0$	114.11 ± 0.17	110.49 ± 0.16
$180.0 - 250.0$	27.42 ± 0.08	30.57 ± 0.09
$250.0 - 500.0$	5.54 ± 0.04	5.99 ± 0.04
$500.0 - 1000.0$	0.00 ± 0.00	0.00 ± 0.00

Table 6.10: QCD backgrounds forward and backward contibutions for the different mass bins of CC-EC events

6.4 Comparison between Data and Signal+QCD+SM backgrounds:

Using the event selection cuts described before, we compare the invariant mass, $\cos\theta^*$, electron/positron p_T, detector η, detector ϕ and Vtx-Z of selected data and signal+QCD+SM events. The CC-CC and CC-EC comparisons are shown from Fig. 6.3 to Fig. 6.10. Good agreement between real data and MC signal + SM and QCD backgrounds are observed for all distributions. We also give the KS probability between the two histograms.

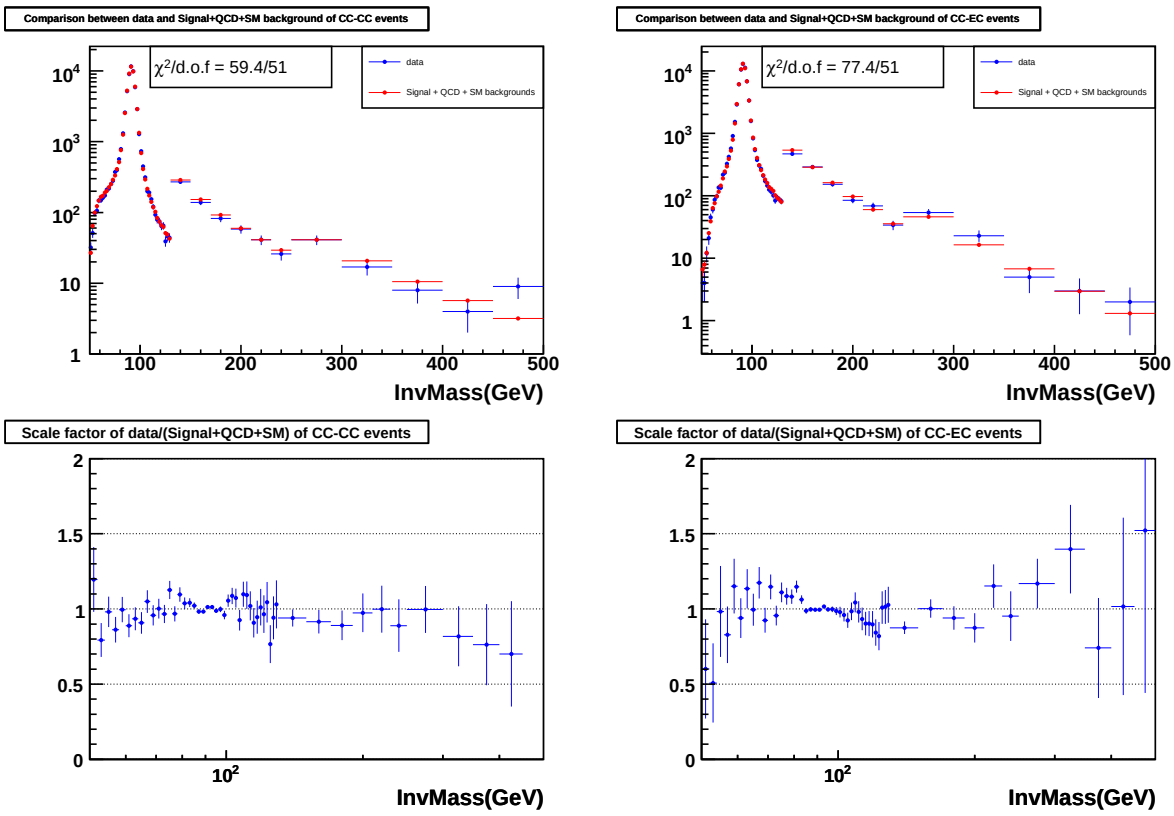

Figure 6.3: Invariant mass comparison for CC-CC and CC-EC events and also the ratio between data and signal + backgrounds. The discontinuity in the mass distribution is due to different bin size. The KS probabilities are 0.9996 and 0.4860 for CC-CC and CC-EC.

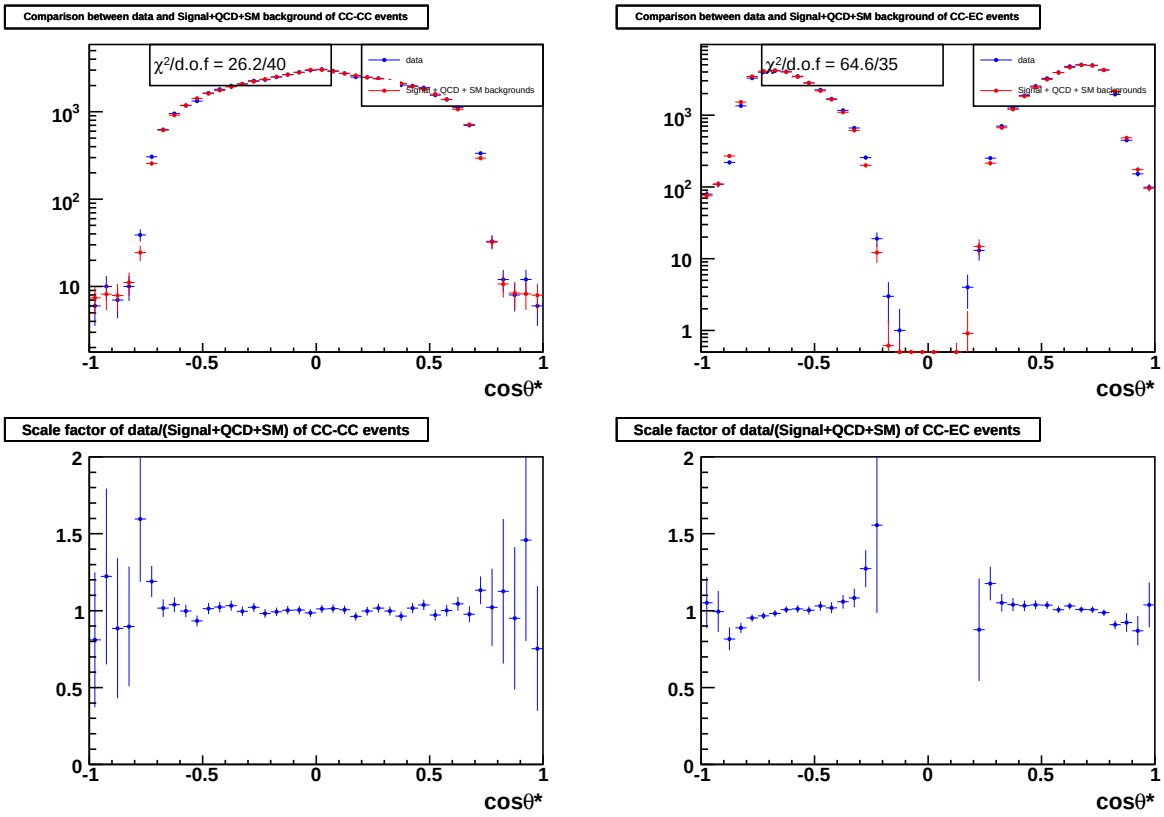

Figure 6.4: $\cos\theta^*$ distribution for CC-CC and CC-EC events and also the ratio between data and signal + backgrounds. The KS probabilities are 0.995 and 0.026 for CC-CC and CC-EC.

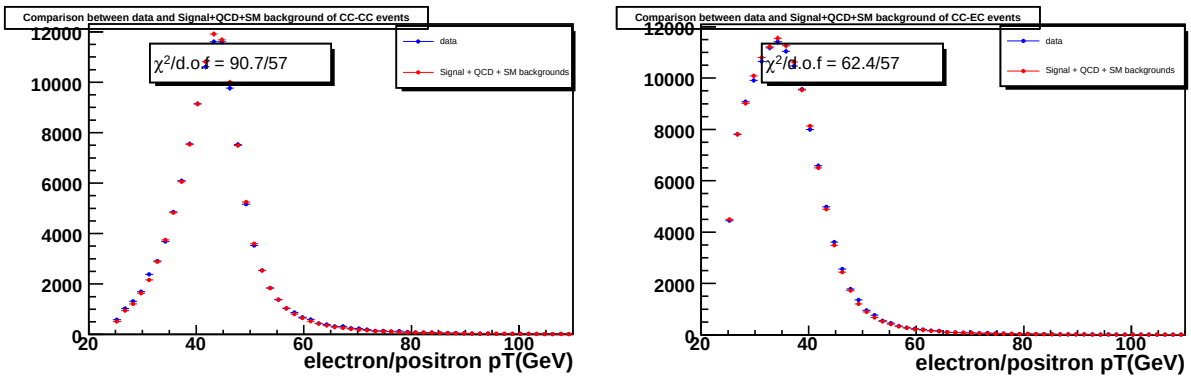

Figure 6.5: Electron/positron p_T comparison for CC-CC and CC-EC events. The KS probabilities are 0.153 and 0.115 for CC-CC and CC-EC.

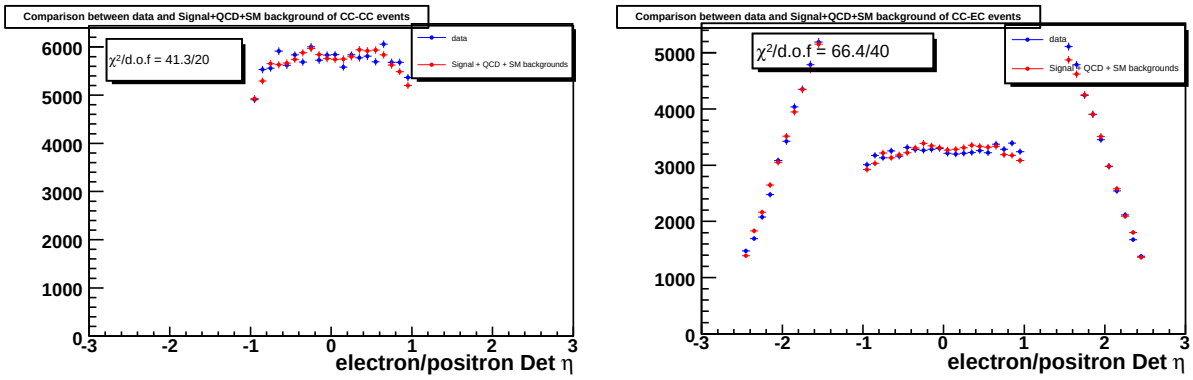

Figure 6.6: Electron/positron detector η comparison for CC-CC and CC-EC events. The KS probabilities are 0.213 and 0.136 for CC-CC and CC-EC.

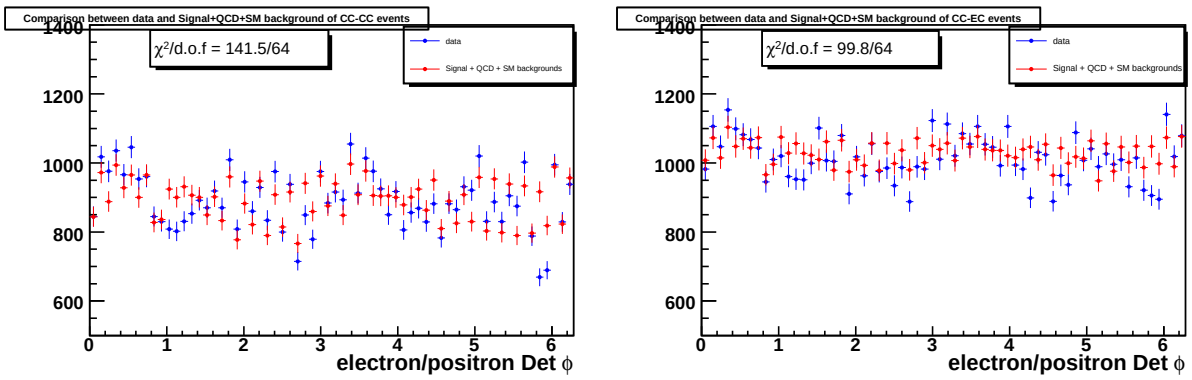

Figure 6.7: Electron/positron detector ϕ comparison for CC-CC and CC-EC events. The KS probabilities are 0.334 and 0.493 for CC-CC and CC-EC.

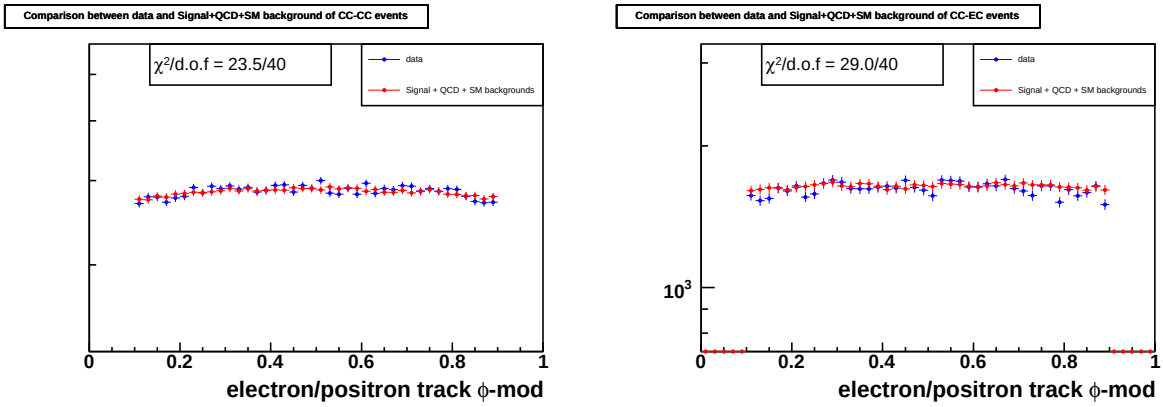

Figure 6.8: CC (no EC electrons included) Electron/positron track PhiMod comparison for CC-CC and CC-EC events. The KS probabilities are 0.981 and 0.314. Since we only cut on the track PhiMod for electrons in CC, we do not care about PhiMod distribution in EC.

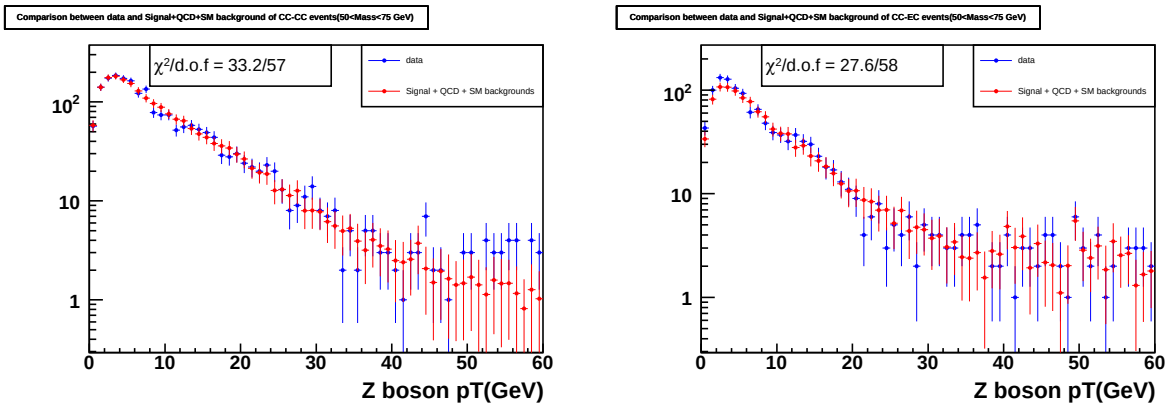

Figure 6.9: Z boson p_T comparison for CC-CC and CC-EC events at low mass region(50-75 GeV).

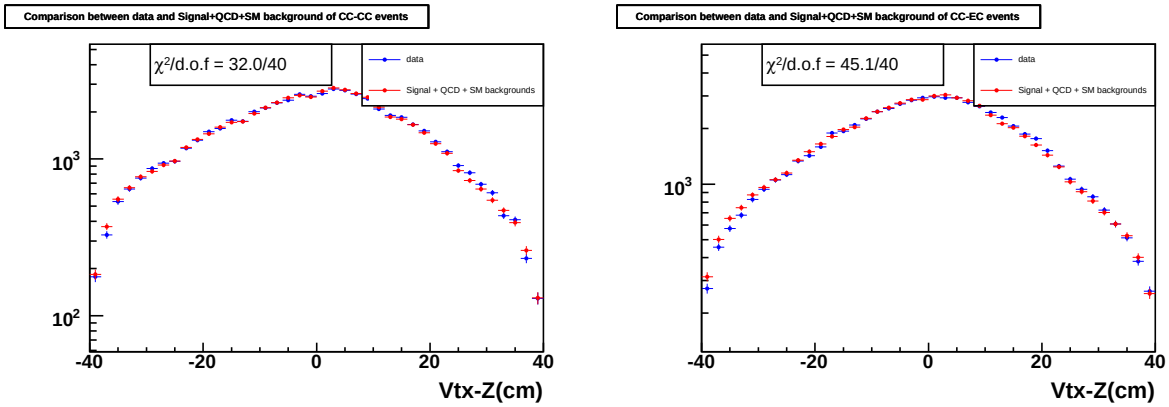

Figure 6.10: Vtx-Z comparison for CC-CC and CC-EC events. The KS function probabilities are 0.479 and 0.069 for CC-CC and CC-EC.

We also compared $\cos\theta^*$ distribution in three different mass regions where the A_{FB} is at extreme: $60 < M < 75$ GeV (most negative), $75 < M < 105$ GeV (close to 0) and $105 < M < 500$ GeV (most positive). The comparison plots can be found from Fig. 6.11 to Fig. 6.13. The $\cos\theta^*$ comparison plots for all 14 mass bins are included in the Appendix B and all $\chi^2/d.o.f$ are reasonable. Fig. 6.14 shows M_{ee} and $\cos\theta*$ distributions between data and signal+backgrounds.

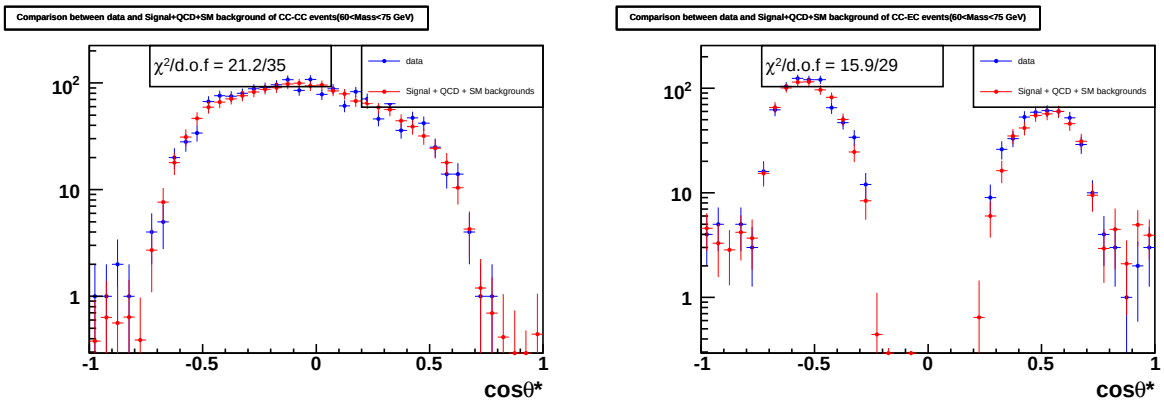

Figure 6.11: $\cos\theta^*$ comparison for CC-CC and CC-EC events in the low mass region ($60 < M < 75$ GeV). In this mass region, A_{FB} is negative, and we observe more backward events ($\cos\theta^* < 0$) than forward events ($\cos\theta^* > 0$). The worse overall χ^2 for CC-EC events mainly comes from the seventh and eighth bins and also the seventh bin from the last. The KS probabilities are 1. and 0.857 for CC-CC and CC-EC.

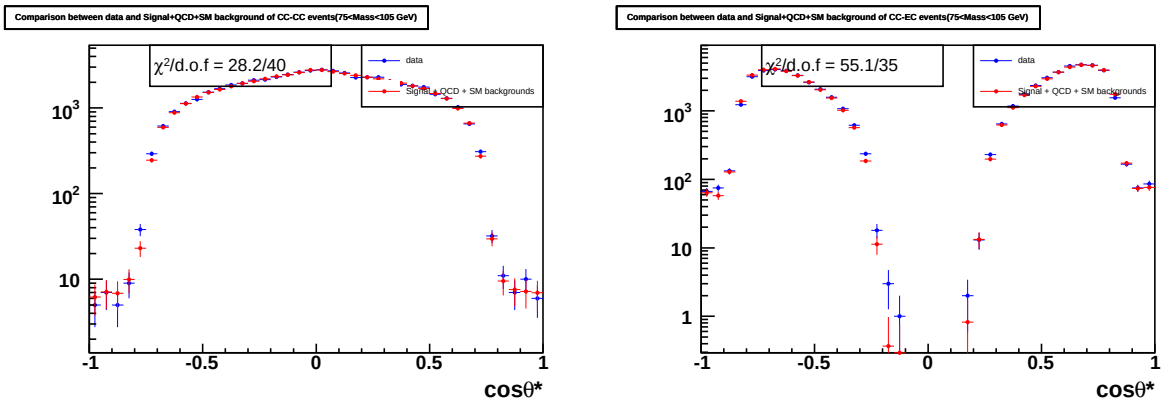

Figure 6.12: $\cos\theta^*$ comparison for CC-CC and CC-EC events in the middle mass region ($75 < M < 105$ GeV). In this mass region, A_{FB} is close to 0, and we observe similar number of backward events ($\cos\theta^* < 0$) and forward events ($\cos\theta^* > 0$). The KS probabilities are 0.959 and 0.046 for CC-CC and CC-EC.

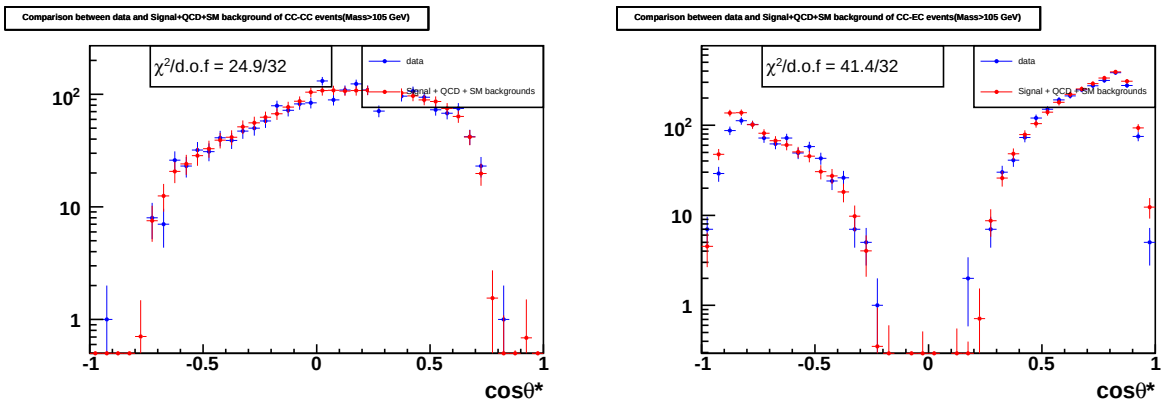

Figure 6.13: $\cos\theta^*$ comparison for CC-CC and CC-EC events in high mass region ($105 < M < 500$ GeV). In this mass region, A_{FB} is positive, and we observe more forward events ($\cos\theta^* > 0$) than backward events ($\cos\theta^* < 0$). The worse overall χ^2 for CC-EC events mainly comes from the second, third and the last bins. The KS probabilities are 0.931 and 0.474 for CC-CC and CC-EC.

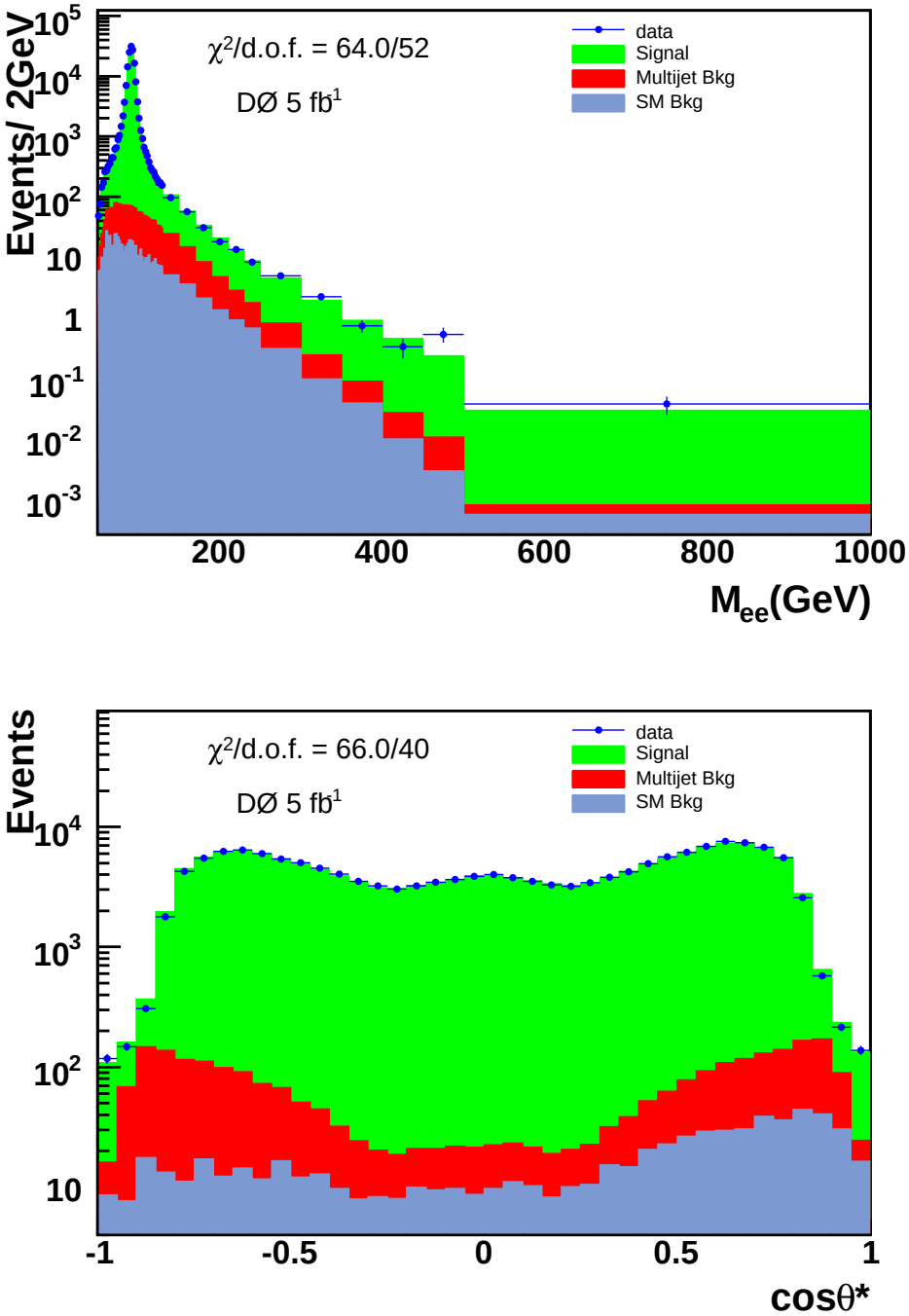

Figure 6.14: M_{ee} and $\cos\theta^*$ distributions between data and Signal+backgrounds.

Chapter 7

Unfolding and Closure test

In order to correct the raw forward-backward asymmetry and obtain the generator-level A_{FB}, this measurement must account for any acceptances and detector effects that can change the number of forward and backward events found in each M_{ee} bin. The dominant contributions to the detector acceptance are kinematic acceptance, geometric acceptance, and electron selection efficiencies. The major effect that contributes to event migration between M_{ee} bins is the energy resolution of the detector. The PYTHIA GEANT MC simulation is used to determine the corresponding corrections.

7.1 Detector resolution unfolding

We measure A_{FB} as a function of the dielectron invariant mass (M_{ee}) in twelve bins. The measurement is complicated by detector energy resolution and QED radiation which cause the true and measured M_{ee} and $\cos\theta^*$ diff. Events in one invariant-mass bin may migrate to another invariant-mass bin. A correction needs to be made in order to unfold the detector effect. We used the matrix method introduced by CDF Run II

[27]. The method is as follows:

We compute the response matrix R_{ij}^{FF} for an event that is measured as forward in bin i to be found as forward and in M_{ee} bin j at the generator level. Likewise, we also calculate the response matrices for backward events being found as backward (R_{ij}^{BB}), forward as backward (R_{ij}^{FB}), and backward as forward (R_{ij}^{BF}). R^{FB} and R^{BF} approximately represent the event bin migration, and these off-diagonal elements are much smaller than the diagonal elements due to the bin width we chose. These four matrices are:

$$R_{ij}^{FF} = \frac{N_j^F(\text{generator})}{N_i^F(\text{measured})}; \qquad R_{ij}^{FB} = \frac{N_j^F(\text{generator})}{N_i^B(\text{measured})} \tag{7.1}$$

$$R_{ij}^{BF} = \frac{N_j^B(\text{generator})}{N_i^F(\text{measured})}; \qquad R_{ij}^{BB} = \frac{N_j^B(\text{generator})}{N_i^B(\text{measured})} \tag{7.2}$$

where $N_i^F(\text{generator})[N_i^B(\text{generator})]$ is the number of forward [backward] events generated in the i-th M_{ee} bin, an $N_j^F(\text{measured})[N_j^B(\text{measured})]$ is the number of forward [backward] events measured in the j-th M_{ee} bin.

As a result, the number of generator level events in each mass bin can be calculated using the number of measured events in each mass bin and the response matrix:

$$N_i^F(\text{generator}) = \sum \left[R_{ij}^{FF} \cdot N_j^F(\text{measured}) + R_{ij}^{FB} \cdot N_j^B(\text{measured})\right] \tag{7.3}$$

$$N_i^B(\text{generator}) = \sum \left[R_{ij}^{BB} \cdot N_j^B(\text{measured}) + R_{ij}^{BF} \cdot N_j^F(\text{measured})\right] \tag{7.4}$$

We first tune GEANT MC so that the detector resolution in MC agrees with what we measured from the real data, then the response matrix is derived from the tuned

GEANT MC and used to get number of expected events in each mass bin with kinematic and geometric acceptance applied. The response matrix is shown in Fig. 7.1 for CC-CC events and Fig. 7.2 for CC-EC events. As expected, R_{ij}^{FF} and R_{ij}^{BB} are mostly diagonalized.

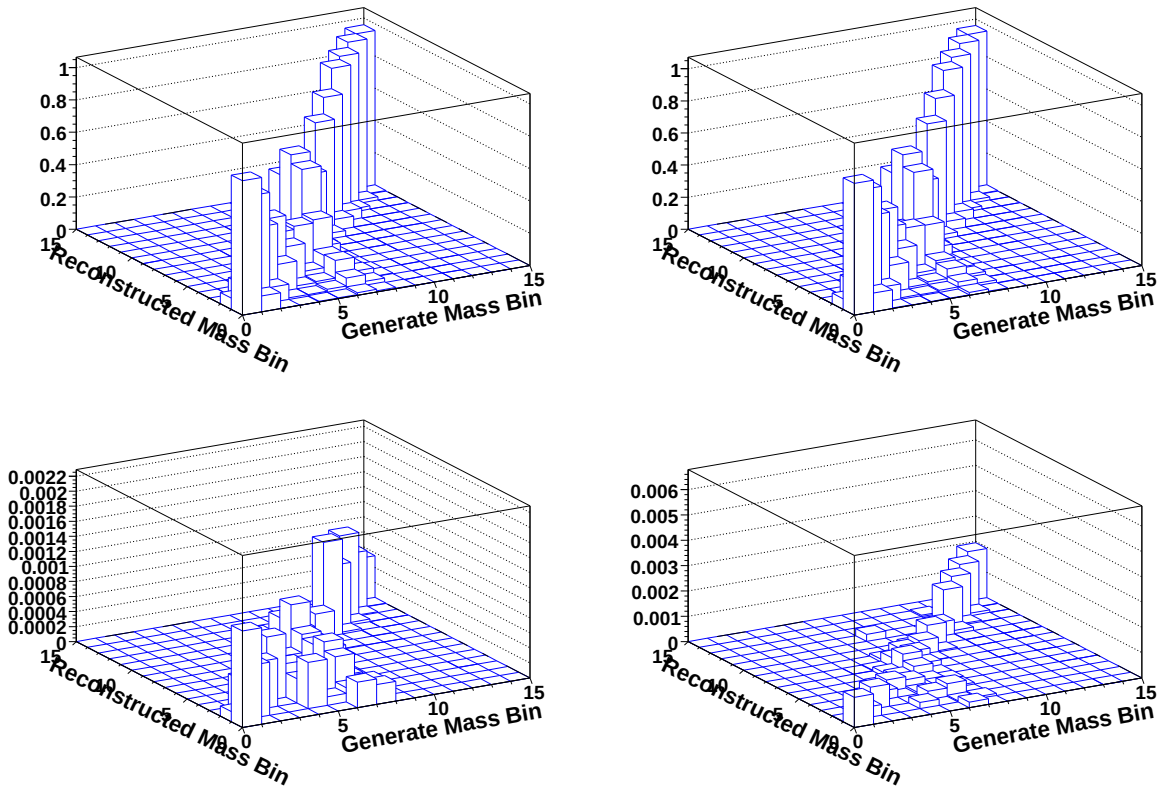

Figure 7.1: Response matrix for CC-CC events. The axes are labeled by the M_{ee} bin number where bin 1 is the lowest mass bin and bin 12 is the highest mass bin. The four plots are for R_{ij}^{FF}, R_{ij}^{BB}, R_{ij}^{BF} and R_{ij}^{FB} respectively. The definition of each response matrix element can be found in the text.

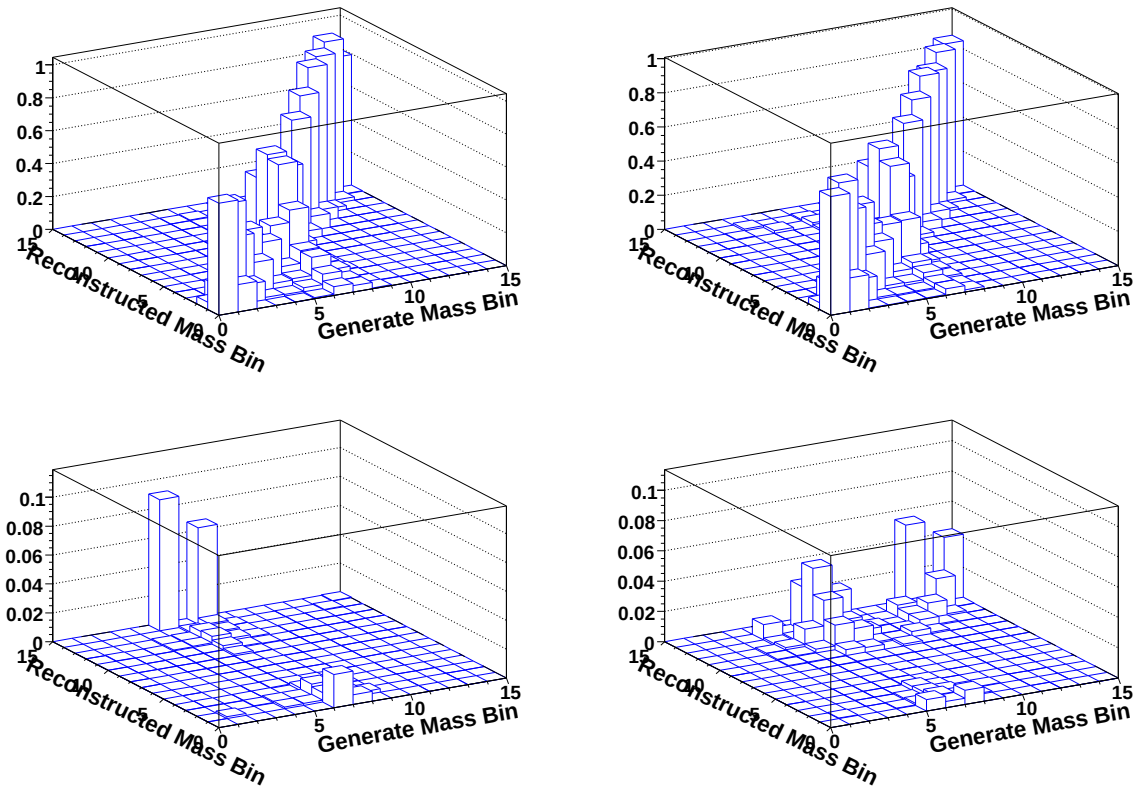

Figure 7.2: Response matrix for CC-EC events. The axes are labeled by the M_{ee} bin number where bin 1 is the lowest mass bin and bin 12 is the highest mass bin. The four plots are for R_{ij}^{FF}, R_{ij}^{BB}, R_{ij}^{BF} and R_{ij}^{FB} respectively. The definition of each response matrix element can be found in the text.

7.2 Acceptance and efficiencies corrections

Since we applied many electron criteria to select Z/γ^* candidates, these selection criteria can change the number of forward and backward events found in each M_{ee} bin. Although there is very little in the detector and analysis that treats forward and backward events differently, the angular distribution of the events and photon radiation can change event acceptances and the reconstructed invariant mass so that net differences arise for forward and backward events. As described in Sect.5.2 and Sect.6.4, the PYTHIA GEANT MC are tuned to agree with data, scale factors for different efficiencies are applied in GEANT MC, and also the prediction of the peak and width of Z candidates agrees with real data measurement. We can use PYTHIA GEANT MC to derive acceptance corrections. The dominant contributions to the detector acceptances are kinematic acceptance, geometric acceptance and electron identification efficiency. The following sections use PYTHIA generator level events to understand the the various effects on the final A_{FB} measurement.

7.2.1 Kinematic and geometric effects

Fig. 7.3 shows the effect of kinematic and geometric cuts on $\cos\theta^*$ distributions based on PYTHIA generator-level information.

More useful information can be found in Fig. 7.4 and Fig. 7.5, where we compare theA_{FB} distributions with different cuts applied at the generator level. The kinematic and geometric cuts are not very sensitive to the A_{FB} distribution around Z peak region.

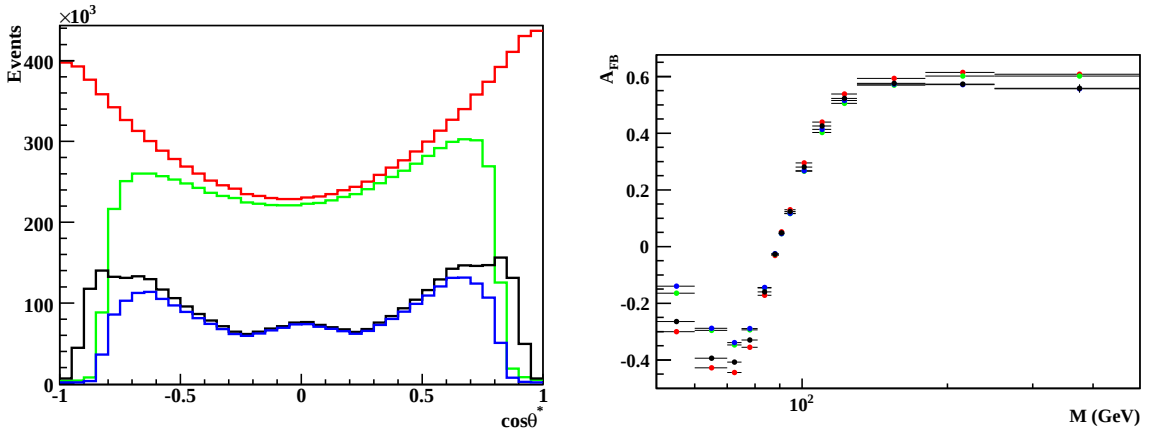

Figure 7.3: Effects of kinematic and geometric cuts on $\cos\theta^*$ (Left) and A_{FB} (Right) distributions using PYTHIA generator-level information ($50 < M < 500$ GeV). The red curve is without any cuts, the green curve is with $p_T > 25$ GeV requirement on both electron and positron, the black curve is with physics η requirements ($|\eta| < 1$ (PhiMod cut also applied) or $1.5 < |\eta| < 2.5$, no EC-EC events) on both electron and positron, and the blue curve is with both p_T and acceptance cuts applied.

The kinematic cut ($p_T > 25$ GeV), is relatively insensitive to A_{FB} in the high-mass region and pretty sensitive in the low-mass region. For the geometric cut, it is sensitive to A_{FB} in both the high- and low-mass regions.

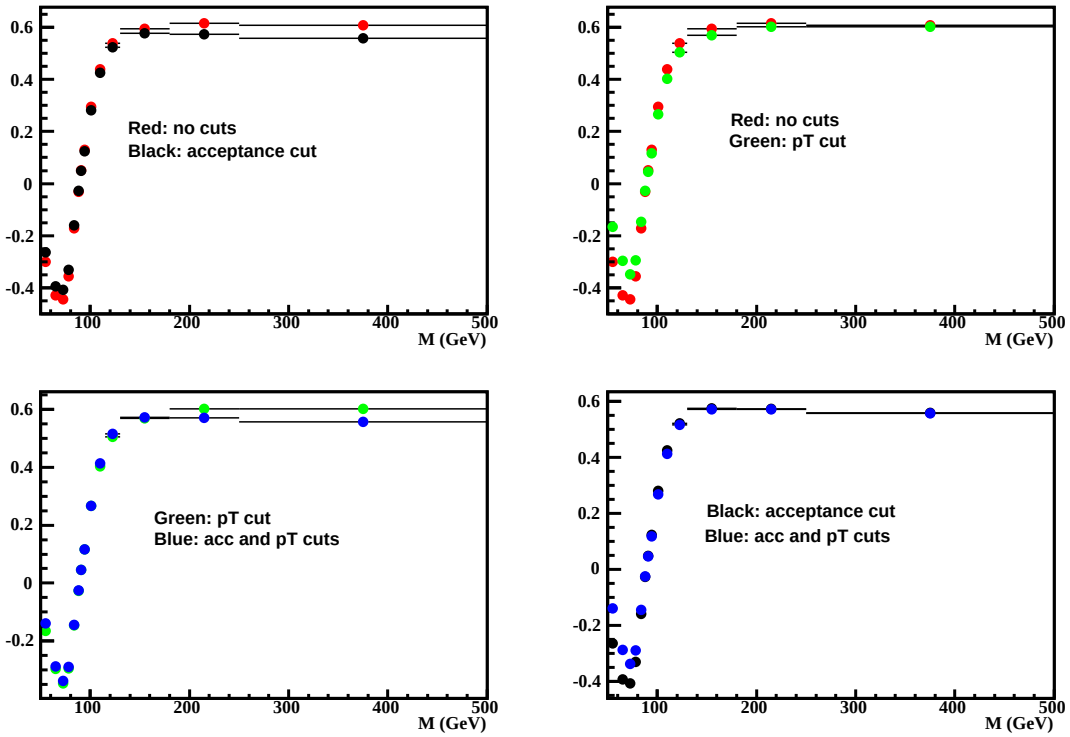

Figure 7.4: Effects of kinematic and geometric cuts on and A_{FB} distribution using PYTHIA generator-level information. The red curve is without any cuts, the green curve is with $p_T > 25$ GeV requirement on both electron and positron, the black curve is with physics η requirements ($|\eta| < 1$ (PhiMod cut also applied) or $1.5 < |\eta| < 2.5$, no EC-EC events) on both electron and positron, and the blue curve is with both p_T and acceptance cuts applied.

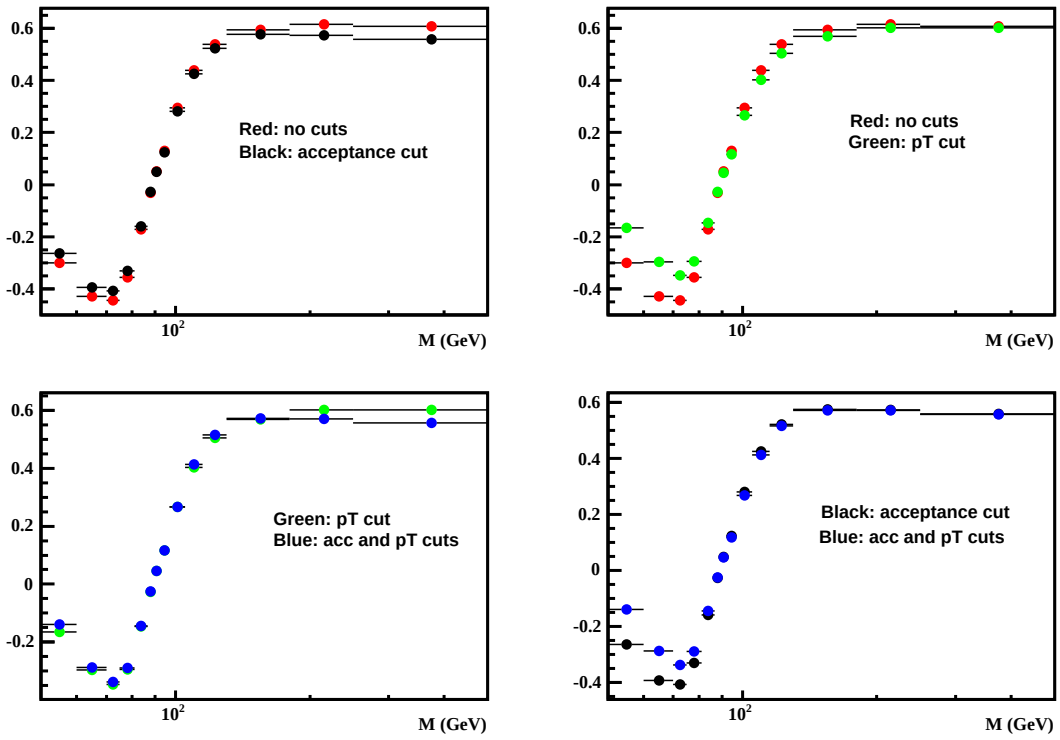

Figure 7.5: Effects of kinematic and geometric cuts on and A_{FB} distribution using PYTHIA generator-level information. Same information as Fig. 7.4 except the x-axis is plotted at log scale.

7.2.2 QED final state radiation effects

The invariant mass of the dielectron pair can be mis-measured due to final state QED radiation or external bremsstrahlung. If we ignore the radiated photon, the effect is significant for the mass region below Z peak, as shown on the left plot of Fig. 7.6 where we plot A_{FB} vs invariant mass for PYTHIA events without and with electron-photon merging. Fortunately, most of these photons are emitted co-linearly with the electron and are reconstructed as one single EM object by the DØ detector, which makes the measured A_{FB} less sensitive to the FSR effect. The right plot of Fig. 7.6 shows A_{FB} distributions with electron-photon merging cone size $R = 0.2$ and $R = 0.3$. Since the A_{FB} is measured as a function of the propagator Z/γ^* mass, the effect is expected to be very small.

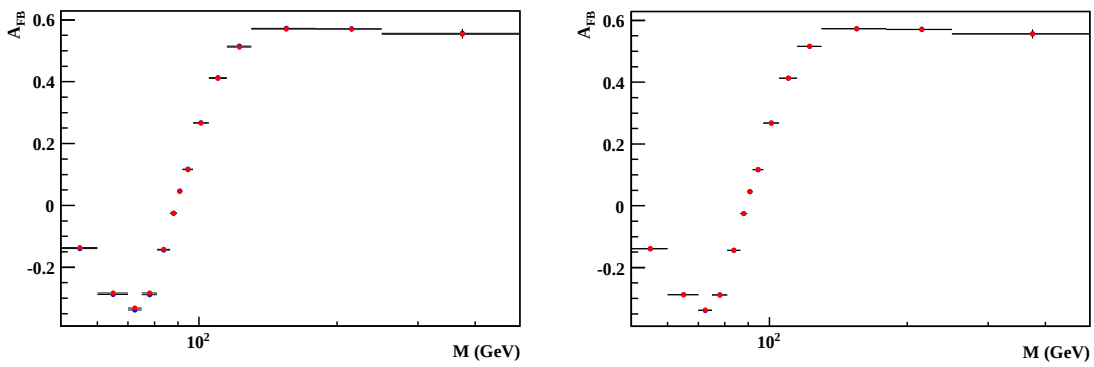

Figure 7.6: Effects of electron-photon merging cone size on A_{FB} using PYTHIA generator-level information. The kinematic and geometric cuts described before already applied for all histograms. For the left plot, we compare the A_{FB} with electron-photon merging cone size $R = 0.3$ (Blue curve) and without electron-photon merging (Red curve). For the right plot, we compare the A_{FB} with electron-photon merging cone size $R = 0.3$ (Blue curve) and with electron-photon merging cone size $R = 0.2$ (Red curve).

7.2.3 Final acceptance × efficiencies

The final acceptance × efficiencies for CC-CC and CC-EC are measured by applying the same selection cuts on GEANT MC events, Fig. 7.7 shows the acceptance × efficiencies for forward and backward events as a function of the generator-level Z/γ^* mass. The numbers for all mass bins are shown in Table. 7.1 for CC-CC and CC-EC events separately. Table. 7.2 lists the overall acceptance × efficiencies for both CC-CC and CC-EC events.

Since all selection efficiency are all close to 1, the overall acceptance × efficiencies is mainly caused by the kinematic and geometric acceptance. At high mass, Z boson tends to be produced with small rapidity, and thus the overall acceptance increases for CC-CC events and decreases for CC-EC events.

7.3 Charge mis-identification

7.3.1 Effect of charge mis-identification

Charge measurement is important for this analysis since we rely on the track charge to determine electron and positron, and then use their four vectors to calculate $\cos\theta^*$ to determine forward or backward event.

Assuming the charge mis-identification rate is f_Q; for CC-CC event, we require the two EM clusters must have opposite charge, and thus have very low probability

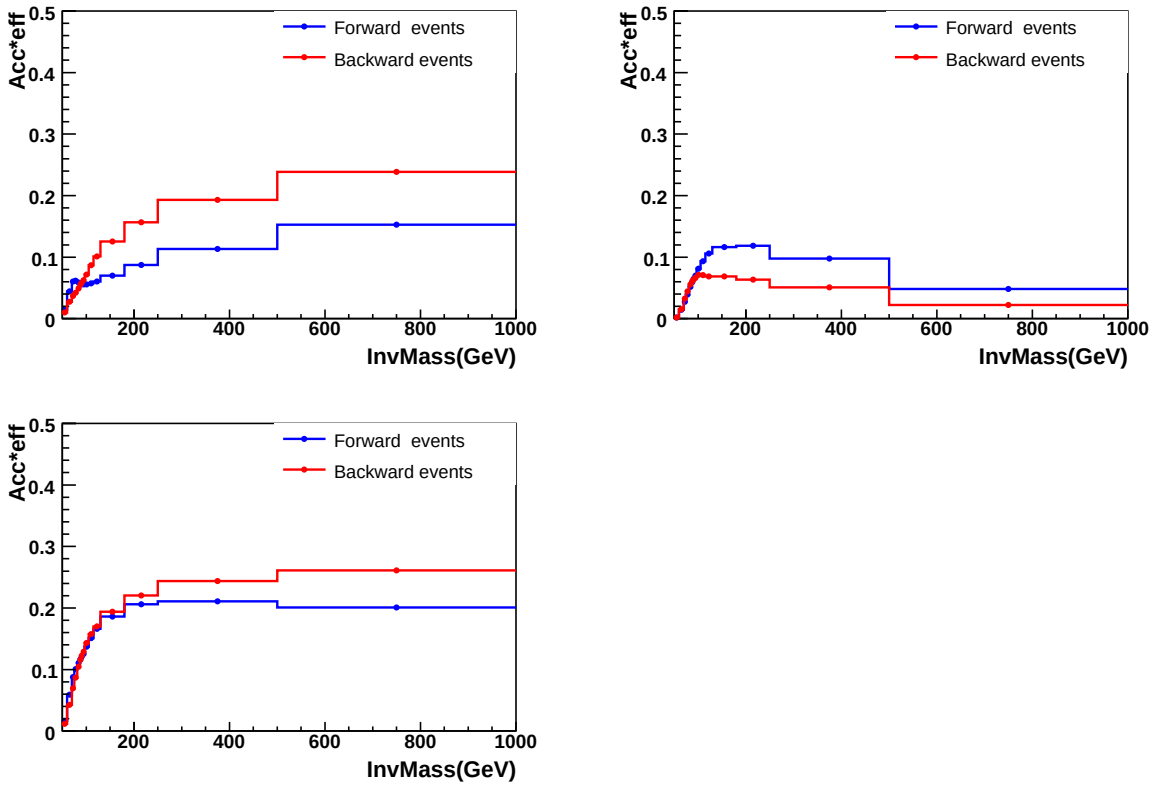

Figure 7.7: Acceptances×efficiencies for CC-CC (top left) and CC-EC (top right) and both (bottom left) events. For acceptances×efficiencies calculation, the denominator is the total number of generated $Z/\gamma* \rightarrow ee$ events and the numerator is the number of events passed the offline selections.

Mass Range (GeV)	CC-CC		CC-EC	
	Forward	Backward	Forward	Backward
50.0< M_{ee} < 60.0	0.015± 0.000	0.010± 0.000	0.002± 0.000	0.002± 0.000
60.0< M_{ee} < 70.0	0.044± 0.001	0.027± 0.000	0.015± 0.000	0.015± 0.000
70.0< M_{ee} < 75.0	0.060± 0.001	0.037± 0.000	0.027± 0.001	0.033± 0.000
75.0< M_{ee} < 81.0	0.062± 0.001	0.042± 0.000	0.039± 0.001	0.044± 0.000
81.0< M_{ee} < 86.5	0.059± 0.000	0.049± 0.000	0.052± 0.000	0.056± 0.000
86.5< M_{ee} < 89.5	0.057± 0.000	0.055± 0.000	0.060± 0.000	0.061± 0.000
89.5< M_{ee} < 92.0	0.056± 0.000	0.059± 0.000	0.065± 0.000	0.064± 0.000
92.0< M_{ee} < 97.0	0.056± 0.000	0.062± 0.000	0.070± 0.000	0.066± 0.000
97.0< M_{ee} < 105.0	0.056± 0.000	0.072± 0.001	0.081± 0.000	0.071± 0.001
105.0< M_{ee} < 115.0	0.058± 0.001	0.087± 0.001	0.094± 0.001	0.071± 0.001
115.0< M_{ee} < 130.0	0.060± 0.001	0.101± 0.002	0.106± 0.001	0.069± 0.001
130.0< M_{ee} < 180.0	0.070± 0.000	0.125± 0.000	0.116± 0.000	0.068± 0.000
180.0< M_{ee} < 250.0	0.087± 0.000	0.157± 0.001	0.119± 0.000	0.064± 0.001
250.0< M_{ee} < 500.0	0.113± 0.000	0.193± 0.000	0.098± 0.000	0.051± 0.000
500< M_{ee} < 1000	0.153± 0.000	0.239± 0.001	0.048± 0.000	0.022± 0.000

Table 7.1: Acceptance × efficiencies of forward and backward events in different mass bins for CC-CC and CC-EC respectively.

to identify forward (backward) event as backward (forward) event. While for CC-EC events, we only require the CC electron has a track match, and just use the charge of this track to determine forward or backward for the whole event, the mis-identification

Mass Range (GeV)	CC-CC and CC-EC	
	Forward	Backward
50.0< M_{ee} < 60.0	0.016± 0.000	0.012± 0.000
60.0< M_{ee} < 70.0	0.059± 0.001	0.043± 0.000
70.0< M_{ee} < 75.0	0.088± 0.001	0.070± 0.001
75.0< M_{ee} < 81.0	0.101± 0.001	0.087± 0.001
81.0< M_{ee} < 86.5	0.111± 0.001	0.105± 0.000
86.5< M_{ee} < 89.5	0.117± 0.000	0.116± 0.000
89.5< M_{ee} < 92.0	0.121± 0.000	0.122± 0.000
92.0< M_{ee} < 97.0	0.126± 0.000	0.129± 0.000
97.0< M_{ee} < 105.0	0.137± 0.001	0.143± 0.001
105.0< M_{ee} < 115.0	0.151± 0.001	0.158± 0.001
115.0< M_{ee} < 130.0	0.166± 0.001	0.170± 0.002
130.0< M_{ee} < 180.0	0.186± 0.000	0.194± 0.001
180.0< M_{ee} < 250.0	0.206± 0.001	0.220± 0.001
250.0< M_{ee} < 500.0	0.210± 0.000	0.244± 0.000
500< M_{ee} < 1000	0.201± 0.001	0.261± 0.001

Table 7.2: Acceptance × efficiencies of forward and backward events in different mass bins for both CC-CC and CC-EC events.

probability is thus higher.

$$A^{true} = \frac{N^F_{true} - N^B_{true}}{N^F_{true} + N^B_{true}}, \qquad A^{meas} = \frac{N^F_{meas} - N^B_{meas}}{N^F_{meas} + N^B_{meas}} \tag{7.5}$$

For CC-CC events, we have:

$$\begin{aligned} A^{meas} &= \frac{N^F_{meas} - N^B_{meas}}{N^F_{meas} + N^B_{meas}} \\ &= \frac{[(1-f_Q)^2 N^F_{true} + f_Q^2 N^B_{true}] - [(1-f_Q)^2 N^B_{true} + f_Q^2 N^F_{true}]}{[(1-f_Q)^2 N^F_{true} + f_Q^2 N^B_{true}] + [(1-f_Q)^2 N^B_{true} + f_Q^2 N^F_{true}]} \\ &= \frac{(1-2f_Q)}{(1-2f_Q+2f_Q^2)} A^{true} \end{aligned}$$

For CC-EC events, we have:

$$\begin{aligned} A^{meas} &= \frac{N^F_{meas} - N^B_{meas}}{N^F_{meas} + N^B_{meas}} \\ &= \frac{[N^F_{true} + f_Q N^B_{true} - f_Q N^F_{true}] - [N^B_{true} - f_Q N^B_{true} + f_Q N^F_{true}]}{[N^F_{true} + f_Q N^B_{true} - f_Q N^F_{true}] + [N^B_{true} - f_Q N^B_{true} + f_Q N^F_{true}]} \\ &= (1-2f_Q) A^{true} \end{aligned}$$

As shown in the above equations, if $f_Q = 50\%$, which means a track has equal probability to be identified as positive or negative, we can not measure the charge asymmetry since $1 - 2f_Q = 1 - 2 \times 50\% = 0$.

After we subtract backgrounds and apply all acceptance and resolution corrections, we can get the corrected A_{FB}, which will then be related to the true A_{FB} by the dilution factor $\mathcal{D}$:

$$A^{true}_{FB} = A^{meas}_{FB} / \mathcal{D} \tag{7.6}$$

where $\mathcal{D} = (1-2f_Q)/(1-2f_Q+2f_Q^2)$ for CC-CC events and $\mathcal{D} = 1-2f_Q$ for CC-EC events.

7.3.2 Determination of Charge mis-identification

The charge mis-identification rate is measured by using the same selection cuts as is used for the signal CC-CC events, except that no opposite charge required. The charge

misID rate is given by

$$f_Q = \frac{1}{2}\frac{N_{SS}}{N_{OS} + N_{SS}} \tag{7.7}$$

where N_{SS} is the total number of same-sign events and N_{OS} is the total number of opposite-sign events in the Z-peak region. The Z mass distributions for the same-sign and opposite-sign Z events are shown in Fig. 7.8. We also use the tag-probe method as a consistency check by requiring very tight cuts on the tag electron to make sure the charge is determined correctly, and then measure the fake rate by looking at the charge of the probe electron. The results from the two methods agree with each other.

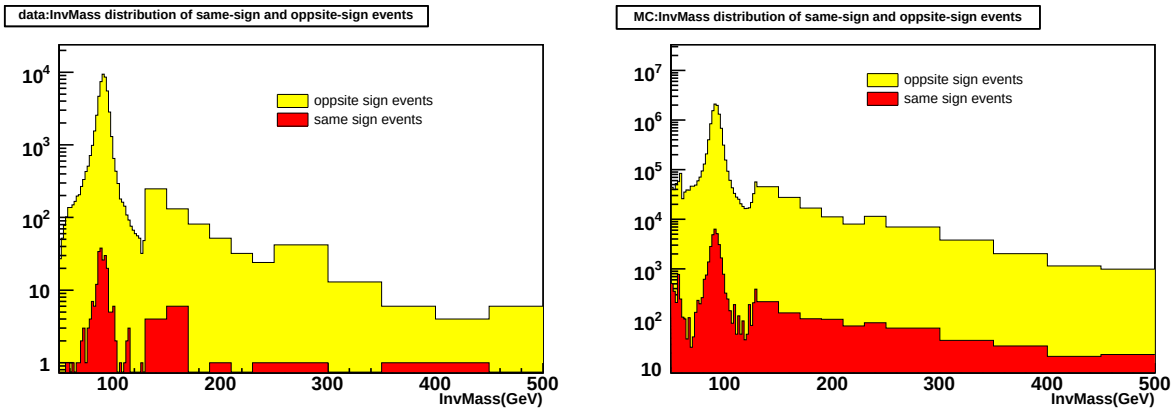

Figure 7.8: Invariant mass distributions for same-sign and opposite-sign events in data (left) and GEANT MC (right).

The same method is applied for real data and GEANT MC events. The average charge misID rate for CC electrons is found to be $\langle f_Q \rangle = (0.23 \pm 0.03)\%$ for real data and $\langle f_Q \rangle = (0.06 \pm 0.006)\%$ for GEANT MC events. The charge misID is roughly a factor of 3 worse in data than in GEANT MC. The main reasons for the data-GEANT MC difference can be less amount of materials for the tracking system in GEANT simulation, and the non-perfect alignment of the real detector. The charge misID rate as a function of invariant mass is also shown in Fig. 7.9 for both data and GEANT MC.

At higher energies, the tracks become almost straight and the charge determination has a higher probability of being wrong. More detailed information about charge misID rate can be found in [48]. The error is calculated using Bayesian uncertainties.

In real data, due to the limited statistics, we did not observe any same-sign events with $M > 250$ GeV, but it does not really mean the charge misID rate is zero for $M > 250$ GeV. We use GEANT MC events to model the charge misID rate for high-mass region, the charge misID rate in GEANT MC is rescaled to match with the misID rate in data at Z-pole. The comparision for the charge misID rate between data and the rescaled GEANT MC can be found in Fig. 7.10 (left) for the whole mass region and Fig.7.10 (right) for the region $50 < M < 130$ GeV, good agreement for the charge misID rate between the data and the rescaled GEANT MC are observed for each bin.

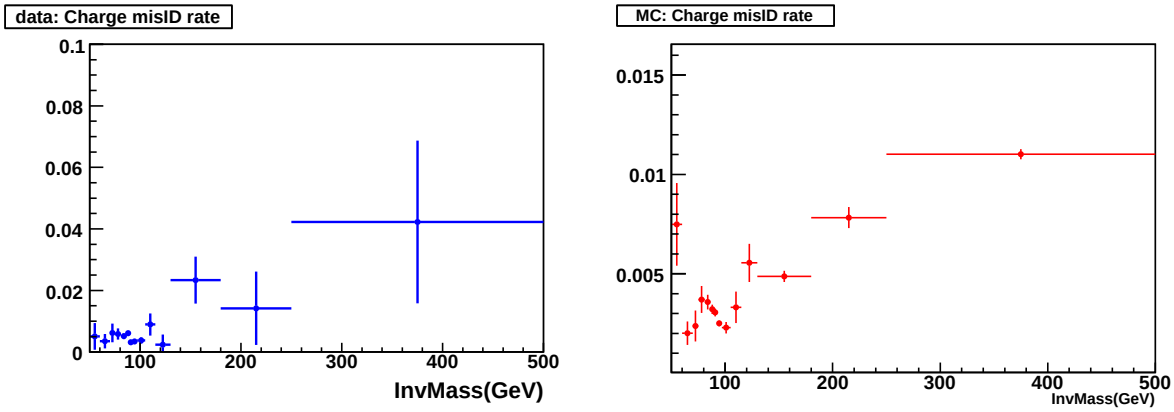

Figure 7.9: Data (blue) and GEANT MC (red) charge misID rate as a function of invariant mass.

For the final charge misID rate, we use the central values from the rescaled GEANT MC samples and the uncertainties from real data. These values are listed in Table 7.3 together with the dilution factor $\mathcal{D}$ for CC-CC and CC-EC. For CC-CC region, the effect is pretty small and almost no correction is needed. For CC-EC region, the effect

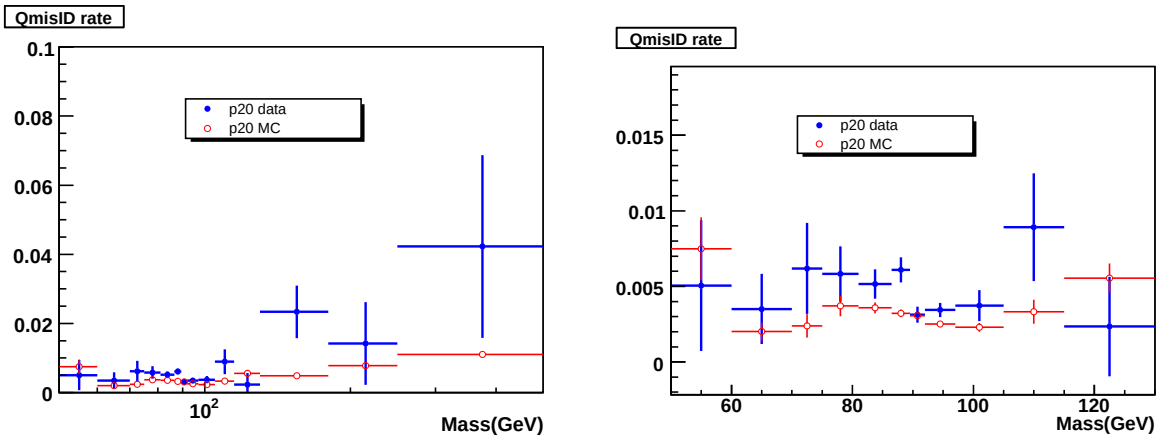

Figure 7.10: Data (blue) and GEANT MC (red) charge misID rate as a function of invariant mass. The charege misID rate in GEANT MC is rescaled to match with data at Z-pole. The left plot is for the whole mass region and the right plot is for $50 < M < 130$ GeV.

is also pretty small ($< 1\%$ for the first twelve bins) except 1.2% for $180 < M < 250$ GeV and 2.3% for $250 < M < 500$ GeV.

7.4 Unfolding precedure and Closure test

Before we apply the detector resolution, acceptance $\times$ efficiency unfolding and charge misID rate on real data, we apply the same techniques on the GEANT MC simulation. We then compare the unfolded A_{FB} with the truth A_{FB} distribution from PYTHIA to make sure that we can get back the input A_{FB} distribution. We did three GEANT MC closure tests as described below.

7.4.1 First closure test on the unfolding method

We used the GEANT MC samples as described in Chapter 4, apply the selection cuts and get the raw A_{FB} and derive all corrections. Then we compare the unfolded A_{FB}

Mass Range (GeV)	f_Q	$\mathcal{D}$ for CC-CC	$\mathcal{D}$ for CC-EC
$50.0 < M_{ee} < 60.0$	0.0075± 0.0043	0.999888	0.985021
$60.0 < M_{ee} < 72.0$	0.0020± 0.0023	0.999992	0.995978
$72.0 < M_{ee} < 75.0$	0.0024± 0.0030	0.999989	0.995240
$75.0 < M_{ee} < 81.0$	0.0037± 0.0018	0.999972	0.992581
$81.0 < M_{ee} < 86.5$	0.0036± 0.0010	0.999974	0.992844
$86.5 < M_{ee} < 89.5$	0.0032± 0.0008	0.999979	0.993573
$89.5 < M_{ee} < 92.0$	0.0031± 0.0005	0.999981	0.993891
$92.0 < M_{ee} < 97.0$	0.0025± 0.0005	0.999987	0.994972
$97.0 < M_{ee} < 105.0$	0.0023± 0.0010	0.999990	0.995419
$105.0 < M_{ee} < 115.0$	0.0033± 0.0036	0.999978	0.993363
$115.0 < M_{ee} < 130.0$	0.0056± 0.0033	0.999938	0.988899
$130.0 < M_{ee} < 180.0$	0.0049± 0.0076	0.999953	0.990269
$180.0 < M_{ee} < 250.0$	0.0078± 0.0119	0.999877	0.984341
$250.0 < M_{ee} < 500.0$	0.0110± 0.0265	0.999757	0.977974
$500.0 < M_{ee} < 1000$	0.0318± 0.0905	0.99785	0.936471

Table 7.3: Charge misID rate used for final analysis and also the dilution factor for CC-CC and CC-EC.

distribution with the truth distribution.

7.4.1.1 Applying detector resolution unfolding

The comparison between the raw A_{FB} after applying event selection, A_{FB} after applying detector resolution unfolding and the truth A_{FB} can be found in Fig. 7.11.

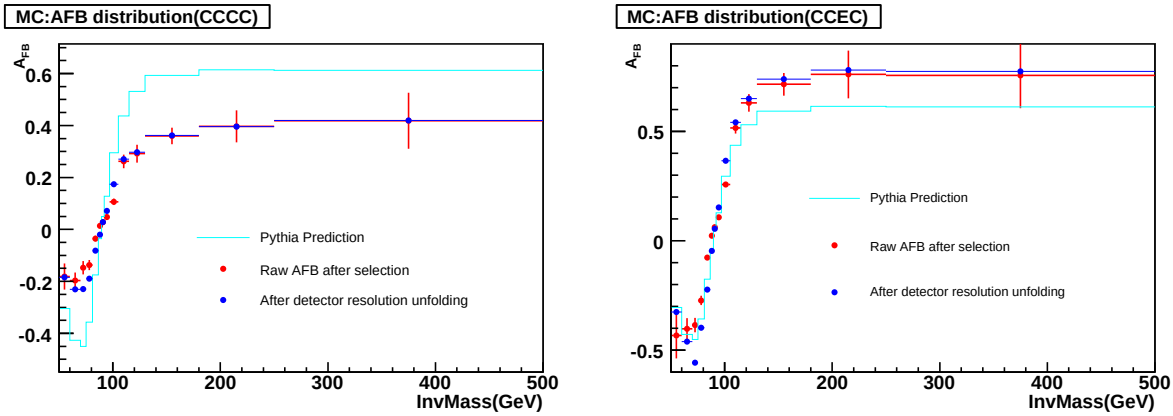

Figure 7.11: Applying detector resolution unfolding on Geant MC sample, for CC-CC and CC-EC events.

7.4.1.2 Applying detector resolution and acc×eff unfolding

The comparison between A_{FB} after applying detector resolution unfolding, A_{FB} after applying detector resolution and acc×eff unfolding, and the truth A_{FB} can be found in Fig. 7.12.

7.4.1.3 Applying detector resolution, acc×eff and charge mis-ID rate

The charge mis-identification rate is very small in GEANT MC, and the charge misID correction has negligible effect on the final A_{FB} distribution. Fig. 7.13 shows the differences between the truth A_{FB} and A_{FB} after detector resolution and acc×eff unfolding, and also charge mis-identification rate corrections.

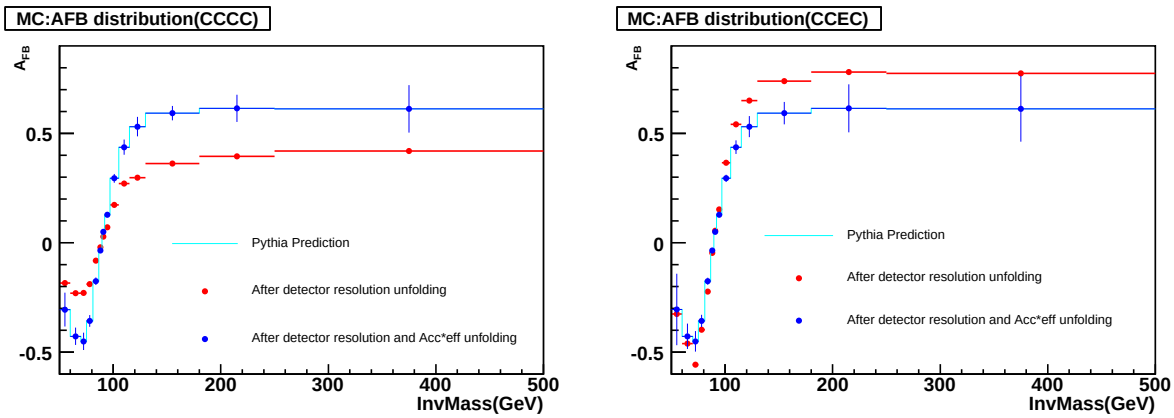

Figure 7.12: Applying detector resolution and acc×eff unfolding on Geant MC sample, for CC-CC and CC-EC events.

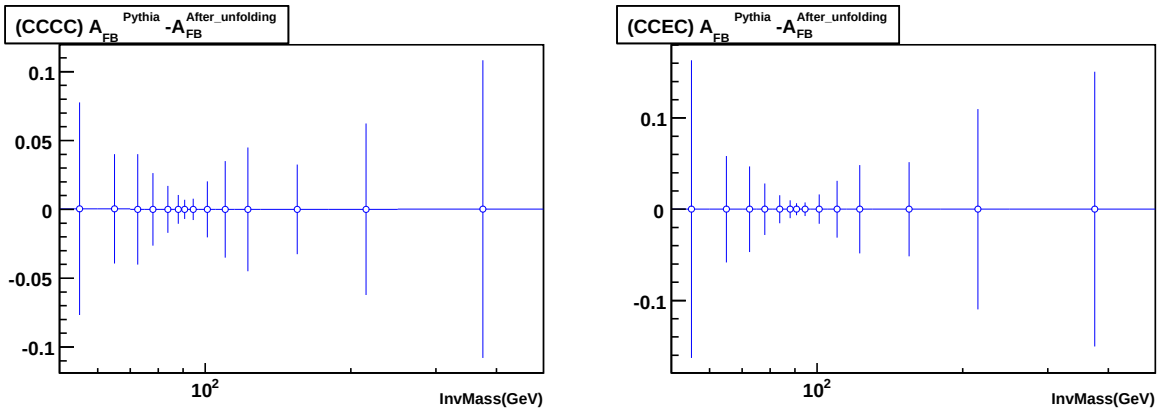

Figure 7.13: Differences between the truth A_{FB} from PYTHIA and A_{FB} after all corrections applied for CC-CC and CC-EC events.

7.4.2 Second closure test on the unfolding method

Since we rely on the GEANT MC simulation for the response matrix and also the acceptance corrections, we did another closure test. At generator level, we introduced a random number (50%) to reverse forward (backward) events into backward (forward) events. As a result, the generator-level A_{FB} distribution has changed totally. We used this new GEANT MC events and applied the same techniques to correct the measured A_{FB}. The final unfolded A_{FB} with the modified generate-level A_{FB} is shown in Fig. 7.14, pretty good agreement has been observed.

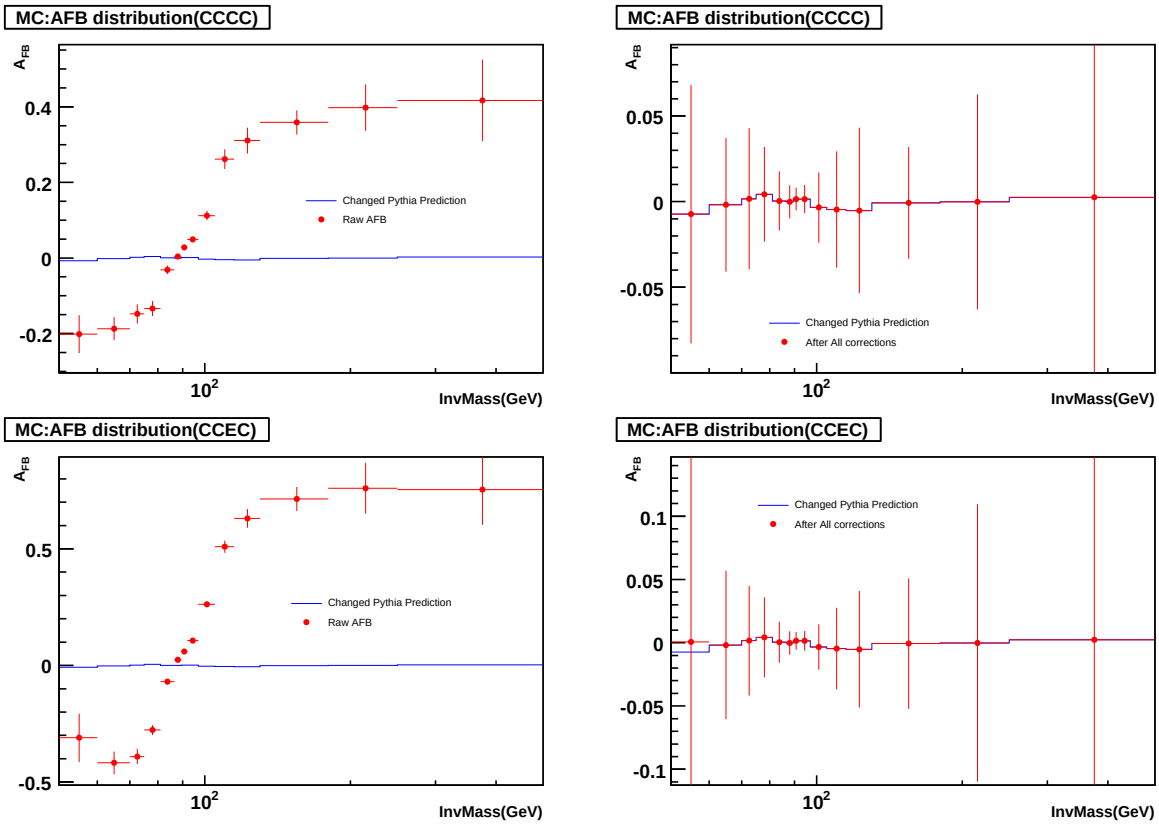

Figure 7.14: Comparison between changed generate-level A_{FB} and unfolded A_{FB} of Geant MC sample, for CC-CC and CC-EC events.

7.4.3 Third closure test on the unfolding method

For the above two closure tests, we used the same GEANT MC sample to measure raw A_{FB} and derive detector resolution unfolding and acc×eff corrections, and we got perfect agreement. We also split the GEANT MC sample into two sub-samples, and use the first sample to measure raw A_{FB} distribution and use the second sample to measure all corrections, the final unfolded A_{FB} with the generate-level A_{FB} is shown in Fig. 7.15.

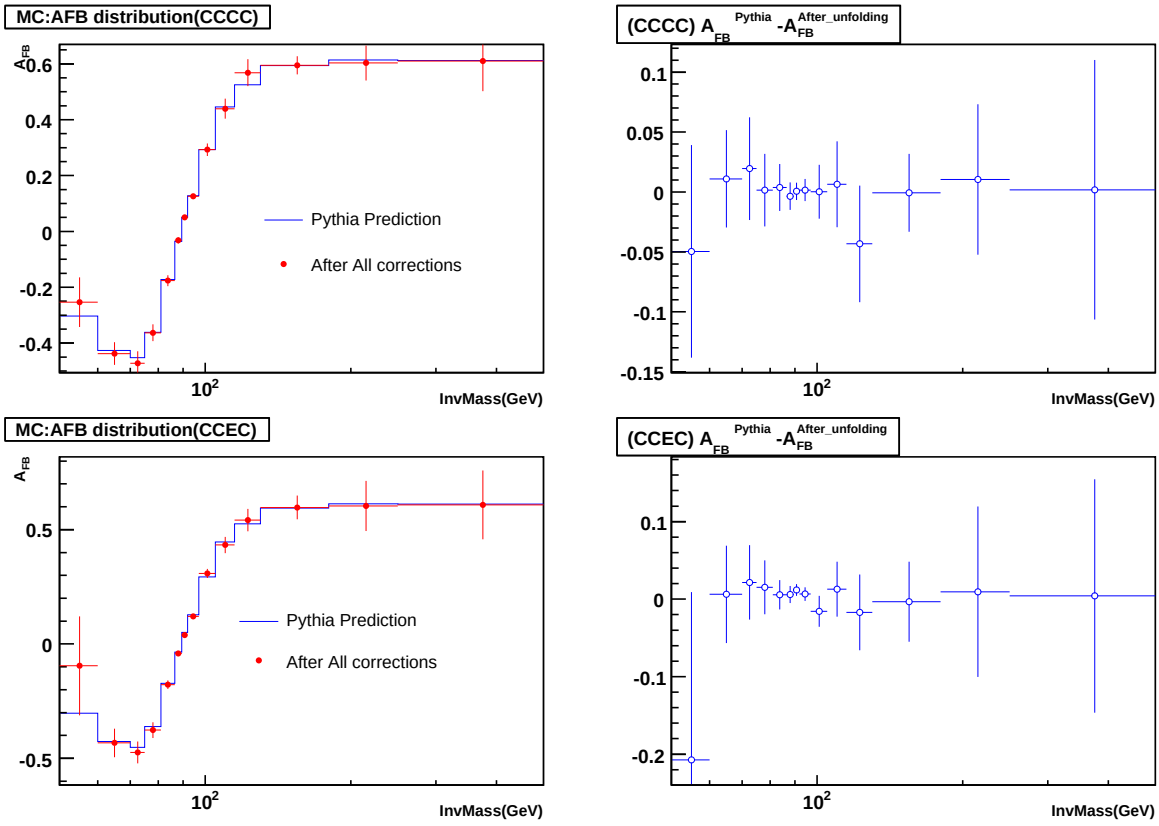

Figure 7.15: Differences between the truth A_{FB} from PYTHIA and A_{FB} after all corrections applied for CC-CC and CC-EC events.

Chapter 8

Forward-Backward Charge Asymmetry measurement

8.1 Bias due to the unfolding method

We used the GEANT MC events to measure the response matrix, acceptance × efficiency corrections, and these corrections depends on the input A_{FB} distribution, and the unfolded A_{FB} spectrum may be biased.

To measure the bias due to the unfolding method, we used a simple fast MC program. The fast MC simulation has reasonable assumptions about the detector energy resolution, kinematic+geometric acceptances and also selection efficiencies:

- the primary vertex is smeared with a Gaussian function with a width of 25 cm;
- both electron and positron are extrapolated from the primary vertex to the EM3 layer, detector eta and phi are calculated;

- electron and positron energy are smeared assuming 3% resolution;
- the normal CC and EC detector eta and phi cuts are applied on the smeared electron to simulate detector acceptance and an overall efficiency of 80% and 90% is assumed for CC and EC electrons according to the values we measured in data;
- $p_T > 25$ GeV cut applied on electron and positron.

We then run this fast MC simulation on 5 M PYTHIA generator-level events (with $\sin^2\theta_W = 0.2315$) to measure the response matrix, acc×eff corrections. And we then use two 4 M PYTHIA samples generated with $\sin^2\theta_W = 0.22702$ and $\sin^2\theta_W = 0.23602$ to measure the raw A_{FB} distributions. These two samples are the samples with the biggest deviations that we generated before and correspond to about ± 3 σ of our uncertainty and ± 30 σ of the world average uncertainty. We then unfold the raw A_{FB} distributions for $\sin^2\theta_W = 0.22702$ and 0.23602 with the response matrix and acc×eff corrections measured from the sample with $\sin^2\theta_W = 0.2315$ to get the unfolded A_{FB} distribution. We used two independent 1 M PYTHIA samples with $\sin^2\theta_W = 0.22702$ and 0.23602 to get the theoretical predictions so that we do not need to worry about the correlations between the generator-level and smeared-level events.

The difference between the PYTHIA predicted and unfolded A_{FB} distributions can be found at Fig. 8.1. We can see that there is a bias near the Z-pole: when all corrections are measured using a sample with higher input value of $\sin^2\theta_W$, the unfolded A_{FB} tends to be lower than the true A_{FB}, and vice versa.

To remove this bias, we followed the suggestion of Thomas Nunnemann and Heidi

Schellman and did an iterative unfolding. The idea is first use corrections measured derived from a MC sample with very different input $\sin^2\theta_W$, and then use the unfolded A_{FB} distribution to determine the best $\sin^2\theta_W$. Then we use another MC sample with the measured $\sin^2\theta_W$ to obtain all corrections as input for the next iteration of unfolding. The above steps are repeated until the measured $\sin^2\theta_W$ is stable. The convergence is pretty fast, for -3σ sample with true $\sin^2\theta_W = 0.22702$, we only need two steps: first 0.23152 and then 0.2272 for the input $\sin^2\theta_W$ value to measure all corrections. For $+3\sigma$ sample with true $\sin^2\theta_W = 0.23572$, we need four steps: 0.23152, 0.2346, 0.2351, and then 0.2355 for the input $\sin^2\theta_W$ value to measure all corrections.

The difference between the PYTHIA predicted and unfolded A_{FB} distributions after using all corrections derived from the MC sample with the best measured $\sin^2\theta_W$ values can be found at Fig. 8.2. No obvious trend remains and the remaining difference between the unfolded and the true A_{FB} can be due to the fluctuation of the MC samples used to measure all corrections (described in Sect. 8.3.7).

For the unfolding applied on real data, we also applied the same analysis procedure described above, and the best measured $\sin^2\theta_W$ quickly converged to the extracted A_{FB} explained in Sect. 9.3. We used the Geant MC samples with the measured A_{FB} and $\pm1\sigma$ variations to estimate the uncertainty on the unfolded A_{FB} distribution (as described in Sect. 8.3.10).

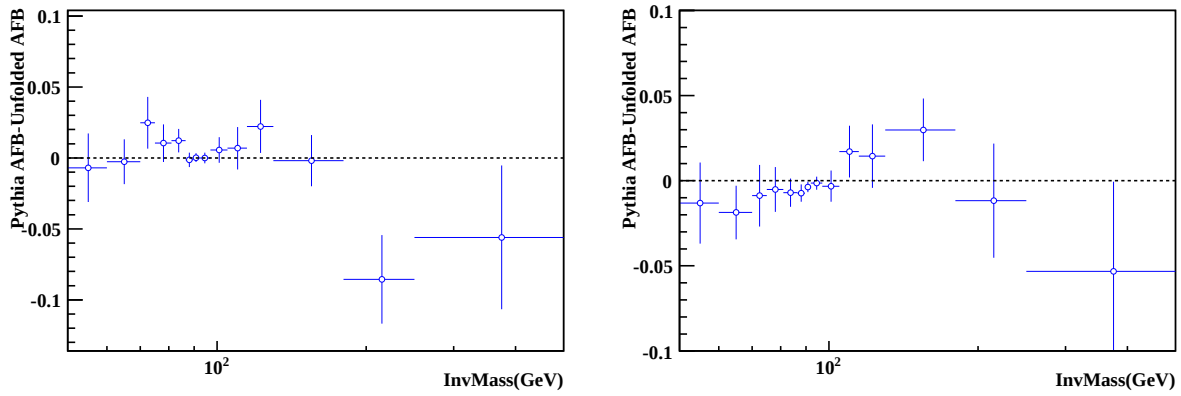

Figure 8.1: Difference between the PYTHIA predicted and unfolded A_{FB} for $\sin^2\theta_W$ = 0.22702 (Left) and $\sin^2\theta_W$ = 0.23702 (Right) but using the response matrix, acc × eff corrections measured from events generated with $\sin^2\theta_W = 0.23152$.

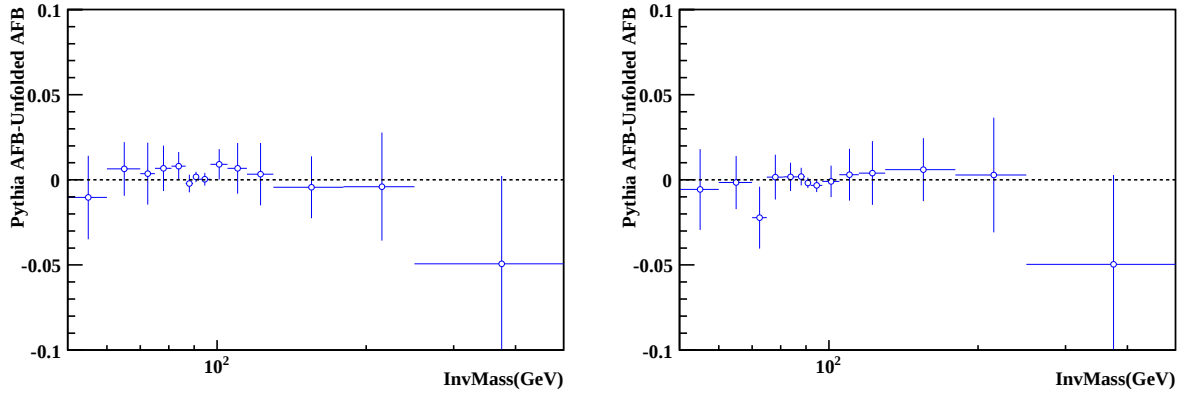

Figure 8.2: Difference between the PYTHIA predicted and unfolded A_{FB} for $\sin^2\theta_W$ = 0.22702 (Left) and $\sin^2\theta_W$ = 0.23702 (Right) but using the response matrix, acc × eff corrections derived from events generated with the best measured $\sin^2\theta_W$ values: $\sin^2\theta_W$ = 0.2272 and $\sin^2\theta_W = 0.2355$.

8.2 Data unfolding

After we tested all analysis processes using full MC events, we apply the same procedure on real data. Fig. 8.3 to Fig. 8.5 show the raw A_{FB} distribution and the A_{FB} distribution after each correction: (1) detector resolution unfolding; (2) acceptance $\times$ efficiency corrections; (3) charge misID rate corrections. The final value of A_{FB} for both CCCC and CCEC events can be found in Tab. 8.1.

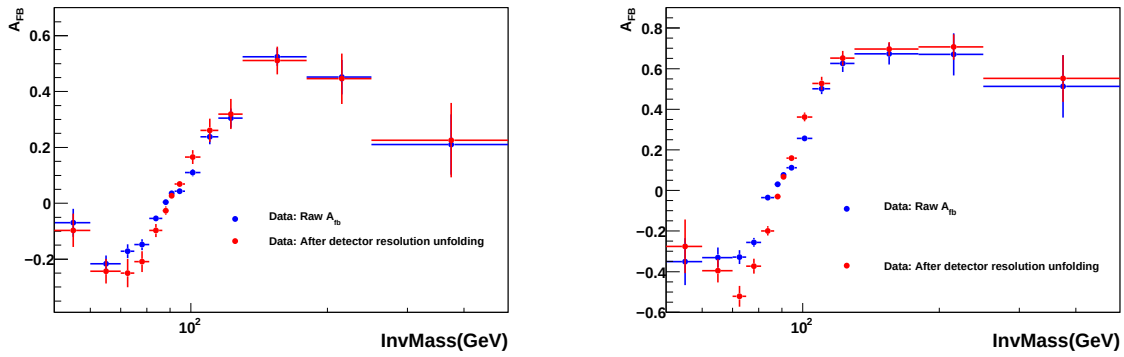

Figure 8.3: Data raw A_{FB} and after detector resolution unfolding A_{FB} for CC-CC and CC-EC events.

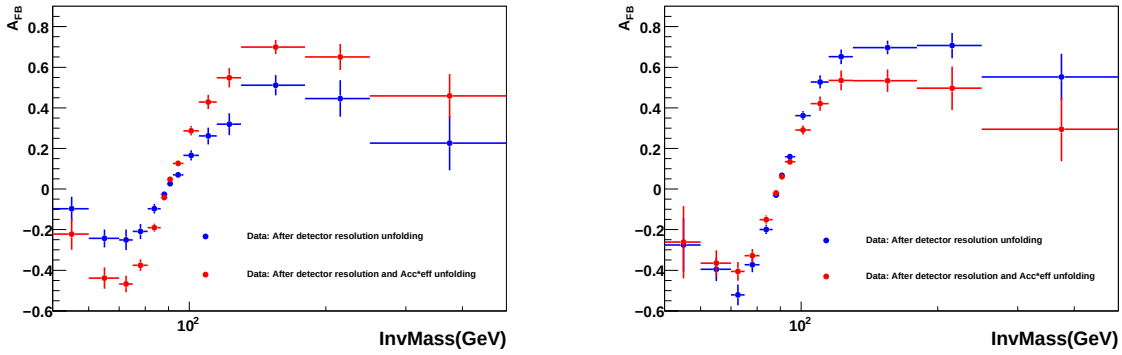

Figure 8.4: Data after detector resolution unfolding A_{FB} and after detector resolution and Acc×eff unfolding A_{FB} for CC-CC and CC-EC events.

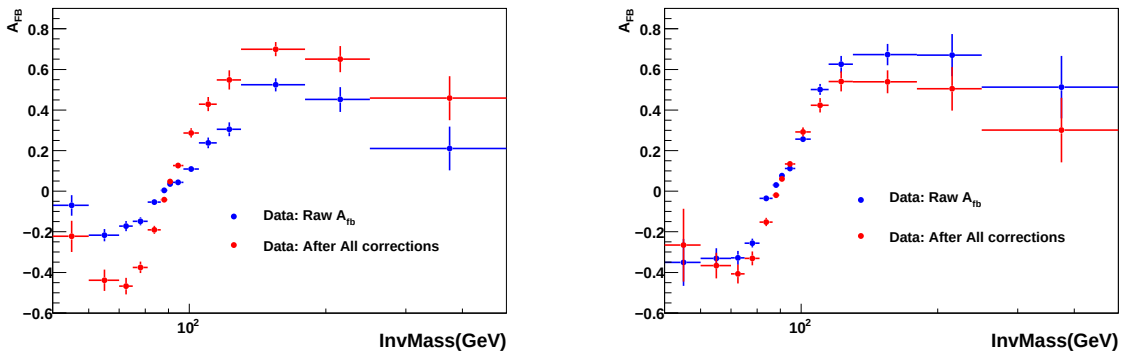

Figure 8.5: Data raw A_{FB} and after all corrections A_{FB} for CC-CC and CC-EC events.

$\langle M_{ee} \rangle$ (GeV)	Predicted A_{FB}		Unfolded A_{FB}
	PYTHIA	ZGRAD2	
54.5	-0.293	-0.307	$-0.280 \pm 0.037 \pm 0.022$
64.9	-0.426	-0.431	$-0.456 \pm 0.020 \pm 0.016$
72.6	-0.449	-0.452	$-0.430 \pm 0.015 \pm 0.020$
78.3	-0.354	-0.354	$-0.343 \pm 0.011 \pm 0.013$
84.4	-0.174	-0.166	$-0.175 \pm 0.006 \pm 0.011$
88.4	-0.033	-0.031	$-0.033 \pm 0.003 \pm 0.005$
90.9	0.051	0.052	$0.052 \pm 0.003 \pm 0.004$
93.4	0.127	0.129	$0.130 \pm 0.003 \pm 0.005$
99.9	0.289	0.296	$0.303 \pm 0.007 \pm 0.012$
109.1	0.427	0.429	$0.441 \pm 0.014 \pm 0.015$
121.3	0.526	0.530	$0.572 \pm 0.020 \pm 0.016$
147.9	0.593	0.603	$0.677 \pm 0.022 \pm 0.014$
206.4	0.613	0.600	$0.613 \pm 0.042 \pm 0.016$
310.5	0.616	0.615	$0.440 \pm 0.068 \pm 0.008$
584.4	0.616	0.615	$0.813 \pm 0.170 \pm 0.010$

Table 8.1: The first column shows the cross section weighted average of the invariant mass in each mass bin derived from PYTHIA. The second and third columns show the A_{FB} predictions from PYTHIA and ZGRAD2. The last column is the unfolded A_{FB}; the first uncertainty is statistical, and the second is systematic.

8.3 Uncertainties

8.3.1 Systematic uncertainty from efficiency scale factors

As we apply data-MC efficiency scale factors on GEANT MC events, we need to know the uncertainty due to the electron efficiency scale factors. Each scale factor is fitted with a straight line, and the fitted errors (both $+\sigma$ and $-\sigma$) are used to estimate the systematic uncertainty on A_{FB}. We find that the uncertainties due to the scale factors are negligible, the main reason is the scale factors are applied on both forward and backward events, while changing both forward and backward events at the same time will have no effect on the final A_{FB} distribution.

8.3.2 Systematic uncertainty from efficiency difference between forward and backward events

As mentioned in Sect. 5, the EMID efficiencies between forward and backward events are consistent with each other for both data and GEANT MC. In both data and GEANT MC, the forward and backward events are treated the same way, possible differences between forward and backward events can cause systematic uncertainties on the final A_{FB} distribution. The ratio for the forward and backward efficiencies can be found in Table. 5.4.

$$\begin{aligned} A_{FB} &= \frac{N^F_{meas} - N^B_{meas}}{N^F_{meas} + N^B_{meas}} \\ &= \frac{N^F_{all} \cdot \epsilon_F - N^B_{all} \cdot \epsilon_B}{N^F_{all} \cdot \epsilon_F + N^B_{all} \cdot \epsilon_B} \end{aligned}$$

$$= \frac{\frac{N^F_{all}}{N^B_{all}} \cdot \frac{\epsilon_F}{\epsilon_B} - 1}{\frac{N^F_{all}}{N^B_{all}} \cdot \frac{\epsilon_F}{\epsilon_B} + 1}$$
$$= \frac{a \cdot f - 1}{a \cdot f + 1}$$

where

- a : $\frac{N^F_{all}}{N^B_{all}}$,since it's only a fraction of numbers, so we will use $\frac{N^F_{meas}}{N^B_{meas}}$ instead of $\frac{N^F_{all}}{N^B_{all}}$
- f : $\frac{\epsilon_F}{\epsilon_B}$ is the factor we get in Table. 5.4.
  - For CCCC events:

$$f_{CCCC} = (\frac{\epsilon^{PreID}_F(CC) \cdot \epsilon^{EMID}_F(CC) \cdot \epsilon^{TrkMatch}_F(CC)}{\epsilon^{PreID}_B(CC) \cdot \epsilon^{EMID}_B(CC) \cdot \epsilon^{TrkMatch}_B(CC)})^2$$
$$= (f^{PreID}(CC) \cdot f^{EMID}(CC) \cdot f^{TrkMatch}(CC))^2$$

  - For CCEC events:

$$f_{CCEC} = \frac{\epsilon^{PreID}_F(CC) \cdot \epsilon^{EMID}_F(CC) \cdot \epsilon^{TrkMatch}_F(CC)}{\epsilon^{PreID}_B(CC) \cdot \epsilon^{EMID}_B(CC) \cdot \epsilon^{TrkMatch}_B(CC)} \times \frac{\epsilon^{PreID}_F(EC) \cdot \epsilon^{EMID}_F(EC)}{\epsilon^{PreID}_B(EC) \cdot \epsilon^{EMID}_B(EC)}$$
$$= f^{PreID}(CC) \cdot f^{EMID}(CC) \cdot f^{TrkMatch}(CC) \cdot f^{PreID}(EC) \cdot f^{EMID}(EC)$$

So uncertainties for each mass bins can be get like:

$$\sigma_{\frac{F}{B}} = \frac{a \cdot \sigma_f(a \cdot \sigma_f + 1) - a \cdot \sigma_f(a \cdot \sigma_f - 1)}{(a \cdot f + 1)^2}$$
$$= \frac{2a \cdot \sigma_f}{(a \cdot f + 1)^2}$$

The uncertainties due to differences between forward and backward efficiencies are shown in Tab. 8.2

Mass region(GeV/c^2)	CCCC	CCEC
$50.0 < M_{ee} < 60.0$	0.0020	0.0016
$60.0 < M_{ee} < 72.0$	0.0019	0.0016
$72.0 < M_{ee} < 75.0$	0.0019	0.0016
$75.0 < M_{ee} < 81.0$	0.0020	0.0017
$81.0 < M_{ee} < 86.5$	0.0020	0.0018
$86.5 < M_{ee} < 89.5$	0.0020	0.0018
$89.5 < M_{ee} < 92.0$	0.0020	0.0018
$92.0 < M_{ee} < 97.0$	0.0020	0.0018
$97.0 < M_{ee} < 105.0$	0.0020	0.0017
$105.0 < M_{ee} < 115.0$	0.0019	0.0014
$115.0 < M_{ee} < 130.0$	0.0018	0.0012
$130.0 < M_{ee} < 180.0$	0.0014	0.0011
$180.0 < M_{ee} < 250.0$	0.0016	0.0011
$250.0 < M_{ee} < 500.0$	0.0019	0.0014
$500 < M_{ee} < 1000$	0.0005	0.0011

Table 8.2: CC-CC and CC-EC events AFB systematic Uncertainty due to difference between Forward and Backward efficiency.

8.3.3 Systematic uncertainty from energy scale and energy resolution

The systematic uncertainty due to energy scale is shown in Table 8.4 and the uncertainty due to energy scale is shown in Table 8.3 The columns which are all 0s are due to the fact that the EC energy scale and smear parameters will not affect CC-CC events. And for the uncertainty due to electron energy non-linearity, we use the differences between the unfolded A_{FB} distributions with and without non-linearity term, the uncertainties are shown in Table 8.5.

8.3.4 Systematic uncertainty from PDF

The systematic uncertainty due to PDF is estimated by reweighting the central PDF to 40 CTEQ6.1 error PDF sets, and the PDF uncertainty is calculated using the prescription suggested by CTEQ group:

$$\Delta A^{\pm} = \sqrt{\sum_{i=1}^{20} (A_i^{\pm} - A_0)^2} \tag{8.1}$$

where $A_i^{\pm}$ is the asymmetry measured for PDF error set i and A_0 is the asymmetry for the central PDF set. This will give asymmetric errors and we decided to use the maximum of positive and negative uncertainties as the final uncertainty. The uncertainty for each bin is listed in Tab. 8.6.

8.3.5 Systematic uncertainty from higher order corrections

So far we only used LO PYTHIA generator for the A_{FB} calculation. Higher-order QCD, QED and electroweak corrections can change the generator-level A_{FB} predictions. Due

Mass region(GeV/c^2)	CCCC(CC/EC)		CCEC(CC/EC)	
$50.0 < M_{ee} < 60.0$	0.0004	0.0000	0.0016	0.0022
$60.0 < M_{ee} < 70.0$	0.0013	0.0000	0.0020	0.0034
$70.0 < M_{ee} < 75.0$	0.0025	0.0000	0.0005	0.0013
$75.0 < M_{ee} < 81.0$	0.0027	0.0000	0.0025	0.0015
$81.0 < M_{ee} < 86.5$	0.0026	0.0000	0.0018	0.0025
$86.5 < M_{ee} < 89.5$	0.0008	0.0000	0.0007	0.0011
$89.5 < M_{ee} < 92.0$	0.0011	0.0000	0.0011	0.0010
$92.0 < M_{ee} < 97.0$	0.0007	0.0000	0.0008	0.0007
$97.0 < M_{ee} < 105.0$	0.0025	0.0000	0.0029	0.0034
$105.0 < M_{ee} < 115.0$	0.0019	0.0000	0.0009	0.0014
$115.0 < M_{ee} < 130.0$	0.0040	0.0000	0.0006	0.0007
$130.0 < M_{ee} < 180.0$	0.0016	0.0000	0.0001	0.0002
$180.0 < M_{ee} < 250.0$	0.0002	0.0000	0.0003	0.0004
$250.0 < M_{ee} < 500.0$	0.0003	0.0000	0.0001	0.0003
$500 < M_{ee} < 1000$	0.0001	0.0000	0.0001	0.0006

Table 8.3: CC-CC and CC-EC A_{FB} systematic uncertainty due to CC or EC energy smearing parameters. The systematic shift is tested in two directions ($+1\sigma$ and -1σ of the each variables, and we choose the larger one.) As expected, the EC energy smearing parameter has no effect on CCCC A_{FB} distribution.

to the fact that $\cos\theta^*$ is calculated in the Collin-Soper frame, the impact of the initial-state QCD correction is minimized. The QED correction is minimized due to the fact

Mass region(GeV/c^2)	CCCC(CC/EC)		CCEC(CC/EC)	
$50.0 < M_{ee} < 60.0$	0.0006	0.0000	0.0020	0.0023
$60.0 < M_{ee} < 70.0$	0.0021	0.0000	0.0031	0.0032
$70.0 < M_{ee} < 75.0$	0.0011	0.0000	0.0011	0.0027
$75.0 < M_{ee} < 81.0$	0.0010	0.0000	0.0010	0.0006
$81.0 < M_{ee} < 86.5$	0.0020	0.0000	0.0016	0.0027
$86.5 < M_{ee} < 89.5$	0.0006	0.0000	0.0015	0.0016
$89.5 < M_{ee} < 92.0$	0.0007	0.0000	0.0010	0.0007
$92.0 < M_{ee} < 97.0$	0.0010	0.0000	0.0012	0.0018
$97.0 < M_{ee} < 105.0$	0.0005	0.0000	0.0023	0.0034
$105.0 < M_{ee} < 115.0$	0.0017	0.0000	0.0016	0.0016
$115.0 < M_{ee} < 130.0$	0.0031	0.0000	0.0003	0.0020
$130.0 < M_{ee} < 180.0$	0.0011	0.0000	0.0003	0.0003
$180.0 < M_{ee} < 250.0$	0.0003	0.0000	0.0003	0.0004
$250.0 < M_{ee} < 500.0$	0.0003	0.0000	0.0002	0.0001
$500 < M_{ee} < 1000$	0.0001	0.0000	0.0003	0.0000

Table 8.4: CC-CC and CC-EC A_{FB} systematic uncertainty due to CC or EC energy scale factor. The systematic shift is tested in two directions ($+1\sigma$ and -1σ of the each variables, and we choose the larger one.) As expected, EC energy scale factor has no effect on CCCC A_{FB} distribution.

that electrons and the emitted photons are very close to each other and can not be distinguished in the detector.

Mass	CCCC	CCEC
$50.0 < M_{ee} < 60.0$	0.0129	0.0191
$60.0 < M_{ee} < 70.0$	0.0019	0.0019
$70.0 < M_{ee} < 75.0$	0.0028	0.0039
$75.0 < M_{ee} < 81.0$	0.0003	0.0012
$81.0 < M_{ee} < 86.5$	0.0002	0.0006
$86.5 < M_{ee} < 89.5$	0.0000	0.0001
$89.5 < M_{ee} < 92.0$	0.0000	0.0002
$92.0 < M_{ee} < 97.0$	0.0002	0.0002
$97.0 < M_{ee} < 105.0$	0.0001	0.0008
$105.0 < M_{ee} < 115.0$	0.0034	0.0024
$115.0 < M_{ee} < 130.0$	0.0006	0.0043
$130.0 < M_{ee} < 180.0$	0.0010	0.0005
$180.0 < M_{ee} < 250.0$	0.0049	0.0035
$250.0 < M_{ee} < 500.0$	0.0061	0.0006
$500 < M_{ee} < 1000$	0.0111	0.0622

Table 8.5: Systematic uncertainties on A_{FB} measurement for CCCC and CCEC events due to energy non-linearity.

For the theoretical predictions, we tried the following generators:

(1) 5M $Z/\gamma^* \to ee$ events using PYTHIA;

(2) 5M $Z/\gamma^* \to ee$ events using PYTHIA with tuned Z boson p_T distribution;

(3) 5M $Z/\gamma^* \to ee$ events using PYTHIA with internal bremsstrahlung turned off, later

Mass region (GeV/c^2)	PDF uncertainty
$50 < M_{ee} < 60$	0.0073
$60 < M_{ee} < 70$	0.0103
$70 < M_{ee} < 75$	0.0113
$75 < M_{ee} < 81$	0.0097
$81 < M_{ee} < 86.5$	0.0051
$86.5 < M_{ee} < 89.5$	0.0015
$89.5 < M_{ee} < 92$	0.0016
$92 < M_{ee} < 97$	0.0034
$97 < M_{ee} < 105$	0.0075
$105 < M_{ee} < 115$	0.0102
$115 < M_{ee} < 130$	0.0107
$130 < M_{ee} < 180$	0.0095
$180 < M_{ee} < 250$	0.0072
$250 < M_{ee} < 500$	0.0048
$500 < M_{ee} < 1000$	0.0010

Table 8.6: Systematic Uncertainty due to PDF uncertainty.

these events are passed through PHOTOS to simulate final state radiation;

(4) 5M $Z/\gamma^* \rightarrow ee$ events using ZGRAD with tuned Z boson p_T distribution.

Fig. 8.6 shows the comparison of the generator-level A_{FB} distribution for sample (1) and (2) (Left) and for sample (1) and (3) (Right) to show the effect of QCD and QED corrections on A_{FB} separately. Fig. 8.7 shows the comparison of the generator-

level A_{FB} distribution between sample (1) and (4), since the samples (1) and (4) have different QCD, QED and electroweak corrections, we decided to use their difference as the systematic uncertainty due to all higher-order corrections. The systematic uncertainties for all 14 mass bins are listed in Tab. 8.7.

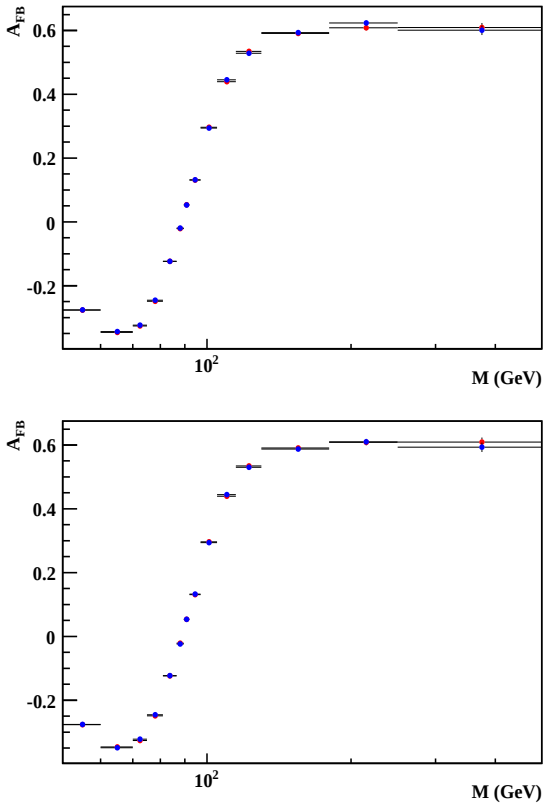

Figure 8.6: Left: A_{FB} predictions from the default PYTHIA (Red) and PYTHIA with tuned Z boson p_T distribution (Blue). Right: A_{FB} distribution from the default PYTHIA (Red) and PYTHIA with internal bremsstrahlung turned off but later pass through PHOTOS for FSR simulation (Blue).

The systematic uncertainty due to the electron and photon merging cone size (detector effect) is estimated using the generator level information, and the uncertainty is assigned as the A_{FB} difference using electron-photon merging cone size $R = 0.2$ and

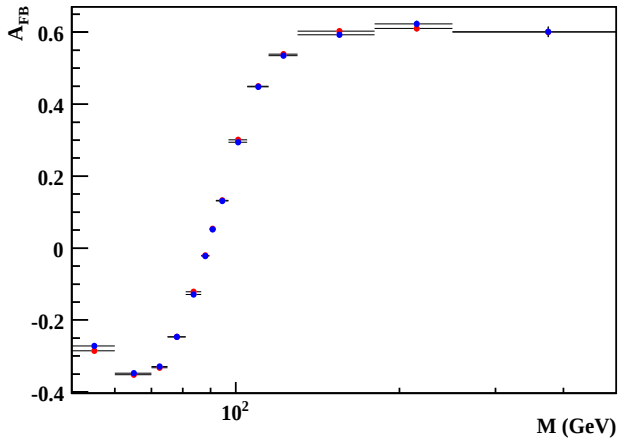

Figure 8.7: A_{FB} predictions from ZGRAD (Red) and PYTHIA (Blue).

$R = 0.3$, the uncertainties are found to be negligible.

8.3.6 Systematic uncertainty from background subtraction

To estimate the uncertainty due to QCD background, we change the electron shower shape requirements on the electron. We use HMx7 > 30 in CC and HMx8 > 40 in EC as the default, and use the shape measured from HMx7 > 12 (CC) and HMx8 > 20 (EC) and HMx7 > 50 (CC) and HMx8 > 75 (EC) to estimate the systematic uncertainty.

The uncertainty due to background subtraction is shown in Tab. 8.8.

8.3.7 Systematic uncertainty due to full MC statistics

To determine the systematic uncertainty due to the statistical uncertainty on the response matrix and acc $\times$ eff corrections, we divided the full MC events into ten subsamples and did ten pseudo-experiments. The spread of the ten unfolded A_{FB} for each bin divided by $\sqrt{10}$ is the systematic uncertainty due to the limited full MC statistics.

Mass region (GeV/c^2)	A_{FB} uncertainty
$50 < M_{ee} < 60$	0.0137
$60 < M_{ee} < 70$	0.0048
$70 < M_{ee} < 75$	0.0033
$75 < M_{ee} < 81$	0.0000
$81 < M_{ee} < 86.5$	0.0078
$86.5 < M_{ee} < 89.5$	0.0015
$89.5 < M_{ee} < 92$	0.0015
$92 < M_{ee} < 97$	0.0020
$97 < M_{ee} < 105$	0.0066
$105 < M_{ee} < 115$	0.0019
$115 < M_{ee} < 130$	0.0039
$130 < M_{ee} < 180$	0.0102
$180 < M_{ee} < 250$	0.0130
$250 < M_{ee} < 500$	0.0012
$500 < M_{ee} < 1000$	0.0012

Table 8.7: Systematic uncertainty due to QCD, QED and electroweak corrections.

The uncertainties for all mass bins are shown in Table 8.9.

Mass region(GeV/c^2)	CCCC(Shape/NOR)		CCEC(Shape/NOR)	
$50 < M_{ee} < 60$	0.0008	0.0000	0.0078	0.0001
$60 < M_{ee} < 70$	0.0002	0.0000	0.0004	0.0001
$70 < M_{ee} < 75$	0.0004	0.0000	0.0011	0.0001
$75 < M_{ee} < 81$	0.0002	0.0000	0.0007	0.0000
$81 < M_{ee} < 86.5$	0.0001	0.0000	0.0001	0.0000
$86.5 < M_{ee} < 89.5$	0.0000	0.0000	0.0001	0.0000
$89.5 < M_{ee} < 92$	0.0000	0.0000	0.0000	0.0000
$92 < M_{ee} < 97$	0.0000	0.0000	0.0001	0.0000
$97 < M_{ee} < 105$	0.0000	0.0000	0.0001	0.0002
$105 < M_{ee} < 115$	0.0000	0.0000	0.0007	0.0001
$115 < M_{ee} < 130$	0.0006	0.0000	0.0023	0.0002
$130 < M_{ee} < 180$	0.0005	0.0000	0.0076	0.0004
$180 < M_{ee} < 250$	0.0003	0.0000	0.0018	0.0003
$250 < M_{ee} < 500$	0.0005	0.0000	0.0091	0.0001
$500 < M_{ee} < 1000$	0.0003	0.0000	0.0054	0.0002

Table 8.8: CC-CC and CC-EC A_{FB} systematic uncertainty due to QCD background shape and normalization.

Mass region(GeV/c^2)	CCCC	CCEC
$50.0 < M_{ee} < 60.0$	0.0057	0.0184
$60.0 < M_{ee} < 70.0$	0.0074	0.0203
$70.0 < M_{ee} < 75.0$	0.0189	0.0159
$75.0 < M_{ee} < 81.0$	0.0073	0.0070
$81.0 < M_{ee} < 86.5$	0.0052	0.0031
$86.5 < M_{ee} < 89.5$	0.0039	0.0031
$89.5 < M_{ee} < 92.0$	0.0016	0.0015
$92.0 < M_{ee} < 97.0$	0.0023	0.0018
$97.0 < M_{ee} < 105.0$	0.0069	0.0049
$105.0 < M_{ee} < 115.0$	0.0125	0.0052
$115.0 < M_{ee} < 130.0$	0.0106	0.0055
$130.0 < M_{ee} < 180.0$	0.0019	0.0020
$180.0 < M_{ee} < 250.0$	0.0030	0.0036
$250.0 < M_{ee} < 500.0$	0.0014	0.0012
$500 < M_{ee} < 1000$	0.0031	0.0063

Table 8.9: CC-CC and CC-EC events AFB systematic uncertainty due to statistics of MC sample.

8.3.8 Systematic uncertainty from acceptance × efficiency corrections

To determine the systematic uncertainty due to acceptance and efficiency corrections, we use number of forward (N_F^{unfold}) and backward (N_B^{unfold}) events after detector res-

olution unfolding, the central values and the uncertainties for acceptance × efficiency can be found in Table. 7.1. The uncertainties for all mass bins are shown in Table 8.10.

Mass region(GeV/c^2)	CCCC	CCEC
$50 < M_{ee} < 60$	0.0074	0.0190
$60 < M_{ee} < 70$	0.0085	0.0147
$70 < M_{ee} < 75$	0.0107	0.0149
$75 < M_{ee} < 81$	0.0084	0.0098
$81 < M_{ee} < 86.5$	0.0056	0.0057
$86.5 < M_{ee} < 89.5$	0.0036	0.0035
$89.5 < M_{ee} < 92$	0.0018	0.0017
$92 < M_{ee} < 97$	0.0025	0.0024
$97 < M_{ee} < 105$	0.0059	0.0056
$105 < M_{ee} < 115$	0.0092	0.0093
$115 < M_{ee} < 130$	0.0103	0.0123
$130 < M_{ee} < 180$	0.0016	0.0029
$180 < M_{ee} < 250$	0.0034	0.0057
$250 < M_{ee} < 500$	0.0016	0.0030
$500 < M_{ee} < 1000$	0.0018	0.0034

Table 8.10: CC-CC and CC-EC events AFB systematic uncertainty due to acceptance and efficiency corrections.

8.3.9 Systematic uncertainty from charge misID

To determine the systematic uncertainty due to charge mis-identification of CC electrons, we use the charge misID rate and uncertainties of each mass bins in Table 7.3. Since the effect of charge misID is very small in CC-CC events, we only do charge misID unfolding on CC-EC events. The uncertainties for all mass bins are shown in Table 8.11.

8.3.10 Systematic uncertainty from the input A_{FB} distribution

This uncertainty comes from the bias of unfolding method due to the input A_{FB} distribution (Sect. 8.1). To estimate this uncertainty we use the measured $\sin^2\theta_W$, and use Geant MC samples with the input $\sin^2\theta_W$ equals to the measured $\sin^2\theta_W$ central value plus and minus 1σ (described in Sect. 9.3) to measure the response matrix and acc $\times$ eff corrections, and then unfold the raw data. The uncertainties for all mass bins are shown in Table 8.12.

8.3.11 Uncertainties distribution

The statistics and systematic uncertainties of CCCC and CCEC events are compared in Fig. 8.8.

Mass region(GeV/c^2)	CCEC
$50 < M_{ee} < 60$	0.0331
$60 < M_{ee} < 70$	0.0285
$70 < M_{ee} < 75$	0.0255
$75 < M_{ee} < 81$	0.0161
$81 < M_{ee} < 86.5$	0.0124
$86.5 < M_{ee} < 89.5$	0.0061
$89.5 < M_{ee} < 92$	0.0042
$92 < M_{ee} < 97$	0.0062
$97 < M_{ee} < 105$	0.0141
$105 < M_{ee} < 115$	0.0160
$115 < M_{ee} < 130$	0.0185
$130 < M_{ee} < 180$	0.0180
$180 < M_{ee} < 250$	0.0204
$250 < M_{ee} < 500$	0.0231
$500 < M_{ee} < 1000$	0.1784

Table 8.11: CC-EC events AFB systematic uncertainty due to charge mis-identification.

8.4 Comparison of A_{FB} between corrected data and PYTHIA predictions

The final A_{FB} distribution for data after all corrections applied (here we assume SM couplings) and PYTHIA prediction can be found in Fig. 8.9. The comparison plots

Mass region(GeV/c^2)	CCCC	CCEC
$50 < M_{ee} < 60$	0.0031	0.0024
$60 < M_{ee} < 70$	0.0008	0.0017
$70 < M_{ee} < 75$	0.0004	0.0016
$75 < M_{ee} < 81$	0.0036	0.0009
$81 < M_{ee} < 86.5$	0.0025	0.0006
$86.5 < M_{ee} < 89.5$	0.0030	0.0010
$89.5 < M_{ee} < 92$	0.0033	0.0009
$92 < M_{ee} < 97$	0.0021	0.0020
$97 < M_{ee} < 105$	0.0018	0.0011
$105 < M_{ee} < 115$	0.0010	0.0032
$115 < M_{ee} < 130$	0.0004	0.0004
$130 < M_{ee} < 180$	0.0009	0.0011
$180 < M_{ee} < 250$	0.0001	0.0001
$250 < M_{ee} < 500$	0.0001	0.0002
$500 < M_{ee} < 1000$	0.0009	0.0341

Table 8.12: CC-CC and CC-EC events AFB systematic uncertainty due to the input A_{FB} of the Geant MC sample used to derive the response matrix and acc $\times$ eff corrections.

for $50 < M_{ee} < 130$ GeV can be found in Fig. 8.10. The χ^2 value in the plots is calculated using the method described in Appendix C. And the discussion of EC electron with/without track-match cut is shown in Appendix D

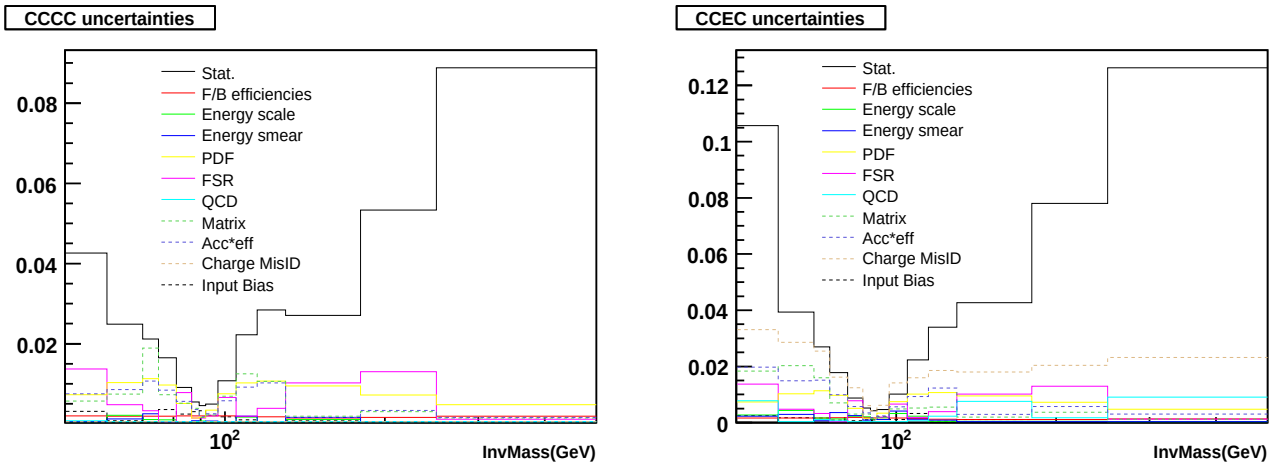

Figure 8.8: Comparison between statistics and all systematic uncertainties described in Chapter 10.

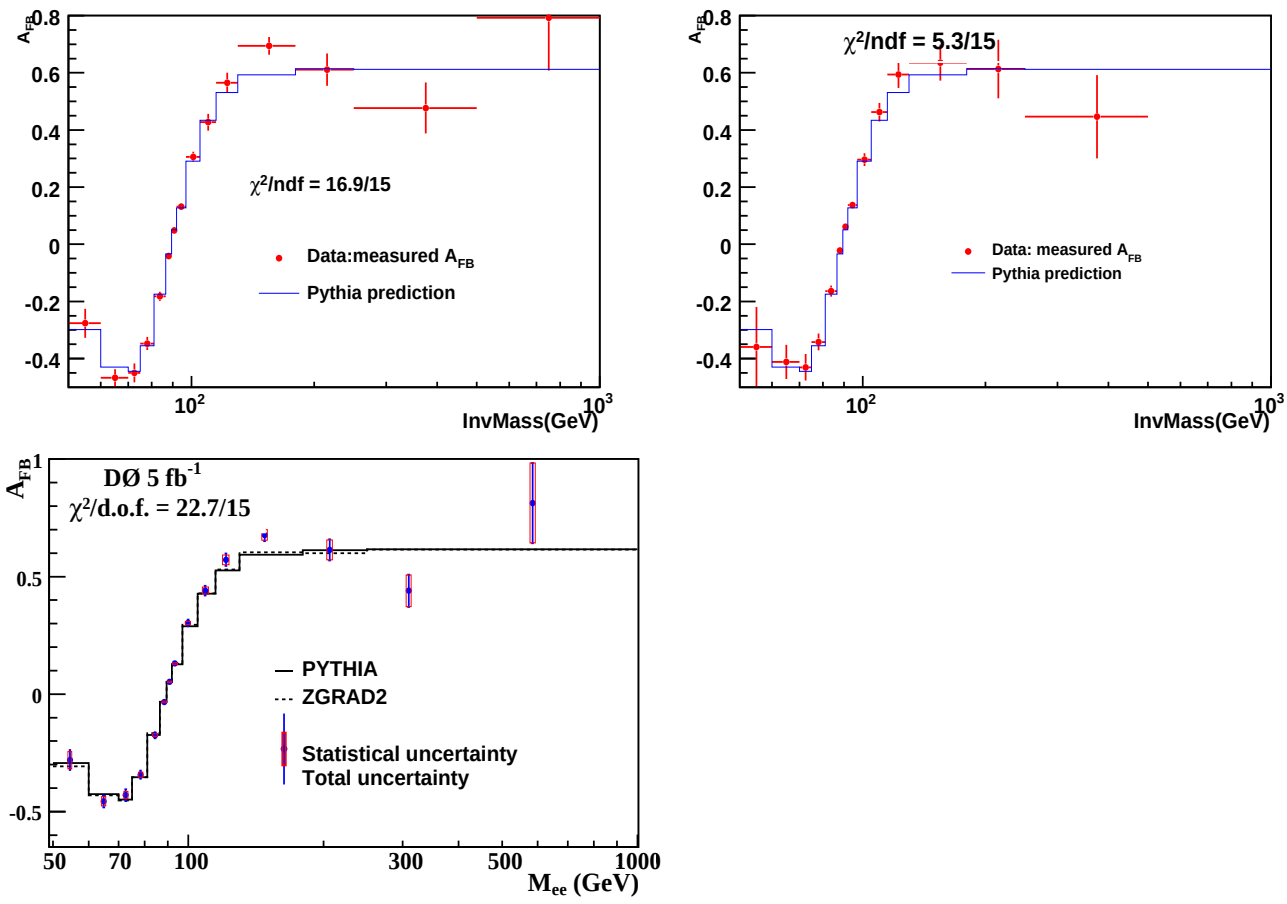

Figure 8.9: A_{FB} for data after all corrections and PYTHIA prediction for CCCC, CCEC and All events.

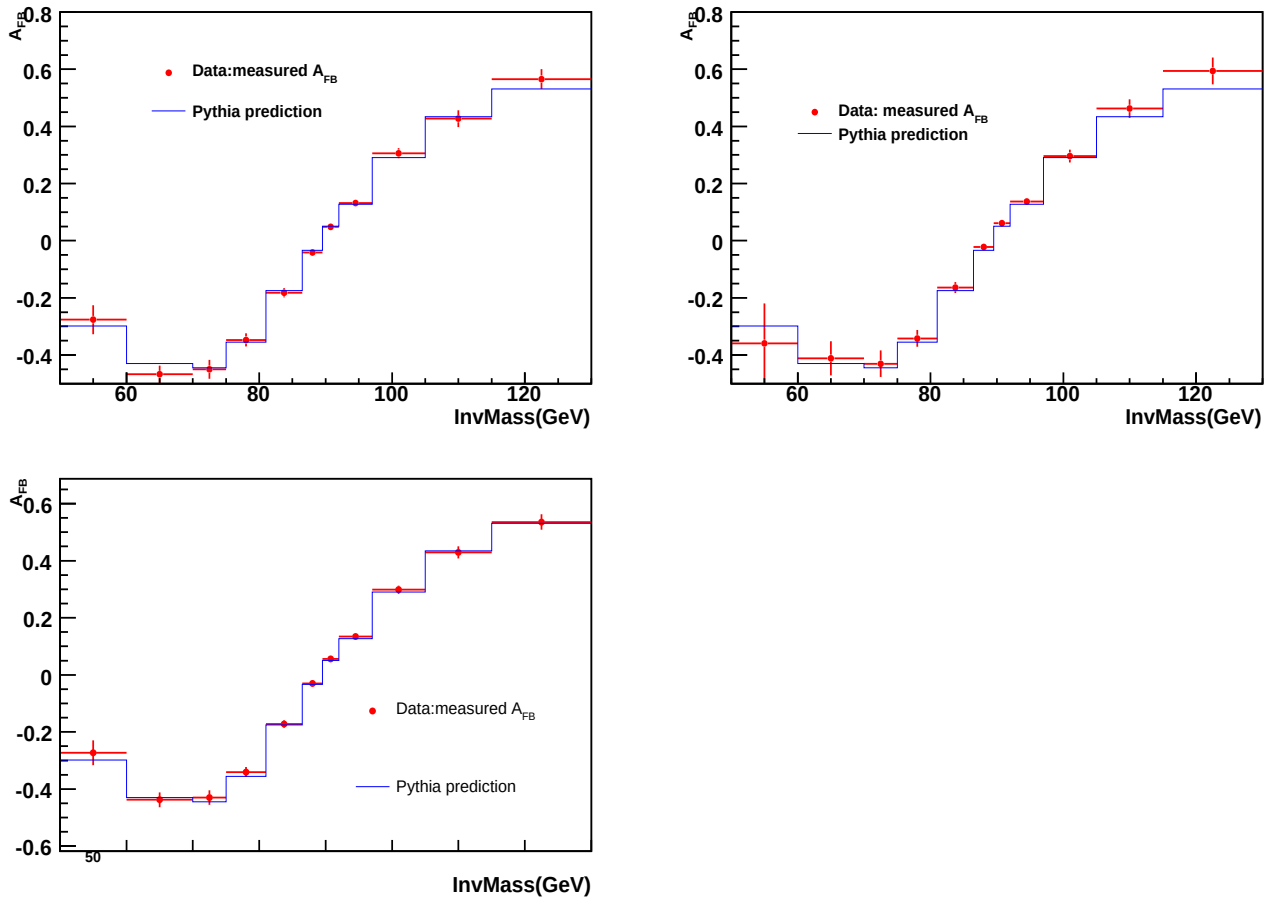

Figure 8.10: A_{FB} for data after all corrections and PYTHIA prediction for CCCC, CCEC and All in $50 < M < 130$ GeV.

8. FORWARD-BACKWARD CHARGE ASYMMETRY MEASUREMENT

Chapter 9

Weak Mixing angle measurement

9.1 Bin centering

The bin center is determined as the average value of M_{ee} for each mass bin using 20M PYTHIA events. The bin centers for all 14 bins are: 54.53, 64.86, 72.57, 78.30, 84.36, 88.40, 90.89, 93.39, 99.90, 109.10, 121.30, 147.90, 206.40, 310.50.

9.2 Reweighting GEANT MC samples to different input $\sin^2\theta_W$

The default GEANT MC files were generated with $\sin^2\theta_W = 0.232$, while we need to have GEANT MC files generated with other values of $\sin^2\theta_W$. We can realize this by reweighting the generator-level $M_{Z/\gamma^*} - \cos\theta^*$ distribution. To demonstrate the method works, we generate 5 M PYTHIA events with two different values of $\sin^2\theta_W$: 0.2315 and 0.2375, measure the ratio of $M_{Z/\gamma^*} - \cos\theta^*$ between the two samples, and then reweight

the sample with 0.2375 back to 0.2315. Fig. 9.1 and Fig. 9.2 show the electron and positron physics η distributions before and after reweighting (Blue for $\sin^2\theta_W = 0.2315$ and Red for $\sin^2\theta_W = 0.2375$). Good agreement is observed for these two samples after reweighting. This demonstrates that by doing 2D reweighting $M_{Z/\gamma^*} - \cos\theta^*$, we can get have GEANT MC samples for any arbitrary value of $\sin^2\theta_W$ from a given GEANT MC events generated at just one $\sin^2\theta_W$.

We generate 40 PYTHIA samples with $\sin^2\theta_W$ from 0.22552 to 0.23722 with step size 0.0003, and each sample contains 5 M events. The 2D $M_{Z/\gamma^*} - \cos\theta^*$ reweighting factors between samples with a given $\sin^2\theta_W$ and the sample with the SM $\sin^2\theta_W$ are derived. By reweighting the PYTHIA generator-level distribution, we can get 40 GEANT MC samples with $\sin^2\theta_W$ from 0.22552 to 0.23722.

9.3 Extraction of $\sin^2\theta_W$ using PYTHIA

The A_{FB} distribution is sensitive to $\sin^2\theta_W$; we compare the raw A_{FB} from real data with the predicted "measured" A_{FB} from GEANT MC samples with different input $\sin^2\theta_W$ to extract the best value of $\sin^2\theta_W$. By using raw A_{FB} instead of unfolded A_{FB} distribution, we eliminate the uncertainties due to the unfolding method and can extract $\sin^2\theta_W$ with smaller uncertainty. The comparisons between data raw A_{FB} and MC raw A_{FB} are shown in Fig. 9.3 for CCCC, CCEC and both CCCC and CCEC.

Using both CCCC and CCEC events, we measure $\sin^2\theta_W = 0.2306 \pm 0.0009$ (stat)

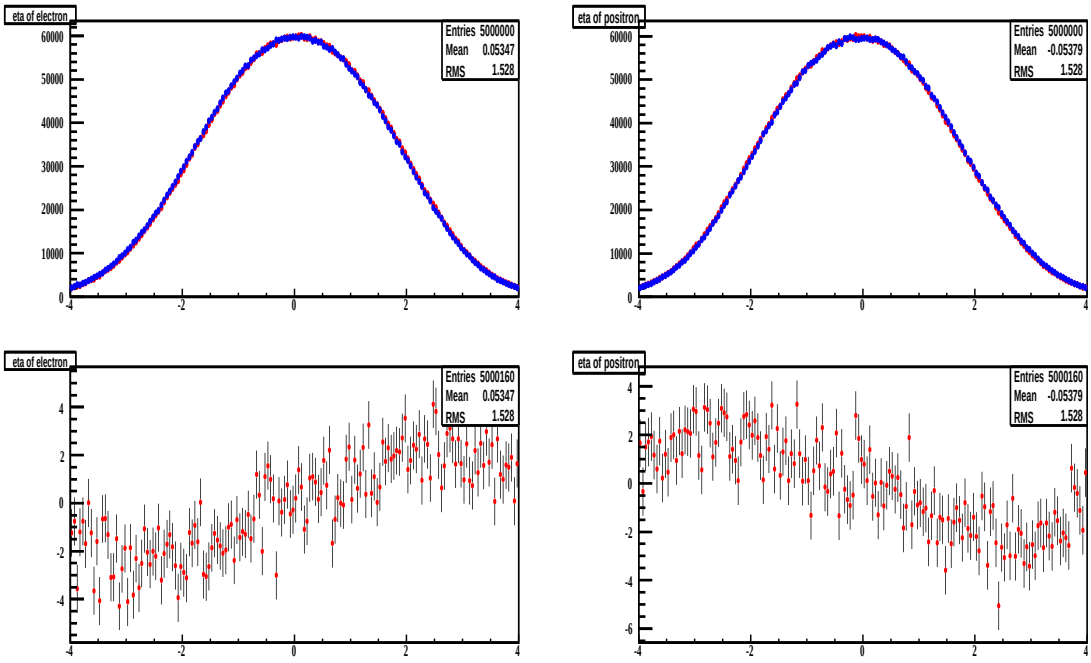

Figure 9.1: Electron and positron physics η distribution before $M_{Z/\gamma^*} - \cos\theta^*$ reweight, Blue for $\sin^2\theta_W = 0.2315$ and Red for $\sin^2\theta_W = 0.2375$. The bottom plot is χ distribution between the two histograms.

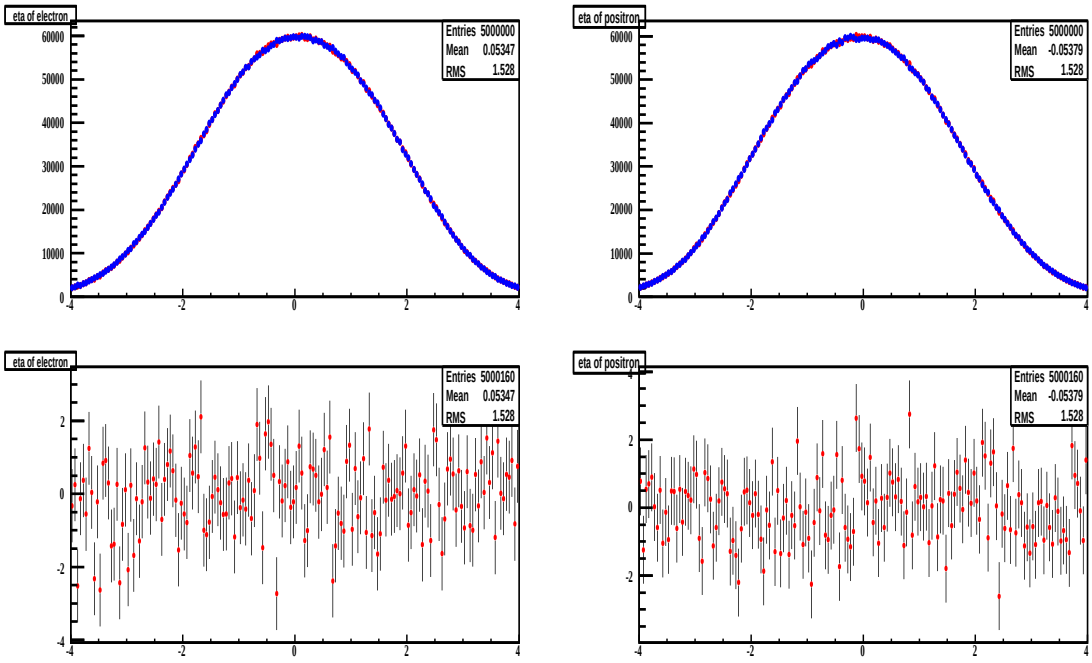

Figure 9.2: Electron and positron physics η distribution before $M_{Z/\gamma^*} - \cos\theta^*$ reweight, Blue for $\sin^2\theta_W = 0.2315$ and Red for $\sin^2\theta_W = 0.2375$. The bottom plot is χ distribution between the two histograms.

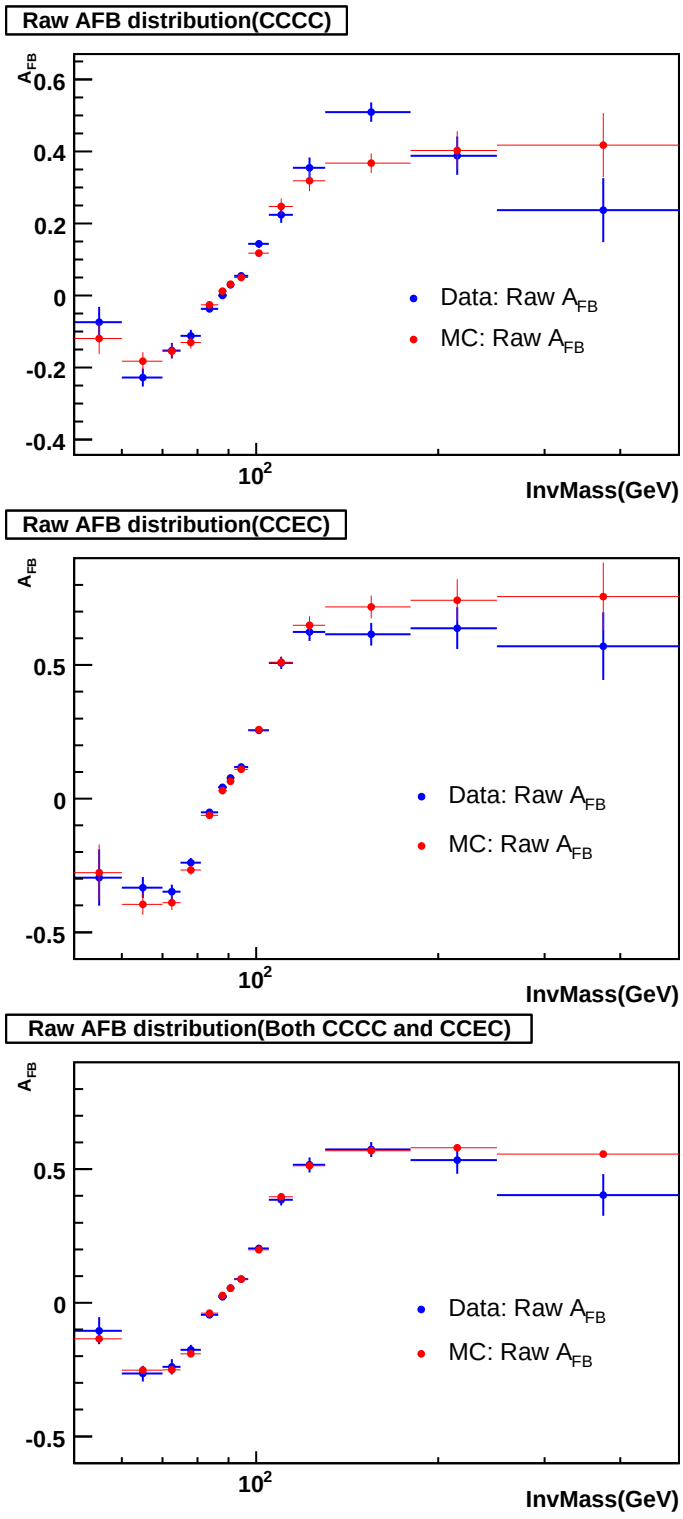

Figure 9.3: Comparisons plots between data raw A_{FB} and MC raw A_{FB}.

with $\chi^2/dof = 9.5/14$ for $50 < M < 500$ GeV. Fig. 9.4 shows the χ^2 between the raw data A_{FB} and the predicted "measured" A_{FB} distributions vs the input $\sin^2\theta_W$. There are several sources of systematic uncertainty due to PDF, EM scale and resolution, backgrounds, electron-photon merging cone size, QCD corrections and QED corrections.

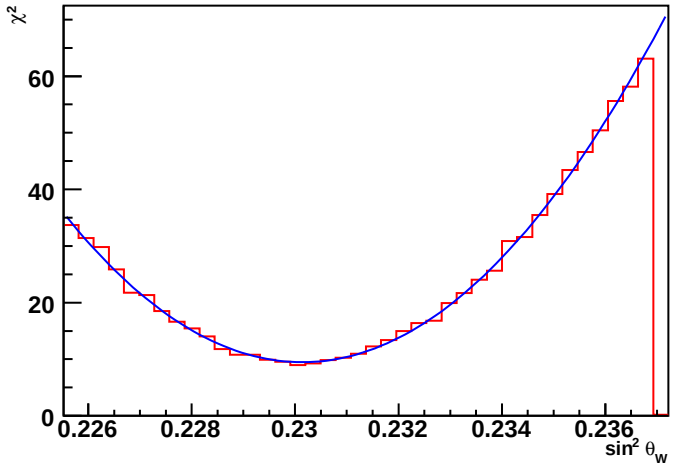

Figure 9.4: χ^2 between the raw A_{FB} from real data and the predicted "measured" A_{FB} from GEANT MC as a function of the input $\sin^2\theta_W$ in the GEANT MC sample. The black line is a second-order polynomial fit.

The vector and the axial couplings of the u and d quarks to the Z boson are different, the forward-backward asymmetry is expected to depend on the ratio of the u to d quark PDF's. Thus, the choice of the PDF's will affect the predicted "measured" A_{FB} distributions. The PDF uncertainty is calculated using a set of 40 PDFs provided by the CTEQ collaboration [56]. To estimate the systematic uncertainty on the extracted $\sin^2\theta_W$, we reweight the GEANT MC samples to get the predicted "measured" A_{FB} distributions and extract $\sin^2\theta_W$ for each PDF set. The PDF uncertainty is calculated

using the quadrature sum of all eigenvector contributions:

$$\Delta \sin^2\theta_W = \sqrt{\sum_{i=1}^{20} \left[(\sin^2\theta_W)_i^{\pm} - (\sin^2\theta_W)_0\right]^2} \tag{9.1}$$

where $(\sin^2\theta_W)_i$ represents the extracted $\sin^2\theta_W$ for the shifts in eigenvector i. The systematic uncertainty on the extracted $\sin^2\theta_W$ due to PDF is measured to be 0.00046 for positive and 0.00048 for negative PDF sets using the above formula. We use 0.00048 as the final uncertainty. Fig. 9.5 shows the difference between the extracted $\sin^2\theta_W$ for each PDF set and the central PDF set.

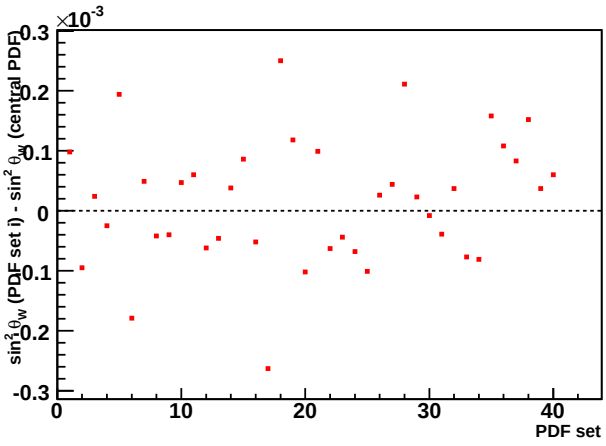

Figure 9.5: The difference between the extracted $\sin^2\theta_W$ from each PDF set and the central PDF set for 40 CTEQ6.1M PDF sets.

Using different energy scale and smearing in GEANT MC will also change the predicted "measured" A_{FB} distribution and thus affect the extracted $\sin^2\theta_W$. The systematic uncertainty on $\sin^2\theta_W$ is 0.000178 due to uncertainty on CC energy scale, 0.000045 due to uncertainty on CC energy smearing, 0.000215 due to uncertainty on EC energy scale and 0.000044 due to uncertainty on EC energy smearing. The overall uncertainty due to energy smearing parameters is 0.000286.

Another source of systematic uncertainty is the subtraction of backgrounds. Due to the very tight selection cuts on the electrons, the backgrounds are pretty small ($\sim$ 0.88% for $70 < M < 130$ GeV). The uncertainties described in Sect. 6.2 and Sect. 6.3 are included for the final systematic uncertainty calculation, the systematic uncertainty on the extracted $\sin^2\theta_W$ due to the backgrounds is found to be 0.00001.

We also considered the uncertainty from full MC samples. To estimate this uncertainty, we split our MC samples into 10 smaller ones, reweighted those 10 smaller samples with 40 $\sin^2\theta_W$ sets, then extracted $\sin^2\theta_W$ for CCCC/CCEC events and both of them. With the extracted $\sin^2\theta_W$ values, we fitted them with Gaus, take $RMS/\sqrt{10}$ as uncertainty, 0.0006 is found for CCCC events, 0.0002 for CCEC events and 0.0002 for both CCCC and CCEC events.

Since only events near the Z-pole is sensitive to $\sin^2\theta_W$, we also measure $\sin^2\theta_W = 0.23052 \pm 0.0009$ (Stat.) using events with $70 < M < 130$ GeV and $\sin^2\theta_W = 0.23063 \pm 0.0009$ (Stat.) using events with $81 < M < 105$ GeV.

We also measure $\sin^2\theta_W = 0.2319 \pm 0.0019$ (Stat.) using CCCC events(0.06 sigma from PYTHIA default) and $\sin^2\theta_W = 0.2293 \pm 0.0010$ (Stat.)(2.6 sigma from PYTHIA default) using CCEC events. Even though we have similar number of CCCC and CCEC events, the A_{FB} distribution is more sensitive to $\sin^2\theta_W$ for events in CCEC than events in CCCC.

In Ref. [61], the authors estimated the statistical and systematic uncertainties expected in Run II using 10 fb^{-1} data. The studies were done based on the performance expected for the Run II DØ detector, and is thus very useful to compare the predictions with the results based on data collected by the real detector. Based on their studies, the

estimated DØ precision on A_{FB} achievable with 10 fb^{-1} integrated luminosity in electron channel together with uncertainties from this measurement are shown in Tab. 9.1. Based on the statistical uncertainty from the 4 fb^{-1} measurement, we expect to have a statistical uncertainty of 0.000567 for 10 fb^{-1} of data, which is close to the statistical uncertainty (0.0005) in the pre-Run II studies.

Error source	Estimated $\Delta\sin^2\theta_W$ using 10 fb^{-1} simulated events	Measured $\Delta\sin^2\theta_W$ using 5 fb^{-1} data
Statistical	0.0005	0.000897
Systematics	0.0001	0.00056
PDF	0.00007	0.00048
EM scale/resolution	0.00007	0.00029
Backgrounds	0.00005	0.00001
Total uncertainty	0.0005	0.00106

Table 9.1: Comparison of **estimated uncertainties** on $\sin^2\theta_W$ for an integrated luminosity of **10 fb^{-1}** taken from the study done in Ref. [61] and the **measured uncertainties** using **5.0 fb^{-1}** of real data. Both studies are done in electron channel using CCCC and CCEC events. The statistical uncertainties are consistent with each other taken into account the difference of the integrated luminosity. The PDF uncertainty in the pre-Run II studies was estimated before the appearance of the CTEQ6.1M error PDF sets.

9.4 Correction of the extracted $\sin^2\theta_W$ using ZGRAD

The $\sin^2\theta_W$ described in the above section is obtained by comparing the data raw A_{FB} distribution with the predictions of "measured" A_{FB} distribution using PYTHIA GEANT MC samples generated with different input $\sin^2\theta_W$. And we need to make the correction for the extracted $\sin^2\theta_W$ due to high-order QCD, QED and electroweak corrections.

We first generated about 5M ZGRAD events with input $\sin^2\theta_W = 0.2317$ and get the generator-level A_{FB} distribution, then we compare with the A_{FB} distribution from ZGRAD with PYTHIA $\sin^2\theta_W$ templates with $\sin^2\theta_W$ from 0.22552 to 0.23722. The best agreement is PYTHIA sample with $\sin^2\theta_W = 0.2312$. We correct the final PYTHIA-extracted $\sin^2\theta_W$ by $0.2317 - 0.2312 = 0.0005$ to include higher-order effects.

9.5 Final extracted $\sin^2\theta_W$ value

After using the correction from ZGRAD due to higher-order QCD, QED and electroweak corrections, the final extracted $\sin^2\theta_W$ is: $\sin^2\theta_W = 0.2311 \pm 0.0009(\text{Stat.}) \pm 0.0006(\text{Syst.}) = 0.2311 \pm 0.0010$.

The uncertainty of this measurement is better than the uncertainty from the NuTeV Collaboration ($\sin^2\theta_W = 0.22773 \pm 0.0016$) [22] and also that of the inclusive hadronic charge asymmetry (Q_{FB}^{had}) measurements at LEP ($\sin^2\theta_W = 0.2324 \pm 0.0012$). Our uncertainty is still about seven times worse than the current world average uncertainty $\sin^2\theta_W = 0.23152 \pm 0.00014$ [4], but our measurement is sensitive to the couplings of light quarks to Z bosons, which can not be easily probed at the LEP experiments.

The comparison plot between DØ $5fb^{-1}$ $\sin^2\theta_W$ with other experiments is shown in Fig. 9.6

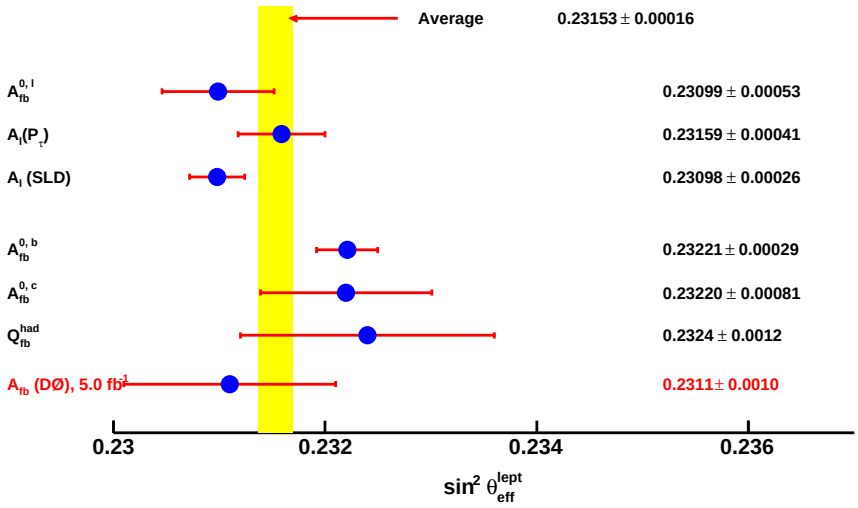

Figure 9.6: $\sin^2\theta_W$ comparison between different experiments.

Chapter 10

Z to light $quark$ couplings measurement

10.1 Extraction method

The LEP/SLD collaborations have measured A_{FB}^{eff} using processes that only depend on Z-lepton couplings and processes that also depend on Z-quark couplings [21]. The A_{FB}^{eff} results from processes that only depend on Z-lepton couplings seem to have lower values compared with the results from processes that also depend on Z-quark couplings. For LEP/SLD experiments, the Z-b and Z-c quark couplings can be measured well, while the Z-light quark couplings were extracted assuming SM relations. The precision from direct measurements of Z-light quark couplings have poor precision compared with direct measurements of Z-heavy quark couplings.

The Drell-Yan process ($u\bar{u}(d\bar{d}) \rightarrow Z/\gamma^* \rightarrow ee$) at the Tevatron is directly related with $Z-u$, $Z-d$ and $Z-e$ couplings. By comparing the **RAW** A_{FB} distribution with

predictions with different Z-u and Z-d couplings in the Z ploe region (70 - 130 GeV), we can determine these couplings. When we change the coupling values to generate the grids file, it will change the coupling values for all up-(or down-) type quarks.

10.1.1 RESBOS modifications for the measurement of Z-light quark couplings

There are two files we need to modify in RESBOS: resbos.f and resbosm.f. In resbosm.f, there are the left and right handed couplings of Z to the up- and down-types quarks and also the charged leptons, we need to translate the vector and axial vector couplings into the left and right couplings. In resbos.f, we add four input parameters to allow us to change the couplings (g_V^u, g_A^u, g_V^d and g_A^d), and another four parameters to control those studies.

With the modified RESBOS, we generate 16×16 $g_V^u - g_A^u$ grids with a step size of 0.010 for g_V^u and a step size of 0.024 for g_A^u when we study Z to up-type quark couplings. We generate 16×16 $g_V^d - g_A^d$ grids with a step size of 0.024 for g_V^d and a step size of 0.034 for g_A^d when we study Z to down-type quark couplings. 15M RESBOS events are generated for each point.

For the couplings measurement, we compare unfolded A_{FB} distribution with predicted unfolded A_FB templates using different values of $Z-u$ and $Z-d$ couplings. The templates are generated using reweighted PYTHIA events, the generator-level PYTHIA $M - \cos\theta^*$ distributions are reweighted to agree with the generatorl-level RESBOS distributions, which are generated with different couplings. The purpose of this reweighting is to make sure we have the higher order QED and electroweak corrections included

for the Z/γ^* boson.

10.2 Extraction of couplings

10.2.1 Couplings of Z to u/d quark

The measured $Z-u$ and $Z-d$ coupling results are shown in Fig. 10.1 using the combined Run IIa and Run IIb Z/γ^* data in Z mass peak region ($70 < M_{ee} < 130$ GeV). The best fit results are shown in Tab. 10.1. And the correlation matrices for Z to u/d quark couplings are shown in Tab. 10.2 and Tab. 10.3. The systematic uncertainties due to various sources such as energy scale, smearing, efficiency scale factors, backgrounds and PDFs are also shown on these plots.

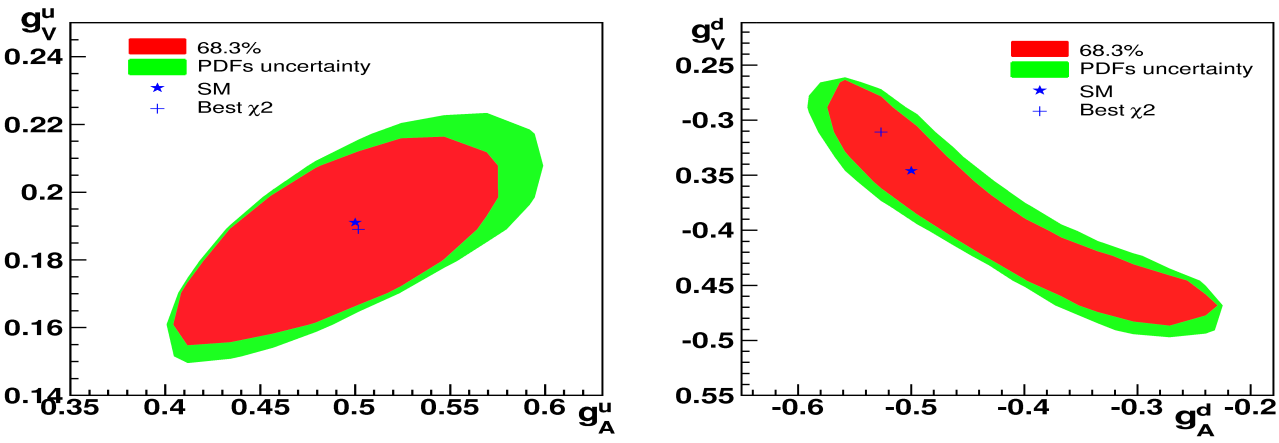

Figure 10.1: Z to u/d quark couplings results. The blue star is SM value, the red region is the measured 68.3% confidence level contour due to statistical uncertainty, the green region is the systematic uncertainty, the blue plus is the point with best χ^2.

The comparison plots for $g_A^d - g_V^d$ and $g_A^u - g_V^u$ results from different experimeters are shown in Fig. 10.2

	g_A^u	g_V^u	g_A^d	g_V^d
SM	0.500	0.1913	-0.500	-0.3457
measured	0.502 ± 0.037	0.189 ± 0.015	-0.527 ± 0.033	-0.311 ± 0.027

Table 10.1: The measured coupling values compared with SM predictions.

Parameter	Value	Correlations	
		g_A^u	g_V^u
g_A^u	0.502 ± 0.037	1.00	
g_V^u	0.189 ± 0.015	0.675	1.00

Table 10.2: Correlation matrix for the Z to u quark couplings.

Parameter	Value	Correlations	
		g_A^d	g_V^d
g_A^d	-0.527 ± 0.033	1.00	
g_V^d	-0.311 ± 0.027	-0.926	1.00

Table 10.3: Correlation matrix for the Z to d quark couplings.

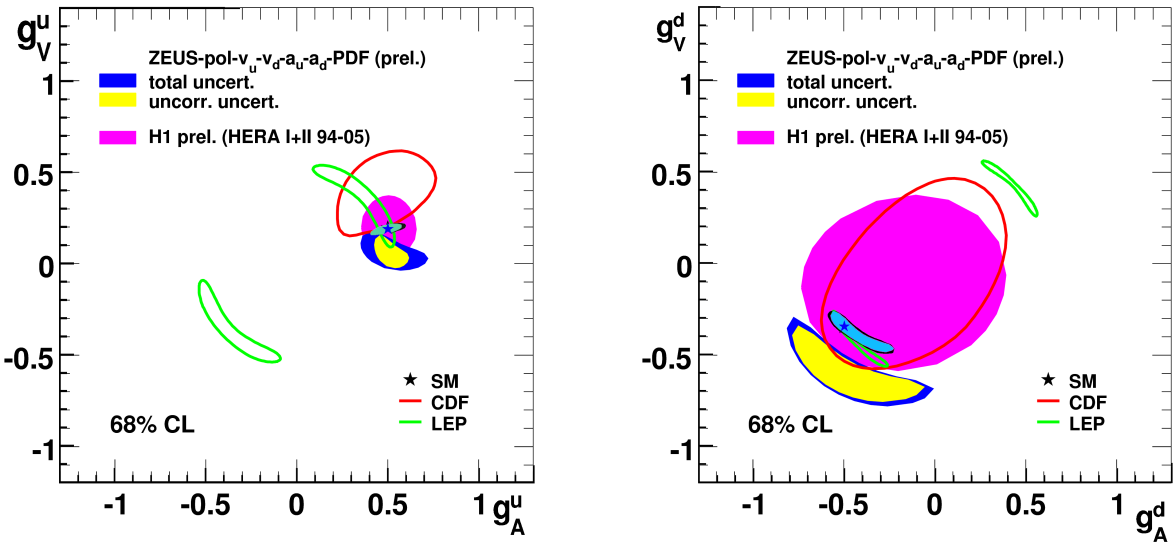

Figure 10.2: Z to u/d quark couplings results from DØ , CDF, ZEUS, H1 and LEP.

Chapter 11

Differential cross section measurement

11.1 Introduction of differential cross section

The differential cross section is calculated by correcting the background-subtracted signal in each Mass bins by the acceptance×efficiency, unfolding correction and integrated luminosity:

$$\frac{d\sigma}{dM} = \frac{N - B}{\varepsilon \times \beta \times L \times \Delta M}$$

where :

- N = number of observed events in bin i
- B = number of estimated background in bin i (incluing SM and QCD background)
- ε = total event selection efficiencies in each mass bins

- β = unfolding correction factor for acceptance, detector resolution in each mass bins

- L = integrated luminosity

- ΔM = bin width of each bins

11.2 Theoretical prediction

With PYTHIA generator and mass depended k-factor, the prediction is shown in Fig. 11.1

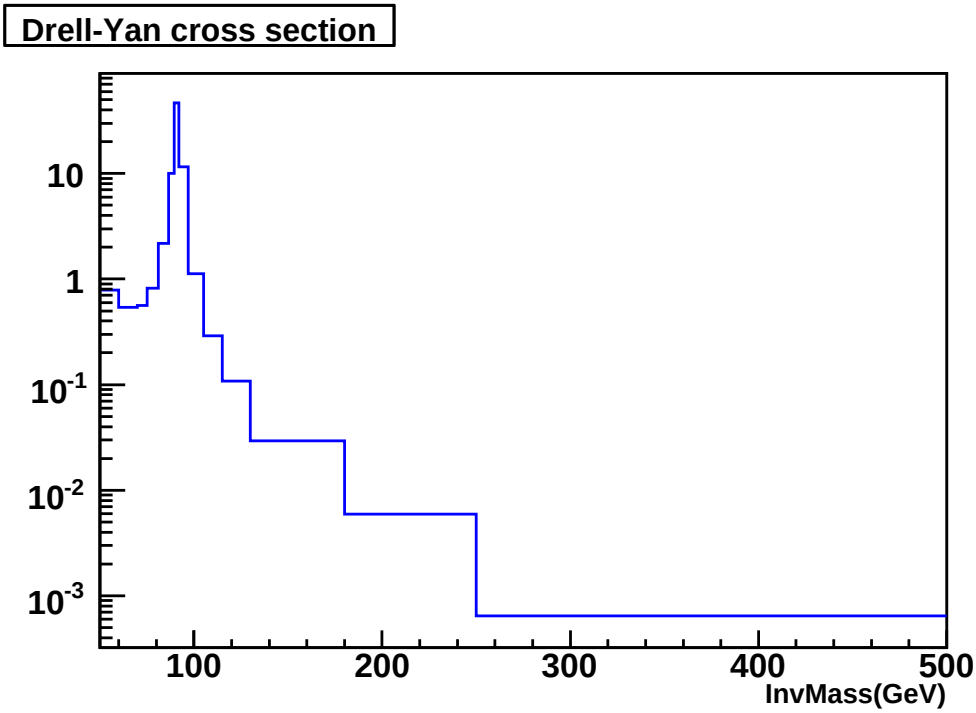

Figure 11.1: PYTHIA prediction(with k-factor) differential cross section($d\sigma/dM$).

11.3 Unfolding

In order to get the $\frac{d\sigma}{dM}$ distribution, we measured the $\varepsilon \times \beta$ from full MC, which are shown in Fig. 11.2 and Tab. 11.1 and unfold the raw InvMass distribution into the generator level one. The $\frac{1}{\sigma} \times \frac{d\sigma}{dM}$ for CCCC, CCEC and CCCC/CCEC are shown in Fig. 11.3.

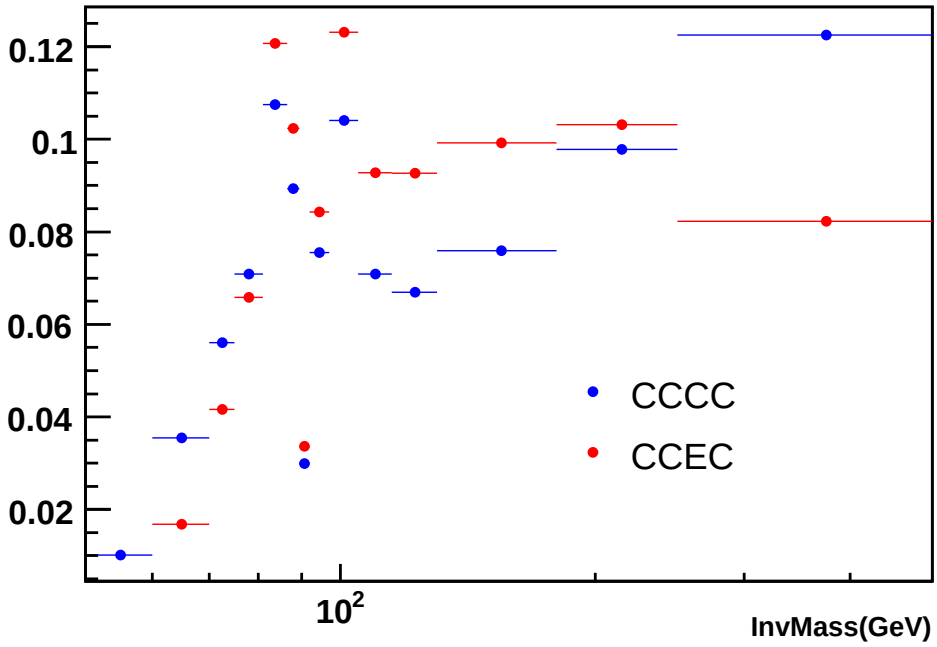

Figure 11.2: $\varepsilon \times \beta$ distribution for CCCC and CCEC events.

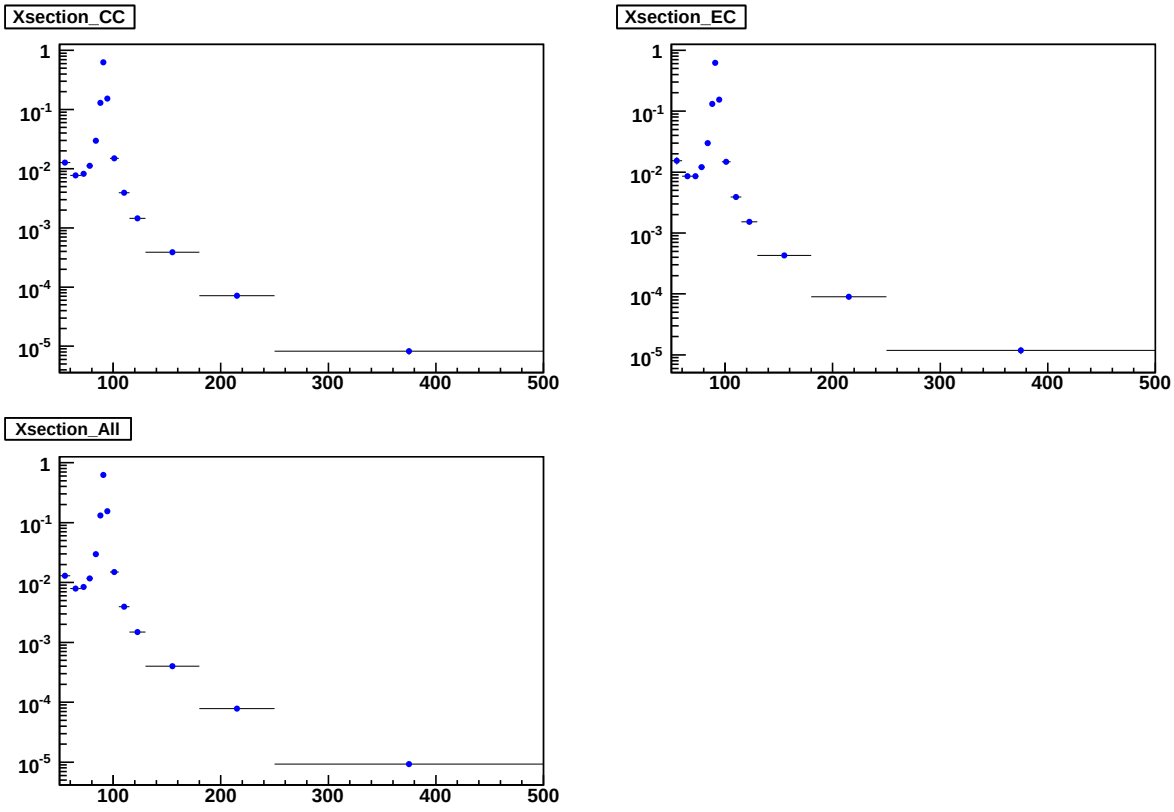

Figure 11.3: Measured normalized differential cross section($\frac{1}{\sigma} \times \frac{d\sigma}{dM}$) for CCCC, CCEC and both CCCC and CCEC events.

Mass Range (GeV)	CC-CC	CC-EC
50.0< M_{ee} < 60.0	0.010± 0.000	0.001± 0.000
60.0< M_{ee} < 70.0	0.036± 0.000	0.017± 0.000
70.0< M_{ee} < 75.0	0.056± 0.001	0.042± 0.000
75.0< M_{ee} < 81.0	0.071± 0.000	0.066± 0.000
81.0< M_{ee} < 86.5	0.107± 0.000	0.121± 0.000
86.5< M_{ee} < 89.5	0.089± 0.000	0.102± 0.000
89.5< M_{ee} < 92.0	0.030± 0.000	0.034± 0.000
92.0< M_{ee} < 97.0	0.075± 0.000	0.084± 0.000
97.0< M_{ee} < 105.0	0.104± 0.000	0.123± 0.000
105.0< M_{ee} < 115.0	0.071± 0.001	0.093± 0.001
115.0< M_{ee} < 130.0	0.067± 0.001	0.093± 0.001
130.0< M_{ee} < 180.0	0.076± 0.000	0.099± 0.000
180.0< M_{ee} < 250.0	0.098± 0.000	0.103± 0.000
250.0< M_{ee} < 500.0	0.123± 0.000	0.082± 0.000

Table 11.1: $\varepsilon \times \beta$ in different mass bins for CC-CC and CC-EC respectively.

11.4 Uncertainties

In this section, we mainly focus on the systematic uncertainties and the statistical uncertainty after error correlations correction.

11.4.1 Systematic uncertainty from efficiency scale factors

To get the electron selection cuts uncertainties, we fit each scale factor with a straight line to get errors of scale factor, then shift the scale factor in two directions by $\pm\sigma$. We choose the larger one as the EMID uncertainties. The uncertainties from Pre Selection, EMID and TrkMatch are shown in Tab. 11.2, Tab. 11.3 and Tab. 11.4.

11.4.2 Systematic uncertainty from energy scale and energy smear

The systematic uncertainties due to electron energy scale is shown in Tab. 11.5, and the uncertainties due to energy smear is shown in Tab. 11.6. Since EC energy scale/smear parameters will not affect the CC-CC events, the corresponding columns are all 0s.

Currently the modeling we used to describe the electron energy is a linear equation:

$$E = \alpha E_0$$

but there is a potential possibility, the electron energy response is non-linearity, which will not has no effect in low mass region, but will have a visible effect in the high mass region. So we used a non-linear equation to describe electron energy:

$$E = \alpha E_0 + \gamma(E_0 - 45)^2$$

More details of α and γ parameters tuning are shown in Appendix E. And we take the deviations between linearity and non-linearity modeling as uncertainty in each mass bins, which are shown in Tab. 11.7

Mass	CCCC(CC/EC)		CCEC(CC/EC)	
$50.0 < M_{ee} < 60.0$	0.0014	0.0000	0.0009	0.0018
$60.0 < M_{ee} < 70.0$	0.0008	0.0000	0.0005	0.0010
$70.0 < M_{ee} < 75.0$	0.0009	0.0000	0.0005	0.0010
$75.0 < M_{ee} < 81.0$	0.0012	0.0000	0.0007	0.0014
$81.0 < M_{ee} < 86.5$	0.0032	0.0000	0.0017	0.0035
$86.5 < M_{ee} < 89.5$	0.0143	0.0000	0.0073	0.0156
$89.5 < M_{ee} < 92.0$	0.0689	0.0000	0.0342	0.0732
$92.0 < M_{ee} < 97.0$	0.0168	0.0000	0.0085	0.0183
$97.0 < M_{ee} < 105.0$	0.0016	0.0000	0.0008	0.0017
$105.0 < M_{ee} < 115.0$	0.0004	0.0000	0.0002	0.0005
$115.0 < M_{ee} < 130.0$	0.0002	0.0000	0.0001	0.0002
$130.0 < M_{ee} < 180.0$	0.0000	0.0000	0.0000	0.0001
$180.0 < M_{ee} < 250.0$	0.0000	0.0000	0.0000	0.0000
$250.0 < M_{ee} < 500.0$	0.0000	0.0000	0.0000	0.0000

Table 11.2: CCCC and CCEC events differential cross section Uncertainties due to CC or EC PreSelection .The systematic shift is tested in two directions($+1sigma$ and $-1sigma$ of the each variables, and we choose the larger one.)

11.4.3 Systematic uncertainty from PDF

The systematic uncertainty due to PDF is estimated by reweighting the central PDF to 40 CTEQ6.1 error PDF sets, and the PDF uncertainty is calculated using the pre-

Mass	CCCC(CC/EC)		CCEC(CC/EC)	
$50.0 < M_{ee} < 60.0$	0.0026	0.0000	0.0016	0.0035
$60.0 < M_{ee} < 70.0$	0.0016	0.0000	0.0009	0.0019
$70.0 < M_{ee} < 75.0$	0.0017	0.0000	0.0009	0.0019
$75.0 < M_{ee} < 81.0$	0.0023	0.0000	0.0012	0.0027
$81.0 < M_{ee} < 86.5$	0.0060	0.0000	0.0031	0.0067
$86.5 < M_{ee} < 89.5$	0.0266	0.0000	0.0136	0.0298
$89.5 < M_{ee} < 92.0$	0.1281	0.0000	0.0636	0.1392
$92.0 < M_{ee} < 97.0$	0.0313	0.0000	0.0159	0.0347
$97.0 < M_{ee} < 105.0$	0.0031	0.0000	0.0015	0.0033
$105.0 < M_{ee} < 115.0$	0.0008	0.0000	0.0004	0.0009
$115.0 < M_{ee} < 130.0$	0.0003	0.0000	0.0002	0.0003
$130.0 < M_{ee} < 180.0$	0.0001	0.0000	0.0000	0.0001
$180.0 < M_{ee} < 250.0$	0.0000	0.0000	0.0000	0.0000
$250.0 < M_{ee} < 500.0$	0.0000	0.0000	0.0000	0.0000

Table 11.3: CCCC and CCEC events differential cross section Uncertainties due to CC or EC EMIDSelection .The systematic shift is tested in two directions($+1sigma$ and $-1sigma$ of the each variables, and we choose the larger one.)

scription suggested by CTEQ group:

$$\Delta B^{\pm} = \sqrt{\sum_{i=1}^{20} (B_i^{\pm} - B_0)^2} \tag{11.1}$$

Mass	CCCC	CCEC(CC)
$50.0 < M_{ee} < 60.0$	0.0039	0.0023
$60.0 < M_{ee} < 70.0$	0.0023	0.0013
$70.0 < M_{ee} < 75.0$	0.0025	0.0013
$75.0 < M_{ee} < 81.0$	0.0034	0.0018
$81.0 < M_{ee} < 86.5$	0.0090	0.0046
$86.5 < M_{ee} < 89.5$	0.0396	0.0202
$89.5 < M_{ee} < 92.0$	0.1907	0.0947
$92.0 < M_{ee} < 97.0$	0.0465	0.0236
$97.0 < M_{ee} < 105.0$	0.0046	0.0023
$105.0 < M_{ee} < 115.0$	0.0012	0.0006
$115.0 < M_{ee} < 130.0$	0.0004	0.0002
$130.0 < M_{ee} < 180.0$	0.0001	0.0001
$180.0 < M_{ee} < 250.0$	0.0000	0.0000
$250.0 < M_{ee} < 500.0$	0.0000	0.0000

Table 11.4: CCCC and CCEC events differential cross section Uncertainties due to CC or EC TrkMatchSelection .The systematic shift is tested in two directions($+1sigma$ and $-1sigma$ of the each variables, and we choose the larger one.)

where $B_i^{\pm}$ is the differential cross section measured for PDF error set i and B_0 is the asymmetry for the central PDF set. This will give asymmetric errors and we decided to use the maximum of positive and negative uncertainties as the final uncertainty. The uncertainty for each bin is listed in Tab. 11.8.

Mass	CCCC(CC/EC)		CCEC(CC/EC)	
$50.0 < M_{ee} < 60.0$	0.0068	0.0000	0.0057	0.0112
$60.0 < M_{ee} < 70.0$	0.0047	0.0000	0.0012	0.0021
$70.0 < M_{ee} < 75.0$	0.0012	0.0000	0.0013	0.0034
$75.0 < M_{ee} < 81.0$	0.0104	0.0000	0.0053	0.0086
$81.0 < M_{ee} < 86.5$	0.0661	0.0000	0.0308	0.0514
$86.5 < M_{ee} < 89.5$	0.2164	0.0000	0.1143	0.1884
$89.5 < M_{ee} < 92.0$	0.2259	0.0000	0.0396	0.0769
$92.0 < M_{ee} < 97.0$	0.2368	0.0000	0.1287	0.2165
$97.0 < M_{ee} < 105.0$	0.0357	0.0000	0.0159	0.0272
$105.0 < M_{ee} < 115.0$	0.0029	0.0000	0.0011	0.0025
$115.0 < M_{ee} < 130.0$	0.0010	0.0000	0.0008	0.0010
$130.0 < M_{ee} < 180.0$	0.0000	0.0000	0.0000	0.0000
$180.0 < M_{ee} < 250.0$	0.0000	0.0000	0.0000	0.0000
$250.0 < M_{ee} < 500.0$	0.0000	0.0000	0.0000	0.0000

Table 11.5: CCCC and CCEC events differential cross section uncertainties due to CC or EC electron energy scale. The systematic shift is tested in two directions($+1\sigma$ and -1σ of the each variables, and we choose the larger one.)

11.4.4 Systematic uncertainty from FSR

To estimate the uncertainties from Final State Radiation(FSR), we use the method described in AFB($\mu\mu$) note. Reweight events with $M_{Z0} - M_{ee} > 1$ GeV by $\pm 10\%$, those events's FSR effect will distinguished in the detector. Here, M_{Z0} is PYTHIA

Mass	CCCC(CC/EC)		CCEC(CC/EC)	
$50.0 < M_{ee} < 60.0$	0.0056	0.0000	0.0049	0.0069
$60.0 < M_{ee} < 70.0$	0.0019	0.0000	0.0014	0.0007
$70.0 < M_{ee} < 75.0$	0.0010	0.0000	0.0030	0.0005
$75.0 < M_{ee} < 81.0$	0.0074	0.0000	0.0040	0.0051
$81.0 < M_{ee} < 86.5$	0.0642	0.0000	0.0264	0.0306
$86.5 < M_{ee} < 89.5$	0.0337	0.0000	0.0047	0.0043
$89.5 < M_{ee} < 92.0$	0.8616	0.0000	0.4434	0.5196
$92.0 < M_{ee} < 97.0$	0.0475	0.0000	0.0112	0.0081
$97.0 < M_{ee} < 105.0$	0.0341	0.0000	0.0151	0.0175
$105.0 < M_{ee} < 115.0$	0.0011	0.0000	0.0010	0.0012
$115.0 < M_{ee} < 130.0$	0.0002	0.0000	0.0001	0.0002
$130.0 < M_{ee} < 180.0$	0.0001	0.0000	0.0000	0.0000
$180.0 < M_{ee} < 250.0$	0.0000	0.0000	0.0000	0.0000
$250.0 < M_{ee} < 500.0$	0.0000	0.0000	0.0000	0.0000

Table 11.6: CCCC and CCEC events differential cross section uncertainties due to CC or EC energy smear. The systematic shift is tested in two directions($+1\sigma$ and -1σ of the each variables, and we choose the larger one.)

generator level $Z0$ mass and M_{ee} is the generator level invariant mass of the final state diem system. Comparing the reweighted results with non-reweighted results, we take the larger shift as FSR uncertainty. The uncertainty for each bin is listed in Tab. 11.9.

Mass	CCCC	CCEC
$50.0 < M_{ee} < 60.0$	0.0203	0.0111
$60.0 < M_{ee} < 70.0$	0.0015	0.0028
$70.0 < M_{ee} < 75.0$	0.0031	0.0021
$75.0 < M_{ee} < 81.0$	0.0009	0.0053
$81.0 < M_{ee} < 86.5$	0.0044	0.0171
$86.5 < M_{ee} < 89.5$	0.0095	0.0239
$89.5 < M_{ee} < 92.0$	0.1230	0.2276
$92.0 < M_{ee} < 97.0$	0.0025	0.0335
$97.0 < M_{ee} < 105.0$	0.0098	0.0081
$105.0 < M_{ee} < 115.0$	0.0015	0.0011
$115.0 < M_{ee} < 130.0$	0.0011	0.0006
$130.0 < M_{ee} < 180.0$	0.0002	0.0001
$180.0 < M_{ee} < 250.0$	0.0001	0.0001
$250.0 < M_{ee} < 500.0$	0.0000	0.0000

Table 11.7: CCCC and CCEC events differential cross section uncertainties due to Non-linearity energy smear.

11.4.5 Systematic uncertainty from background subtraction

The QCD background is the largest background in this analysis, so it is very important to get the uncertainties from QCD. There are two sources of uncertainty due to QCD background, one is the QCD InvMass distribution, another one is the QCD contribution. For the QCD distribution uncertainty, we change the electron shower

Mass region (GeV/c^2)	PDF uncertainty
$50.0 < M_{ee} < 60.0$	0.0138
$60.0 < M_{ee} < 70.0$	0.0066
$70.0 < M_{ee} < 75.0$	0.0045
$75.0 < M_{ee} < 81.0$	0.0039
$81.0 < M_{ee} < 86.5$	0.0052
$86.5 < M_{ee} < 89.5$	0.0116
$89.5 < M_{ee} < 92.0$	0.0512
$92.0 < M_{ee} < 97.0$	0.0181
$97.0 < M_{ee} < 105.0$	0.0045
$105.0 < M_{ee} < 115.0$	0.0022
$115.0 < M_{ee} < 130.0$	0.0013
$130.0 < M_{ee} < 180.0$	0.0002
$180.0 < M_{ee} < 250.0$	0.0001
$250.0 < M_{ee} < 500.0$	0.0000

Table 11.8: Systematic uncertainty due to PDF uncertainty.

shape requirements in two directions. The default cuts in this analysis is HMx7>30 for CC electrons and HMx8>40 for EC electrons, so we use the shape measured from HMx7>12(CC)/HMx8>20(EC) and HMx7>50(CC)/HMx8>75(EC) to estimate this uncertainty.For the QCD contribution uncertainty, we shift the QCD background contribution by $\pm 1\sigma$, and choose the larger one as uncertainty. The uncertainties due to QCD background are listed in Tab. 11.10.

Mass region (GeV/c^2)	uncertainty
$50.0 < M_{ee} < 60.0$	0.0044
$60.0 < M_{ee} < 70.0$	0.0019
$70.0 < M_{ee} < 75.0$	0.0012
$75.0 < M_{ee} < 81.0$	0.0011
$81.0 < M_{ee} < 86.5$	0.0012
$86.5 < M_{ee} < 89.5$	0.0001
$89.5 < M_{ee} < 92.0$	0.0110
$92.0 < M_{ee} < 97.0$	0.0062
$97.0 < M_{ee} < 105.0$	0.0016
$105.0 < M_{ee} < 115.0$	0.0006
$115.0 < M_{ee} < 130.0$	0.0004
$130.0 < M_{ee} < 180.0$	0.0000
$180.0 < M_{ee} < 250.0$	0.0000
$250.0 < M_{ee} < 500.0$	0.0000

Table 11.9: Systematic uncertainty due to FSR.

11.4.6 Systematic uncertainty due to acceptance method

The unfolding acceptance for each bins are derived from PYTHIA Full MC, have uncertainties come from Full MC statistics. To estimate this uncertainty, we propagate the acceptance uncertainty into $\frac{d\sigma}{dM}$ uncertainty, which is shown in Tab. 11.11.

Mass	CCCC(Shape/NOR)		CCEC(Shape/NOR)	
$50.0 < M_{ee} < 60.0$	0.0155	0.0065	0.0407	0.0133
$60.0 < M_{ee} < 70.0$	0.0071	0.0033	0.0186	0.0066
$70.0 < M_{ee} < 75.0$	0.0049	0.0018	0.0098	0.0035
$75.0 < M_{ee} < 81.0$	0.0036	0.0012	0.0096	0.0024
$81.0 < M_{ee} < 86.5$	0.0021	0.0006	0.0051	0.0012
$86.5 < M_{ee} < 89.5$	0.0023	0.0006	0.0062	0.0012
$89.5 < M_{ee} < 92.0$	0.0070	0.0017	0.0156	0.0028
$92.0 < M_{ee} < 97.0$	0.0029	0.0005	0.0078	0.0010
$97.0 < M_{ee} < 105.0$	0.0018	0.0003	0.0040	0.0006
$105.0 < M_{ee} < 115.0$	0.0021	0.0003	0.0052	0.0005
$115.0 < M_{ee} < 130.0$	0.0016	0.0002	0.0041	0.0003
$130.0 < M_{ee} < 180.0$	0.0007	0.0001	0.0017	0.0001
$180.0 < M_{ee} < 250.0$	0.0001	0.0000	0.0003	0.0000
$250.0 < M_{ee} < 500.0$	0.0000	0.0000	0.0000	0.0000

Table 11.10: CCCC and CCEC events differential cross section uncertainties due to QCD background shape and normalization.

11.4.7 Systematic uncertainty due to full MC statistics

We use about 15M full MC in Z peak region to measure $\frac{d\sigma}{dM}$, but still suffers from low statistics in some unfolding matrix bins. To estimate this uncertainty due to statistics of full MC, we divided MC samples into 10 sub-samples and did ten pseudo-experiments. We take he spread of 10 $\frac{d\sigma}{dM}$ for each mass bins and divided by $\sqrt{10}$ as the uncertainty,

Mass region(GeV/c^2)	CCCC	CCEC
$50.0 < M_{ee} < 60.0$	0.0069	0.0242
$60.0 < M_{ee} < 70.0$	0.0069	0.0080
$70.0 < M_{ee} < 75.0$	0.0106	0.0072
$75.0 < M_{ee} < 81.0$	0.0118	0.0061
$81.0 < M_{ee} < 86.5$	0.0267	0.0074
$86.5 < M_{ee} < 89.5$	0.0568	0.0222
$89.5 < M_{ee} < 92.0$	0.0450	0.0891
$92.0 < M_{ee} < 97.0$	0.0383	0.0205
$97.0 < M_{ee} < 105.0$	0.0123	0.0042
$105.0 < M_{ee} < 115.0$	0.0035	0.0022
$115.0 < M_{ee} < 130.0$	0.0015	0.0012
$130.0 < M_{ee} < 180.0$	0.0001	0.0001
$180.0 < M_{ee} < 250.0$	0.0000	0.0000
$250.0 < M_{ee} < 500.0$	0.0000	0.0000

Table 11.11: CC-CC and CC-EC events differential cross section uncertainty due to acceptance corrections.

which can be found in Tab. 11.12.

Mass	CCCC	CCEC
$50.0 < M_{ee} < 60.0$	0.0080	0.0181
$60.0 < M_{ee} < 70.0$	0.0048	0.0102
$70.0 < M_{ee} < 75.0$	0.0079	0.0075
$75.0 < M_{ee} < 81.0$	0.0065	0.0067
$81.0 < M_{ee} < 86.5$	0.0123	0.0091
$86.5 < M_{ee} < 89.5$	0.0211	0.0162
$89.5 < M_{ee} < 92.0$	0.0426	0.0138
$92.0 < M_{ee} < 97.0$	0.0314	0.0151
$97.0 < M_{ee} < 105.0$	0.0065	0.0032
$105.0 < M_{ee} < 115.0$	0.0037	0.0039
$115.0 < M_{ee} < 130.0$	0.0011	0.0009
$130.0 < M_{ee} < 180.0$	0.0000	0.0001
$180.0 < M_{ee} < 250.0$	0.0000	0.0000
$250.0 < M_{ee} < 500.0$	0.0000	0.0000

Table 11.12: CCCC and CCEC events differential cross section Uncertainties due to statistics of MC sample.

11.4.8 Statistical uncertainty after error correlations correction

Due to the migration between mass bins, the statistical uncertainty for $\frac{d\sigma}{dM}$ derived from the number of events is not suitable one. The correlations between different mass

bins must be considered when calculate the statistical uncertainty. As described in Sec. 11.1, the differential cross section can be calculated like:

$$X = \frac{d_\sigma}{d_M} = \frac{N - B}{\varepsilon \times \beta \times L \times \Delta M} = \frac{N_{sel}}{R \times L \times \Delta M}$$

So,

$$\frac{\partial X[i]}{\partial N_{sel}[j]} = \frac{1}{R[i][j] \times L \times \Delta M}$$

the error matrix is:

$$\mathcal{E}[i][j] = \sum_{m=1}^{14} \frac{\partial X[i]}{\partial N_{sel}[m]} \cdot \frac{\partial X[j]}{\partial N_{sel}[m]} \cdot (\Delta N_{sel}[m])^2$$

the correlation matrix is:

$$\mathcal{C}[i][j] = \frac{\mathcal{E}[i][j]}{\sqrt{\mathcal{E}[i][i] \times \mathcal{E}[j][j]}}$$

The statistical uncertainties after correlation corrections for each mass bins are shown in Tab. 11.13. The correlation matrices for CCCC and CCEC events are shown in Appendix C.

11.4.9 Uncertainties distribution

The statistics and systematic uncertainties of CCCC and CCEC events are compared in Fig. 11.4.

11.5 Final results

Final results of normalized differential cross section measured from RunIIb 3.9 fb^{-1} are shown below: The final differential cross section of $p\bar{p} \to Z/\gamma^* \to e^+e^-$ are shown

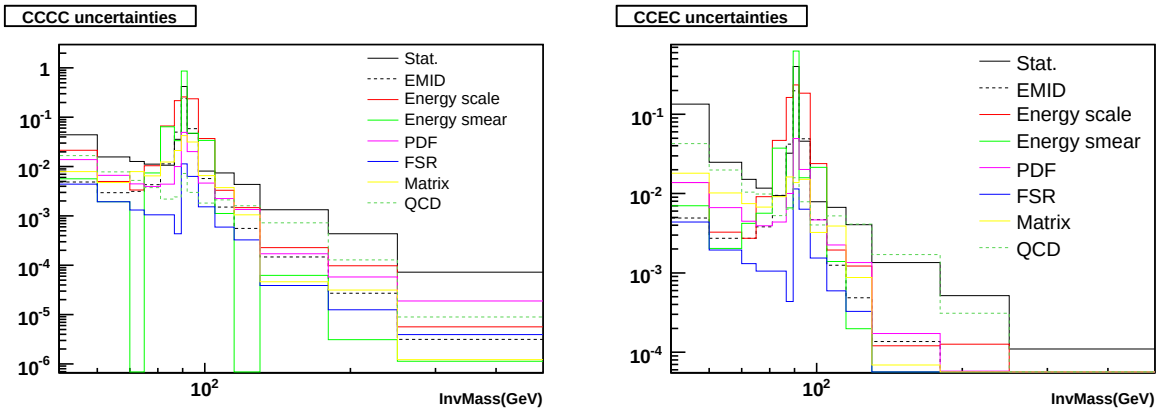

Figure 11.4: Comparison between statistics and all systematic uncertainties described in Chapter 13.

in Tab. 11.13.

M_{ee} (GeV)	Prediction		$\frac{1}{\sigma} \times \frac{d\sigma}{dM}$
	PYTHIA	NLO	
$50.0 < M_{ee} < 60.0$	0.0109	0.0105	$0.0129 \pm 0.0005 \pm 0.0004$
$60.0 < M_{ee} < 70.0$	0.0073	0.0072	$0.0079 \pm 0.0002 \pm 0.0002$
$70.0 < M_{ee} < 75.0$	0.0076	0.0075	$0.0084 \pm 0.0001 \pm 0.0002$
$75.0 < M_{ee} < 81.0$	0.0110	0.0109	$0.0117 \pm 0.0001 \pm 0.0002$
$81.0 < M_{ee} < 86.5$	0.0293	0.0291	$0.0298 \pm 0.0001 \pm 0.0008$
$86.5 < M_{ee} < 89.5$	0.1342	0.1340	$0.1313 \pm 0.0003 \pm 0.0021$
$89.5 < M_{ee} < 92.0$	0.6249	0.6254	$0.6232 \pm 0.0037 \pm 0.0075$
$92.0 < M_{ee} < 97.0$	0.1543	0.1547	$0.1540 \pm 0.0004 \pm 0.0023$
$97.0 < M_{ee} < 105.0$	0.0149	0.0150	$0.0149 \pm 0.0001 \pm 0.0004$
$105.0 < M_{ee} < 115.0$	0.0038	0.0039	$0.0039 \pm 0.0001 \pm 0.0001$
$115.0 < M_{ee} < 130.0(\times 10^{-3})$	1.4118	1.4383	$1.4846 \pm 0.0380 \pm 0.0362$
$130.0 < M_{ee} < 180.0(\times 10^{-3})$	0.3811	0.3920	$0.4007 \pm 0.0122 \pm 0.0094$
$180.0 < M_{ee} < 250.0(\times 10^{-3})$	0.0757	0.0786	$0.0781 \pm 0.0043 \pm 0.0021$
$250.0 < M_{ee} < 500.0(\times 10^{-3})$	0.0083	0.0086	$0.0093 \pm 0.0008 \pm 0.0003$

Table 11.13: The first column shows the bin size. The second and third columns show the $\frac{1}{\sigma} \times \frac{d\sigma}{dM}$ predictions from PYTHIA and NLO generator ZGRAD2. The third column is the measured $\frac{1}{\sigma} \times \frac{d\sigma}{dM}$; the first uncertainty is statistical, the second is systematic.

Chapter 12

Conclusion

We report a measurement of the forward-backward charge asymmetry of electron pairs resulting from the process $p\bar{p} \rightarrow Z/\gamma^* + X \rightarrow ee + X$, and we also use the A_{FB} distribution to extract $\sin^2\theta_W$ and $Z-$light quark couplings. The overall uncertainty on the measured $\sin^2\theta_W$ is smaller than the combined uncertainty from LEP measurements of the inclusive hadronic charge asymmetry. And our uncertainty is also close to the combined uncertainty from LEP and SLD A_{FB} measurements using c quark. With 8-10 fb^{-1} data, combine both electron and μ channel with CDF, the expected precision will be comparable with the current world average value. The Z to light quark couplings determined using the unfolded A_{FB} distribution represent the world's most precise direct measurements of those parameters. We also present the first Run II measurement of the normalized differential cross section measurement for $p\bar{p} \rightarrow Z/\gamma^* \rightarrow e^+e^-$ events.

Appendix A

Luminosity reweight and vertex reweight

A.1 Luminosity reweight

GEANT MC simulation and real data have different instantaneous luminosity profile. We reweighted the instantaneous luminosity distribution on GEANT MC to remove agree with that in real data. The instantaneous luminosity distributions before and after reweighting are shown in Fig. A.1

A.2 Vertex reweight

The primary vertex distribution in data and GEANT MC is different, we need to do vertex reweighting to remove this effect. The primary vertex distribution before and after reweighting is shown in Fig. A.2

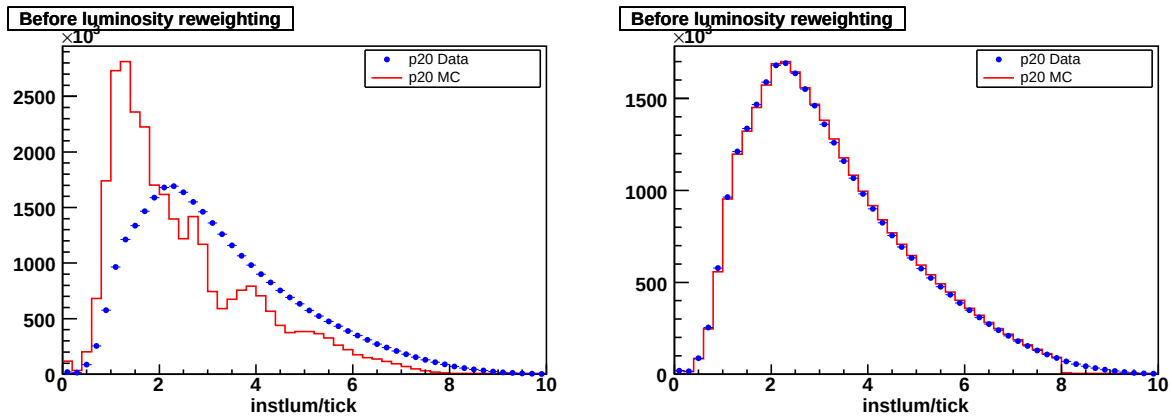

Figure A.1: Comparison of instantaneous luminosity between data and GEANT MC before (Left) and after (Right) luminosity reweighting.

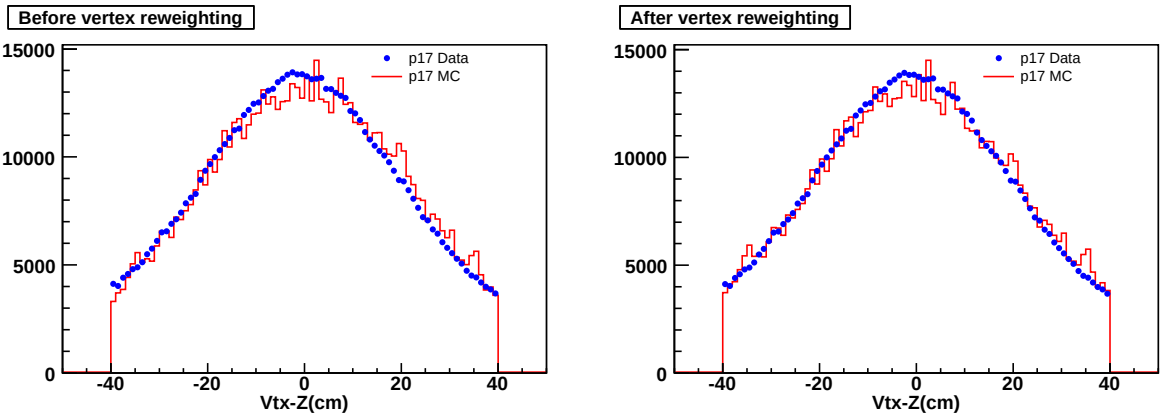

Figure A.2: Comparison of primary vertex distributions between data and GEANT MC before (Left) and after (Right) vertex reweighting.

Appendix B

Comparison of $\cos\theta^*$ for each mass bin

B.1 Collin comparison in each mass bins

We also compare $\cos\theta^*$ distribution in each mass bin between data and signal+QCD+SM.

The CC-CC and CC-EC comparisons are shown from Fig. B.1 to Fig. B.14.

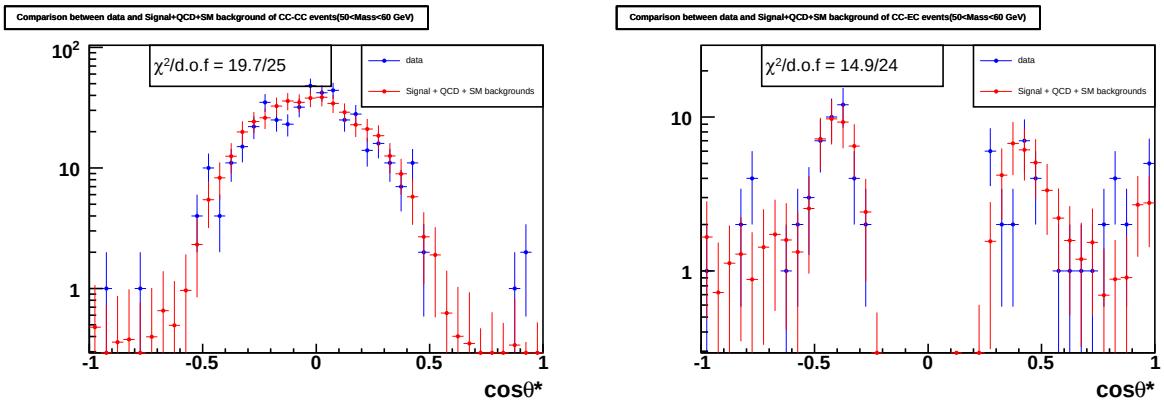

Figure B.1: $\cos\theta^*$ comparsion in mass region (50-60 GeV)

B. COMPARISON OF $\cos\theta^*$ FOR EACH MASS BIN

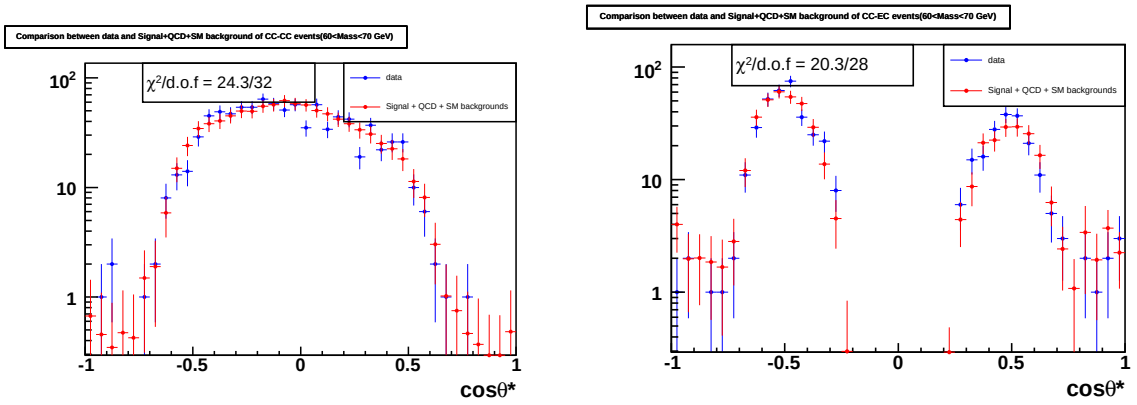

Figure B.2: $\cos\theta^*$ comparsion in mass region (60-70 GeV)

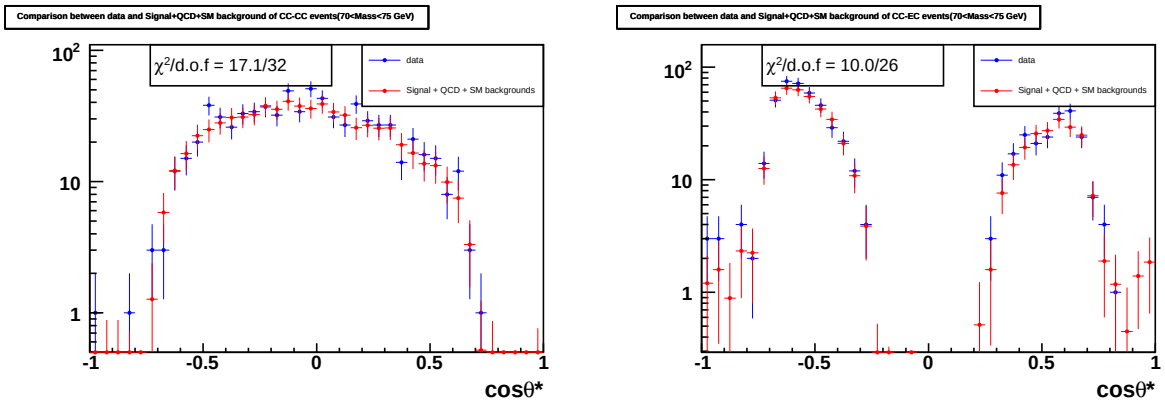

Figure B.3: $\cos\theta^*$ comparsion in mass region (70-75 GeV)

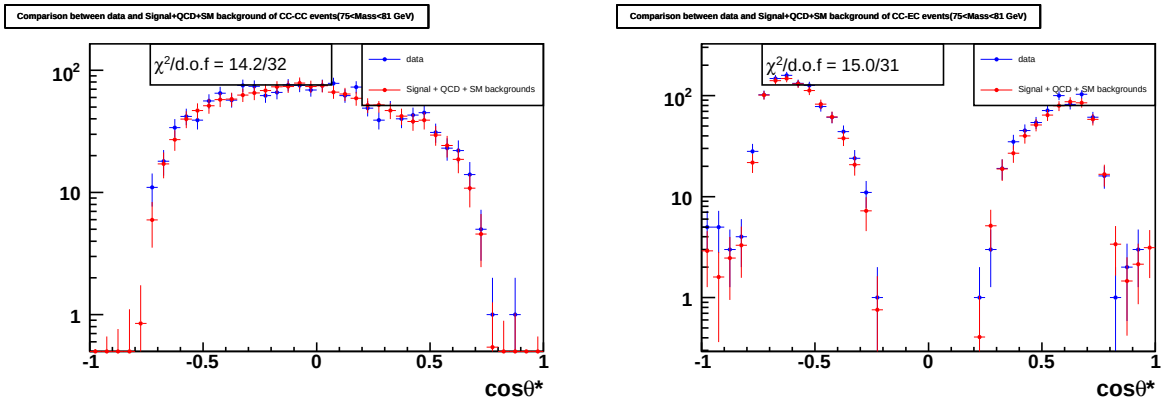

Figure B.4: $\cos\theta^*$ comparsion in mass region (75-81 GeV)

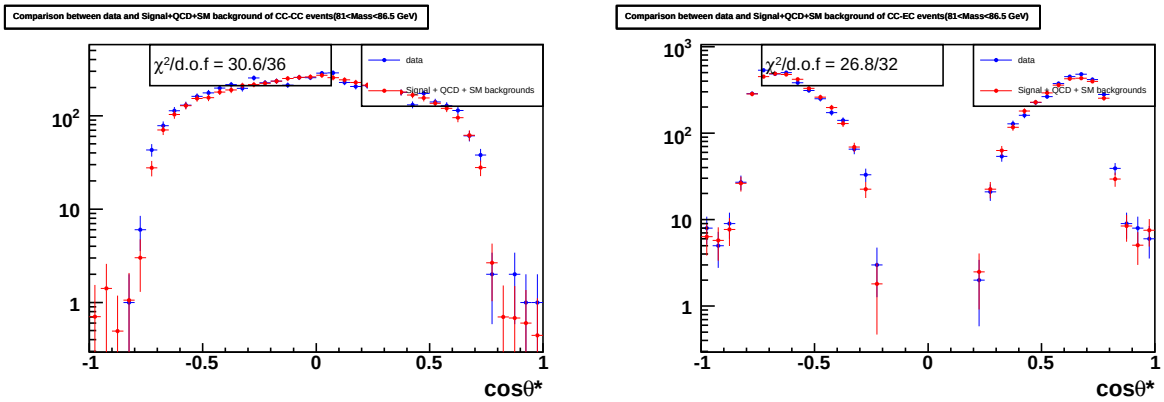

Figure B.5: $\cos\theta^*$ comparsion in mass region (81-86.5 GeV)

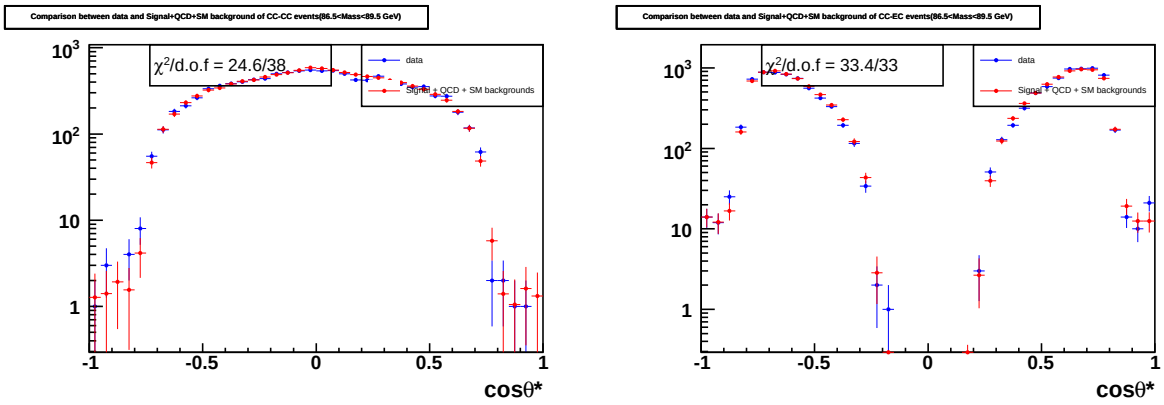

Figure B.6: $\cos\theta^*$ comparsion in mass region (86.5-89.5 GeV)

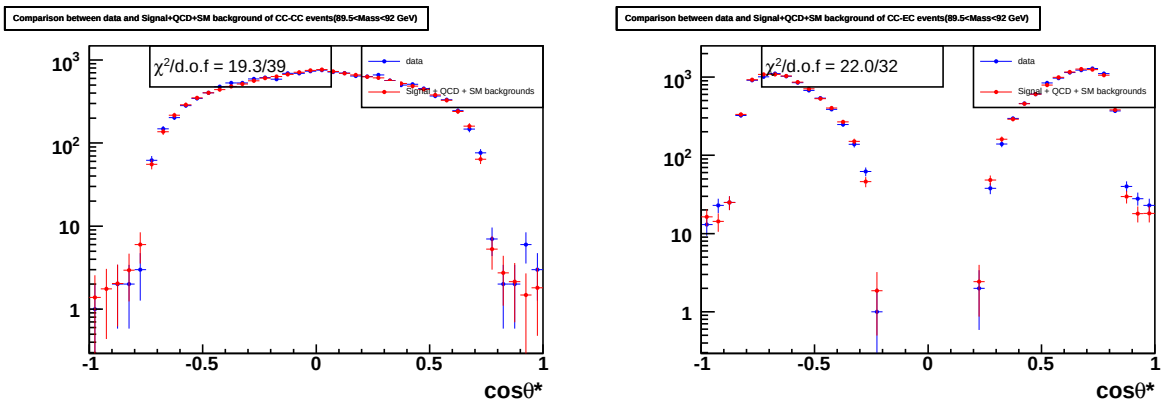

Figure B.7: $\cos\theta^*$ comparsion in mass region (89.5-92 GeV)

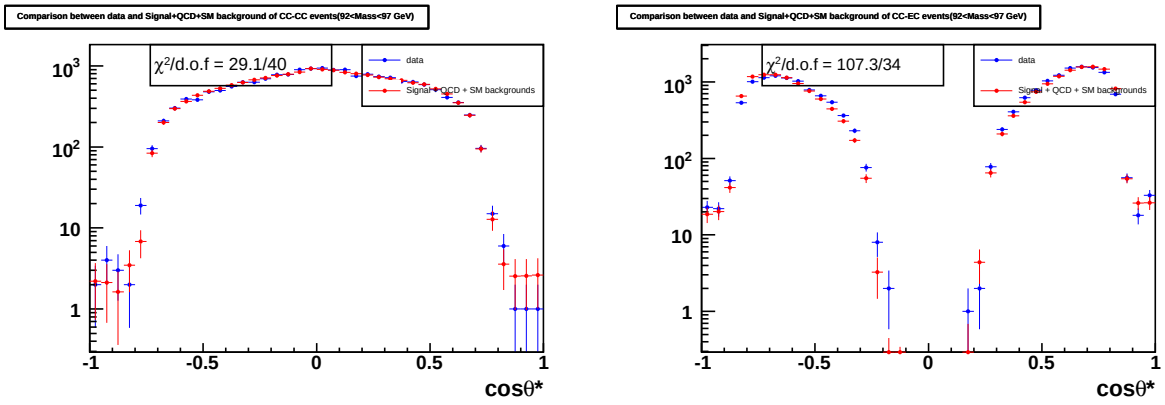

Figure B.8: $\cos\theta^*$ comparsion in mass region (92-97 GeV)

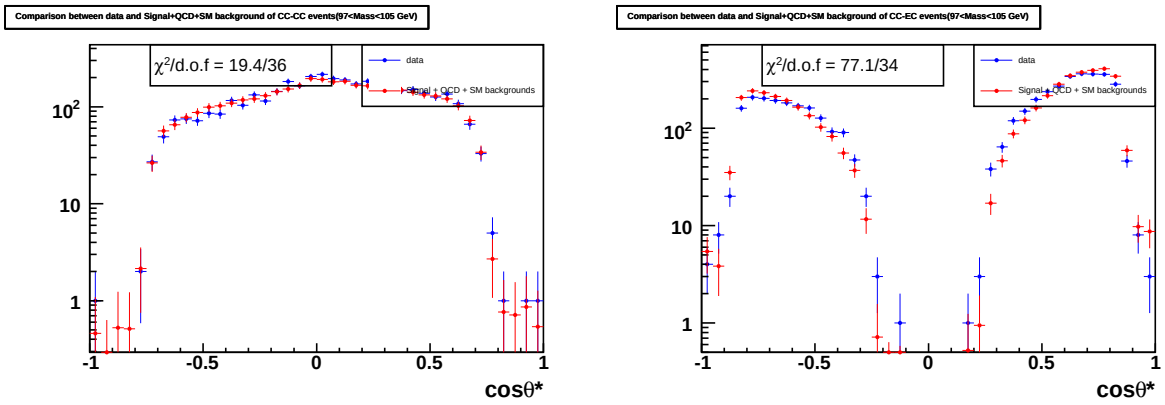

Figure B.9: $\cos\theta^*$ comparsion in mass region (97-105 GeV)

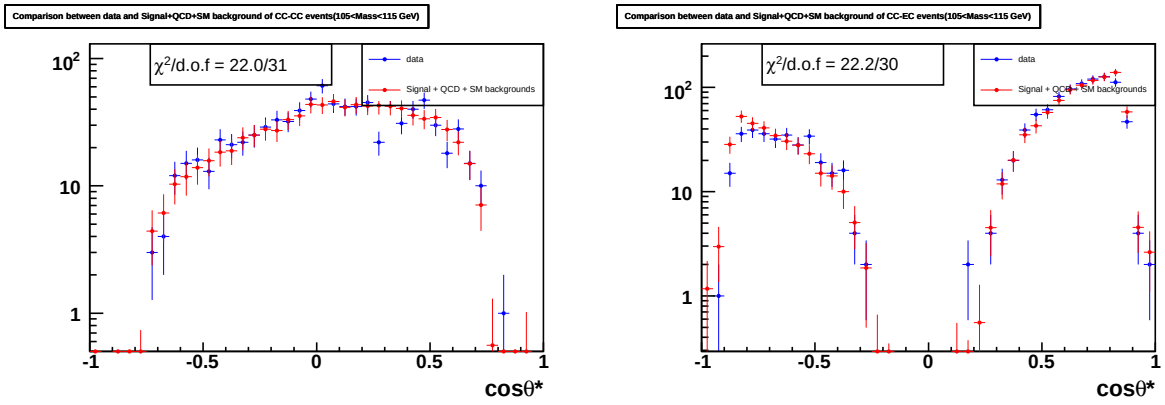

Figure B.10: $\cos\theta^*$ comparsion in mass region (105-115 GeV)

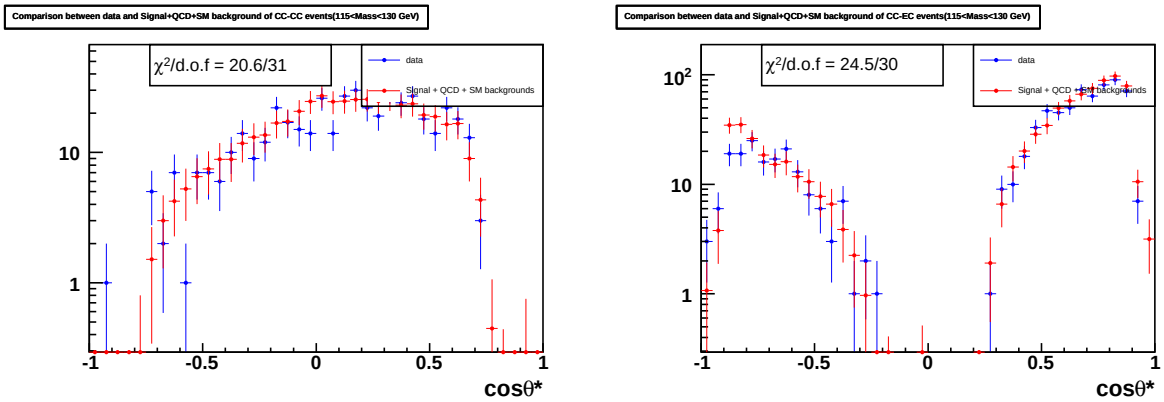

Figure B.11: $\cos\theta^*$ comparsion in mass region (115-130 GeV)

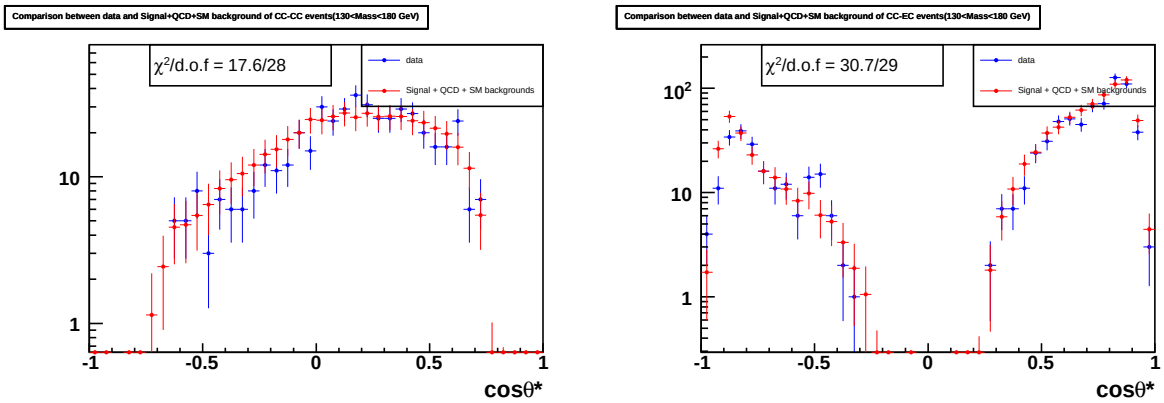

Figure B.12: $\cos\theta^*$ comparsion in mass region (130-180 GeV)

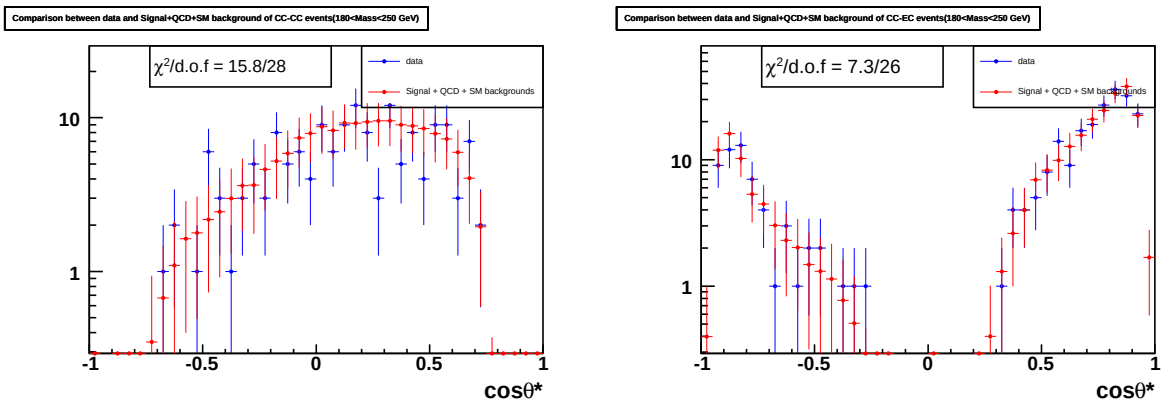

Figure B.13: $\cos\theta^*$ comparsion in mass region (180-250 GeV)

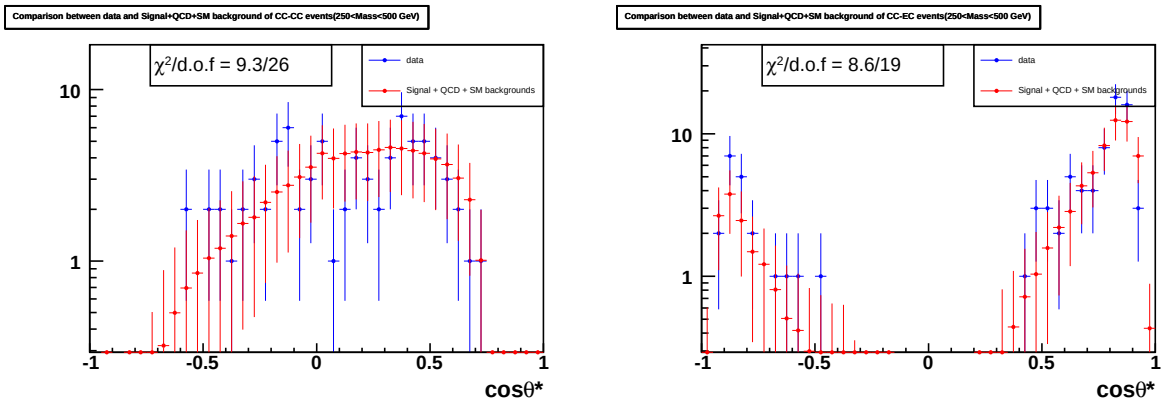

Figure B.14: $\cos\theta^*$ comparsion in mass region (250-500 GeV)

Appendix C

Calculation of correlation matrix

C.1 Correlation matrix

Using numbers of unfolded forward and backward events, A_{FB} can be calculated as the following:

$$\begin{aligned} A_{FB}[i] &= \frac{N^F_{unfold2}[i] - N^B_{unfold2}[i]}{N^F_{unfold2}[i] + N^B_{unfold2}[i]} \\ &= \frac{\frac{N^F_{unfold1}[i]}{Acc_F[i]} - \frac{N^B_{unfold1}[i]}{Acc_B[i]}}{\frac{N^F_{unfold1}[i]}{Acc_F[i]} + \frac{N^B_{unfold1}[i]}{Acc_B[i]}} \end{aligned}$$

where

- $R_{FF}[i][j]$,$R_{FB}[i][j]$,$R_{BF}[i][j]$ and $R_{BB}[i][j]$ are elements of the detector response matrices. (Sect. 7.1)
- $Acc_F[i]$ and $Acc_B[i]$ are acc×eff for forward and backward events. (Sect. 7.2)
- N^F_{raw} and N^B_{raw} are number of raw forward and backward events.
- $N^F_{unfold1}$ and $N^B_{unfold1}$ are numbers of forward and backward events after detector

resolution unfolding.

$$N^F_{unfold1}[i] = \sum_j \left(R_{FF}[i][j] \times N^F_{raw}[j] + R_{FB}[i][j] \times N^B_{raw}[j]\right)$$
$$N^B_{unfold1}[i] = \sum_j \left(R_{BF}[i][j] \times N^F_{raw}[j] + R_{BB}[i][j] \times N^B_{raw}[j]\right)$$

- $N^F_{unfold2}$ and $N^B_{unfold2}$ are numbers of forward and backward events after detector resolution unfolding and acc×eff unfolding.

$$N^F_{unfold2}[i] = \frac{N^F_{unfold1}[i]}{Acc_F[i]}$$
$$N^B_{unfold2}[i] = \frac{N^B_{unfold1}[i]}{Acc_B[i]}$$

The A_{FB} uncertainty due to the statistical uncertainties on N^F_{raw} and N^B_{raw} can be calculated as

$$\Delta A_{FB}[i] = \sqrt{\sum_j \left(\frac{\partial A_{FB}[i]}{\partial N^F_{raw}[j]}\Delta N^F_{raw}[j]\right)^2 + \sum_j \left(\frac{\partial A_{FB}[i]}{\partial N^B_{raw}[j]}\Delta N^B_{raw}[j]\right)^2}$$

where

$$\frac{\partial A_{FB}[i]}{\partial N^F_{raw}[j]} = \frac{-2 \times N^B_{unfold2}[i] \times R_{FF}[i][j]}{Acc_F[i] \times (N^F_{unfold2}[i] + N^B_{unfold2}[i])^2} + \frac{2 \times N^F_{unfold2}[i] \times R_{BF}[i][j]}{Acc_B[i] \times (N^F_{unfold2}[i] + N^B_{unfold2}[i])^2}$$
$$\frac{\partial A_{FB}[i]}{\partial N^B_{raw}[j]} = \frac{-2 \times N^B_{unfold2}[i] \times R_{FB}[i][j]}{Acc_F[i] \times (N^F_{unfold2}[i] + N^B_{unfold2}[i])^2} + \frac{2 \times N^F_{unfold2}[i] \times R_{BB}[i][j]}{Acc_B[i] \times (N^F_{unfold2}[i] + N^B_{unfold2}[i])^2}$$

The error matrix is:

$$\mathcal{E}[i][j] = \sum_{m=1}^{14} \frac{\partial A_{FB}[i]}{\partial N^F_{raw}[m]} \cdot \frac{\partial A_{FB}[j]}{\partial N^F_{raw}[m]} \cdot (\Delta N^F_{raw}[m])^2 + \frac{\partial A_{FB}[i]}{\partial N^B_{raw}[m]} \cdot \frac{\partial A_{FB}[j]}{\partial N^B_{raw}[m]} \cdot (\Delta N^B_{raw}[m])^2$$

and the correlation matrix is

$$\mathcal{C}[i][j] = \mathcal{E}[i][j]/\sqrt{\mathcal{E}[i][i] \times \mathcal{E}[j][j]}$$

We first calculate the error matrix separately for CCCC and CCEC events, then add them together to get the error matrix for both CCCC and CCEC events. Table

C.1, C.2 and C.3 are correlation matrix table. Plots for correlation matrix are shown in Fig. C.1.

	1	2	3	4	5	6	7	8	9	10	11	12	13	14
1	1.00	0.22	0.03	0.00	0.00	0.00	0.00	0.00	0.00	0.00	0.00	0.00	0.00	0.00
2	0.22	1.00	0.35	0.06	0.02	0.02	0.02	0.01	0.00	0.00	0.00	0.00	0.00	0.00
3	0.03	0.35	1.00	0.45	0.10	0.04	0.04	0.03	0.01	0.00	0.00	0.00	0.00	0.00
4	0.00	0.06	0.45	1.00	0.48	0.15	0.07	0.04	0.01	0.00	0.00	0.00	0.00	0.00
5	0.00	0.02	0.10	0.48	1.00	0.71	0.31	0.10	0.01	0.00	0.00	0.00	0.00	0.00
6	0.00	0.02	0.04	0.15	0.71	1.00	0.78	0.39	0.03	0.00	0.00	0.00	0.00	0.00
7	0.00	0.02	0.04	0.07	0.31	0.78	1.00	0.80	0.14	0.01	0.00	0.00	0.00	0.00
8	0.00	0.01	0.03	0.04	0.10	0.39	0.80	1.00	0.48	0.04	0.00	0.00	0.00	0.00
9	0.00	0.00	0.01	0.01	0.01	0.03	0.14	0.48	1.00	0.35	0.03	0.00	0.00	0.00
10	0.00	0.00	0.00	0.00	0.00	0.00	0.01	0.04	0.35	1.00	0.26	0.01	0.00	0.00
11	0.00	0.00	0.00	0.00	0.00	0.00	0.00	0.00	0.03	0.26	1.00	0.15	0.00	0.00
12	0.00	0.00	0.00	0.00	0.00	0.00	0.00	0.00	0.00	0.01	0.15	1.00	0.07	0.00
13	0.00	0.00	0.00	0.00	0.00	0.00	0.00	0.00	0.00	0.00	0.00	0.07	1.00	0.06
14	0.00	0.00	0.00	0.00	0.00	0.00	0.00	0.00	0.00	0.00	0.00	0.00	0.06	1.00

Table C.1: Correlation matrix of CCCC.

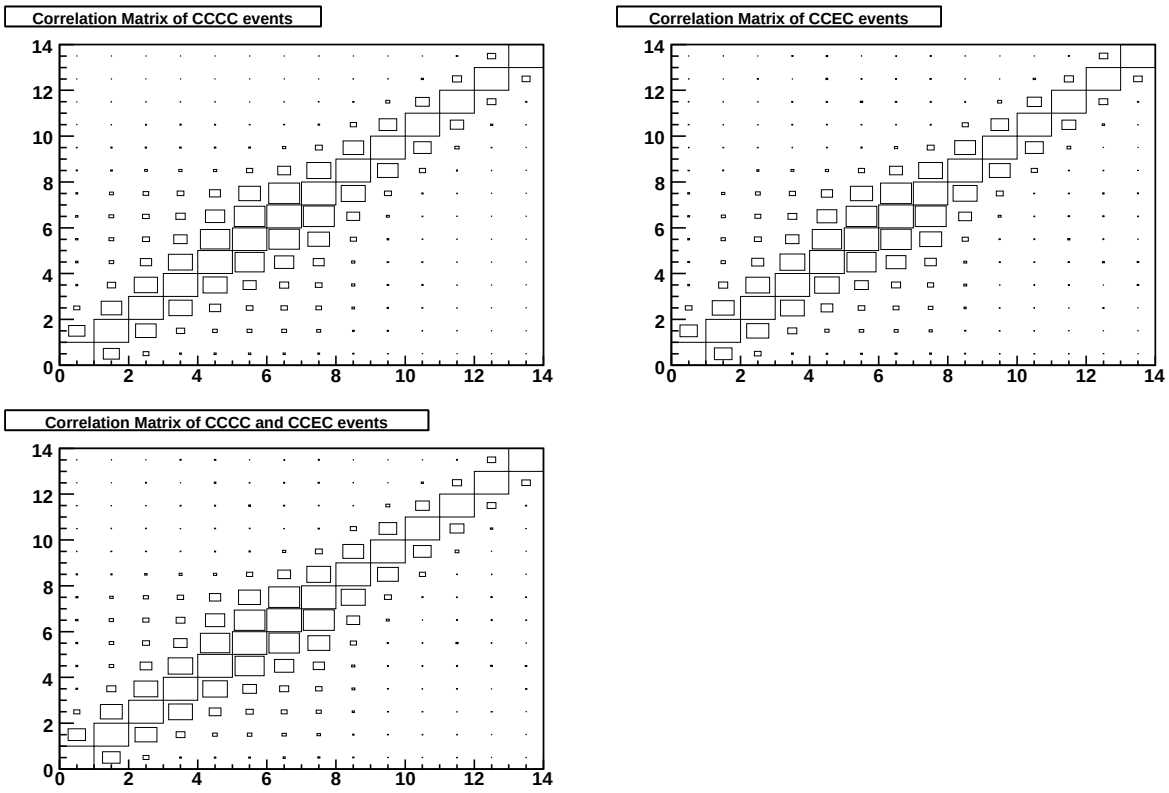

Figure C.1: Correlation matrix for CCCC, CCEC and both of CCCC and CCEC events.

	1	2	3	4	5	6	7	8	9	10	11	12	13	14
1	1.00	0.26	0.04	0.00	0.00	0.00	0.00	0.00	0.00	0.00	0.00	0.00	0.00	0.00
2	0.26	1.00	0.41	0.07	0.02	0.02	0.01	0.01	0.00	0.00	0.00	0.00	0.00	0.00
3	0.04	0.41	1.00	0.47	0.12	0.04	0.03	0.02	0.00	0.00	0.00	0.00	0.00	0.00
4	0.00	0.07	0.47	1.00	0.51	0.15	0.07	0.03	0.01	0.00	0.00	0.00	0.00	0.00
5	0.00	0.02	0.12	0.51	1.00	0.72	0.32	0.11	0.01	0.00	0.00	0.00	0.00	0.00
6	0.00	0.02	0.04	0.15	0.72	1.00	0.78	0.40	0.03	0.00	0.00	0.00	0.00	0.00
7	0.00	0.01	0.03	0.07	0.32	0.78	1.00	0.81	0.14	0.01	0.00	0.00	0.00	0.00
8	0.00	0.01	0.02	0.03	0.11	0.40	0.81	1.00	0.48	0.04	0.00	0.00	0.00	0.00
9	0.00	0.00	0.00	0.01	0.01	0.03	0.14	0.48	1.00	0.36	0.03	0.00	0.00	0.00
10	0.00	0.00	0.00	0.00	0.00	0.00	0.01	0.04	0.36	1.00	0.26	0.01	0.00	0.00
11	0.00	0.00	0.00	0.00	0.00	0.00	0.00	0.00	0.03	0.26	1.00	0.16	0.00	0.00
12	0.00	0.00	0.00	0.00	0.00	0.00	0.00	0.00	0.00	0.01	0.16	1.00	0.07	0.00
13	0.00	0.00	0.00	0.00	0.00	0.00	0.00	0.00	0.00	0.00	0.00	0.07	1.00	0.06
14	0.00	0.00	0.00	0.00	0.00	0.00	0.00	0.00	0.00	0.00	0.00	0.00	0.06	1.00

Table C.2: Correlation matrix of CCEC.

C.2 χ^2 calculation

To calculate χ^2 between PYTHIA and data A_{FB}, we use the following formula:

$$\chi_{raw} = \frac{A_{FB}(Pythia) - A_{FB}(data)}{\sqrt{\sigma_{mc}^2 + \sigma_{data}^2}}$$

$$\chi^2 = \sum_{i,j=1}^{14} \chi_{raw}[i] \times \mathfrak{C}^{-1}[i][j] \times \chi_{raw}[j]$$

The correlation matrix for $d\sigma/dM$ study are shown in Table C.4 and Table C.5.

C. CALCULATION OF CORRELATION MATRIX

	1	2	3	4	5	6	7	8	9	10	11	12	13	14
1	1.00	0.25	0.03	0.00	0.00	0.00	0.00	0.00	0.00	0.00	0.00	0.00	0.00	0.00
2	0.25	1.00	0.40	0.07	0.02	0.02	0.01	0.01	0.00	0.00	0.00	0.00	0.00	0.00
3	0.03	0.40	1.00	0.47	0.11	0.04	0.03	0.02	0.00	0.00	0.00	0.00	0.00	0.00
4	0.00	0.07	0.47	1.00	0.51	0.15	0.07	0.03	0.01	0.00	0.00	0.00	0.00	0.00
5	0.00	0.02	0.11	0.51	1.00	0.72	0.32	0.11	0.01	0.00	0.00	0.00	0.00	0.00
6	0.00	0.02	0.04	0.15	0.72	1.00	0.78	0.40	0.03	0.00	0.00	0.00	0.00	0.00
7	0.00	0.01	0.03	0.07	0.32	0.78	1.00	0.80	0.14	0.01	0.00	0.00	0.00	0.00
8	0.00	0.01	0.02	0.03	0.11	0.40	0.80	1.00	0.48	0.04	0.00	0.00	0.00	0.00
9	0.00	0.00	0.00	0.01	0.01	0.03	0.14	0.48	1.00	0.36	0.03	0.00	0.00	0.00
10	0.00	0.00	0.00	0.00	0.00	0.00	0.01	0.04	0.36	1.00	0.26	0.01	0.00	0.00
11	0.00	0.00	0.00	0.00	0.00	0.00	0.00	0.00	0.03	0.26	1.00	0.16	0.00	0.00
12	0.00	0.00	0.00	0.00	0.00	0.00	0.00	0.00	0.00	0.01	0.16	1.00	0.07	0.00
13	0.00	0.00	0.00	0.00	0.00	0.00	0.00	0.00	0.00	0.00	0.00	0.07	1.00	0.06
14	0.00	0.00	0.00	0.00	0.00	0.00	0.00	0.00	0.00	0.00	0.00	0.00	0.06	1.00

Table C.3: Correlation matrix of All.

	1	2	3	4	5	6	7	8	9	10	11	12	13	14
1	1.00	0.23	0.03	0.00	0.00	0.00	0.00	0.00	0.00	0.00	0.00	0.00	0.00	0.00
2	0.23	1.00	0.34	0.06	0.02	0.02	0.02	0.01	0.00	0.00	0.00	0.00	0.00	0.00
3	0.03	0.34	1.00	0.45	0.10	0.04	0.03	0.03	0.01	0.00	0.00	0.00	0.00	0.00
4	0.00	0.06	0.45	1.00	0.49	0.15	0.07	0.04	0.01	0.00	0.00	0.00	0.00	0.00
5	0.00	0.02	0.10	0.49	1.00	0.71	0.31	0.10	0.01	0.00	0.00	0.00	0.00	0.00
6	0.00	0.02	0.04	0.15	0.71	1.00	0.78	0.40	0.03	0.00	0.00	0.00	0.00	0.00
7	0.00	0.02	0.03	0.07	0.31	0.78	1.00	0.80	0.14	0.01	0.00	0.00	0.00	0.00
8	0.00	0.01	0.03	0.04	0.10	0.40	0.80	1.00	0.48	0.04	0.00	0.00	0.00	0.00
9	0.00	0.00	0.01	0.01	0.01	0.03	0.14	0.48	1.00	0.36	0.03	0.00	0.00	0.00
10	0.00	0.00	0.00	0.00	0.00	0.00	0.01	0.04	0.36	1.00	0.26	0.01	0.00	0.00
11	0.00	0.00	0.00	0.00	0.00	0.00	0.00	0.00	0.03	0.26	1.00	0.15	0.00	0.00
12	0.00	0.00	0.00	0.00	0.00	0.00	0.00	0.00	0.00	0.01	0.15	1.00	0.07	0.00
13	0.00	0.00	0.00	0.00	0.00	0.00	0.00	0.00	0.00	0.00	0.00	0.07	1.00	0.06
14	0.00	0.00	0.00	0.00	0.00	0.00	0.00	0.00	0.00	0.00	0.00	0.00	0.06	1.00

Table C.4: Correlation matrix of CCCC for $d\sigma/dM$.

	1	2	3	4	5	6	7	8	9	10	11	12	13	14
1	1.00	0.24	0.04	0.00	0.00	0.00	0.01	0.00	0.00	0.00	0.00	0.00	0.00	0.00
2	0.24	1.00	0.39	0.07	0.02	0.02	0.01	0.01	0.00	0.00	0.00	0.00	0.00	0.00
3	0.04	0.39	1.00	0.48	0.12	0.04	0.03	0.02	0.00	0.00	0.00	0.00	0.00	0.00
4	0.00	0.07	0.48	1.00	0.51	0.15	0.07	0.03	0.01	0.00	0.00	0.00	0.00	0.00
5	0.00	0.02	0.12	0.51	1.00	0.72	0.32	0.11	0.01	0.00	0.00	0.00	0.00	0.00
6	0.00	0.02	0.04	0.15	0.72	1.00	0.78	0.40	0.03	0.00	0.00	0.00	0.00	0.00
7	0.01	0.01	0.03	0.07	0.32	0.78	1.00	0.81	0.14	0.01	0.00	0.00	0.00	0.00
8	0.00	0.01	0.02	0.03	0.11	0.40	0.81	1.00	0.48	0.05	0.00	0.00	0.00	0.00
9	0.00	0.00	0.00	0.01	0.01	0.03	0.14	0.48	1.00	0.36	0.04	0.00	0.00	0.00
10	0.00	0.00	0.00	0.00	0.00	0.00	0.01	0.05	0.36	1.00	0.28	0.01	0.00	0.00
11	0.00	0.00	0.00	0.00	0.00	0.00	0.00	0.00	0.04	0.28	1.00	0.16	0.00	0.00
12	0.00	0.00	0.00	0.00	0.00	0.00	0.00	0.00	0.00	0.01	0.16	1.00	0.07	0.00
13	0.00	0.00	0.00	0.00	0.00	0.00	0.00	0.00	0.00	0.00	0.00	0.07	1.00	0.06
14	0.00	0.00	0.00	0.00	0.00	0.00	0.00	0.00	0.00	0.00	0.00	0.00	0.06	1.00

Table C.5: Correlation matrix of CCEC for $d\sigma/dM$.

Appendix D

CCEC events: with or without EC track match

When selecting events, we do not apply any tracking cuts on EC electrons, so CC-EC events can be divided into two parts:

- Notrk: EC electron failed track-match cut
- Trk: EC electron passed track-match cut

where track-match cut is track-match-probability $P > 0.001$.

The reason we do not use tracking cuts on EC electron is track-match efficiency is only about 60%. Here, we will prove Notrk and Trk events results are consistence with each other.

D.1 A new EC cuts: trk-iso

RunIIb data was collected with higher instantaneous luminosity then RunIIa data. With high instantaneous luminosity, we expect there is more QCD background contribution in RunIIb than RunIIa, specially for the CC-EC events. Since we already applied very tight selection cuts on CC electron(including track match cut), the high luminosity will only affect CC-EC events. To reduce CC-EC events QCD contribution, we add a new cut on EC region, which is trk-iso cut (Section 4.4). In Fig. D.1, the trk-iso distribution is get from events which passed RunIIa CC-EC selection cuts.

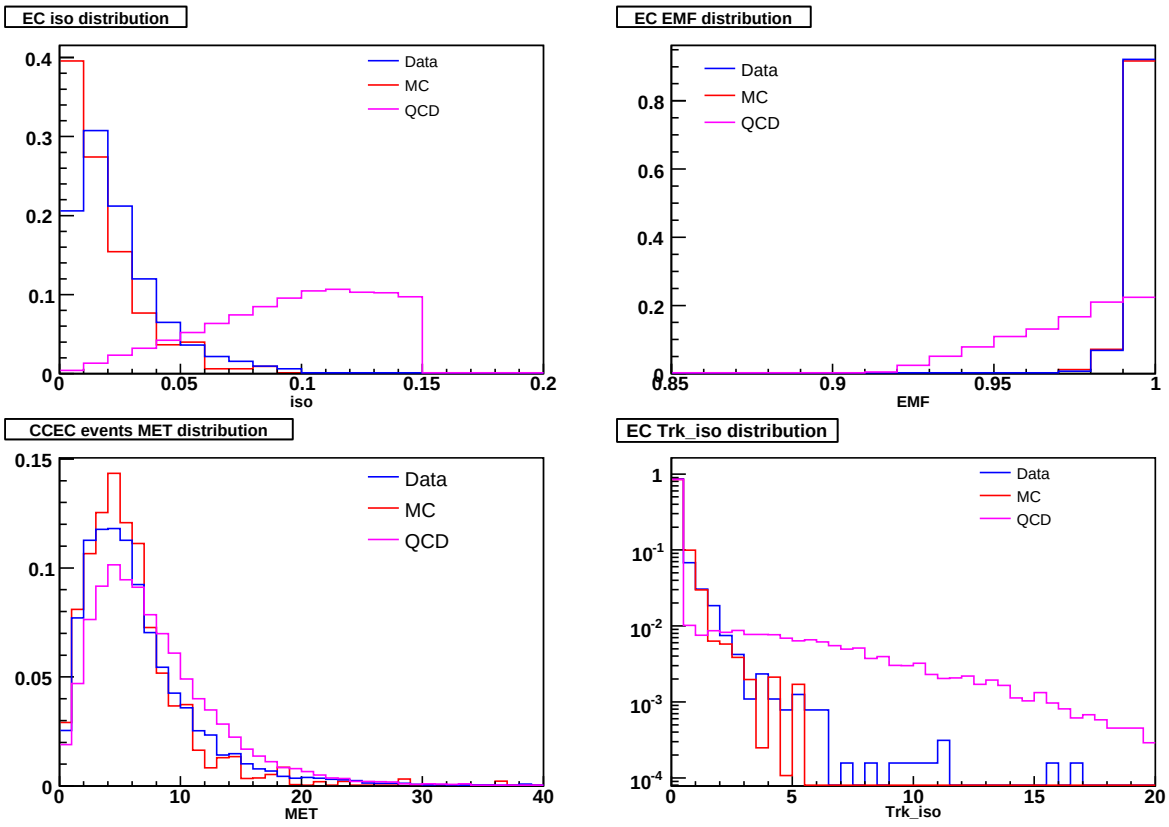

Figure D.1: Comparison of EC isolation, EMF, events MET and trk-iso of data, full MC and QCD background. MET and trk-iso distribution are get from events which passed RunIIa CC-EC selection cuts.

D.2 QCD shape

In this analysis, we use InvMass distribution of data, signal and QCD with Minuit Fitting method to get fraction of QCD contribution, so QCD contribution is sensitive to QCD shape. Considering poor statistics of Trk QCD sample, in the beginning of this study, we use same QCD shape(just invert HMx cut, without track cut) to study Trk and NoTrk events. In this case, for Trk events, signal+All background can not describe data, specially in high mass region(130-250 GeV). The results can be found in Fig.D.2,

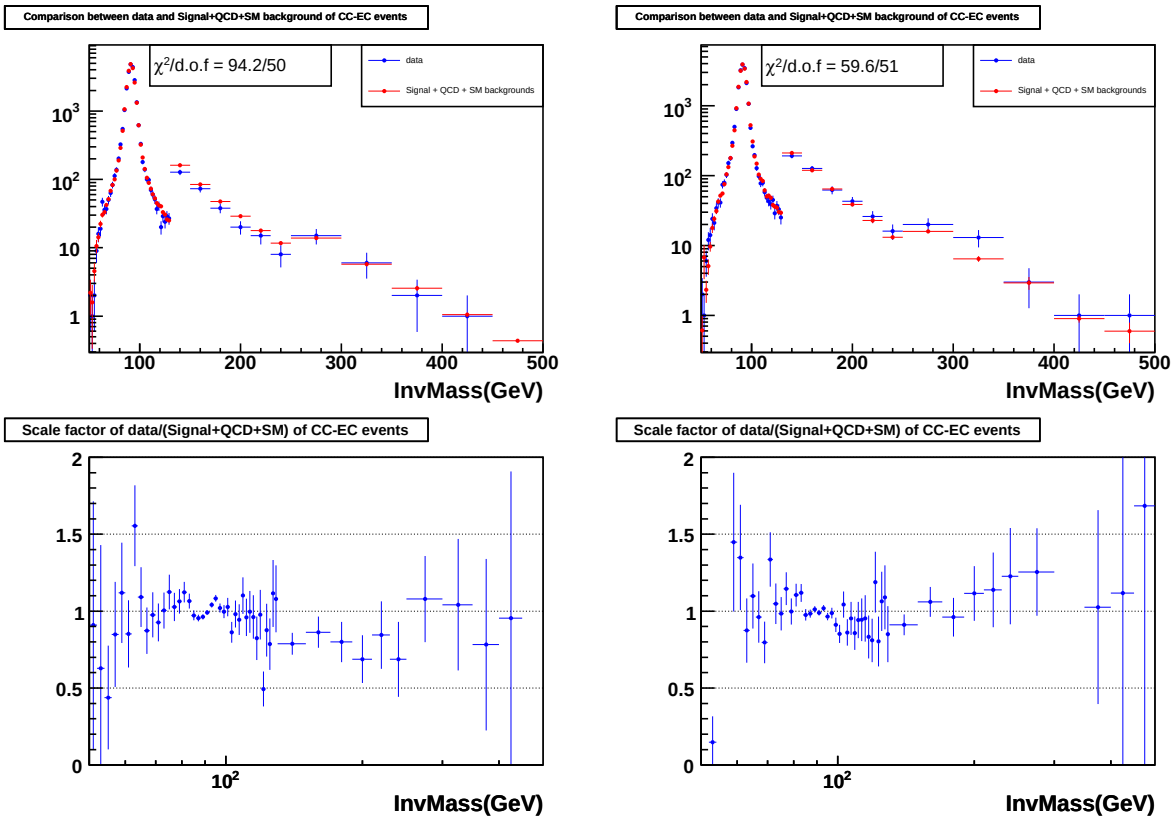

Figure D.2: Invariant mass comparison for CC-EC events and also the ratio between data and signal + backgrounds. Left two plots are results of Trk events, Right two plots are results of NoTrk events.

D. CCEC EVENTS: WITH OR WITHOUT EC TRACK MATCH

In the end, we also divide our QCD sample into two parts, one is EC electron with track-match, another is EC electron without track-match. Trk and NoTrk QCD shape can be found in Fig.D.3

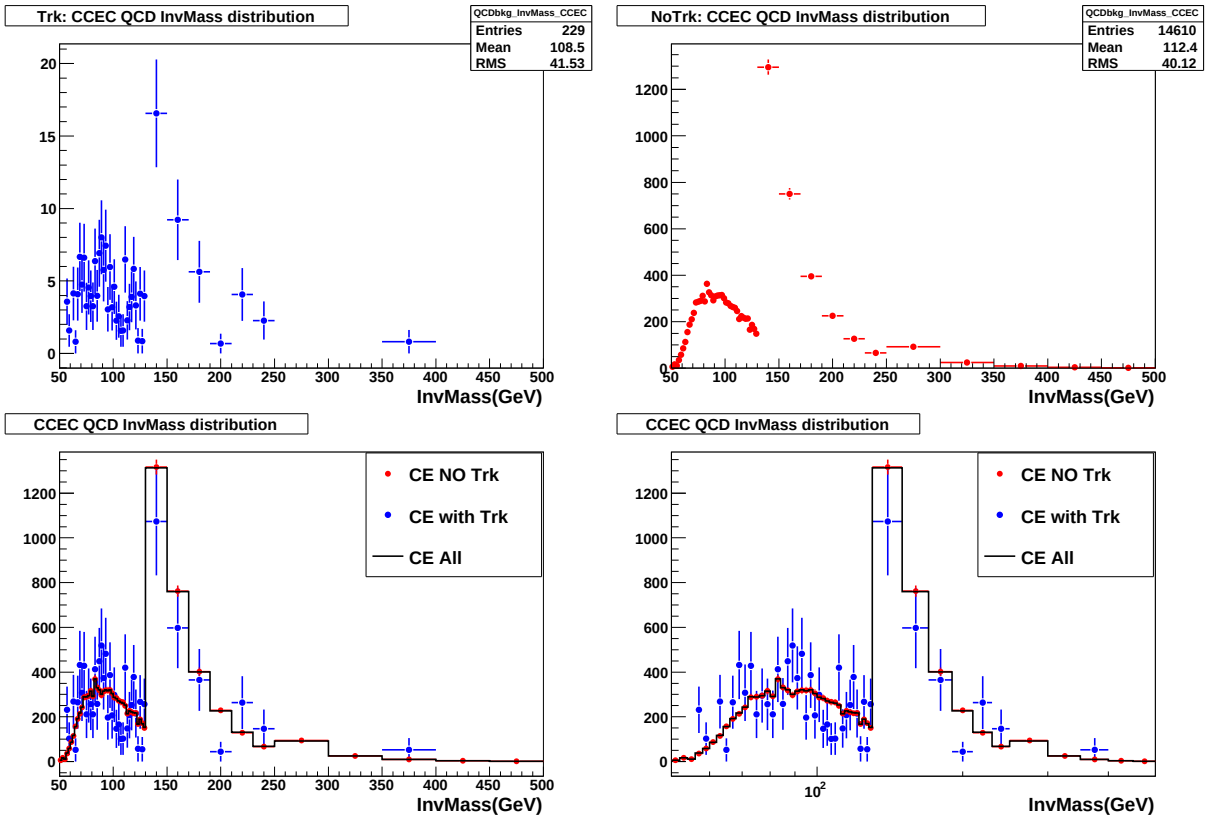

Figure D.3: Top-Left is QCD shape of Trk events; Top-Right is QCD shape of NoTrk events; Bottom-Left is comparison of NoTrk and Trk, both of them are normalized into black line; Bottom-Right is the logx scale of Bottom-Left plots.

D.3 Trk and NoTrk comparison

With QCD shape shown in Fig.D.3, we fit Trk and NoTrk in difference InvMass region. QCD contribution and χ^2 between data and signal + backgrounds in difference InvMass region are shown in Tab.D.1 and Tab.D.2.

InvMass(GeV)	70-110	70-130	70-150	50-150
qcd contribution	208.2	26.3	-0.96	27.3
χ^2	87.5	60.7	60.2	60.9

Table D.1: Trk events QCD contribution and χ^2 between data and signal + backgrounds fitted with difference InvMass region.

InvMass(GeV)	70-110	70-130	70-150	50-150
qcd contribution	381.4	364.5	343.9	347.9
χ^2	59.9	56.9	54.5	55.1

Table D.2: NoTrk events QCD contribution and χ^2 between data and signal + backgrounds fitted with difference InvMass region.

In here, we will use 50-150 GeV fitting results to do some tests If the fitting results are stable, the QCD contribution of Trk and NoTrk should consistence with All CC-EC results, the comparison results can be found in Tab.D.3

With the fitting mass region 50-150 GeV, we can get QCD contribution in each mass bins. Using fixed QCD shape and QCD contribution, results of Trk and NoTrk has a reasonable agreement. The InvMass comparison plots are shown in Fig.D.4, raw A_{FB} and unfolded A_{FB} comparison plots are shown in Fig.D.5 and comparison between MC A_{FB} of Trk and NoTrk are shown in Fig.D.6.

D. CCEC EVENTS: WITH OR WITHOUT EC TRACK MATCH

Mass	All	NoTrk	Trk	NoTrk + Trk
50 - 60	4.3	3.7	0.76	4.5
60 - 70	25.4	22.3	2.32	24.6
70 - 75	22.2	19.4	1.81	21.2
75 - 81	29.9	26.3	1.98	28.3
81 - 86.5	30.9	27.2	1.99	29.2
86.5 - 89.5	15.7	13.7	1.49	15.2
89.5 - 92	12.6	11.0	1.21	12.2
92 - 97	26.5	23.2	2.19	25.4
97 - 105	38.6	34.0	1.98	36.0
105 - 115	41.4	36.5	2.01	38.5
115 - 130	47.8	42.0	3.73	45.7
130 - 180	76.2	67.2	4.16	71.4
180 - 250	19.8	17.4	1.52	18.9
250 - 500	4.4	3.9	0.12	4.0

Table D.3: QCD contribution for difference samples in each mass bins. We can see NoTrk+Trk has good agreement with All(Fitted with Mass in 50-150 GeV).

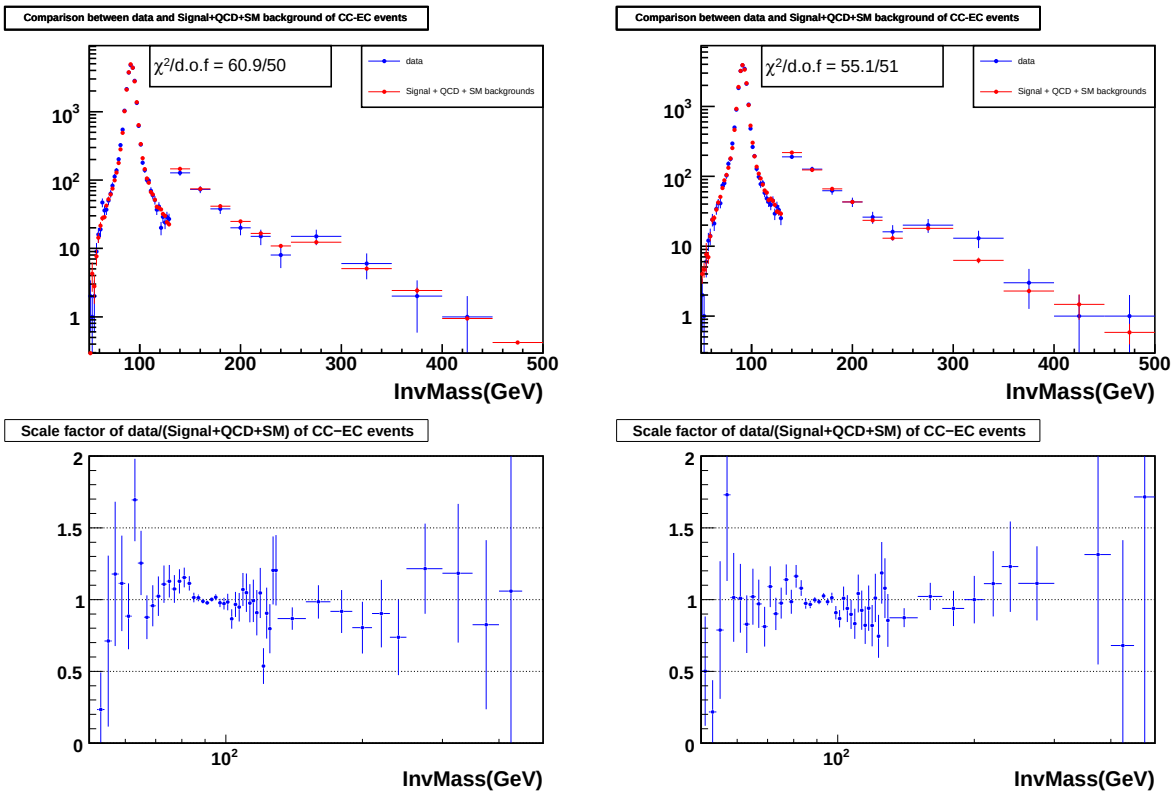

Figure D.4: Invariant mass comparison for CC-EC events and also the ratio between data and signal + backgrounds. Left two plots are results of Trk events, Right two plots are results of NoTrk events.

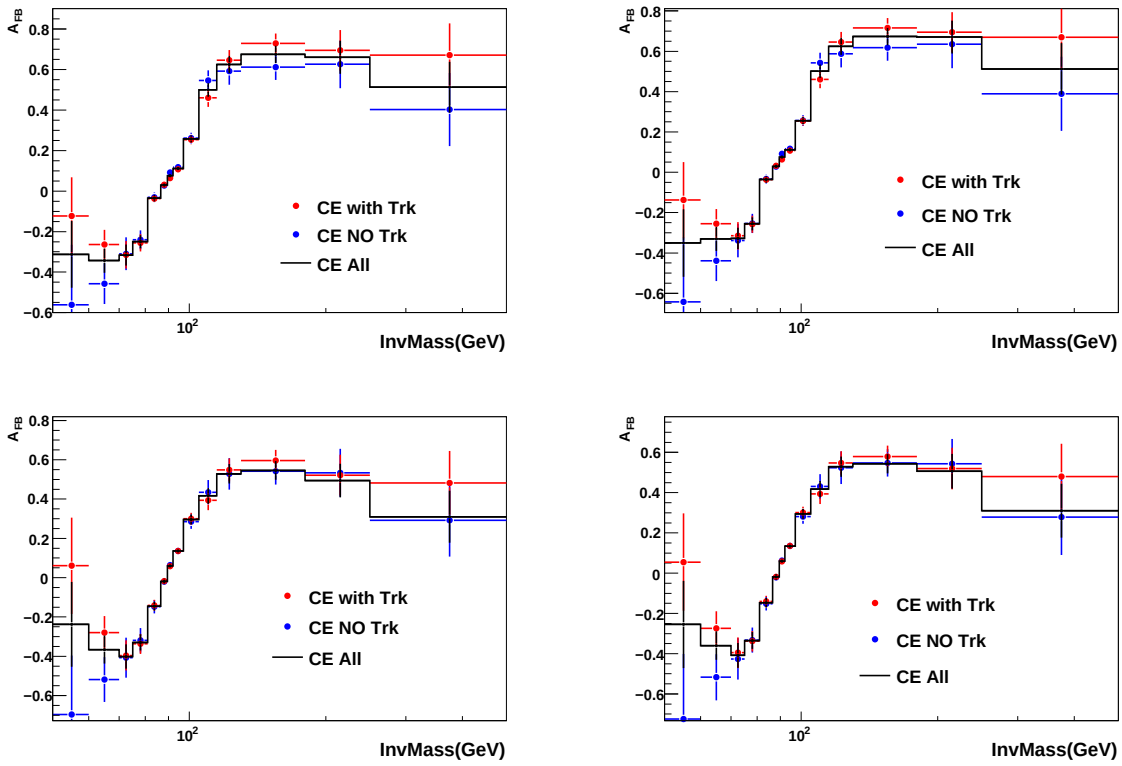

Figure D.5: Top two plots are comparison plots of raw A_{FB} between Trk, NoTrk and All. Bottom two plots are comparison plots of unfolded A_{FB} between Trk, NoTrk and All. For $W + X$ backgrounds contribution, we use both *Pythia* and *Alpgen* $W + X$ samples, left two plots are results with *Pythia* $W + X$ samples; right two plots are results with *Alpgen* $W + X$ samples. There is no big difference between Left and Right plots.

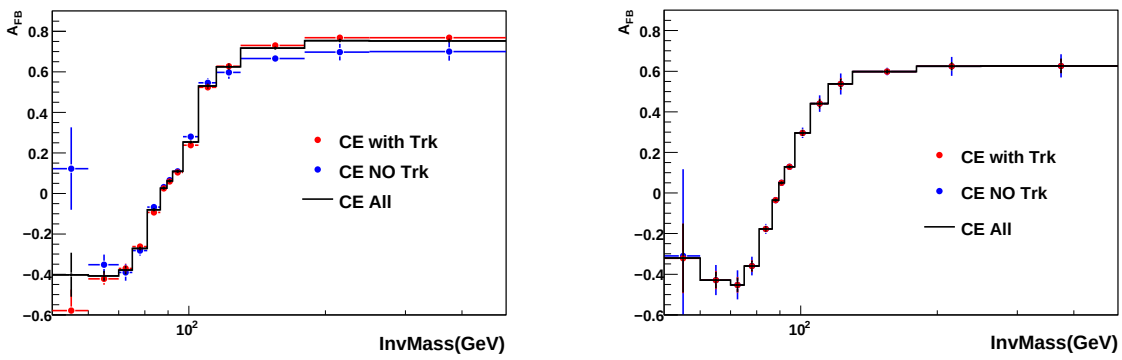

Figure D.6: MC Raw A_{FB} comparison for CC-EC events. Left plot is raw A_{FB} comparison, Right plot is unfolded A_{FB} comparison. The first two mass bins have very poor statistics, difference between data and MC are mainly come from statistics.

D. CCEC EVENTS: WITH OR WITHOUT EC TRACK MATCH

Appendix E

Electron energy modeling

The electron energy-loss corrections have been applied on the measured electron energy from the collider data to reduce the electron energy nonlinearity. We also have reasonable amount of dead material in the full MC simulation that is comparable with what have in the real detector. Previously studies from the W mass group indicate the electron energy response is pretty linear for electrons with energy below ~ 100 GeV, since we are also interested in high mass Drell-Yan events, we also need to estimate the effect of electron energy non-linearity for the AFB measurement. As described in Sec. 5.3.1, we assume the measured electron energy in real data and the Geant-simulated electron energy have a linear relation $E' = \alpha \times E_0$, to investigate the effect of non-linearity, we modify the function to $E' = \alpha \times E_0 + \gamma(E_0 - 45)^2$, the parameter γ is introduced to reflect the energy non-linearity and 45 GeV is the average energy of the electrons from Z decays. We then use the data around the Z peak region ($70 < M_{ee} < 110$ GeV with 2 GeV bin width) and compare with the M_{ee} predictions using different values of α and γ. We then minimize the χ^2 between the M_{ee} distributions from data and Geant

MC simulation to extract the values of α and γ.

The best α and γ values for CC and EC electrons are separately shown in Fig. E.1 and also in Tab. E.1.

To virtually see the effect of γ on the invariant mass distribution, we compared the Geant MC predictions with and without the non-linearity term for both CC-CC and CC-EC events, the comparisons are shown in Fig. E.2 and E.3 to demonstrate agreement in Z peak mass region and effect in the high mass region.

Another fact is the energy linearity has been well tested for electrons with energy below $\sim$ 100 GeV, according to the above formula, a non-linearity term $\gamma = 0.0003$ will only change the energy of a 100 GeV electron by 1 GeV, which is small compared with the bin size of 70 GeV and 250 GeV that we have for the two highest invariant mass bins. The effect on the A_{FB} measurement is further reduced since the energy non-linearity will affect the forward and backward events in the same direction.

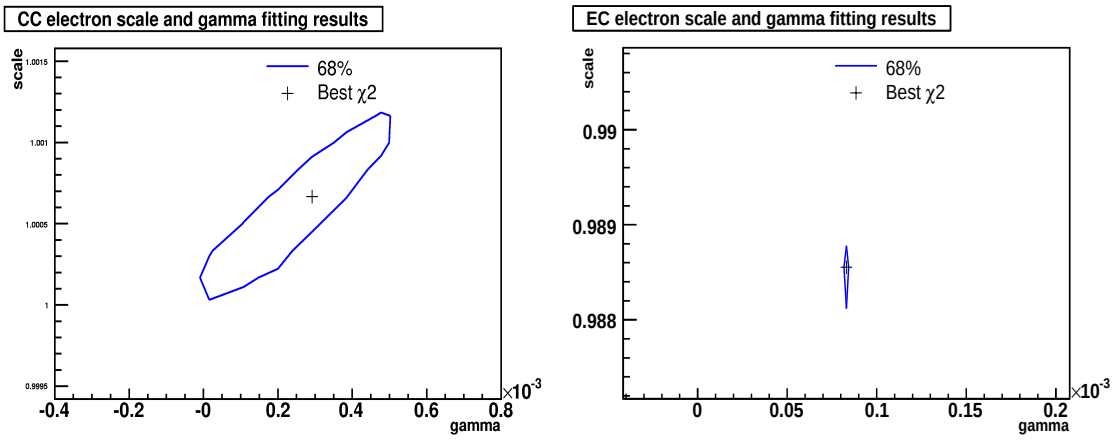

Figure E.1: Electron non-linearity parameters, the black cross corresponds to the best fitted values, the blue contour is 68% contour for α and γ. The left plot is for CC electron, and the right one is for EC electron.

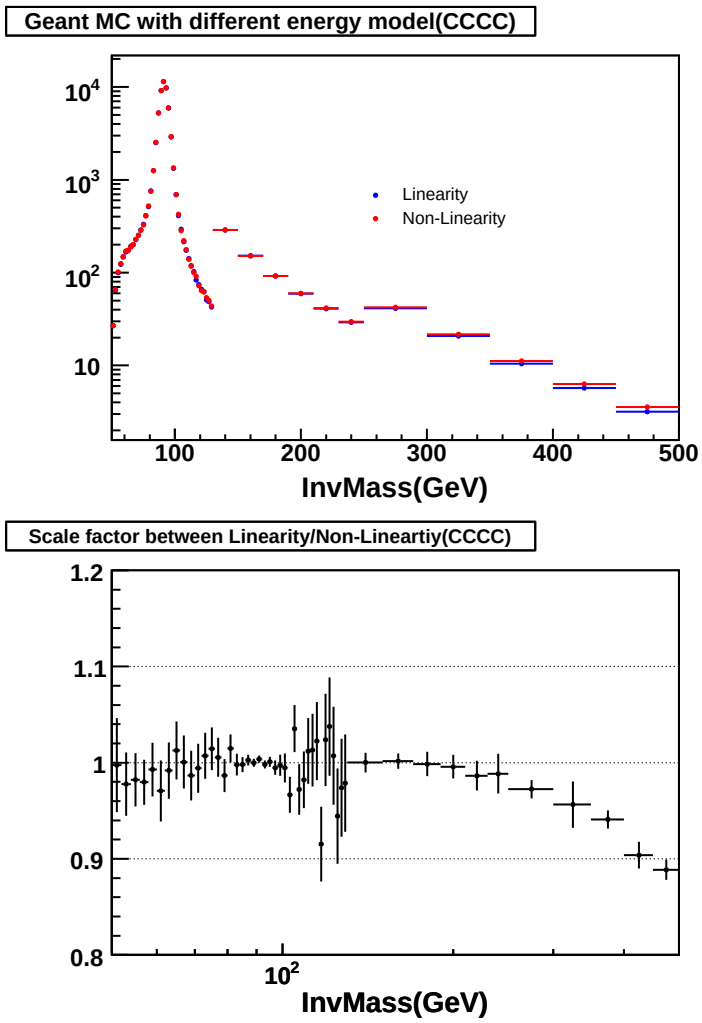

Figure E.2: Linearity and non-linearity energy correction comparison for Geant MC CCCC events. The top plot is InvMass distribution comparison between linearity and non-linearity correction, the bottom plot is the scale factor between linearity InvMass and non-linearity InvMass.

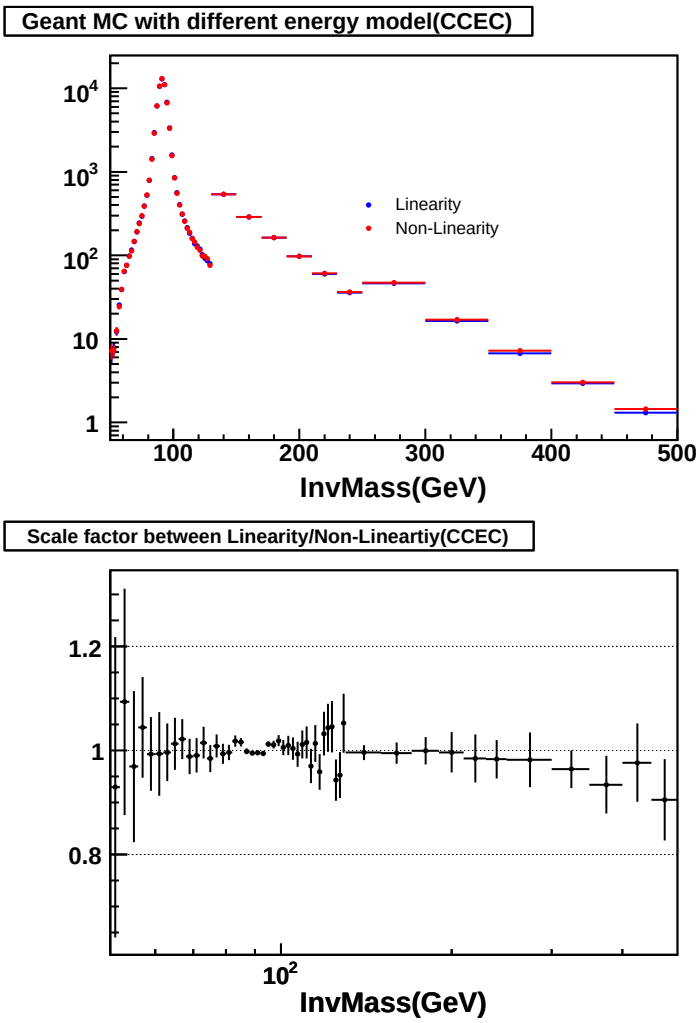

Figure E.3: Linearity and non-linearity energy correction comparison for Geant MC CCEC events. The top plot is InvMass distribution comparison between linearity and non-linearity correction, the bottom plot is the scale factor between linearity InvMass and non-linearity InvMass.

	α	γ
CC	1.00067 $\pm$ 0.00015	0.00029 $\pm$ 0.0001
EC	0.98855 $\pm$ 0.00036	0.000083$\pm$ 0.0000068

Table E.1: CC and CC electron non-linearity parameters values.

References

[1] S.L. Glashow, Nucl. Phys. **B22** 579 (1961); A. Salam and J.C. Ward, Phys. Rev. Lett. **13** 168 (1994); S. Weinberg, Phys. Rev. Lett. **19** 1264 (1967). 1, 5

[2] M. Gell-Mann, Phys. Lett. 8, 214 (1964); G. Zweig, CERN preprint TH401 (1964). 1

[3] D. Karlen, Plenary talk "Experimental Status of the Standard Model" at the International Conference on High Energy Physics, ICHEP98, Cancouver, July 1998. 2

[4] W.-M. Yao *et al.* (Particle Data Group), J. Phys. G 33, 1 (2006) and 2007 partial update for the 2008 edition. 2, 166

[5] B.W. Le and J. Zinn-Justin, Phys. Rev. D 5, 3121, 3137, 3155 (1972) 5

[6] G.T. Hooft and M. Veltman, Nucl. Phys. B 44, 189 (1972); Nucl. Phys. B 50. 318 (1972) 5

[7] F.J. Hasert *et al.* [Gargamelle Neutrino Collaboration], Phys. Lett. B **46**, 138 (1973) 5

[8] A.C Benvenuti *et al.*, Phys. Rev. Lett. **32**, 800 (1974) 5

[9] M. Holder *et al.*, Phys. Lett. B **71**, 222 (1977) 5

[10] G. Arnison *et al.*, Phys. Lett. 122B, 103 (1983); 126B, 398 (1983); 129B, 273 (1983); 134B, 469(1984); 147B, 241 (1984). 5

[11] M. Herrero, "The Standard Model", hep-ph/9812242.

[12] D. Perkins, "Introduction to High Energy Physics". 5

[13] V. Barger and R. Phillips, "Collider Physics", Addison Wesley, 1993. 5

[14] E. Fermi, Nuovo Cimento 11 (1934); Z. Phys. **88** (1934). 7

[15] R.M. Barnett *et al.*, Phys. Rev. **54**, 1 (1996). 8

[16] CERN-PPE/95-172, LEP Electroweak Working Group, 1995. 8

[17] S. C. Bennett and C. E. Wieman, Phys. Rev. Lett. **82**, 2484. 12

[18] 2004 AIPC 721 367Y, Younus, I. 2004, American Institute of Physics Conference Series, 721, 367 12

[19] J.C. Collins and D.E. Soper, Phys. Rev. D **16**, 2219 (1977). 21

[20] J. Ellison and J. Rha, "Measurement of the Forward-Backward Asymmetry in e^+e^- and $\mu^+\mu^-$ events with DØin RunII", DØNote 3756(2000). xviii, 24

[21] The LEP Collaboration ALEPH, DELPHI, L3, OPAL, the LEP Electroweak Working Group, and the SLD Heavy Flavour and Electroweak Groups, LEPEWWG/2003-02, Dec, 2003. xvii, 14, 19, 169

[22] G.P. Zeller *et. al.*, NuTeV Collaboration, Phys. Rev. Lett. 88, 091802 (2002) [Erratum-ibid. 90, 239902 (2003)]. 14, 166

[23] A. Sirlin, Phys. Rev. **D22**, 971 (1980); A. Sirlin, Phys. Rev. **D29**, 89 (1984); D.C. Kennedy *et. al.,* Nucl. Phys. **B321**, 83 (1989); D.C. Kennedy and B.W. Lynn, Nucl. Phys. **B322**, 1 (1989); D.Yu. Bardin *et. al.,* Z. Phys. **C44**, 493 (1989); W. hollik, Fortsch, Phys. **38**, 165 (1990). 9

[24] V.A. Novikov, L.B. Okun, and M.I. Vysotsky, Nucl. Phys. **B351**, 35 (1993) 10

[25] G. Degrassi, S. Fanchiotti, and A. Sirlin, Nucl. Phys. **B351**, 49 (1991) 11

[26] T. Affolder *et. al.*, CDF collaboration, Phys. Rev. Lett. 87, 131802 (2001).

[27] D. Acosta *et. al.*, CDF collaboration, Phys. Rev. D71, 052002 (2005). xvii, 19, 108

[28] V.M. Abazov, *et al*, Phys. Rev. Lett. 101, 191801 (2008). 14

[29] J. Thompson, "Introduction to Colliding Beams at Fermilab", FERMILAB-TM-1909 (1994); Run II Handbook, http://www-bd.fnal.gov/runII/; Accelerator Concepts, V3.0 (2002). 25

[30] S. Abachi *et al.* (DØ Collaboration), Nucl. Instr. and Methods, **A338**, 185 (1994). 28

[31] S. Abachi *et al.* (DØ Collaboration), Phys. Rev. Lett. **74**, 2632 (1995); F. Abe *et al.* (CDF Collaboration), Phys. Rev. Lett. **74**, 2626 (1995). 28

[32] DØ Collaboration, DØ Note **1996**, "The DØ Upgrade: The Detector and Its Physics"; V. Abazov *et al.* (DØ Collaboration), in preparation for submission to Nucl. Instr. and Methods. 29

[33] DØ Upgrade Collaboration, "DØ Silicon Tracker Technical Design Report", http://www-d0.fnal.gov/trigger/stt/smt/smt_tdr.ps. 30

[34] DØ Collaboration, DØ Note **4164**, "Central Fiber Tracker Technical Design Report". 30

[35] DØ Collaboration, DØ Note **3014**, "Design Report of the Central Preshower Detector for the DØ Upgrade". 33

[36] DØ Collaboration, DØ Note **2894**, "The DØ Upgrade: Forward Preshower, Muon System and Level 2 Trigger". 33

[37] S. Abachi *et al.* (DØ Collaboration), Nucl. Instr. and Methods, **A324**, 53 (1993). 36

[38] DØ Collaboration, "Calorimeter Electronics", http://www-d0.fnal.gov/hardware/cal. 39

[39] R. Zitoun, DØ Note **3997**, "Study of the Non Linearity of the DØ Calorimeter Readout Chain"; J. Kotcher, "Upgrade Plans for the DØ Calorimeter"; J. Kourlas, "Calorimeter Electronics for the DØ Upgrade". 39

[40] Q. Zhu, Ph.D. thesis, New York University, 1994, "Measurement of the W Boson Mass in Proton-Antipr oton Collisions at $\sqrt{s} = 1.8$ TeV" (unpublished). 44

[41] T.C. Heuring, Ph.D. thesis, State University of New York at Stony Brook, 1993, "Electrons in the DØ Calorimeter: A Study of the Systematic Biases in the Measurement of the W Mass" (unpublished). 44

[42] B. Abbott *et al.* (DØ Collaboration), Phys. Rev. Lett. **80** (1998); B. Abbott *et al.* (DØ Collaboration), Phys. Rev. **D58** (1998); B. Abbott *et al.* (DØ Collaboration), Phys. Rev. Lett. **84** (2000); B. Abbott *et al.* (DØ Collaboration), Phys. Rev. **D62** (2000); V. Abazov *et al.* (DØ Collaboration), Phys. Rev. **D66** (2002). 44

[43] C. Brown *et al.* (DØ Collaboration), Nucl. Instr. and Methods, **A279** 331 (1989). 44

[44] H. Yin, Trigger Studies Group Meeting, Sep 4 and Oct 30, 2007. 49

[45] H. Yin, Trigger Studies Group Meeting, Feb. 21, 2008. 50

[46] T. Andeen *et al.*, FERMILAB-TM-2365 (2007). 50

[47] D. Khatidze, W/Z properties meeting, Oct 31, 2007. 52

[48] A. Askew, D. Khatidze, H. Yin and J. Zhu, DØ note 5564. 52, 122

[49] J. Stark, Joint Algorithms/Physics Conveners Meeting, April 10, 2009. 74

[50] H. Yin, EMID meeting during collaboration week, Oct. 1, 2009. 74

[51] M. Vesterinen, EMID meeting during collaboration week, Oct. 1, 2009. 76

[52] The ALEPH, DELPHI, L3, OPAL, SLD Collaborations,the LEP Electroweak Working Group,the SLD Electroweak and Heavy Flavour Groups, Physics Reports, Volume 427 Nos. 5-6 (May 2006) 257-454. 76

[53] R. Hamberg, W.L. van Neevrven, and T. Matsuura, Nucl. Phys. B359, 343 (1991). 86

[54] J. M. Campbell and R. K. Ellis, Phys. Rev. D60, 113006 (1999). 86

[55] T. Sjostrand *et. al.*, Comp. Phys. Commun. 135, 238 (2001). 22, 59

[56] J. Pumplin *et. al.*, JHEP, 07, 012 (2002). 59, 162

[57] T. Nunnemann, DØ note 4476. 73

[58] R. Hamberg, W.L. van Neerven, and T. Matsuura, Nucl. Phys. B359, (1991). 73

[59] C. Balazs and C.P. Yuan, Phys. Rev. D56 (1997). 74

[60] S. Yacoob, J. Hays, H. Schellman, DØ note 5273. 74

[61] U. Baur, J. Ellison and J. Rha, hep-ex/0011009. 164, 165